FOLATE RECEPTOR TARGETED AND PEGYLATED PLGA NANOPARTICLES FOR ENHANCING THERAPEUTIC EFFICACY OF NOSCAPINE DERIVATIVES IN BREAST CANCER

Thesis Submitted to Sambalpur University
in Partial Fulfilment of the Requirements for the Degree of

DOCTOR OF PHILOSOPHY
IN

BIOTECHNOLOGY

by

NAMITA BHOI
Regd. No.-05/2023/Biotechnology

Under the joint Supervision of

Supervisor: *Dr. Pradeep Kumar Naik, Professor, Department of Biotechnology & Bioinformatics, Sambalpur University*

Co-supervisor: *Dr. Srinivas Kantevari, Chief Scientist, Indian Institute of Chemical Technology*

DEPARTMENT OF BIOTECHNOLOGY & BIOINFORMATICS,

SAMBALPUR UNIVERSITY, JYOTI VIHAR, BURLA, SAMBALPUR-768 019, ODISHA

DECLARATION

I hereby declare that the work reported in the Ph.D. thesis entitled ***"FOLATE RECEPTOR TARGETED AND PEGYLATED PLGA NANOPARTICLES FOR ENHANCING THERAPEUTIC EFFICACY OF NOSCAPINE DERIVATIVES IN BREAST CANCER"*** *submitted at* ***Sambalpur University*** *is the original report of my research, under the joint guidance of* ***Dr. Pradeep Kumar Naik****, Department of Biotechnology and Bioinformatics, Sambalpur University and* ***Dr. Srinivas Kantevari****, IICT, Hyderabad.*

I have not submitted this work previously to any other organization for any degree or professional qualification. I have confirmed the norms and guidelines given in the ethical code of conduct of the university. Whenever I have used materials (data, theoretical analysis and text) from other sources, I have given due credit to them by citing them in the text of the thesis and given their details in the references.

Date: 15.12.2025 **(Mrs. Namita Bhoi)**

COURSE WORK AND COMPREHENSIVE EXAMINATION COMPLETION CERTIFICATE

This is to certify that ***Mrs. Namita Bhoi****, bearing Registration No-* ***05/2023/Biotechnology****, a bonafide Ph.D. scholar of Sambalpur University, Sambalpur, who has successfully completed her course work and comprehensive examination, which is a part of her Ph.D. Programme.*

Date: 15.12.2025

Dr. Pradeep Kumar Naik
Professor & Head
Dept. of Biotechnology & Bioinformatics,
Sambalpur University, Jyoti Vihar,
Burla, Sambalpur, Odisha, India.

Dr. Pradeep K. Naik
Professor and Head
Dept. of Biotechnology
& Bioinformatics

SAMBALPUR UNIVERSITY
JYOTI VIHAR – 768019
SAMBALPUR, ODISHA
Mob.: +91-9479268802
Fax: (0663) – 2430158
E-mail: pknaik1973@gmail.com

CERTIFICATE

*This is to certify that the research work entitled, "**FOLATE RECEPTOR TARGETED AND PEGYLATED PLGA NANOPARTICLES FOR ENHANCING THERAPEUTIC EFFICACY OF NOSCAPINE DERIVATIVES IN BREAST CANCER**" submitted by **Mrs. Namita Bhoi (Regd. No: 05/2023/Biotechnology)** at **Sambalpur University, Orissa, India** is a bonafide record of her original work carried out under my supervision. This work has not been submitted partially or wholly to any other University orInstitute for any degree or diploma. I recommend this thesis in fulfillment of the award of the degree of **Doctor of Philosophy** in **Biotechnology.***

Date: 15.12.2025

Prof. (Dr.) Pradeep Kumar Naik
Dept. of Biotechnology & Bioinformatics,
Sambalpur University, Jyoti Vihar,
Burla, Sambalpur, Odisha, India.

सीएसआईआर-भारतीय रासायनिक प्रौद्योगिकी संस्थान
CSIR-Indian Institute of Chemical Technology
(विज्ञान एवं प्रौद्योगिकी मंत्रालय, भारत सरकार / Ministry of Science and Technology, Govt. of India)
तारनाका, हैदराबाद - 500007, तेलंगाना, भारत / Tarnaka, Hyderabad - 500 007, Telangana, INDIA

Dr. Srinivas Kantevari
Chief Scientist
Department of Fluoro-Agrochemicals

CERTIFICATE

*This is to certify that the research work entitled, "**FOLATE RECEPTOR TARGETED AND PEGYLATED PLGA NANOPARTICLES FOR ENHANCING THERAPEUTIC EFFICACY OF NOSCAPINE DERIVATIVES IN BREAST CANCER**" submitted by **Mrs. Namita Bhoi** at **Sambalpur University, Orissa, India** is a bonafide record of her original work carried out under my co-supervision. This work has not been submitted partially or wholly to any other University or Institute for any degree or diploma. I recommend this thesis in fulfillment of the award of the degree of **Doctor of Philosophy in Biotechnology**.*

Date: 11th August 2025 *Dr. Srinivas Kantevari*

ACKNOWLEDGMENT

I would like to express my deep sense of gratitude and gratefulness to ***Prof. Pradeep Kumar Naik****, Department of Biotechnology and Bioinformatics, Sambalpur University, for providing this lifetime opportunity to work under him. I express my heartiest thankfulness and indebtedness to him, for his guidance, support, inspiration and constant supervision as well as for providing all the necessary information, facilities and resources for the completion of my PhD research.*

I'm grateful to extending my sincere thanks to all my reverenced teachers, ***Prof. Amiya Kumar Patel, Dr. Bhawani Prasad Bag, Dr. Birendra Behera, and Dr. Chumkijini Chattria*** *of Department of Biotechnology and Bioinformatics, Sambalpur University who have been kind enough to extend their generously and help at the sundry phases of my research whenever I approached them during my research tenure.*

I am also grateful to ***Mr. Prakash C. Pradhan****,* ***Mr. Seshyana Bagarti****,* ***Mr. Ramesh Podh****,* ***Mr. Rajat Kathar****, and all the staffs of Department of Biotechnology and Bioinformatics who always remain with me and have extended their assistance to me whenever I needed their help that cannot be forgotten.*

I am highly grateful to ***Dr. Srinivas Kantevari****, Principal Scientist, Crop Protection Chemical Divisions, IICT, Hyderabad, giving me an opportunity to carry my PhD work in his laboratory. I would also thank him for providing me extended facilities to complete my PhD research work.*

I am grateful to ***Dr. Ishwar Baitharu****, Assistant Professor, Department of Environmental Sciences, Sambalpur University, for his expert guidance, unconditional support and necessary advice for my research work.*

I would also like to thanks ***Dr. Manas Kumar Pradhan*** *(IISER, Bhopal),* ***Mr. Manas Kumar Sahoo*** *(NISER, Bhubaneswar), and* ***Mr. Tankadhar Behera*** *(Sambalpur University) for instrumental support.*

I extend my thanks to all my lab mates, ***Dr. Prajna Parimita Mohanta****,* ***Dr. Pratyush Pragyandipta****,* ***Dr. Lilesh kumar Pradhan****,* ***Dr. Swaraj Kumar Babu****,* ***Dr. Geeta Kumari Wasupalli, Dr. Srichandan Rath****,* ***Mr. Divya Ranjan Sahoo, Dr. Surjeet Verma, Dr. Abhijit Sahu, Monika, Eeshara, Mustaq, Alam, Tapan, Reshma, Baishali, and Archana,*** *COE-NPT laboratory, Dept. of*

Biotechnology and Bioinformatics for their inspirational words, co-operation and encouragement in carrying out my research work. Also, I thank ***Rajendra*** *and* ***Ranjan*** *for their valuable help.*

My sincere and deepest gratitude to my ***parents and parent in-laws, brother, sisters, nephew and my niece*** *for their unfaltering love, support and cooperation provided to me throughout my PhD work and life.*

I also express my sincere gratitude to my beloved husband ***Dr. Bomkesh Bhoi*** *for his constant support and encouragement.*

The financial assistance from Department of Science and Technology, Government of India in the form of ***DST- INSPIRE*** *Fellowship for pursuing my Ph.D. work is greatly acknowledged.*

I would like to place on record my sincere thanks to the ***Centre of Excellence in Natural Products and Therapeutics (COE-NPT)*** *laboratory, and* ***DBT-BUILDER*** *laboratory, Department of Biotechnology and Bioinformatics for providing the laboratory facility to carry out my research work.*

Last but not least, I am thankful to the Almighty, whose guidance has sustained me through every challenge of this journey. May your name be exalted, honored and glorified.

Namita Bhoi

CONTENTS

LIST OF TABLES

LIST OF FIGURES

ABBREVIATIONS

PNs	Polymeric Nanoparticles
EPR	Enhanced Permeability and Retention effect
PLGA	Poly Lactic-co-Glycolic Acid
PEG	Polyethylene Glycol
FA	Folic Acid
PPF NPs	PLGA-PEG-FA nanoparticles
ROS	Reactive Oxygen Species
9-Br-Nos	9-bromo-noscapine
DCC	Dicyclohexylcarbodiimide
NHS	N-hydroxy succinimide
DMSO	Dimethyl sulfoxide
DCM	Dichloromethane
MTT	3-(4,5-dimethylthiazol2-yl)-2,5-diphenyltetrazolium bromide
DMEM	Dulbecco's Modified Eagle Medium
FBS	Fetal Bovine Serum
FTIR	Fourier-transform infrared
NMR	Nuclear magnetic resonance
ppm	Parts per million
PD	PLGA-Drug
PPFD	PLGA-PEG-FA-Drug
PVA	Polyvinyl alcohol
DLS	Dynamic light scattering
EE	Encapsulation efficiency
PBS	Phosphate buffered saline
MMP	Mitochondrial membrane potential
PIC	Protease inhibitor cocktail
PVDF	Polyvinylidene difluoride
H&E	Hematoxylin and eosin
SD	Sprague-Dawley
PDI	Polydispersity index
HD	Hydrodynamic diameter
Mβ-CD	Methyl-β-cyclodextrin
UV–Vis	Ultraviolet-visible
XRD	X-ray diffraction
SEM	Scanning electron microscopy
TGA	Thermo gravimetric analysis
STR	Short tandem repeat
PME	Particle Mesh Ewald
PB	Poisson-Boltzmann
GB	Generalized Born
TMS	Tetramethylsilane
PXRD	Powder X-ray diffraction
RMSD	Root mean square deviation
Rg	Radius of gyration
PI	Propidium iodide

ABSTRACT

Cancer continues to be a leading cause of mortality worldwide, leading to the urgent need for safer and more effective chemotherapeutic agents as well as delivery systems. Noscapine, a naturally occurring benzylisoquinoline alkaloid, has shown significant promise as an anticancer agent because of its ability to bind tubulin and disrupt microtubule dynamics without triggering severe toxicity in normal cells. Noscapine derivatives (known as Noscapinoids), which are structurally modified analogues of the naturally occurring alkaloid noscapine, have shown enhanced anticancer potential by binding tubulin and disrupting microtubule dynamics with improved efficacy and specificity. However, its clinical translation has been hampered by poor aqueous solubility, limited bioavailability, and a lack of tumor specificity. In this context, the present study explores the design and development of advanced drug delivery systems using both synthetic polymeric nanoparticles and cyclodextrin-based inclusion complexes to overcome these challenges and enhance the therapeutic efficacy of noscapinoids. We synthesized a targeted polymeric delivery system using poly(lactic-co-glycolic acid) conjugated with polyethylene glycol and folic acid (PLGA-PEG-FA) for encapsulation of the developed noscapinoids. The rationale behind this design was to leverage the biocompatibility and biodegradability of PLGA, the stealth and solubilizing properties of PEG, and the tumor-targeting ability of folic acid, which binds to overexpressed folate receptors on many cancer cells. Noscapine derivatives, specifically bromo-noscapine (9-Br-Nos), was encapsulated into these nanoparticles via an optimized emulsion coprecipitation technique. The resulting nanoparticles were thoroughly characterized in terms of particle size, morphology, drug loading efficiency, and entrapment efficiency via techniques such as dynamic light scattering (DLS), scanning electron microscopy (SEM), and high-performance liquid chromatography (HPLC). The optimized formulation exhibited a uniform spherical morphology with an average particle size of 122±8 nm and a polydispersity index (PDI) of 0.28. The nanoformulation also showed a high entrapment efficiency of 94.5%, and the drug loading efficiency was approximately 9.45%. SEM analysis also confirmed the aggregation of smooth and spherical nanoparticles. Furthermore, *in vitro* release studies demonstrated sustained release behavior up to 72 hours, which resulted in a cumulative drug release of approximately 60%. In contrast, the free 9-Br-Nos released approximately 100% of the total drug within 2 hours, possibly because of the rapid diffusion of the drug absorbed on the surface of the nanoparticles. These findings indicate that drug-loaded PLGA-PEG-FA nanoparticles have the potential for prolonged systemic circulation and controlled drug availability at the tumor site. In

addition, compared with nontargeted PLGA nanoparticles, the coumarin-6-loaded folate-conjugated formulation exhibited significantly greater cellular uptake, as confirmed by fluorescence microscopy. Cytotoxicity assays (MTT) demonstrated significantly greater anticancer activity for the PLGA-PEG-FA nanoparticles than for the drug-loaded PLGA nanoparticles and the free drug. PLGA-PEG-FA nanoparticles showed the greatest cytotoxicity against different breast cancer cell lines (MDA-MB-231 and MCF-7), with IC_{50} values of 31.27 μg/mL (MDA-MB-231) and 38.81 μg/mL (MCF-7) due to folate receptor-mediated targeting. PLGA nanoparticles exhibited moderate cytotoxicity (93.81 μg/mL and 95.54 μg/mL), whereas free 9-Br-Nos was least effective (230.1 μg/mL and 213.3 μg/mL) due to poor solubility and cellular uptake. Additionally, 9-Br-Nos-loaded PLGA-PEG-FA nanoparticles induced prominent apoptotic changes, including chromatin condensation and nuclear fragmentation. This also significantly disrupted the mitochondrial membrane potential and promoted enhanced ROS-mediated apoptotic activity by increasing oxidative stress and activating the apoptotic pathway more effectively than the free drug did. Furthermore, these folates containing PLGA-PEG nanoparticles demonstrated superior efficacy in disintegrating 3D tumor spheroids, reducing their size from 534.90 μm to 306.34 μm by day 5, whereas only a moderate reduction in free 9-Br-Nos (576.89 μm to 443.05 μm) was observed, highlighting their enhanced therapeutic potential in mimicking *in vivo* tumor environments. Western blot analysis further confirmed enhanced apoptosis with PLGA-PEG-FA nanoparticle treatment, which resulted in the upregulation of proapoptotic Bax and cleaved caspase-3 and the downregulation of antiapoptotic Bcl-2, whereas moderate changes in 9-Br-Nos and no significant alterations were detected in the control group, underscoring the superior apoptotic efficacy of the PLGA-PEG-FA nanoparticles. Compared with free 9-Br-Nos, the PLGA-PEG-FA nanoparticles demonstrated significantly improved *in vivo* pharmacokinetic properties, including a higher Cmax, prolonged half-life (~26 hours), increased area under the curve (AUC), and reduced clearance, indicating sustained drug release and extended systemic retention. Blood biochemical and hematological parameters remained within normal limits, confirming the systemic safety of the formulation. Histopathological analysis also confirmed the safety of the formulation, which resulted in no significant alterations in major organs. Additionally, in a breast cancer xenograft model, the nanoparticle-treated group exhibited pronounced tumor regression compared to the free drug group, supporting its superior anticancer efficacy. These findings collectively highlight the enhanced bioavailability, prolonged circulation, and therapeutic potential of the PPFD nanoparticle system over the free drug.

In the second phase of the study, a parallel cyclodextrin-based system was developed in which methyl-β-cyclodextrin (Mβ-CD) was used to form an inclusion complex with 9-Br-Noscapine. Cyclodextrins are known to increase the solubility and stability of hydrophobic drugs through host–guest interactions within their hydrophobic cavity. Molecular docking and 100 ns molecular dynamics simulations confirmed the formation of a stable 1:1 inclusion complex between 9-Br-Nos and Mβ-CD, with a docking energy of –5.0 kcal/mol. RMSD and Rg analyses revealed structural stability after 30 ns, whereas MM-PBSA calculations revealed a binding free energy of –7.18 ± 6.51 kcal/mol, suggesting that weak interactions are primarily stabilized by three hydrogen bonds (>3.0 Å). These computational results support the feasibility of complex formation and provide a foundation for subsequent experimental validation. The inclusion complex was prepared via the coprecipitation method, and the formation of the complex was characterized via various physicochemical characterization techniques, including UV–visible spectroscopy, Fourier transform infrared spectroscopy (FT–IR), X-ray diffraction (XRD), proton nuclear magnetic resonance (1H NMR) and thermogravimetric analysis (TGA). Phase solubility studies also demonstrated an AL-type curve, along with Job's plot, confirming the formation of a 1:1 stoichiometric complex with increased solubility (R=0.5). Furthermore, the apparent stability constant (K1:1) was calculated to be 3,421 M^{-1}, indicating moderate binding of the host–guest interaction. The FT-IR spectra confirmed inclusion complex formation by showing the disappearance of characteristic peaks, whereas the XRD patterns demonstrated a loss of crystalline peaks of the pure drug, confirming its amorphization within the cyclodextrin cavity. Furthermore, the NMR data revealed upfield shifts in the H3 and H5 protons of MβCD, further supporting the inclusion of the drug inside the cavity. Compared with the free drug, the inclusion complex also resulted in improved dissolution for up to 300 minutes and followed a first-order release kinetics model with R2=0.9952. These findings establish that cyclodextrin-based encapsulation significantly improves the solubility, physical stability, and biological potential of noscapine derivatives. Pharmacokinetic evaluation via UHPLC–Q-TOF/MS revealed that the 9-Br-Nos-Mβ-CD inclusion complex significantly increased the oral bioavailability of 9-Br-Nos, with a relatively high plasma concentration (Cmax = 18.21 ng/mL), prolonged half-life (45.8 h), and sustained drug release for up to 48 hours. Compared with the free drug, the complex showed improved systemic retention (higher AUC), slower clearance, and efficient excretion. An *in vivo* toxicity study was performed through histopathological analysis via hematoxylin & eosin (H&E) staining, which revealed no major tissue damage, and Hoechst staining, which revealed no abnormal nuclear morphology in normal cells. These *in vivo*

pharmacokinetic and safety data validated the suitability of the inclusion complex for therapeutic application and provided a rationale for conducting subsequent *in vitro* cytotoxicity and mechanistic studies. The *in vitro* cytotoxicity evaluation of both delivery systems was carried out using multiple breast cancer cell lines, such as MCF-7 and MDA-MB-231. Cytotoxicity assays (MTT) demonstrated significantly greater anticancer activity of the Mβ-CD inclusion complex than the free drug. The inclusion complex exhibited a notably lower IC_{50} value of 12.87 μg/mL in MDA-MB-231 cells than the substantially higher IC_{50} value of approximately 200 μg/mL for the free drug. Similarly, in MCF-7 cells (Fig. 3.9B), the inclusion complex demonstrated a low IC_{50} value of 13.07 μg/mL, which was markedly lower than the free drug's IC_{50} value of approximately 150 μg/mL. The cytotoxicity study was followed by Hoechst staining to visualize nuclear condensation and fragmentation. Furthermore, Western blot analysis confirmed the expression of key apoptotic markers (upregulated Bax, cleaved caspase-3, and p-JNK), and flow cytometry-based Annexin V-FITC/PI apoptosis assay confirmed significant apoptotic induction in 9-Br-Nos-Mβ-CD inclusion complex-treated MDA-MB-231 cells, with significantly increased apoptosis (92.9%) compared with that of free 9-Br-Nos (60.97%), as indicated by improved solubility, cellular uptake, and activation of intrinsic apoptotic pathways. Together, these results establish the enhanced therapeutic potential and safety of the 9-Br-Nos-Mβ-CD inclusion complex.

Building upon our earlier findings with 9-Br-Nos, we first employed molecular docking and molecular dynamics simulations to understand the binding interactions and stability of the N-3-Br-benzyl-noscapine derivative (3-Br-Bn-Nos) with key tubulin targets. These in silico studies revealed strong binding affinity and stable interaction profiles, indicating potential for enhanced anticancer efficacy. The drug was then encapsulated in folic acid conjugated PLGA-PEG nanoparticles to improve the bioavailability and targeted delivery to the tumor site. The formulation was thoroughly characterized using techniques such as DLS, and SEM to confirm nanoparticle size (155 ± 2), morphology (spherical), surface modification, and drug encapsulation efficiency. *In vitro* studies using MCF-7, MDA-MB-231, and T47D breast cancer cell lines showed significant cytotoxicity with the nanoparticle formulation by inducing mitochondrial depolarization, ROS generation, and nuclear fragmentation, as validated by JC-1, DCFDA, Hoechst, and AO/EtBr staining. Against MDA-MB-231, MCF-7 and T47D cell lines, the IC_{50} values of FPP loaded 3-Br-Bn-Nos were found to be 37.2, 28.9 and 22.7 μg/mL, respectively which were significantly outperforming free 3-Br-Bn-Nos (IC_{50} values were 73.6, 59.8 and 54.1μg/mL, respectively). Additionally, anti-migratory and anti-spheroid effects were confirmed using

wound healing and 3D spheroid assays. The *in vivo* evaluation in MDA-MB-231 xenograft-bearing mice demonstrated a significant reduction in tumor volume without any systemic toxicity. Acute and subacute toxicity studies in rats further validated the safety profile, as no adverse changes were observed in body weight, food and water intake, blood biochemical and hematological parameters or histopathological examination of vital organs. These findings highlight the therapeutic promise of PLGA-PEG-FA loaded N-3-Br-benzyl-noscapine for targeted breast cancer therapy.

To expand the therapeutic scope, two additional novel noscapine derivatives, compound 13, and 14 were synthesized and structurally characterized. These derivatives were systematically evaluated to identify structural modifications that could further enhance anticancer activity and therapeutic outcomes. To gain molecular insights into the drug–target interactions, molecular docking and molecular dynamics (MD) simulations were performed. The docking studies confirmed that all the noscapine derivatives bind at the interface of the α- and β-tubulin subunits with favourable binding energies, ranging from –4.41 to –8.99 kcal/mol. The binding was primarily stabilized through van der Waals interactions, with calculated interaction energies ranging from –28.76 to –45.90 kcal/mol. Furthermore, 100 ns MD simulation was conducted to analyze the stability and conformational behavior of the tubulin–noscapine complexes. Root mean square deviation (RMSD) and root mean square fluctuation (RMSF) analyses revealed that the ligand–protein complexes were stable after 20 ns of simulation, and minimal fluctuations were observed in the binding region. The five lowest-energy conformations obtained from the MD trajectory were averaged to determine the dominant binding mode, which revealed that the ligands remained stably bound within the tubulin binding cleft throughout the simulation period. These computational findings corroborated the *in vitro* results and reinforced the structural compatibility and potential mechanism of action of noscapinoids. Inspired by the *in silico* calculation both the novel noscapine derivatives were synthesized and structurally characterized via ^{1}H NMR, ^{13}C NMR, FT-IR, UV-visible and mass spectrometry to explore their enhanced therapeutic potential. We have comprehensively evaluated the anticancer efficacy and safety of the noscapine derivatives, 13, and 14 in breast cancer cells. Cytotoxicity assays revealed dose-dependent antiproliferative activity in the MCF-7, MDA-MB-231, and T47D cell lines, with compound 13 demonstrating the higher potency, particularly in the MDA-MB-231 cells. Nuclear fragmentation and chromatin condensation were evident through Hoechst and AO/EtBr staining, confirming the induction of apoptosis. JC-1 and DCFDA staining further revealed that these compounds, especially compound 13, caused significant mitochondrial depolarization and

ROS generation. Anti-migratory and anti-spheroid effects were validated by wound healing and 3D spheroid assays, highlighting the strong potential of compound 13 in inhibiting tumor progression. *In vivo*, the noscapine derivatives significantly reduced tumor volume in an MDA-MB-231 xenograft mouse model without inducing systemic toxicity. Acute and subacute toxicity studies in rats confirmed safety, with no adverse effects on body weight, food or water intake, and hematological or serum biochemical parameters. Histopathological analyses of brain, heart, liver, and kidney tissues revealed no structural damage, confirming the derivatives' biocompatibility at therapeutic doses.

In conclusion, this thesis provides a comprehensive evaluation of two nanotechnology-enabled delivery strategies for noscapine derivatives: the polymeric and host–guest inclusion approaches. The results demonstrate that both PLGA-PEG-FA nanoparticles and Mβ-CD inclusion complexes can substantially improve the solubility, stability, cellular uptake, and anticancer performance of noscapine derivatives. These findings pave the way for the development of clinically viable formulations of noscapinoids and support further preclinical and *in vivo* studies. Future research could focus on pharmacokinetic profiling, biodistribution studies, and targeted delivery in animal tumor models to validate the translational potential of these systems.

CHAPTER-1

Introduction

&

Review Literature

1. Introduction

1.1. Cancer: A comprehensive overview

Cancer continues to be a major global health issue, with recent data reflecting both advancements and ongoing challenges in combating the disease. According to a comprehensive report by Sung *et al.* 2021 published in CA; A Cancer Journal for Clinicians, cancer was responsible for nearly 10 million deaths in 2020, making it one of the leading causes of mortality worldwide. (Sung & Kim, 2020) The most common types of cancer include breast, lung, colorectal, and prostate cancer. Recent statistics from Siegel *et al*. 2023 in CA, indicate that in 2023, an estimated 1.9 million new cancer cases were diagnosed in the United States alone, with approximately 609,000 cancer-related deaths expected. (Siegel *et al*., 2023) Advances in early detection and treatment have contributed to a decline in mortality rates for several common cancers over the past decades. For example, the five-year survival rate for patients with breast cancer has significantly improved because of early screening and effective therapies. However, disparities in cancer outcomes persist, particularly among low- and middle-income countries, where access to quality healthcare and cancer treatments is limited. In these regions, late-stage diagnoses and a lack of advanced medical care contribute to higher mortality rates. Furthermore, lifestyle factors such as tobacco use, unhealthy diets, and physical inactivity continue to drive the incidence of certain cancers. Overall, the fight against cancer involves a multifaceted approach, including ongoing research, public health initiatives, and efforts to improve healthcare accessibility and equity. Understanding recent data and trends is crucial for guiding these efforts and ultimately reducing the global burden of cancer.

1.2. Breast Cancer: Current Perspectives

Breast cancer remains a significant global health burden, with approximately 2.3 million new cases diagnosed annually worldwide. (Arnold *et al*., 2022) It is the most common cancer among women and affects both developed and developing countries. Advances in research have improved our understanding of breast cancer biology, leading to more effective treatment strategies and improved survival rates. For example, targeted therapies such as HER2-targeted therapies have revolutionized the treatment landscape for HER2-positive breast cancer, significantly improving outcomes for patients with this subtype. (Slamon *et al*., 2001) Additionally, early detection through mammography screening programs has played a crucial role in reducing mortality rates by detecting tumors at earlier stages when they are more treatable. Despite these advancements, challenges remain, including disparities in access to healthcare and the emergence of treatment resistance in

certain patient populations, necessitating ongoing research and innovation in breast cancer management.

1.3. Comprehensive Approaches to Cancer Treatment

a) Surgery:

Surgical intervention plays a crucial role in treating localized cancers by removing the tumor and surrounding tissue. It is often the primary treatment for solid tumors and can be curative if the cancer has not spread beyond the surgical site. For example, surgical outcomes in breast cancer patients include improved survival rates and reduced recurrence when combined with adjuvant therapies. Studies have shown that surgical resection provides curative outcomes in various cancers, such as breast, colorectal, and early-stage lung cancers. (Siegel *et al*., 2023) Moreover, advances in surgical techniques, such as laparoscopic and robotic-assisted procedures, have significantly improved postoperative outcomes by reducing recovery time, minimizing blood loss, and decreasing infection rates. In certain malignancies, neoadjuvant chemotherapy or radiotherapy is administered prior to surgery to reduce the tumor size and improve resectability, thereby enhancing the prognosis. Surgery for cancer treatment is limited by its ineffectiveness in patients with metastatic disease, potential complications, and risk of recurrence or functional impairment. (Tohme *et al*., 2017)

b) Chemotherapy:

Chemotherapy involves the use of drugs to kill or slow the growth of cancer cells throughout the body. It is effective against rapidly dividing cells but can also affect healthy cells, leading to side effects. Studies have shown significant advancements in chemotherapy regimens, such as combination therapies tailored to specific cancer types, which improve efficacy and reduce toxicity. One of the primary drawbacks is its lack of selectivity, as most chemotherapeutic agents target rapidly dividing cells indiscriminately, affecting not only cancer cells but also healthy tissues such as the bone marrow, gastrointestinal tract, and hair follicles. (Anand *et al*., 2023)

c) Radiation Therapy:

By utilizing high-energy rays or particles, radiation therapy targets and destroys cancer cells or inhibits their growth. It can be delivered externally (external beam radiation) or internally (brachytherapy). Advances in radiation technology, such as intensity-modulated radiation therapy (IMRT), have increased precision and reduced side effects. One of the main concerns is collateral damage to surrounding healthy tissues, particularly when

tumors are located near vital organs. This off-target exposure can lead to acute and long-term side effects such as skin irritation, fatigue, fibrosis, and damage to organs such as the lungs, heart, or brain, depending on the radiation site. (Baskar *et al*., 2012)

d) Targeted Therapy:

Targeted therapies interfere with specific molecules or pathways involved in cancer growth and survival. They are often less harmful to normal cells than traditional chemotherapy. For example, HER2-targeted therapies have revolutionized the treatment of HER2-positive breast cancer, significantly improving outcomes. (Swain *et al*., 2023)

e) Immunotherapy:

Immunotherapy enhances the ability of the body's immune system to recognize and attack cancer cells. Checkpoint inhibitors, monoclonal antibodies, and adoptive cell transfer are examples of immunotherapy approaches that have shown remarkable success in treating various cancers, including melanoma and lung cancer. (Ling *et al*., 2022)

f) Hormone Therapy:

Hormone therapy is used in hormone-sensitive cancers (e.g., breast and prostate cancers) to block or lower hormone levels, thereby slowing or stopping cancer growth. It has significantly improved outcomes in hormone receptor-positive breast cancer patients. However, hormone therapy is limited by several important factors. A major limitation is the eventual development of hormone resistance, where cancer cells adapt through mechanisms such as receptor mutations, activation of alternative signalling pathways, or loss of hormone receptor expression, rendering treatment ineffective over time. (Puhalla *et al*., 2012)

g) Stem Cell Transplantation:

Stem cell transplantation, including bone marrow transplantation, is used to treat cancers affecting the blood and lymphatic system (e.g., leukemia and lymphoma). It involves replacing diseased bone marrow with healthy stem cells after high-dose chemotherapy or radiation.

These treatments are often combined with multidisciplinary approaches tailored to individual patients, aiming to achieve the best possible outcomes while minimizing side effects. Ongoing research and clinical trials continue to refine and innovate cancer treatment strategies, offering hope for improved survival and quality of life for cancer patients worldwide. (Chu *et al*., 2020)

1.4. Microtubule structure and function in cell division

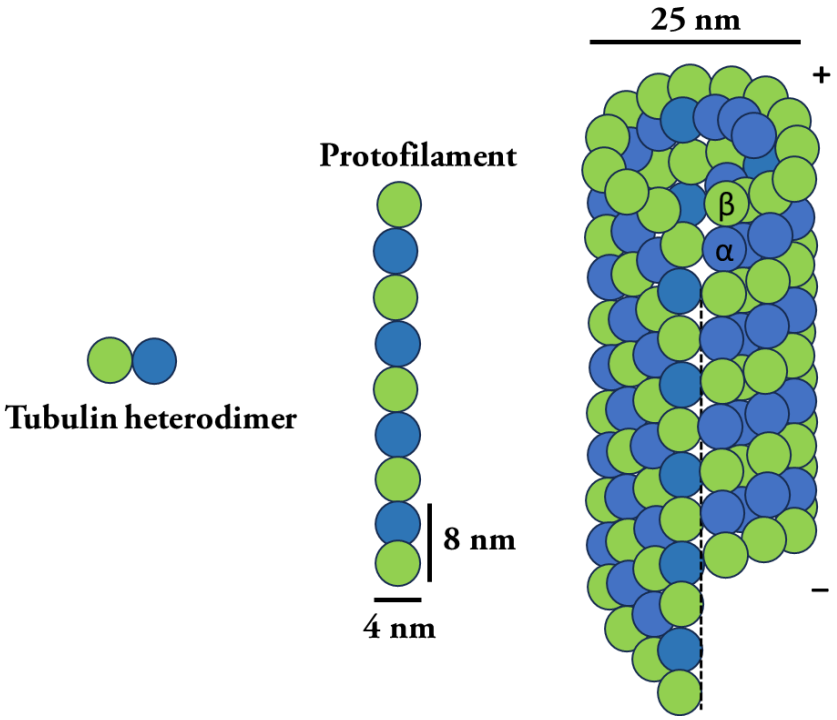

Figure 1.1. Schematic illustration of the microtubule structure. Microtubules are cylindrical, hollow structures composed of linear chains called protofilaments. Each protofilament consists of repeating α- and β-tubulin heterodimers, which polymerize primarily at the plus (+) end of the microtubule.

Microtubules are dynamic, cylindrical polymers composed of α- and β-tubulin heterodimers arranged in a head-to-tail fashion, forming protofilaments that typically associate laterally to create a hollow tube with 13 protofilaments (Figure 1.1). (Huang *et al*., 2022; Vleugel *et al*., 2016) This structural organization imparts inherent polarity to microtubules, with a fast-growing plus (+) end and a slower-growing minus (−) end, which is critical for their role in intracellular transport, cell division, and structural support. They are fundamental components of the cytoskeleton, and most importantly, play a critical role in the regulation and execution of mitosis during cell division. During cell division, microtubules undergo extensive reorganization to form the mitotic spindle, a bipolar structure that ensures accurate chromosome segregation. (Barisic *et al*., 2021) They also serve as tracks for motor proteins such as kinesins and dyneins, which facilitate the transport of organelles, vesicles, and macromolecular complexes. The mitotic spindle is composed of three main types of microtubules: astral microtubules, which anchor the spindle poles to the cell cortex; kinetochore microtubules, which attach to chromosomes at specialized regions known as kinetochores; and interpolar microtubules, which overlap at the spindle midzone and contribute to spindle stability and elongation (Figure 1.2). (Tolić,

2018) The coordinated dynamics of polymerization and depolymerization, referred to as dynamic instability, enable microtubules to probe the intracellular space and make critical attachment to chromosomes. The function of microtubules in mitosis begins in prophase, when centrosomes migrate to opposite poles of the cell and start nucleating spindle microtubules. During prometaphase, microtubules connect to kinetochores on condensed chromosomes, establishing a stable bipolar attachment. The alignment of chromosomes at the metaphase plate ensures that each daughter cell receives an identical set of chromosomes. During anaphase, shortening of kinetochore microtubules pulls sister chromatids apart toward opposite poles, whereas interpolar microtubules push against each other to elongate the cell. Finally, in telophase, the spindle disassembles, and the nuclear envelopes reform around the segregated chromosomes, followed by cytokinesis, which physically separates the cytoplasm. (Goodson & Jonasson, 2018)

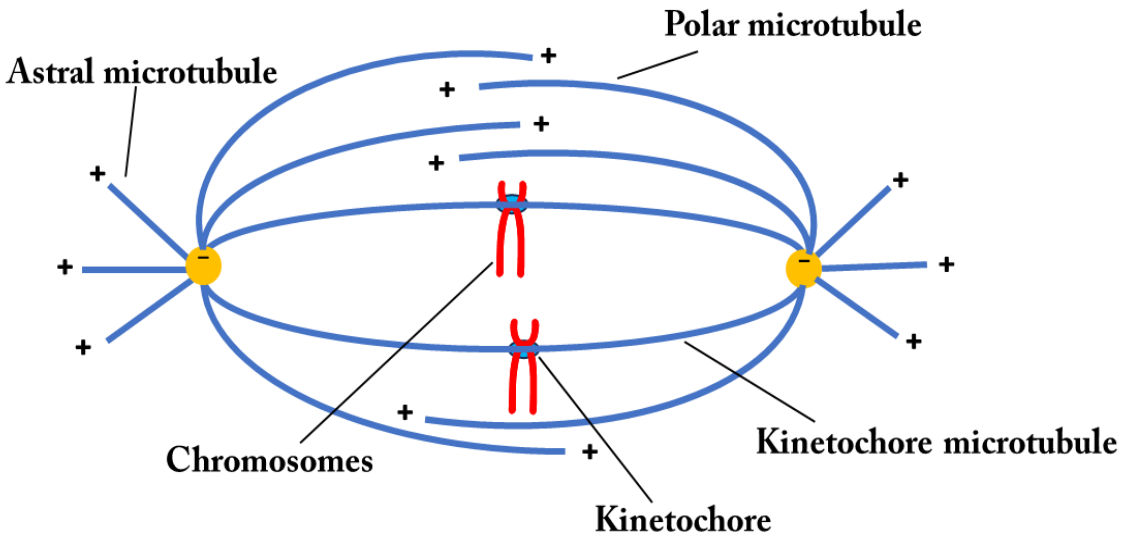

Figure 1.2. Schematic representation of the metaphase stage of mitosis. The diagram illustrates the alignment of duplicated chromosomes at the metaphase plate, with sister chromatids attached to spindle fibres originating from opposite spindle poles. The microtubules (blue) extend from centrosomes and attach to the kinetochores (yellow dots) at the centromeres of each chromosome, ensuring proper chromosome segregation during cell division.

The dynamic behaviour of microtubules is intricately regulated by the competing actions of both stabilizing and destabilizing factors. Stabilizing influences include microtubule-associated proteins (MAPs), such as tau, MAP1, MAP2, MAP4, and XMAP215, which promote microtubule assembly and stability. (J. J. Correia *et al*., 1988; Papasozomenos Ch. *et al*., 1985; Ramkumar *et al*., 2018) Conversely, regulatory proteins such as stathmin, XKCM1, XKIF2, and katanin facilitate microtubule destabilization by promoting depolymerization. Additionally, the variable expression of tubulin isotypes contributes to the modulation of microtubule dynamics. A distinctive feature of microtubule behavior, termed "dynamic instability," describes the stochastic switching between phases of growth and rapid shrinkage. Within a population of slowly elongating microtubules, individual microtubules can suddenly undergo a catastrophic transition, rapidly depolymerizing until they vanish. Conversely, shortening microtubules may pause and subsequently resume growth, a process known as "rescue." The key parameters defining this dynamic instability include the growth rate, shortening rate, catastrophe frequency (the rate at which microtubules switch from growth to shortening), and rescue frequency (the rate at which they transition from shortening back to growth) (Figure 1.3) (Gardner *et al*., 2008).

(A)

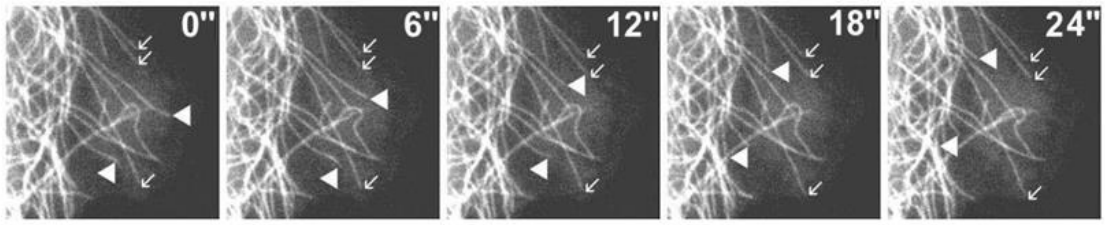

(B)

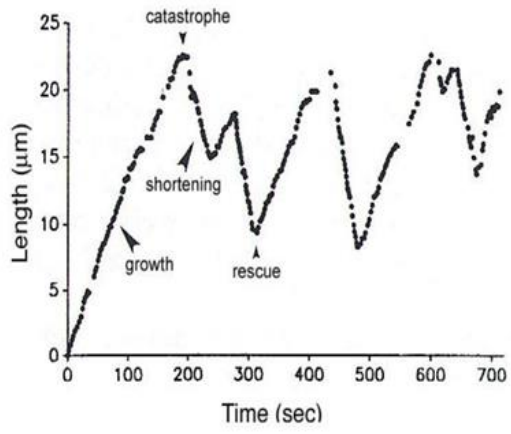

(C)

Dynamic parameters	74 MTs (n=20)
Growth	
Rate (mm/min)	9.15 ± 2.72
Distance (mm)	1.88 ± 0.44
Duration (sec)	14.33 ± 1.22
Shrink	
Rate (mm/min)	12.04 ± 3.63
Distance (mm)	1.99 ± 0.56
Duration (sec)	13.11 ± 1.45
Average pause duration	8.16 ± 2.42
Percentage time per phase	
Growth/ Shrink/ Pause	41.8/36.3/21.8
Rescue frequency (sec-1)	0.077 ± 0.015
Catastrophe frequency (sec-1)	0.086 ± 0.023
Dynamicity (mm/min)	6.61 ± 2.36

Figure 1.3. Visualization of microtubule dynamics and analysis of dynamic parameters.

(A) Time-lapse images captured at 6-second intervals display the behavior of the microtubule plus ends. (B) A representative trace of a single microtubule plus end shows typical dynamic instability, characterized by alternating phases of growth and rapid shortening, with minimal pausing. The transitions between phases include sudden catastrophes (growth to shortening) and rescues (shortening to growth). (C) Quantitative analysis of the dynamic parameters of microtubules.

1.5. Cell cycle and cell cycle checkpoints

The cell cycle is a highly regulated and intricately controlled series of events that enables cells to grow, replicate their DNA, and divide to form two daughter cells. This process is fundamental to the development, growth, maintenance, and repair of tissues in multicellular organisms. It also plays a critical role in maintaining cellular homeostasis and ensuring genetic stability. The cell cycle is traditionally divided into several distinct phases, each characterized by specific biochemical and structural changes within the cell. The **G_1 phase** (Gap 1) marks the initial stage following mitosis, during which the cell increases in size and actively synthesizes proteins and enzymes required for DNA replication. This phase is crucial for monitoring internal and external conditions, such as nutrient availability and growth signals, to determine whether the cell should commit to another cycle. Upon receiving the appropriate signals, the cell enters the **S phase** (synthesis phase), where the entire genome is faithfully duplicated, ensuring that each daughter cell inherits a complete set of chromosomes. Following DNA replication, the cell progresses into the **G_2 phase** (Gap 2), where it continues to grow and produce additional proteins, including those involved in mitotic spindle formation, while also undergoing checks to ensure that DNA replication is complete without errors. The cell then enters the **M phase** (mitosis), a complex and highly ordered process that includes prophase, metaphase, anaphase, telophase, and cytokinesis, ultimately resulting in the physical separation of the cell into two genetically identical daughter cells. In some cases, cells exit the cycle and enter a resting state known as the G_0 phase, where they remain metabolically active but no longer divide. (Gabrielli *et al*., 2012) This phase may be temporary, as observed in certain stem or immune cells, or permanent, as observed in terminally differentiated neurons or muscle cells. Collectively, these phases ensure that cells divide in a controlled manner and that the integrity of the genetic material is preserved across generations. Dysregulation of the cell cycle is a hallmark of many pathological conditions, particularly cancer, where uncontrolled proliferation results from defects in the regulatory mechanisms that normally govern these processes. The activity of these CDKs is controlled

by their phosphorylation and binding with cyclins. Dysregulation of cyclin-CDK complexes is a hallmark of many cancers and contributes to uncontrolled proliferation. (Graña & Premkumar Reddy, 1995) Cell cycle checkpoints are essential surveillance mechanisms that preserve genomic stability by monitoring the orderly progression of the cell cycle and ensuring that critical events such as DNA replication and chromosome segregation occur accurately. (Figure 1.4) These checkpoints act as molecular brakes that temporarily halt the cycle in response to DNA damage, replication errors, or spindle defects, providing the cell with an opportunity to repair damage or, if irreparable, to initiate programmed cell death (apoptosis). The G_1/S checkpoint, also known as the restriction point, is the first major control mechanism where the cell evaluates whether it has sufficient nutrients, proper cell size, and undamaged DNA before committing to DNA replication. This checkpoint is tightly regulated by proteins such as p53, p21, and Cyclin D/CDK4/6 complexes. Upon detection of DNA damage, p53 becomes stabilized and activates the transcription of p21, a cyclin-dependent kinase inhibitor (CKI) that inhibits Cyclin E/CDK2 activity, thereby preventing the cell from entering the S phase. The S phase checkpoint monitors the fidelity of DNA replication and detects stalled replication forks or DNA lesions. Key players in this checkpoint include ATR (ataxia telangiectasia and Rad3-related protein), Chk1 kinase, and BRCA1, which coordinate a response to replication stress and prevent the progression of replication forks until the damage is resolved. The G_2/M checkpoint ensures that DNA replication has been fully completed and that the genetic material is intact before the cell undergoes mitosis. DNA damage at this stage activates checkpoint kinases such as Chk1 and Chk2, which in turn inhibit CDC25 phosphatases, blocking the activation of the Cyclin B/CDK1 complex and thus delaying mitotic entry. Finally, the spindle assembly checkpoint (SAC) operates during mitosis at the metaphase–anaphase transition. This ensures that all chromosomes are correctly attached to the mitotic spindle through their kinetochores before sister chromatid separation. This checkpoint inhibits the anaphase-promoting complex/cyclosome (APC/C) through the action of regulators such as MAD2, BUB1, and Aurora B kinase, thereby preventing premature chromatid segregation and aneuploidy. (Yam *et al.*, 2022) Collectively, these checkpoints play a vital role in maintaining cell cycle fidelity and preventing the propagation of genetic errors, making them critical targets in cancer therapy.

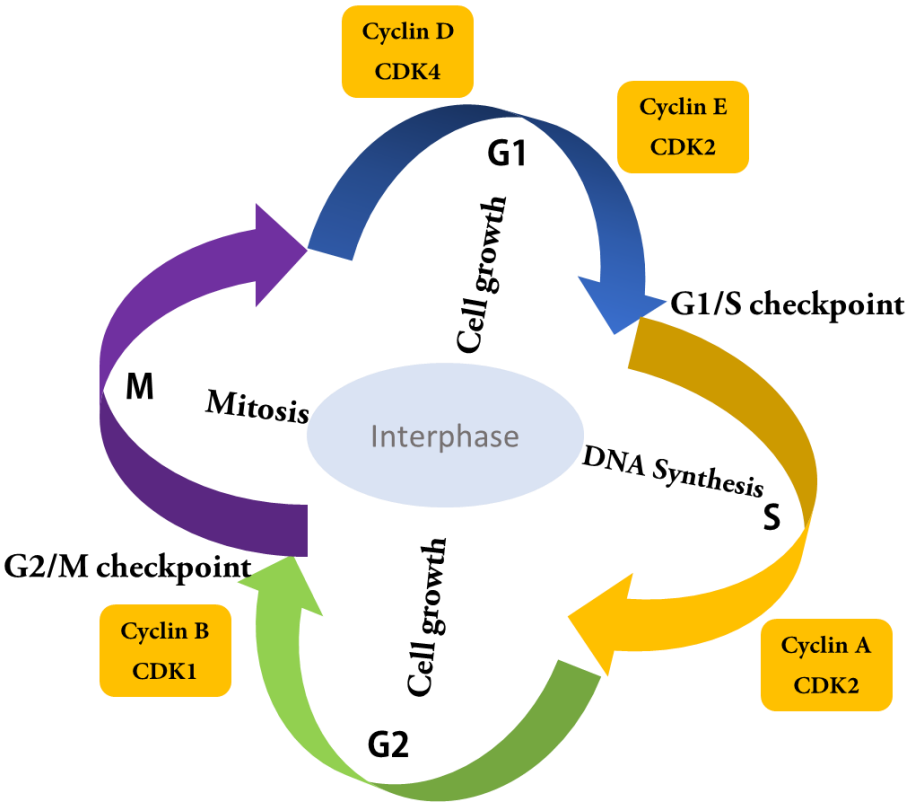

Figure 1.4. Regulation of cell cycle progression through checkpoints. The cell cycle is a highly coordinated process controlled by a series of checkpoints that monitor the successful completion of key events at each stage.

1.6. Microtubule-interacting agents

Microtubule-interacting agents (MIAs) are a diverse group of compounds that target the microtubule network within cells, interfering with the dynamic processes of microtubule polymerization and depolymerization. These agents have garnered significant interest in cancer therapy because of the important role of microtubules in the process of cell division, particularly in mitotic spindle formation, chromosome alignment, and segregation. By disrupting microtubule dynamics, MIAs effectively impair the progression of mitosis, leading to mitotic arrest and the activation of apoptotic pathways, especially in rapidly proliferating cancer cells. MIAs are broadly categorized into two main classes on the basis of their mode of action: microtubule-stabilizing agents and microtubule-destabilizing agents. Stabilizing agents, such as paclitaxel (Taxol) and docetaxel, promote microtubule polymerization and prevent depolymerization, resulting in the formation of overly stable microtubules that cannot reorganize during mitosis. This leads to defective spindle assembly and prolonged mitotic arrest. On the other hand, destabilizing agents, including vincristine, vinblastine, colchicine, and nocodazole, bind to tubulin and inhibit its

polymerization, leading to microtubule depolymerization and spindle disassembly, thereby preventing chromosome alignment and segregation. (Mukhtar *et al*., 2014)

1.7. Paclitaxel and vinca alkaloids as anticancer drugs

Antimitotic agents exert their effects by binding to specific sites on the tubulin heterodimer, targeting either the unassembled or assembled forms of tubulin. The following primary drug-binding domains have been characterized: the colchicine-binding site and the vinca alkaloid-binding site located on α-tubulin. (J. Correia & Lobert, 2005) Colchicine binds at the interface region of tubulin, disrupting lateral contacts between protofilaments and thereby inhibiting microtubule polymerization. (Jordan *et al*., 1998) In contrast, vinca alkaloids act by cross-linking interdimer interfaces, which sterically distort the protofilament structure and promote the formation of aberrant tubulin polymers, effectively preventing normal microtubule assembly. (Downing & Nogales, 1998) Paclitaxel and vinca alkaloids are among the most widely used and clinically validated microtubule-targeting agents in the treatment of various malignancies (Figure 1.5). These agents exert their anticancer effects by disrupting the highly dynamic microtubule network essential for proper mitotic spindle assembly and chromosome segregation, ultimately leading to mitotic arrest and apoptotic cell death. Despite their differing mechanisms of action, both classes are central to many chemotherapy protocols because of their potent efficacy against rapidly dividing tumor cells. Paclitaxel, which was originally derived from the bark of the Pacific yew tree (*Taxus brevifolia*), is a microtubule-stabilizing agent that binds to the β-subunit of tubulin within assembled microtubules. This binding promotes and stabilizes microtubule polymerization and prevents depolymerization, thereby freezing the microtubule dynamics required for mitosis. As a result, cells treated with paclitaxel are unable to progress through metaphase, causing cell cycle arrest at mitosis and the eventual activation of apoptosis. Paclitaxel has demonstrated remarkable success in the treatment of breast, ovarian, lung, and pancreatic cancers. However, its clinical use is often limited by solubility issues, neurotoxicity, and the emergence of drug resistance. In contrast, vinca alkaloids such as vincristine, vinblastine, and vinorelbine, which were originally isolated from *Catharanthus roseus* (Madagascar periwinkle), function as microtubule-destabilizing agents. These compounds bind to tubulin dimers at different sites than does paclitaxel and inhibit the addition of tubulin to the growing ends of microtubules. This action results in microtubule depolymerization and the collapse of the mitotic spindle, thereby preventing chromosome alignment and segregation. (Ngan *et al*., 2000) Like paclitaxel, vinca alkaloids cause mitotic arrest and subsequent apoptosis. They are widely used to treat

hematologic malignancies (e.g., leukemia, lymphoma) as well as solid tumors such as breast and lung cancer.

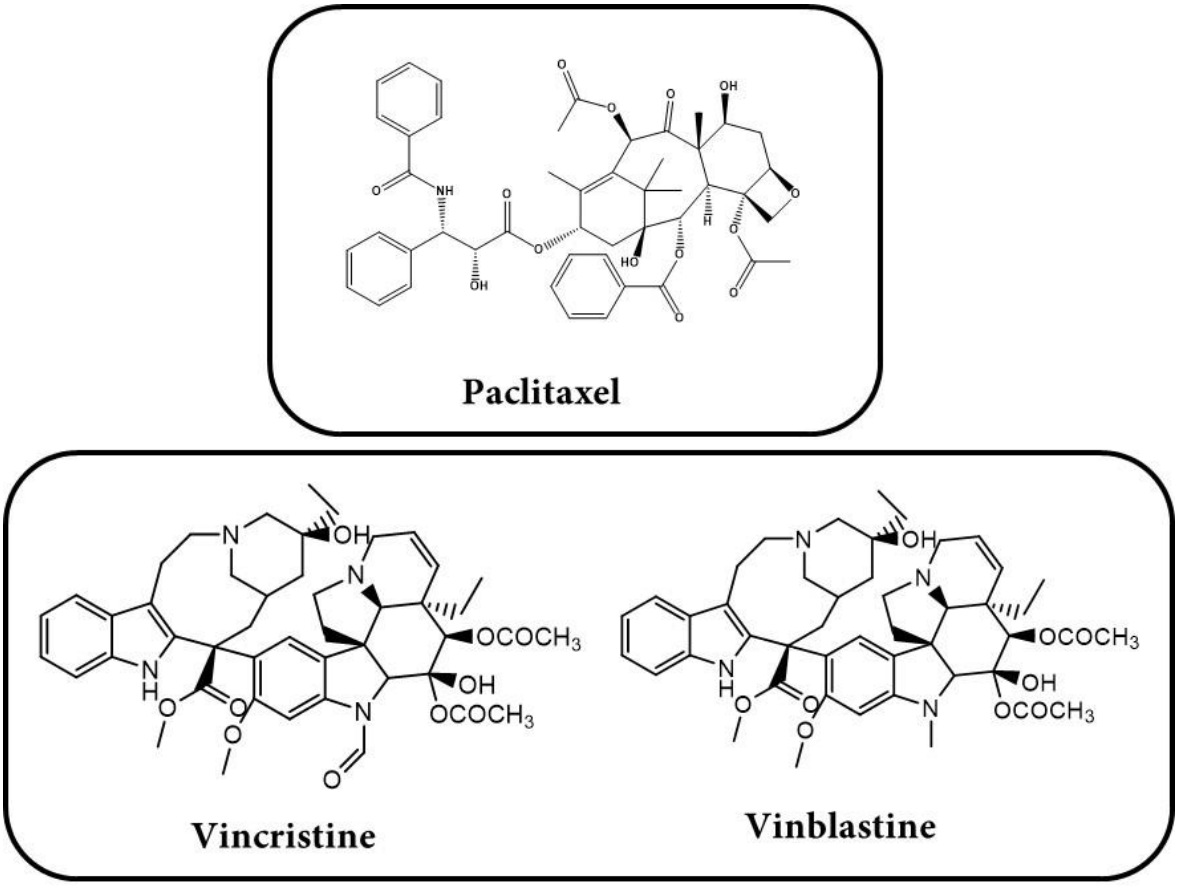

Figure 1.5. Chemical structures of paclitaxel and vinca alkaloids.

1.8. Limitations of currently available microtubule-interacting anticancer drugs

Despite the clinical success of microtubule-interacting agents (MIAs), such as paclitaxel, docetaxel, and vinca alkaloids, in treating a wide spectrum of cancers, their use is significantly hindered by several limitations that impact therapeutic efficacy, safety, and patient compliance. These include dose-limiting toxicities such as peripheral neurotoxicity, multidrug resistance (especially due to P-glycoprotein-mediated drug efflux), and poor solubility, which often necessitate the use of toxic solvents. The nonspecific targeting of both cancerous and healthy dividing cells leads to side effects such as myelosuppression and gastrointestinal toxicity, reducing the therapeutic window. Furthermore, their limited ability to penetrate the blood–brain barrier restricts their use in brain tumors. These limitations have prompted the ongoing search for novel agents with improved selectivity and reduced toxicity. (Pettit, 1996)

1.9. Noscapine as an antimitotic drug (mechanism, safety, and advantages)

Noscapine, also known as narcotine, is a naturally occurring phthalideisoquinoline alkaloid derived from the opium poppy (*Papaver somniferum*). Unlike other major opium alkaloids, such as morphine and codeine, noscapine is nonnarcotic and nonaddictive. Its discovery and subsequent evolution from a cough suppressant to a promising anticancer agent represent a unique journey in pharmaceutical science.

Noscapine was first isolated in 1817 by the French chemist Pierre Jean Robiquet, who also played a significant role in the identification of codeine. (Rowinsky *et al*., 1993) Initially, named "narcotine," it was identified as one of the nonnarcotic components of opium. Over time, it was renamed "noscapine" to reflect its distinct pharmacological profile and to avoid confusion with narcotic agents. For much of the 19th and 20th centuries, noscapine was widely used as a central antitussive agent owing to its ability to suppress cough through action on the brainstem without producing sedation or dependence. It is included in many over-the-counter cough remedies, especially in Europe and parts of Asia, because of its relatively safe profile. (Karlsson *et al*., 1988; Sebak *et al*., 2010)

In the latter part of the 20th century, particularly in the 1990s, researchers began to uncover the unexpected cytostatic and anticancer properties of noscapine. The seminal work by Dr. Joshi and colleagues at Emory University was critical in this regard. They discovered that noscapine binds to tubulin, modulate microtubule dynamics, arresting cells in mitosis and promoting apoptosis in cancer cells without significantly affecting normal cells.

Noscapine exerts its anticancer effects primarily through its ability to bind tubulin and modulate microtubule dynamics. Unlike traditional microtubule-targeting agents such as paclitaxel and vincristine, which either overly stabilize or depolymerize microtubules, noscapine binds to a unique site on tubulin and subtly alters microtubule behavior without affecting the total polymer mass. (Martino *et al*., 2018) This binding interferes with the normal dynamic instability of microtubules, specifically by reducing their rates of polymerization and depolymerization and increasing the duration of pause phases, thereby impairing the assembly of the mitotic spindle required for chromosome segregation. This prolonged metaphase arrest and activation of the spindle assembly checkpoint (SAC), particularly through proteins such as BubR1 and Mad2. (Lara-Gonzalez *et al*., 2021) Sustained mitotic arrest subsequently activates the intrinsic (mitochondrial) apoptotic pathway. Biochemically, noscapine upregulates the proapoptotic protein Bax and downregulates the antiapoptotic protein Bcl-2, causing mitochondrial outer membrane

permeabilization (MOMP). (Quisbert-Valenzuela & Calaf, 2016) This results in the release of cytochrome c into the cytosol, where it forms an apoptosome complex with Apaf-1 and procaspase-9, leading to the activation of caspase-9 and the downstream effector caspase-3. (Bratton & Salvesen, 2010) Activated caspase-3 cleaves PARP and other substrates, causing in DNA fragmentation, chromatin condensation, and formation of apoptotic body , marking the execution phase of apoptosis.

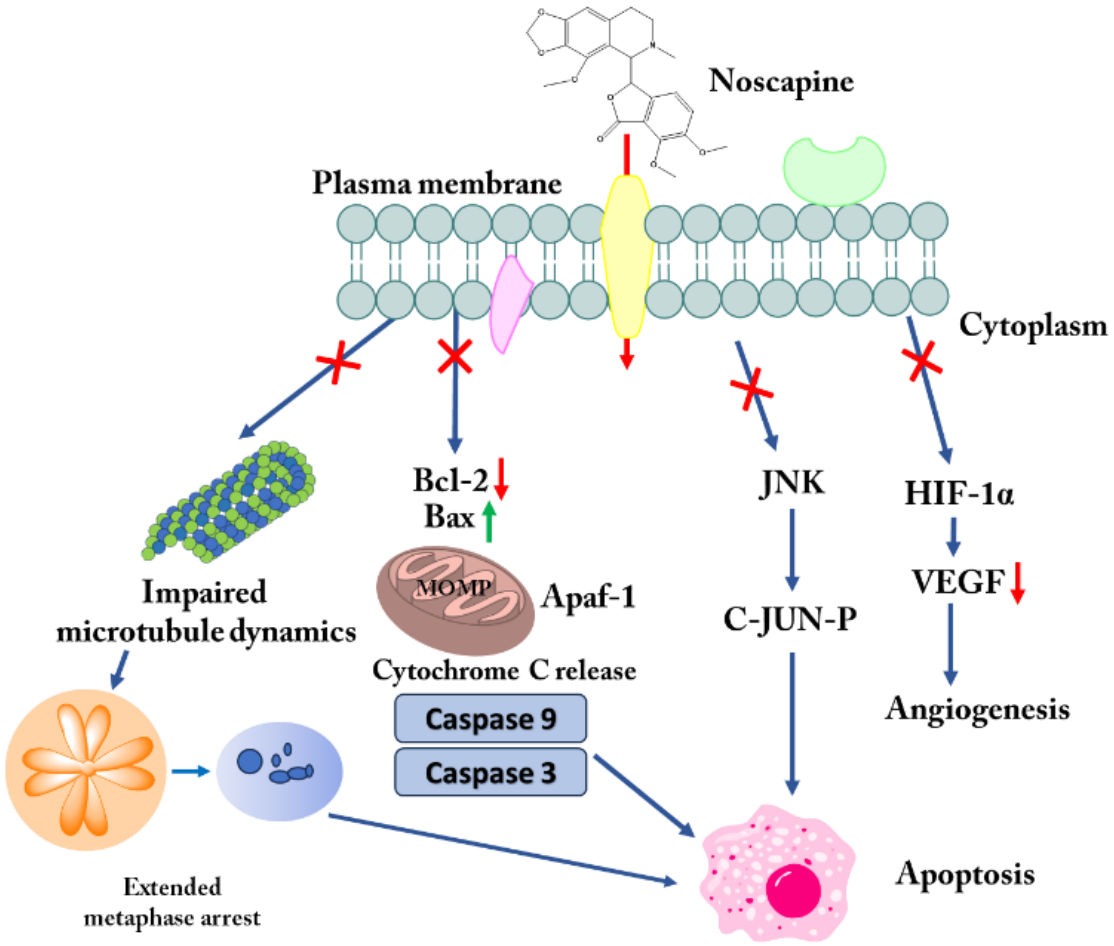

Figure 1.6. Biochemical mechanism of noscapine-induced apoptosis and antiangiogenesis in cancer cells.

In addition, noscapine has been shown to increase intracellular reactive oxygen species (ROS) levels in certain cancer cell types, further contributing to mitochondrial dysfunction and caspase activation. In addition to its ability to induce apoptosis, noscapine also exhibits potent antiangiogenic activity. It downregulates the expression of vascular endothelial growth factor (VEGF), a key mediator of angiogenesis, through the inhibition of hypoxia-inducible factor-1α (HIF-1α) stabilization under hypoxic tumor conditions. This suppression of VEGF signalling impairs endothelial cell proliferation, migration, and tube formation, thereby inhibiting neovascularization, which is essential for tumor growth and

metastasis. (Newcomb *et al*., 2006) Additionally, the c-Jun-N-terminal kinase pathway (JNK pathway) activates various cellular responses, such as stress-induced apoptosis. This activation of the JNK pathway by microtubule-targeted drugs such as noscapine has also been reported (Figure 1.6). (Calaf *et al*., 2024) Noscapine also reduces microvessel density in tumor tissues, further demonstrating its antiangiogenic potential. By targeting both cancer cell survival and tumor vascularization, noscapine exerts dual effects that enhance its overall anticancer efficacy while maintaining a favourable toxicity profile.

Noscapine has been demonstrated to suppress the growth of both murine and human tumors in mice, primarily by inducing apoptosis.(Ye *et al*., 1998) Experimental studies conducted both in vitro and in mouse xenograft models have confirmed that noscapine and its derivatives are effective against a wide range of cancer types, including colon, nonsmall cell lung, brain, ovarian, kidney, prostate, leukemia, and breast and bladder cancers. (Ke *et al*., 2000; Zhou *et al*., 2003) A significant advantage of noscapine is that, although it is an opium derivative, it is nonnarcotic and does not have analgesic, sedative, or respiratory-depressant effects, nor does it induce euphoria or dependency. Unlike conventional microtubule-targeting agents such as taxanes and vinca alkaloids, which are often associated with considerable toxicity, noscapine has a much more favourable safety profile. For example, paclitaxel has been linked to several adverse effects, including neurotoxicity, (van Gerven *et al*., 1994) cardiotoxicity, (Osman & Elkady, 2017) bone marrow suppression, (Pearl *et al*., 1995) allergic reactions, (Guchelaar *et al*., 1994) hair loss, (Sibaud *et al*., 2016) and gastrointestinal toxicity. (Hruban *et al*., 1989) In contrast, noscapine has shown potent antitumour activity in models of murine lymphoma, melanoma, and human breast cancer xenografts without causing histological or hematological damage to critical organs such as the kidney, liver, heart, spleen, or small intestine in treated mice, indicating its nontoxic nature.

Noscapine possesses a unique set of advantages that contribute to its growing interest as a therapeutic agent, as mentioned below. (Figure 1.7)

- Noscapine is well tolerated, even at high oral doses, with minimal side effects.
- Noscapine does not induce significant peripheral neuropathy, a common dose-limiting side effect in cancer therapy.
- Noscapine has shown promise in overcoming multidrug resistance (MDR) in cancer cells through the evasion of efflux pumps and other resistance mechanisms.
- Noscapine can be administered orally with reasonably good absorption and the pharmacokinetic clearance is approximately 6–10 hours.

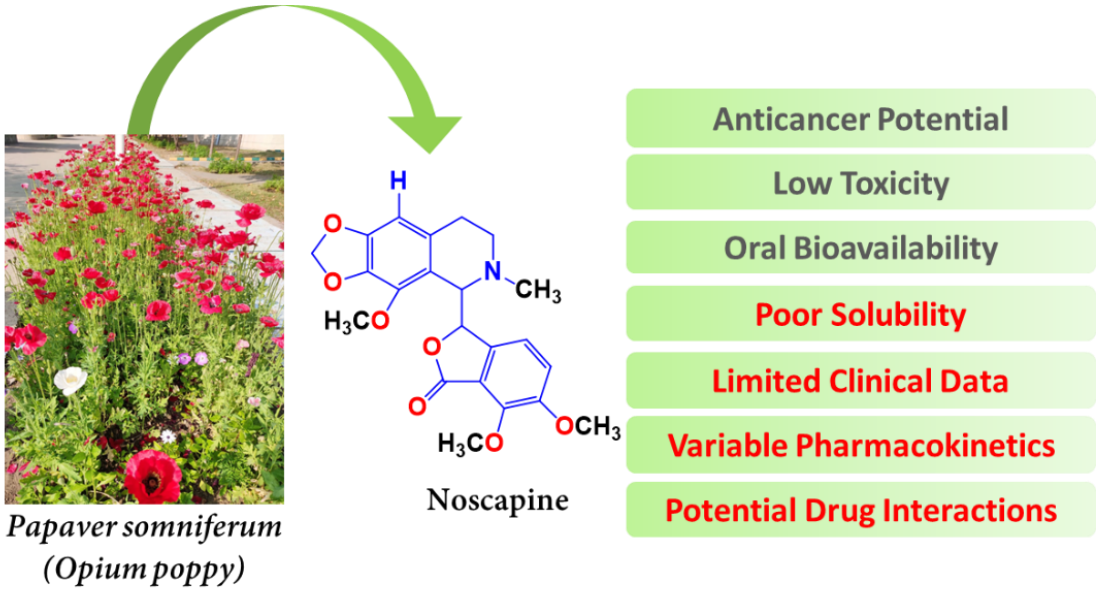

Figure 1.7. Therapeutic potential and associated limitations of noscapine in cancer treatment.

1.10. Analogues of noscapine

Noscapine, although widely recognized as a safe and well-tolerated opium alkaloid with decades of clinical use as a cough suppressant, is limited in its broader therapeutic applications, particularly in oncology, owing to notable pharmacokinetic and pharmacodynamic drawbacks. One of the most significant challenges associated with noscapine is its poor aqueous solubility, which impairs its dissolution in biological fluids and consequently reduces its absorption in the gastrointestinal tract following oral administration. (Kumar *et al*., 2021) This leads to low systemic bioavailability, meaning that only a small fraction of the administered drug reaches circulation in an active form, limiting its therapeutic impact at clinically acceptable doses. To overcome these limitations, researchers have developed a wide range of synthetic and semisynthetic derivatives of noscapine (known as noscapinoids). (DeBono *et al*., 2015) These chemical modifications aim to increase water solubility, improve membrane permeability, and increase metabolic stability, thereby allowing for better absorption, prolonged *in vivo* circulation time, and enhances delivery to the target tissues. A range of noscapine derivatives, known as noscapinoids, have been synthesized by modifying both the isoquinoline and isobenzofuranone moieties of the natural α-noscapine molecule (Figure 1.8) Some of these analogues exhibit significantly improved therapeutic potential and

enhanced pharmacological properties. Over three generations of noscapinoids have been designed and chemically synthesized, and their efficacy against cancer cells, water solubility, and toxicity toward normal cells have been extensively evaluated. (Aneja *et al*., 2006; Naik, Santoshi, *et al*., 2011) The first generation of these compounds was created through structural modifications of the parent noscapine molecule, specifically at diverse sites labelled 'A' and 'B' on the isoquinoline ring and 'C' on the benzofuranone ring system. Various substituents, including nitro, azido, amino, and halogen atoms such as fluorine, chlorine, bromine, and iodine, were introduced at site 'A', while site 'C' was modified by reducing the oxygen content. (Aneja *et al*., 2006)

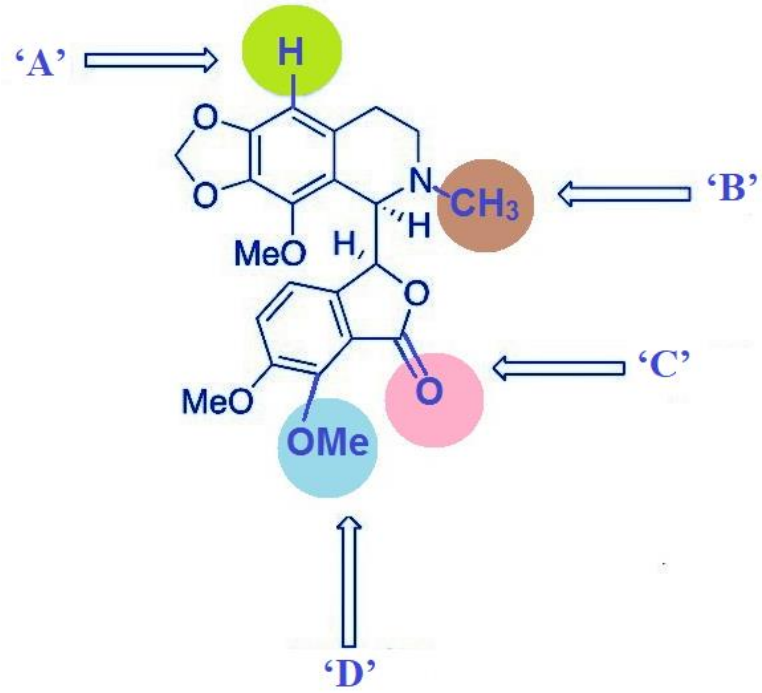

Figure 1.8. Chemical structure of the noscapine scaffold and its modification sites.

The first-generation noscapinoids demonstrated greater efficacy than did the parent compound. (Landen *et al*., 2004; Naik, Chatterji, *et al*., 2011; Santoshi *et al*., 2011) Thus, second-generation noscapine analogues were developed by introducing modifications at the 7-position of the benzofuranone moiety. These analogues, which included O-alkylated and acylated derivatives, were created through chemical modifications at diversity point 'D' of the original noscapine scaffold and exhibited improved antiproliferative activity. (Landen *et al*., 2004; Manchukonda *et al*., 2013; Naik, Chatterji, *et al*., 2011; Santoshi *et al*., 2011) However, despite the enhanced potency observed in preliminary *in vitro* studies, a major limitation encountered in translating these compounds to *in vivo* studies was their poor aqueous solubility. This limitation is largely attributed to the hydrophobic nature of

the substituted isoquinoline and isobenzofuranone rings, which significantly reduce water solubility. Poor solubility negatively impacts drug absorption and distribution, thereby reducing bioavailability. Consequently, solubility becomes a critical factor in the early stages of drug development, especially for preclinical animal studies. Key indicators such as the partition coefficient and topological polar surface area (TPSA) are often employed to optimize the physicochemical properties of drug candidates. To overcome these solubility-related challenges and enhance therapeutic potential, further structural refinement of noscapine analogues is necessary. The third-generation noscapinoids focus on modifications at diversity point 'B' of the isoquinoline ring. These derivatives, which involve primarily the functionalization of the nitrogen atom in the isoquinoline unit of α-noscapine, exhibited significantly greater cytotoxicity against a wide range of tumor cell lines than did the parent molecule.

1.11. Computer-aided design of novel and potent noscapine analogues

The process of discovering and developing new drugs is both lengthy and costly, often requiring 10-15 years and approximately US$500-800 million to bring a single drug to market (Shamima Shultana *et al*., 2021). To address these challenges, computer-aided drug design (CADD) has become an integral part of pharmaceutical research, significantly enhancing the efficiency of drug discovery and their development. CADD enables researchers to prioritize the most promising candidates, thereby reducing the time and resources spent on chemical synthesis and biological testing. (Niazi & Mariam, 2024) A variety of computational strategies have been employed to identify and design small molecules with therapeutic potential tailored to specific targets and research objectives. The selection of CADD techniques typically depends on the availability of experimentally resolved three-dimensional (3D) structures of target proteins. In cases where such structural information is unavailable, ligand-based methods, such as quantitative structure–activity relationship (QSAR) models and pharmacophore mapping, are applied. (Aparoy *et al*., 2012) Conversely, when 3D structures are accessible, structure-based techniques such as molecular docking can be used to design novel compounds with enhanced efficacy by modelling their interaction with the target site. (Meng *et al*., 2012) As the number of solved protein structures continues to grow, the accuracy of predictive models is expected to improve. These advanced computational tools have already proven valuable in developing drugs for a wide range of diseases, particularly in oncology. In the context of noscapine analogues, the availability of structure–activity relationship (SAR) data for various derivatives supports the construction of predictive theoretical models that can guide the

rational design of more potent compounds. Among the computational tools, molecular docking stands out for its ability to predict how small molecules interact with target receptors by generating plausible binding poses and estimating their binding efficacy through scoring functions. However, these functions used in docking are often overly simplistic, failing to account for key factors such as the shape complementarity between the ligand and receptor or the effects of solvation on electrostatic interactions. Owing to these limitations, relying solely on molecular docking can lead to reduced predictive accuracy. To address this, more sophisticated computational methods are necessary to rescore docking results. Approaches such as molecular mechanics combined with solvation models, such as the linear interaction energy (LIE) approach using a surface generalized born (SGB) model or the generalized born surface area (GBSA) method, offer improved estimates of the binding affinity between ligands and their target proteins, albeit at a higher computational cost. (Kleinjung & Fraternali, 2014) These refinements help ensure a more reliable design of noscapine derivatives with potential therapeutic benefits.

1.12. Challenges with noscapine and its derivatives

Hydrophobic drugs present significant challenges in drug delivery because of their poor solubility in aqueous environments, which often results in low bioavailability and inconsistent absorption. These drugs tend to aggregate in the bloodstream, potentially causing embolism and poor distribution to target sites, thereby increasing the risk of off-target effects and toxicity. Additionally, these drugs are prone to rapid clearance from the body, which can shorten their therapeutic duration. The formulation of effective delivery systems for these drugs is complex and costly, often requiring advanced techniques such as nanoparticle encapsulation or liposomes to increase their solubility and stability. The narrow therapeutic window further complicates the clinical use of hydrophobic drugs, necessitating careful design and optimization of delivery systems to maximize efficacy while minimizing adverse side effects. (Lipinski, 2000; Mitchell *et al*., 2021; J. K. Patra *et al*., 2018)

Noscapine and its derivatives hold significant promise in cancer therapy, but their clinical potential can be further enhanced through the use of advanced drug delivery carriers. One of the primary challenges with noscapine is its relatively low bioavailability and suboptimal pharmacokinetic profile, which can limit its therapeutic efficacy. Moreover, the lack of targeted delivery mechanisms and limited tissue penetration further reduce the effectiveness of noscapine in solid tumors. Addressing these challenges requires advanced drug delivery strategies, such as nanoformulations, prodrug approaches, and targeted

conjugates, to ensure effective delivery and sustained therapeutic concentrations in tumor tissues. Different drug delivery carriers, such as cyclodextrin complexes, polymeric nanoparticles, and liposomes, have been explored. (Cai *et al*., 2021) For example, encapsulating noscapine in PLGA-PEG-FA nanoparticles not only improves its solubility and stability but also allows for targeted delivery to tumor cells via the folate receptor-mediated pathway, thereby increasing drug accumulation at the tumor site and reducing systemic toxicity. (A. Patra *et al*., 2022) Similarly, incorporating noscapine into cyclodextrin complexes enhances its aqueous solubility, facilitating better absorption and distribution. (Madan *et al*., 2012) These delivery systems can also provide controlled release of noscapine, maintaining therapeutic drug concentrations over an extended period and reducing the frequency of dosing. By using these advanced carriers, the therapeutic potential of noscapine and its derivatives can be significantly increased, offering a more effective and targeted approach to cancer treatment.

1.13. Drug delivery carriers

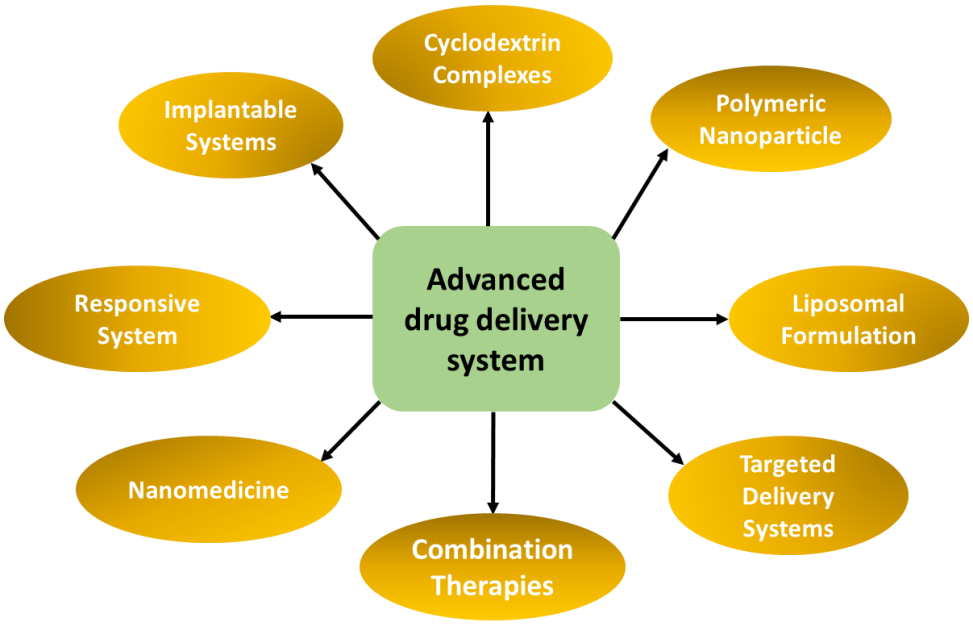

Figure 1.9. Applications of various drug delivery carriers.

Drug delivery carriers are specialized systems designed to transport therapeutic agents to targeted sites in the body in a controlled, efficient, and safe manner. These carriers play crucial roles in modern medicine by increasing the solubility, stability, bioavailability, and therapeutic index of drugs, especially those with poor water solubility or unfavourable pharmacokinetics (Figure 1.9). Traditional drug administration often results in nonspecific distribution, rapid clearance, and systemic side effects. Drug delivery carriers address these challenges by encapsulating or complexing the drug, thereby protecting it from

degradation, enabling controlled release, and improving its accumulation at the disease site. (Adepu & Ramakrishna, 2021) Various types of carriers have been developed, including polymeric nanoparticles, lipid-based systems, micelles, dendrimers, cyclodextrins, and inorganic nanomaterials. Each carrier system offers unique advantages depending on the drug's physicochemical properties and therapeutic application. For example, polymeric carriers such as PLGA or PEG-based nanoparticles provide controlled release and biodegradability, whereas cyclodextrins enhance aqueous solubility through inclusion complex formation. Liposomes and micelles are particularly effective for encapsulating hydrophobic drugs, and ligand-modified carriers enable active targeting to specific cells or tissues, such as tumors expressing folate or transferrin receptors. With advances in nanotechnology and materials science, drug delivery carriers are increasingly being tailored for personalized medicine, improving treatment outcomes while minimizing adverse effects (Table 1.1).

Table 1.1. Table showing different types of drug delivery carriers along with representative examples, their key physicochemical and biological properties, and their therapeutic applications in drug delivery.

Carrier Type	Examples	Properties	Applications	References
Polymeric Nanoparticles	PLGA, PEG, PLGA-PEG-FA, Chitosan	Biodegradable, tunable size, controlled release	Cancer therapy, gene delivery	(Abdipour *et al*., 2024)
Liposomes	Lipoplatin	Phospholipid bilayer, encapsulate hydrophilic & hydrophobic drugs	Chemotherapy, antifungal delivery	(Jehn *et al*., 2007)
Solid Lipid Nanoparticles (SLNs)	Compritol 888 ATO, glyceryl monostearate	High stability, suitable for topical & oral delivery	Skin delivery, oral sustained release	(Duong *et al*., 2020)
Nanostructured Lipid Carriers (NLCs)	Mix of solid & liquid lipids	Improved loading, less drug expulsion	Anti-inflammatory, anticancer agents	(Elmowafy & Al-Sanea, 2021)

Cyclodextrins	β-CD, γ-CD, M-β-CD	Form inclusion complexes, enhance solubility	Poorly soluble drugs (e.g., paclitaxel, noscapine)	(Madan *et al*., 2010; Mognetti *et al*., 2012)
Dendrimers	PAMAM, PPI dendrimers	Branched structure, high payload, surface modification	Gene/drug delivery, diagnostics	(Zenze *et al*., 2023)
Polymeric Micelles	PEG-PLA, PEG-PCL	Amphiphilic block copolymers, solubilize hydrophobic drugs	Parenteral chemotherapy	(Cho *et al*., 2016; Endres *et al*., 2011)
Inorganic Nanoparticles	Gold NPs, Iron oxide NPs, silica NPs	Good for imaging, photothermal therapy, drug loading	Theranostics, targeted delivery	(Unnikrishnan *et al*., 2023)
Hydrogels	PEG hydrogel, alginate, chitosan	Swellable, injectable, biocompatible	Tissue engineering, sustained release	(Tan & Marra, 2010)
Carbon-Based Carriers	Carbon nanotubes, graphene oxide	High surface area, functionalization potential	Gene delivery, imaging	(Mahor *et al*., 2021)

1.14. Targeted drug delivery

Drug delivery methods for cancer treatment have evolved significantly, with a focus on enhancing the specificity, efficacy, and safety of therapeutic agents. While effective, traditional chemotherapy often lacks selectivity, leading to severe side effects due to damage to healthy tissues. To address this, advanced delivery systems such as nanoparticles, liposomes, and polymeric micelles have been developed to improve drug targeting and reduce systemic toxicity. These nanocarriers can be engineered to passively accumulate in tumor tissues through the enhanced permeability and retention (EPR) effect or actively target cancer cells by conjugating ligands specific to tumor-associated antigens.

Additionally, stimuli-responsive systems that release drugs in response to environmental triggers such as pH, temperature, or enzymes within the tumor microenvironment are being explored to further increase treatment precision. Innovations such as antibody–drug conjugates (ADCs) and gene delivery systems also show promise in providing targeted therapy with minimal off-target effects. (Yao *et al*., 2020; Yu *et al*., 2010) These advanced drug delivery methods aim to maximize the therapeutic index of anticancer drugs, ensuring that high drug concentrations reach the tumor site while minimizing harm to normal cells.

1.14.1. Polymeric nanoparticle-based drug delivery systems

Polymeric nanoparticles are among the most extensively studied drug delivery platforms because of their biocompatibility, tunable physicochemical properties, and ability to provide controlled and targeted release of therapeutic agents. They can encapsulate both hydrophilic and hydrophobic drugs, protect them from enzymatic degradation, and improve their pharmacokinetic profiles. Functionalization with ligands such as folic acid, antibodies, or peptides further enhances their specificity toward target cells or tissues, making them particularly valuable in cancer therapy, gene delivery, and vaccine development (Figure 1.10). (Guidi *et al*., 2024) These nanoparticles, particularly those composed of poly(lactic-co-glycolic acid) (PLGA) conjugated with polyethylene glycol-folic acid (PEG-FA), offer significant advantages as drug delivery carriers, especially in cancer treatment. PLGA is a biodegradable and biocompatible polymer that has been extensively used in drug delivery systems because of its ability to protect encapsulated drugs from degradation, thereby increasing their stability and prolonging their release. The addition of PEG to PLGA improves the circulation time of the nanoparticles by preventing recognition and clearance by the immune system, a process known as the "stealth" effect. Furthermore, the conjugation of folic acid (FA) to PEGylated nanoparticles allows active targeting of cancer cells, as many tumors overexpress folate receptors. Folate receptors (FRs), particularly the alpha isoform (FR-α), are overexpressed on various cancer cells surface, including ovarian, breast, lung, and prostate tumors. Folic acid (vitamin B9), a high-affinity ligand for FR-α, is a small, stable, and nonimmunogenic molecule that can be easily conjugated to drug-loaded carriers such as nanoparticles, liposomes, dendrimers, and micelles. (Cheung *et al*., 2016) Once bound to the folate receptor, folic acid-conjugated nanocarriers are internalized by cancer cells via receptor-mediated endocytosis, allowing for the selective delivery of therapeutic agents while minimizing off-target toxicity. This targeted approach not only increases the accumulation of the drug in the tumor tissue but also reduces the systemic toxicity and side effects typically associated with conventional

chemotherapy. Additionally, PLGA-PEG-FA nanoparticles can encapsulate a variety of therapeutic agents, including hydrophobic drugs, nucleic acids, and proteins, offering versatility in treatment strategies. These properties make PLGA-PEG-FA nanoparticles an attractive platform for delivering drugs with enhanced efficacy and safety profiles. (Lakkireddy & Bazile, 2016; Ledermann *et al.*, 2015)

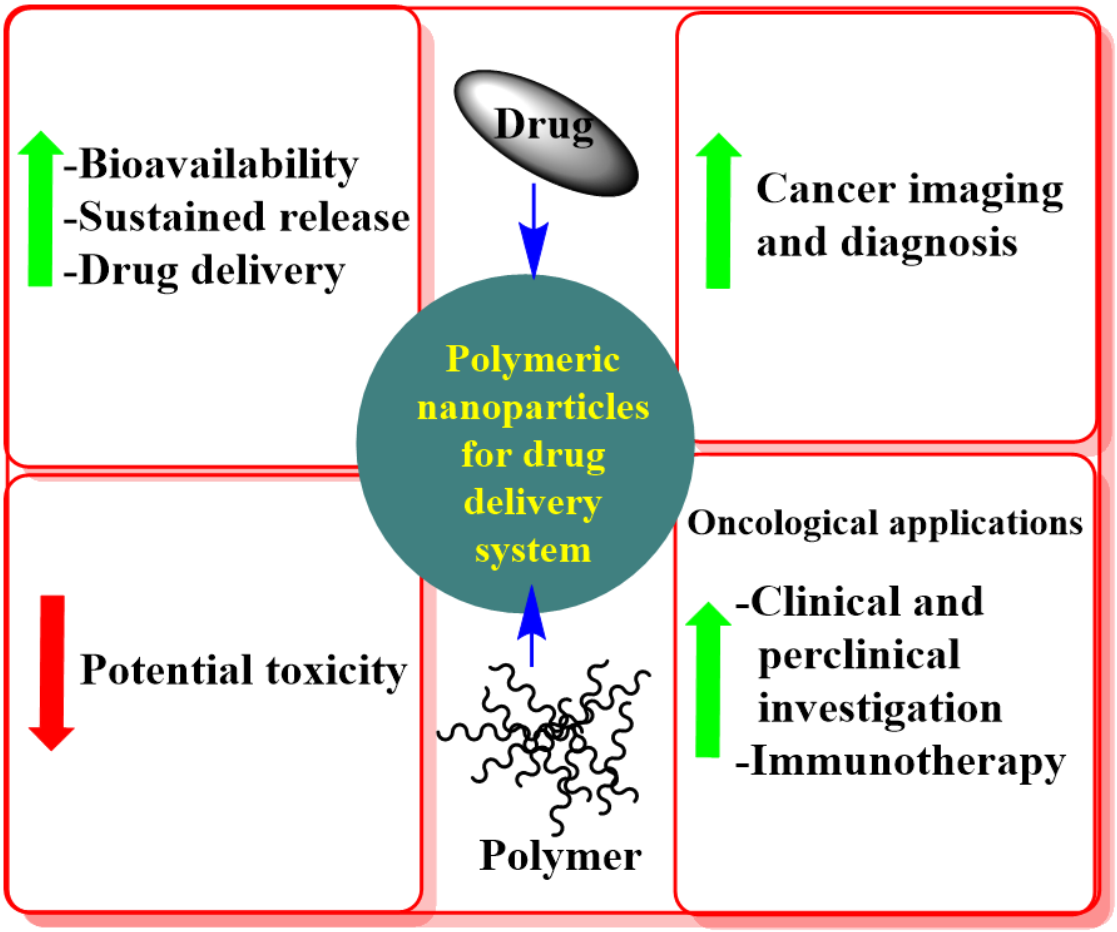

Figure 1.10. Polymeric nanocarriers engineered for targeted and efficient cancer therapy are designed to increase drug delivery specificity, improve pharmacokinetics, and reduce systemic toxicity.

1.14.2. Cyclodextrin-based drug delivery systems

Cyclodextrins (CDs) offer several advantages as drug delivery carriers, particularly for improving the solubility, stability, and bioavailability of poorly water-soluble drugs (Figure 1.11). (Kali *et al.*, 2024) These cyclic oligosaccharides have a hydrophobic inner cavity and a hydrophilic outer surface, allowing them to form inclusion complexes with a wide

range of drugs. This encapsulation can significantly increase the solubility of hydrophobic drugs in aqueous environments, facilitating their absorption and improving their bioavailability. Cyclodextrins also protect drugs from degradation by shielding them from environmental factors such as light, heat, and oxygen, thereby increasing the stability of the drug. Furthermore, cyclodextrins can reduce drug toxicity by minimizing irritation to tissues and preventing the release of the drug in nontargeted areas. Their ability to form complexes with drugs without covalent bonding ensures that the drug can be released at the target site, often in response to changes in the local environment, such as pH. (Payamifar & Poursattar Marjani, 2023) The table lists cyclodextrin variants, their corresponding drug delivery applications, and examples of drugs formulated with them (Table 1.2). Additionally, cyclodextrins are generally known as safe (GRAS) and have low immunogenicity, making them suitable for a wide range of drug delivery applications, including oral, topical, and injectable formulations.

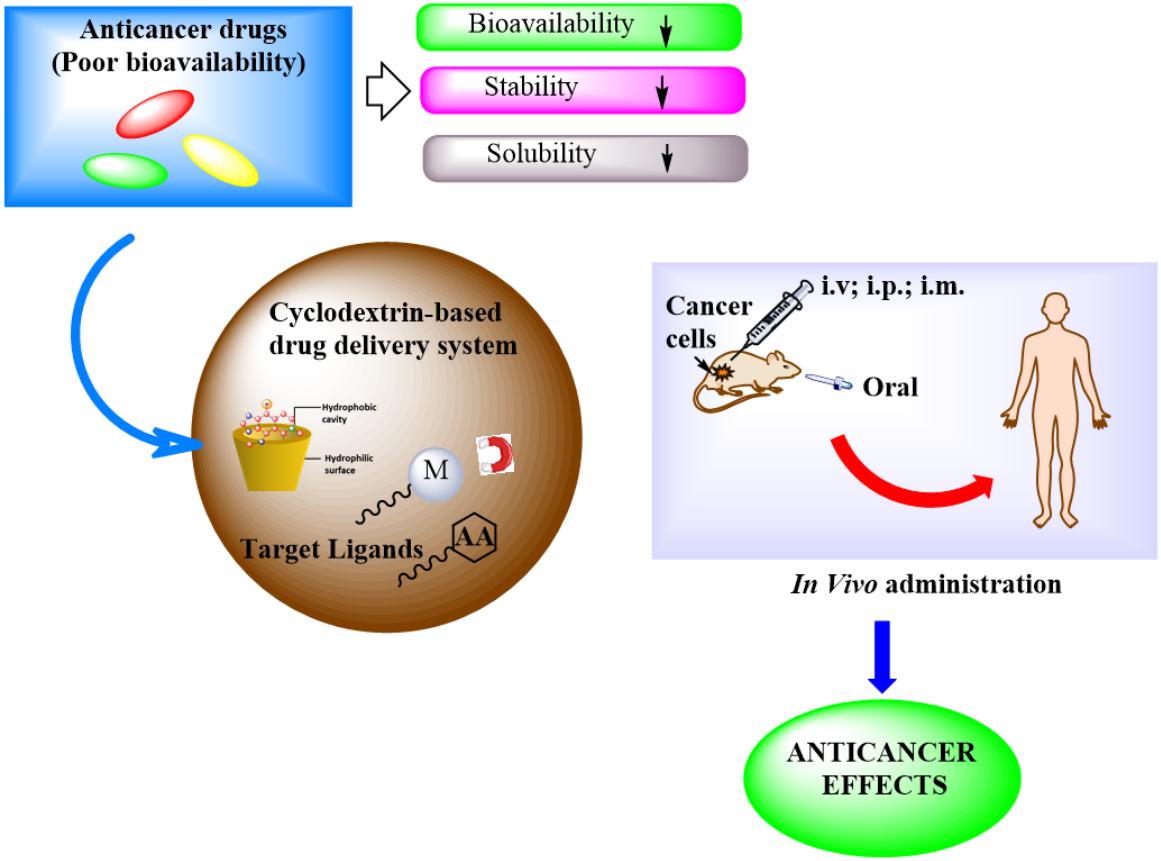

Figure 1.11. Schematic illustration of a cyclodextrin-based drug delivery system for enhancing the therapeutic efficacy of anticancer drugs.

Table 1.2. Overview of different types of cyclodextrins used in drug delivery applications, highlighting their roles in enhancing the solubility, stability, and bioavailability of specific therapeutic agents.

SI. No.	Cyclodextrin Type	Drug Delivery Application	Specific Drugs	References
1	α-Cyclodextrin	Improvement of Drug Solubility and Stability	Anti-inflammatory drugs, hormones (e.g., insulin)	(Bucur *et al.*, 2022)
2	β-Cyclodextrin	Enhancement of Drug Solubility	Anticancer agents (e.g., paclitaxel), anti-inflammatory drugs	(Franco & De Marco, 2021)
3	γ-Cyclodextrin	Solubilization of Hydrophobic Drugs	Anticancer drugs (e.g., doxorubicin), cardiovascular drugs	(Xu *et al.*, 2014)
4	Hydroxypropyl-β-Cyclodextrin (HP-β-CD)	Enhanced Drug Delivery in Various Formulations	Anticancer agents (e.g., docetaxel), anti-epileptics	(Ferrati *et al.*, 2015)
5	Methyl-β-Cyclodextrin (M-β-CD)	Enhanced Bioavailability and Controlled Release	Anticancer drugs (e.g., noscapine), antifungal agents	(Madan *et al.*, 2014)
6	Dimethyl-β-Cyclodextrin (DM-β-CD)	Improved Drug Solubility and Stability	Anticancer drugs, cardiovascular drugs	(Kerdpol *et al.*, 2023)
7	Sulfobutylether-β-Cyclodextrin (SBE-β-CD)	Enhanced Solubility and Stability in Injectable Formulations	Anticancer drugs (e.g., docetaxel), antibiotics	(Ren *et al.*, 2020)
8	Carboxymethyl-β-Cyclodextrin (CM-β-CD)	Enhanced Solubility and Release Profile of Anticancer Drugs	Anticancer agents (e.g., Gefitinib)	(Shi *et al.*, 2014)
9	2-Hydroxypropyl-β-Cyclodextrin (HP-β-CD)	Increased Solubility and Stability for Oral and Injectable Drugs	Antihypertensives, antidiabetic drugs	(Leonis *et al.*, 2020)

CHAPTER-2

Design and Development of PLGA-PEG-FA Nanoparticles Encapsulating Noscapinoids for Receptor-mediated Breast Cancer Treatment

Abstract

Folate-conjugated PLGA-PEG nanocarriers have emerged as a promising strategy to enhance the targeted delivery and therapeutic efficacy of anticancer agents. In this study, we explored the potential of these nanocarriers to improve the anticancer activity of 9-bromo-noscapine (9-Br-Nos) in breast cancer. The folate-conjugated PLGA-PEG nanocarriers were designed for the selective targeting of folate receptors, which are overexpressed in breast cancer cells. The nanocarriers were synthesized, characterized, and evaluated for size, surface morphology, drug encapsulation efficiency, and *in vitro* release profile. Cytotoxicity studies on the MCF-7 and MDA-MB-231 breast cancer cell lines revealed a significant increase in the anticancer efficacy of 9-Br-Nos when delivered via these nanocarriers compared with free drug treatment. Enhanced cellular uptake, improved mitochondrial membrane potential, and increased reactive oxygen species (ROS) production were observed in the treated cells. In addition, a spheroid disintegration assay was also performed to evaluate the effects of the nanoformulation on a 3-dimensional (3D) tumor model, which closely resembles the tumor microenvironment. To further elucidate the molecular mechanism of action, western blot analysis was performed, which revealed changes in the expression of apoptosis-related proteins, confirming the enhanced anticancer activity of the targeted nanoformulation. Furthermore, pharmacokinetic studies in rats demonstrated a significant improvement in the bioavailability and sustained release of 9-Br-Nos from folate-conjugated nanocarriers compared with free drug administration. The *in vivo* efficacy of the nanoformulation was further validated using a tumor xenograft model, where a marked reduction in tumor volume was observed in animals treated with the folate-conjugated nanoparticles. These results indicated that folate-conjugated PLGA-PEG nanocarriers effectively amplify the anticancer effects of 9-Br-Nos, suggesting a promising strategy for targeted therapy in breast cancer treatment. This study underscores the potential of nanocarrier-based drug delivery systems for improving both the therapeutic efficacy and pharmacokinetic profile of anticancer agents.

Keywords: PLGA-PEG-FA nanoparticle, 9-Br-Nos, Receptor-mediated endocytosis, Breast cancer, Apoptosis.

2.1. Introduction

Currently, nanocarriers play crucial roles in modern pharmacotherapy owing to their efficient drug delivery, targeted specificity, and controlled release properties. (Mitchell *et al*., 2021; Waheed *et al*., 2022) Recent developments in drug delivery systems and therapeutic technologies have introduced novel strategies to improve both the efficacy and safety of conventional drugs. (Ajith *et al*., 2023; Jadhav *et al*., 2024) Among them, polymeric nanoparticles (PNs) offer several key advantages, including the ability to encapsulate high concentrations of water-insoluble drugs within their hydrophobic core. (Sung & Kim, 2020) Polymeric nanoparticles with optimized size and surface properties can localize to tumor tissue through the enhanced permeability and retention effect (EPR). (Elmowafy *et al*., 2023; Gagliardi *et al*., 2021) Furthermore, surface modifications of these nanocarriers could enhance the site-specific targeting of hydrophobic drugs. Poly(lactic-co-glycolic acid) (PLGA), functionalized with polyethylene glycol (PEG) and folic acid (FA), represents one of the most promising polymeric systems for the active targeting of drugs. (Dodda *et al*., 2022; Perinelli *et al*., 2019) PEG covalently linked with PLGA allows prolonged blood circulation by preventing its immediate elimination from the blood by the reticuloendothelial system. However, ligand binding, such as FA, improves tumor penetration through receptor-mediated endocytosis, as folate receptors, such as glycosylphosphatidylinositol-anchored cell surface receptors, are known to be overexpressed in several tumors, such as ovarian and breast cancers. However, normal tissues lack these receptors, thereby reducing off-target toxicity. (Jianian Chen *et al*., 2012; Patra *et al*., 2022)

Compared with the parent compound, 9-Br-Nos, a halogenated derivative of noscapine, has emerged as a potent anticancer agent with improved efficacy. In previous studies, complexation with cyclodextrin was used for the treatment of colon cancer. (Madan *et al*., 2014) Additionally, other groups have developed inhalable nanostructured lipid particles by using 9-Br-Noscapine to treat non-small cell lung cancer. (Jyoti *et al*., 2015) Similarly, PPF NPs have been explored for targeted breast cancer therapy by delivering drugs such as disulfiram and metformin through receptor-mediated uptake. (Fasehee *et al*., 2016; Jafari-Gharabaghlou *et al*., 2023) However, 9-Br-Nos disrupts microtubule dynamics and induces mitotic arrest, leading to apoptosis, which offers new possibilities for the treatment of cancer. (Lopus & Naik, 2015) However, similar to that of noscapine, the clinical application of 9-Br-Nos is hindered by poor aqueous solubility and systemic toxicity, necessitating the development of advanced delivery systems. (Madan *et al*., 2012) PLGA-

PEG-FA nanoparticles (PPF NPs) offer a promising solution by encapsulating 9-Br-Nos within a biodegradable matrix, increasing their solubility, stability, and tumor specificity. Furthermore, this targeted approach can reduce the off-target effects of a drug, improve its safety profile while maintaining its therapeutic efficacy. Currently, there is no specific literature reporting the formulation of 9-Br-Nos using PPF NPs for targeted drug delivery in cancer therapy.

Hence, we report the synthesis and characterization of PPF NPs in targeted drug delivery for breast cancer therapy. These nanoparticles were fabricated via an optimized emulsion–solvent evaporation technique (coprecipitation method) to obtain high drug loading, entrapment efficiency, and stability. The functionalization with FA ensured selective targeting to folate receptor-overexpressing cells, enhancing the potential for localized drug delivery and minimizing systemic toxicity.

2.2. Materials and reagents

PLGA, PEG-bis amine, PLGA-PEG, folic acid, N,N′-dicyclohexylcarbodiimide (DCC), N-hydroxy-succinimide (NHS), anhydrous dimethyl sulfoxide (DMSO), anhydrous dichloromethane (DCM), and MTT (3-(4,5-dimethylthiazol2-yl)-2,5-diphenyltetrazolium bromide) were purchased from Sigma unless otherwise stated. Finally, deionized and filtered water was used in all the experiments (Milli-Q Academic®, Millipore, Molsheim, France).

2.2.1. Cell Culture

MCF-7 and MDA-MB-231 breast cancer cell lines, obtained from NCCS, Pune were maintained in a humidified CO_2 incubator at 37 °C with 5% CO_2. Dulbecco's modified Eagle's medium (DMEM) (Gibco BRL, UK), fetal bovine serum (FBS) (Gibco BRL, UK), 10X phosphate buffer saline (Gibco BRL, UK), 0.003% trypsin 0.25% EDTA (Gibco BRL, UK), 10 mg/mL penicillin/streptomycin solution (Sigma–Aldrich), and DMSO (HIMEDIA), MTT reagent (HIMEDIA) were used in this study for cell culture and treatment. All procedures were performed within a Class A2 biosafety cabinet following rigorous aseptic protocols.

2.2.2. Characterization of the polymer conjugate by FT-IR and ^{1}H NMR

The chemical structure of PLGA-PEG-FA was confirmed via Fourier transform infrared (FT-IR) spectroscopy and nuclear magnetic resonance (NMR) spectroscopy. FT-IR spectra were recorded using a Bruker ALPHA II instrument in ATR mode. Measurements were performed in the scan range of 4000–550 cm^{-1}. The characteristic peaks corresponding to

the functional groups of PLGA, PEG, and folic acid were analysed to verify successful conjugation. ^{1}H NMR spectra was obtained on Bruker Ultra shield 400 MHz NMR spectrometer. The polymer was dissolved in DMSO-d_6, and chemical shifts were recorded in parts per million (ppm).

2.2.3. Preparation of PLGA-based nanoparticles

PLGA-9-Br-Nos (PD), PLGA-PEG-FA-9-Br-Nos (PPFD), PLGA-Coumarin-6, and PLGA-PEG-FA-Coumarin-6 nanoparticles were synthesized via the nanoprecipitation technique. Briefly, 50 mg of the polymer and 5 mg of the drug (10%) were codissolved in 2 mL of acetone. This organic phase was then added to 12 mL of an aqueous solution of 1% polyvinyl alcohol (PVA) and sonicated at 37% amplitude for 1 minute with a pulse of 10 seconds ON and 10 seconds OFF. The mixture was then constantly stirred at 500 rpm for~6 hours, allowing the acetone to evaporate. The emulsion was then sonicated again and centrifuged at 17000 rpm for 30 minutes at 4°C. The supernatant was removed, and the pellet was washed three times with deionized water. The final product was then lyophilized. All the batches were prepared in triplicate. (Hernández-Giottonini *et al*., 2020)

2.2.4. Quantification of folic acid Conjugation Efficiency

2.2.4.1. Calibration Curves for Folic Acid Standard Solutions

Folic acid (5, 10, 15, and 20 µg/mL) was prepared by dilution with DMSO. The absorbance was recored at 256 nm via a UV spectrophotometer (LAB INDIA 3200). A calibration curve was constructed between the FA concentrations and absorbance units.

2.2.4.2. Determination of folic acid Conjugation Efficiency

The percent of conjugation was calculated by determining the amount of FA conjugated in PLGA–PEG–FA. A known amount of dried PLGA–PEG–FA was dissolved in DMSO, and the UV absorbance value at 256 nm was evaluated to determine the concentration of conjugated FA.

2.2.5. Chemical characterization of drug-conjugated PLGA and PLGA-PEG-FA nanoparticles

2.2.5.1. Characterization by particle size analysis via dynamic light scattering (DLS)

The nanoparticles were diluted with deionized water, and the average sizes were recorded via dynamic light scattering (DLS) with a Litesizer DLS 500 instrument. The nanoparticles were diluted with deionized water and sonicated in an ultra-sonicator, and the measurements were performed at 25°C. The hydrodynamic size was reported as the

average of 20 runs, with each run including triplicate measurements. For each sample, the mean particle diameter and polydispersity index were calculated.

2.2.5.2. Nanoparticle surface morphology by Scanning electron microscopy (SEM)

The shape, surface morphology, and particle size distribution of the PPFD nanoparticles (NPs) were characterized via high-resolution field emission scanning electron microscopy (JEOL JSM-6480 LV). The sample was mounted on double-stick conductive carbon tape attached to an aluminium stub and then gold-coated in an argon atmosphere with a sputter coater (SC 7620, mini sputter coater, Quorum Technology Ltd., UK). The analysis was performed at 15 kV accelerating voltage and a working distance of 4.1 mm in high-vacuum mode.

2.2.5.3. Drug loading and encapsulation efficiency

The drug loading and entrapment efficiency of 9-Br-Nos in the PLGA-PEG-FA nanoparticles were calculated by measuring the concentration of free drug in the suspension via HPLC. A calibration curve was prepared with various concentrations of 9-Br-Nos in methanol (50, 75, 100, 200, and 500 µg/mL). The sample was prepared by adding 5 mg/mL nanoparticles to a physiological saline solution. A total of 10 µl of the sample was diluted with 90 µl of DMSO and vortexed for 1 minute, and 900 µl of methanol was then added to precipitate the insoluble polymer. The suspension was vortexed again for 30 seconds, followed by centrifugation at 5000 rpm for 10 minutes. The supernatant was then filtered through a 0.45 µm syringe filter and analysed via HPLC to measure the concentration of the drug. The mobile phase used was a 0.1% orthophosphoric acid solution along with methanol.

Drug loading (DL%) =

(Drug concentration encapsulated in the NPs)/ (Concentration of resulting nanoparticle suspension) ×100

Encapsulation efficiency (EE%) =

(drug concentration encapsulated in the NPs)/(Total drug concentration) ×100

2.2.5.4. *In vitro* drug release study

The nanoformulations were characterized via a drug release study under optimal conditions in normal physiological saline (phosphate-buffered saline, PBS, pH~7.4). Briefly, 5 mg of 9-Br-Nos and PPFD nanoparticles were suspended in 20 mL of PBS in a glass beaker. The beaker was placed on a magnetic stirrer and stirred at ~150 rpm at 37 °C. At predetermined

time intervals (5 min, 10 min, 15 min, 20 min, 25 min, 30 min, 45 min, 1 hr, 2 hr, 3 hr, 4 hr, 6 hr, 12 hr, 24 hr and 48 hr), 2 mL of the release medium was withdrawn and replaced with an equal volume of fresh PBS to regulate the sink condition. The volume withdrawn was then analysed via UV–Visible spectroscopy at λ_{max} 312 nm.

2.2.6. Cellular uptake of Coumarin-6-loaded Nanoparticles

MDA-MB-231 cells were seeded in a 6-well plate at a density of 50,000 cells/well and incubated for 24 hours. After incubation, the medium was replaced with coumarin-6-loaded PLGA and PLGA-PEG-FA nanoparticles at concentrations of 10 and 25 µg/mL. Following 4 hours of incubation, the cells were washed with 1X PBS three times and then fixed with 4% paraformaldehyde. The cells were then incubated with the nuclei-specific dye DAPI for 10 minutes at room temperature, followed by washing twice with PBS. The cells were subsequently visualized via a fluorescence microscope (Nikon ECLIPSE Ts2R).

2.2.7. *In vitro* cell viability study

Cell viability was assessed via an MTT colorimetric assay. MCF-7 and MDA-MB-231 breast cancer cells were seeded at a density of 5,000 cells/well in a 96-well plate containing complete growth medium and incubated for 24 hours. The cells were then treated with various concentrations of the test compounds (ranging from 1 to 50 µg/mL) for 48 to 72 hours. After treatment, MTT solution (0.5 mg/mL) was added to each well, and the plate was incubated in a CO_2 incubator for an additional 4 hours. The resulting formazan crystals were dissolved in 100 µL of DMSO, and the absorbance was measured at 570 nm via a Bio-Rad iMark™ Microplate Absorbance Reader. Untreated cells served as a negative control for assessing cytotoxicity.

2.2.8. Nuclear morphology study by Hoechst 33342 staining

MDA-MB-231 cells were treated to IC_{50} concentrations of 9-Br-Nos and PPFD for 24 hours. After treatment, the cells were washed three times with phosphate-buffered saline (PBS) and then fixed in 100% ice-cold methanol for 15 minutes. Following fixation, the cells were washed again three times with PBS, and their nuclei were stained with Hoechst 33342 (1 µg/mL) for 15 minutes. The stained cells were then examined under a fluorescence microscope (Nikon ECLIPSE Ts2R).

2.2.9. Mitochondrial membrane potential measurement by JC-1 dye

Qualitative and quantitative changes in mitochondrial membrane potential (MMP) were assessed via JC-1 staining. In healthy cells, JC-1 forms J-aggregates that exhibit strong red fluorescence, with excitation and emission at 560 nm and 595 nm, respectively. In

apoptotic cells, JC-1 exists as a monomer and displays strong green fluorescence, with excitation and emission at 485 nm and 535 nm, respectively. The cells were treated for 24 hours with the IC_{50} concentrations of 9-Br-Nos and PPFD. After treatment, the cells were washed with 1x PBS, incubated with 5 mM JC-1 stain for 30 minutes at 37°C, and washed. Images were captured via a Nikon ECLIPSE Ts2R fluorescence microscope. The degree of mitochondrial depolarization in each group was quantified by calculating the ratio of aggregate to monomer fluorescence intensity.

2.2.10. Reactive oxygen species (ROS) estimation by DCF-DA dye

The estimation of ROS by DCF-DA dye was performed via both microscopy and fluorometry. Briefly, a stock solution of 10 mM was made in DMSO and further diluted to a working concentration of 20 μM in the culture medium. MDA-MB-231 cells were treated with the IC_{50} concentrations of 9-Br-Nos and PPFD for 12 hours. The cells were then washed with PBS and incubated with 20 μM DCF-DA at 37°C for 30 minutes. After incubation, the cells were imaged via a fluorescence microscope (Nikon ECLIPSE Ts2R microscope). Then, the cells were lysed in PBS, and the fluorescence intensity was measured via a fluorescence spectrophotometer (Hitachi F 7000).

2.2.11. Three-dimensional (3D) spheroid disintegration assay

The 3D spheroid disintegration assay provides a physiologically suitable *in vitro* model to study the impact of anticancer formulations on 3D tumor-like structures that closely mimic the *in vivo* tumor microenvironment. MDA-MB-231 cells were seeded at a density of 1×10^3 cells per well in ultralow attachment 96-well round bottom plates (Corning) containing 100 μl of complete medium. The plate was then centrifuged at 1000 rpm for 10 minutes for cell aggregation and incubated at 37°C with 5% CO_2 for 7–10 days to allow compact spheroid formation. After the spheroids formed, they were treated with 9-Br-Nos and PPFD nanoparticles, and the untreated cells were used as controls. The spent media was replaced with fresh media every two days. Treatments were then administered in triplicate, and the spheroids were observed for morphological changes such as spheroid integrity, diameter reduction, and disintegration over 5 days via a Nikon inverted phase-contrast microscope. The images were then analysed for size via ImageJ software. (Alserihi *et al*., 2021)

2.2.12. Western blot analysis

MDA-MB-231 breast cancer cells were treated with the 9-Br-Nos-MβCD inclusion complex for 48 hours, with untreated cells serving as a negative control. Total cellular

proteins were extracted via lysis buffer containing 20 mM Tris-HCl (pH 8.0), 1 mM EDTA, 0.5 mM EGTA, 0.1% sodium deoxycholate, 150 mM NaCl, 0.1% IGEPAL, and 10% glycerol, along with a protease inhibitor cocktail (PIC) from Roche, PhosStop (Roche), and 1 mM PMSF. The mixtures were then centrifuged at 12,000 rpm for 25 minutes, and the supernatants were collected. The total protein concentration was determined via a BCA kit. Next, 50 μg of protein from each sample was loaded onto a 10% SDS–PAGE gel, and the proteins were transferred to a polyvinylidene difluoride (PVDF) membrane (Bio-Rad, USA) via a Bio-Rad Trans-Blot® SD Semi-Dry Transfer Cell. The membrane was blocked for 1 hour at room temperature with 5% nonfat milk, followed by overnight incubation at 4°C with the appropriate primary antibody. After the membranes were washed three times with 1X PBS/PBST, they were incubated for 1 hour at room temperature with horseradish peroxidase-conjugated secondary antibodies (1:5000, Promega W4011). The primary antibodies used were against β-actin (1:1000, CST 4967S), Bax (1:1000, CST 2772S), Bcl-2 (1:1000, CST 4223S) and Cleaved caspase 3 (1:1000, CST 9661S).

2.2.13. Acute Toxicity Studies in Rats

A single oral dose of varying concentrations (250, 500, 1000, 2000, and 5000 mg/kg) of the free drug and PPFD nanoparticles was administered to six separate groups of Wistar rats, with each group comprising six animals (n = 6). The rats were monitored over a period of 14 days for signs of toxicity and mortality, following the OECD Guideline 408 (2008). The number of fatalities, if any, was recorded at the end of the observation period.

2.2.14. Sub-Acute Toxicity Evaluation of the free drug and PPFD nanoparticles in Rats

For the sub-acute toxicity assessment, Wistar rats were randomly allocated into two groups with six animals per group (n = 6). Each group received a daily oral dose of 500 mg/kg body weight of the free drug and PPFD nanoparticles for 28 consecutive days, in accordance with OECD Test No. 423, 2008 for repeated dose oral toxicity studies. Throughout the experimental period, animals were observed daily for any clinical abnormalities or mortality. Additionally, food and water consumption as well as body weight were monitored and recorded throughout the 28-day study.

2.2.15. Hematological and Biochemical Analysis

After the study, the animals were subjected to mild anesthesia using isoflurane, followed by euthanasia via cervical dislocation. Blood samples were then collected via cardiac

puncture. Hematological parameters were measured using an automated CBC analyzer (Byovet). For biochemical analysis, the serum was separated by centrifuging the blood at 5000 rpm for 10 minutes using an Eppendorf 5810r centrifuge. Biochemical markers including glucose (GLU), albumin (ALB), urea, creatinine (CREA), cholesterol (CHOL), triglycerides (TG), SGPT, SGOT, total protein (TP), HDL, alkaline phosphatase (ALP), and others were evaluated using an automated biochemical analyzer (Byovet, Smart-5DX) with standard assay kits.

2.2.16. *In vivo* toxicity assessment by hematoxylin & eosin staining of rat tissue

Toxicity in vital organs was evaluated through histopathological analysis via hematoxylin and eosin (H&E) staining of tissue sections from the brain, heart, liver, lungs, and kidneys of rats (n=6) treated with 9-Br-Nos and its inclusion complex. The tissues were collected and fixed in paraformaldehyde solution (4% PFA), followed by immersion in 15% and 30% sucrose solutions for cryoprotection. After dehydration, the tissues were embedded in paraffin wax. Histological sections (10 µm thick) were prepared and stained with H&E. The stained tissue samples were then observed under a Nikon ECLIPSE Ts2R microscope.

2.2.17. Hoechst Staining for Chromatin Condensation in Rat Tissues

Chromatin condensation was assessed as an indicator of apoptotic cell death via Hoechst 33342 staining according to previously reported methods (Baitharu *et al.*, 2014). Heart, liver, kidney, brain, and lung tissues were fixed in a 4% paraformaldehyde solution for 16 hours, followed by a series of washes, dehydration, and paraffin embedding steps. The tissues were then sectioned into thin slices. Specifically, 10 µm thick tissue sections were treated with 0.1% Triton in PBS to facilitate permeabilization and then stained with Hoechst 33342 (1.5 µg/ml) in the dark at room temperature for 15 minutes. After gentle rinsing with 0.1 M PBS, the sections were mounted with glycerol. The extent of chromatin condensation was examined via a Nikon ECLIPSE Ts2R fluorescence microscope with a blue filter and DAPI staining.

2.2.18. *In vivo* Pharmacokinetic Study in Rats via UHPLC-Q-TOF/MS analysis

Three male Sprague–Dawley (SD) rats (250±20 g) were kept in metabolic cages one day before treatment. They received a single oral dose of 5 mg/kg 9-Br-Nos, and 50 mg/kg PPFD. Then, Blood samples (250 µL) were collected from the orbital venous plexus at 0, 2, 6, 12, 24, 36, and, 48 hours post-administration. No dose was administered to the control group. The plasma was then separated from the blood samples by centrifuging at 4000

rpm for 10 minutes, which was then stored at -80°C for further analysis. The samples were analysed via UHPLC-Q-TOF/MS.

2.2.18.1. Plasma sample preparation

Before analysis, the plasma samples were brought to room temperature and redissolved. To prepare the samples, 100 µL of plasma or urine was mixed with 300 µL of a 1:1 methanol:acetonitrile solution in an Eppendorf tube. The mixture was vortexed for 2 minutes, sonicated in an ice–water bath for 2 minutes, and then centrifuged at 15,000 rpm for 10 minutes to remove proteins. The supernatant was transferred to a new tube, leaving the protein residue behind. The collected samples were then dried at room temperature. Before UHPLC-Q-TOF/MS analysis, the dried samples were redissolved in 1.5 mL of methanol, vortexed for 2–3 minutes, sonicated for 15 minutes, centrifuged again at 15,000 rpm for 10 minutes, and filtered. Finally, 10 µL of each prepared sample was injected into the UHPLC-Q-TOF/MS system for analysis.

2.2.19. *In vivo* Antitumor Efficacy Evaluation in MDA-MB-231 Xenograft Model

Female BALB/c athymic nude mice, aged between 8 and 10 weeks, were used for the experiment. Each mouse received a subcutaneous injection of approximately 1×10^6 MDA-MB-231 human breast adenocarcinoma cells in 0.2 mL of phosphate-buffered saline (PBS) into the anterior flank. After 7 to 10 days, once the tumors became palpable, treatment with the free drug and the nanoparticles were initiated via oral gavage. The mice were randomly assigned into two groups, each consisting of five animals. Group 1 served as the untreated control and was given acidified water (pH 4.0), whereas Group 2 received drugs 9-Br-Nos and at a daily oral dose of 150 mg/kg body weight. Tumor growth was monitored every other day using previously established measurement methods. On day 30, all animals were euthanized due to the significant increase in volume of tumor, observed in control group. Final tumor volumes from both control and treated groups were recorded as per the aforementioned procedure. The ethical approval of the animal study (Approval No. NIP/04/2022/PC/476) was obtained from the Institutional Animal Ethics Committee of the NIPER, Hyderabad.

2.2.20. Statistical analysis

The statistical significance of the experimental groups was determined via one-way ANOVA, followed by post hoc analysis with the Newman–Keuls test and Student's t test. A p value of less than 0.05 was considered statistically significant. The data were presented as the mean ± standard deviations for $n \geq 3$. The IC_{50} values for the cell viability assay in

both MDA-MB-231 and MCF-7 cells were calculated via nonlinear curve fitting with GraphPad Prism version 8.0.2 software.

2.3. Results and discussion

2.3.1. Synthesis of the PLGA-PEG-FA conjugates

The synthesis of PLGA-PEG-FA (PPF) polymer conjugate was performed as previously reported with slight modifications (Figure 2.1). (El-Hammadi *et al.*, 2017; Patra *et al.*, 2022)

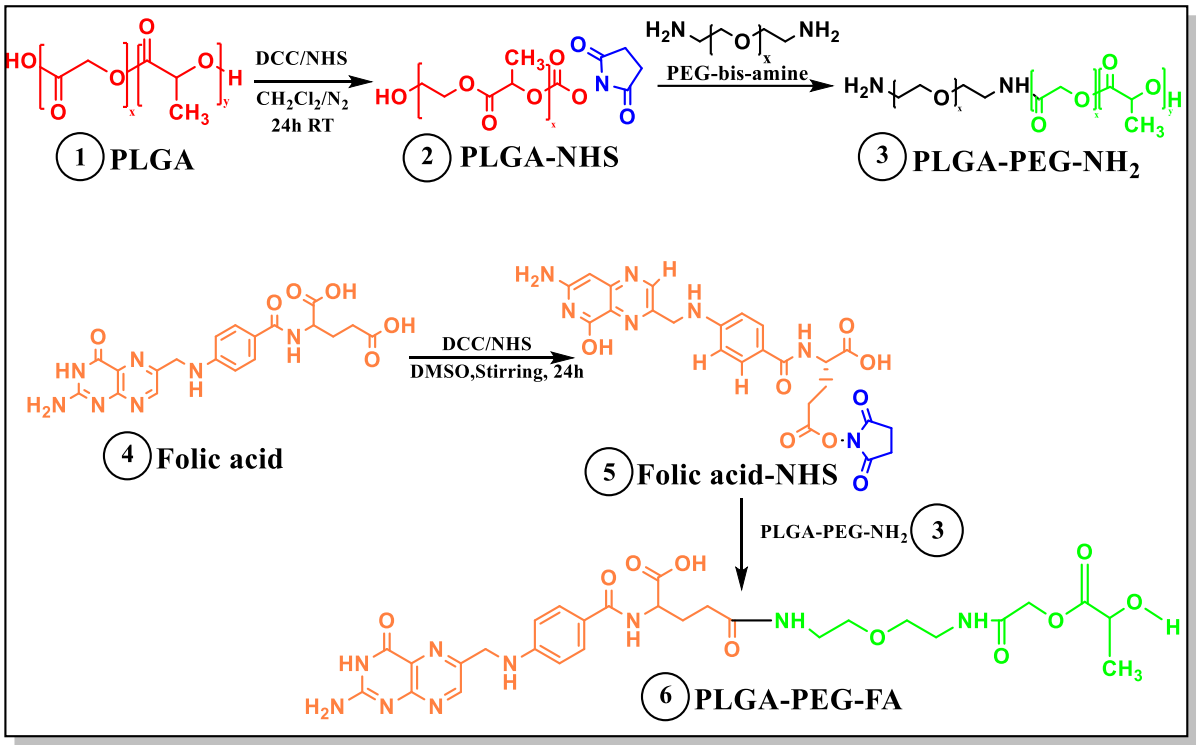

Figure 2.1. Chemical synthetic scheme of PLGA-PEG-FA, illustrating the conjugation of folic acid (FA) to PLGA-PEG via DCC/NHS coupling.

2.3.1.1. Activation of PLGA

PLGA (918 mg, 0.12 mmol), DCC (24.75 mg, 0.24 mmol), and NHS (13.8 mg, 0.24 mmol) were dissolved in 3 mL of anhydrous DCM and stirred at 25°C (RT) under an argon atmosphere for about 24 h (PLGA/NHS/DCC stoichiometric molar ratio was 1:2:2). The resulting mixture was then filtered to remove the byproduct dicyclohexylurea and precipitated by dropping it into ice-cold ether. The solid precipitate was repeatedly washed in an ice-cold 1:1 mixture of ethyl ether and methanol to remove residual NHS. The ether was subsequently decanted, and the activated PLGA was completely dried under vacuum.

2.3.1.2. PEGylation of PLGA

The activated PLGA (385 mg, 0.025 mmol) dissolved in 2 mL of anhydrous DCM was added dropwise to PEG bis(amine) (225 mg, 0.075 mmol) dissolved in 0.5 mL of anhydrous DCM. An excess of PEG bis(amine) was used [PLGA/PEG bis(amine) stoichiometric molar ratio- 1:33] to suppress the formation of PLGA-PEG-PLGA triblock copolymers. The reaction was carried out for 24 h with gentle stirring under an argon atmosphere. The reaction mixture was then precipitated with cold methanol and washed with methanol to eliminate any unreacted PEG. The precipitated final product, the amine-terminated di-block copolymer (PLGA-PEG-NH_2), was filtered and vacuum dried.

2.3.1.3. Activation of folic acid

Folic acid (220.8 mg, 0.5 mmol) was activated with DCC (206.4 mg, 1 mmol) and NHS (115 mg, 1 mmol) in 3 mL DMSO with 0.1 mL of triethylamine as a catalyst under an argon atmosphere overnight, shielded from light. The solution was filtered to remove the dicyclohexylurea byproduct and then precipitated in ice-cold anhydrous ether. The final product obtained in the dry state was then followed several steps of ether washing, decantation, and vacuum drying.

2.3.1.4. Conjugation of folic acid to PLGA-PEG

PEGylated PLGA (470 mg) and activated folic acid (18.09 mg) were codissolved at a 1:4 molar ratio in anhydrous DMSO (4 mL) under a light-protected argon atmosphere for about 24 hours. An excess of folic acid was used to increase the percentage of folic acid conjugation. The reaction mixture was then precipitated by using 150 mL of cold methanol followed by centrifuging at 10,000 rpm for 15 minutes. The precipitate was then purified by column chromatography (60–120 mesh) (50:50 chloroform:methanol).

2.3.2. Characterization of the stepwise synthesized molecules of the polymer conjugates via UV–visible, FTIR and ^{1}H NMR spectroscopy

The synthesized copolymer was subsequently purified by column chromatography (60–120 mesh) with 50:50 chloroform:methanol solvent and characterized on the basis of different spectral and analytical techniques, such as UV–vis, IR, NMR and HPLC. The conjugation of PEG-bisamine and activated folic acid in the target molecule was preliminarily confirmed by the Kaiser test (Ninhydrin), as shown in Figure 2.2(a). The PLGA-PEG-FA conjugate formed a purple complex similar to that formed by PEG-bisamine (control), confirming the presence of a free –NH_2 group. Moreover, the presence of acidic groups

was confirmed by thin-layer chromatographic staining with bromocresol green solutions Figure 2.2(b).

The appearance of yellow spots on a light or dark blue background illustrates the presence of an acidic group in the polymer conjugate.

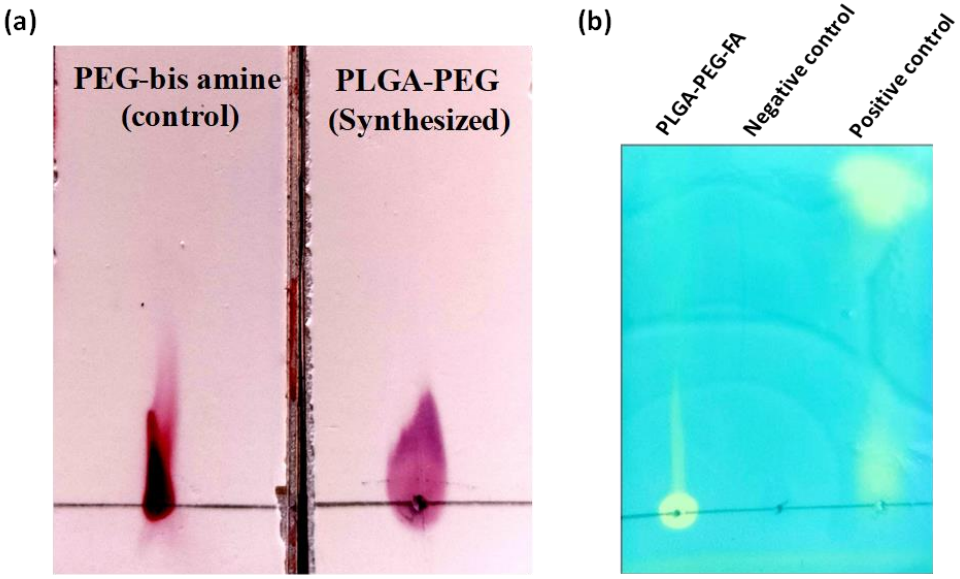

Figure 2.2. TLC analysis of polymer conjugate formation using (a) ninhydrin and (b) bromocresol green to detect amino and carboxyl groups, respectively.

The formation of the PLGA-PEG-FA conjugate was further validated on the basis of UV–visible, FT-IR, ^{1}H NMR and HPLC data. In the FT-IR spectrum of activated PLGA (Figure 2.3(a)), the -OH stretching frequency increased at 3534 $cm^{-1,}$ and the esteric carbonyl furnished a peak at 1751 cm^{-1}. Peaks at 1535 and 1753 cm^{-1} corresponding to N-H and esteric carbonyl groups in the FT-IR spectrum of PLGA-PEG-NH_2 confirmed the conjugation of PEG bis-amine into activated PLGA (Figure 2.3(b)). In the FT-IR spectrum of FA-NHS, two consecutive bands at 3141 and 3256 cm^{-1} were assigned to the primary amine of the pyridine moiety. Another two sharp peaks at 1704 and 1595 cm^{-1} are attributable to acidic and amidic carbonyls, respectively (Figure 2.3(c)). The spectrum of the PLGA-PEG-FA conjugate shows prominent peaks at 3396, 1743 and 1644 $cm^{-1,}$ which are assigned to -OH, esteric and amidic carbonyls, as represented in Figure 2.3(d). In the ^{1}H NMR spectrum of folic acid (Figure 2.4(a)), two separate multiplets at δ 1.852 and 1.997 are assigned to two different aliphatic protons, and the other two aliphatic protons furnish a triplet at δ 2.294. A multiplet and a doublet at δ 4.299 and 4.473 appeared due to one methine and two methylene protons connected to the amino group. Two aromatic protons, the -NH proton and another two aromatic protons, are attributed to a doublet, triplet and doublet at δ 6.626, 6.926 and 7.635, respectively. The signals at δ 8.118 and

8.645 appeared as a doublet and a sharp singlet for their respective amidic and pyrazine protons. In the ^{1}H NMR spectrum of PLGA (Figure 2.4(c)), the signals at δ 1.464, 4.864 and 5.198 are assigned to methyl, methylene and methine protons as singlets and two multiplets, respectively. After the conjugation of the PEG group with PLGA, the signals of the methyl, methylene and methine protons show a singlet and two multiplets at δ 1.463, 4.790 and 5.194, respectively. A sharp singlet at δ 3.505 is attributed to the methylene proton of PEG (Figure 2.4(d)). Moreover, in the ^{1}H NMR spectrum of FA-NHS, two separate multiplets at δ 1.861 and 1.996 were attributed to two different aliphatic protons, and the other two aliphatic protons furnished a triplet at δ 2.294. The presence of a sharp singlet at δ 2.807 confirms the insertion of the cyclopentandione moiety. A multiplet and a doublet at δ 4.296 and 4.480 are assigned to one methine and two methylene protons connected to the amino group. Two aromatic protons, the -NH proton and another two aromatic protons, are attributed to a doublet, triplet and doublet at δ 6.635, 6.916 and 7.639, respectively. The signals at δ 8.081 and 8.648 appeared as a doublet and a sharp singlet for their respective amidic and pyrazine protons (Figure 2.4(b)).

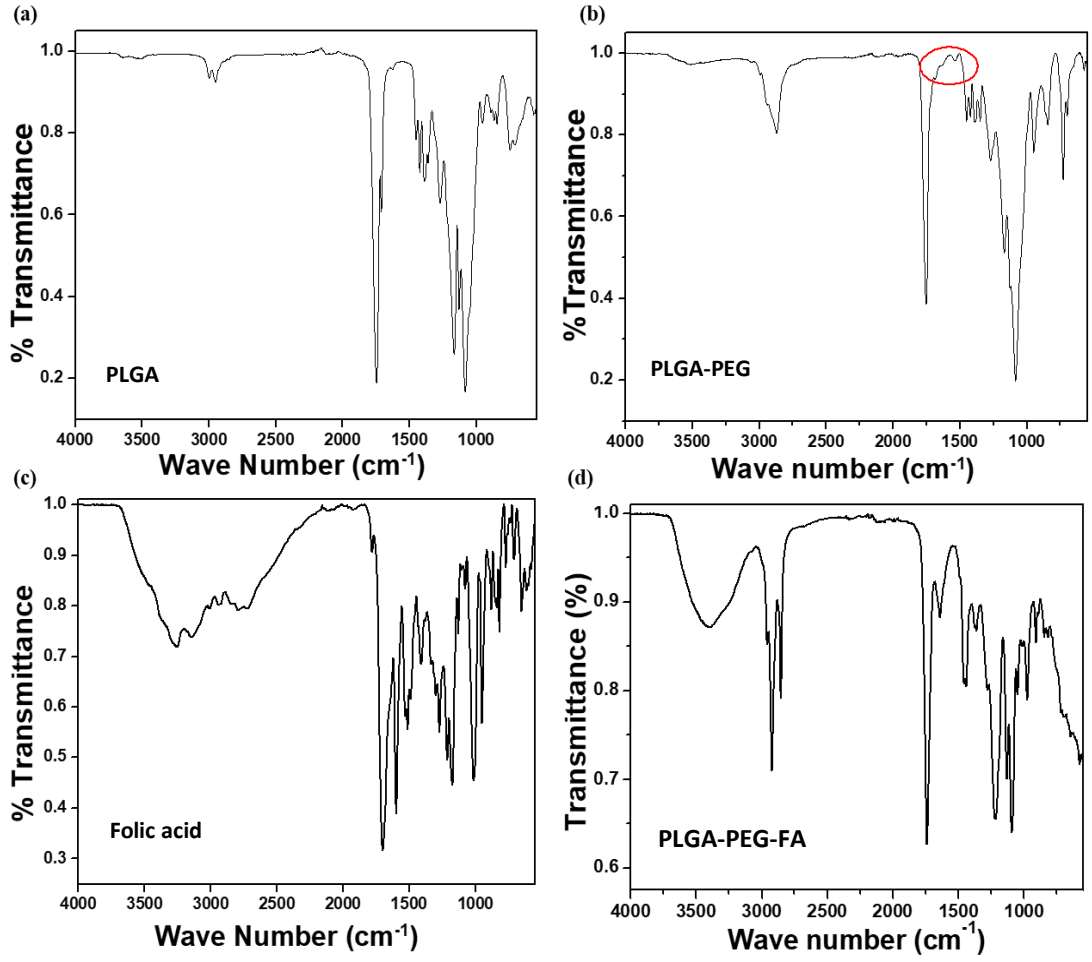

Figure 2.3. FT-IR spectra of (a) 2, (b) 3, (c) 5, and (d) 6.

(a)

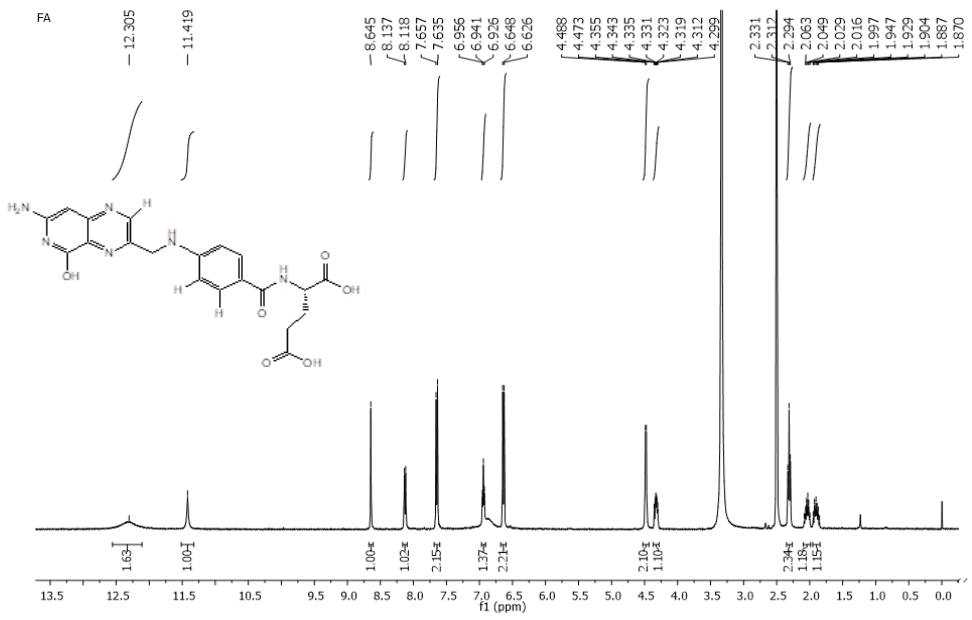

δ 1.852-1.947 (1H, m), 1.997-2.083 (1H, m), 2.294 (2H, t), 4.299-4.355 (1H, m), 4.473 (2H, d, *J* = 6 Hz), 6.626 (2H, d, *J* =8.8 Hz), 6.926(1H, t), 7.635 (2H, d, *J* =8.8 Hz), 8.118 (1H, d, *J* =7.6 Hz), 8.645 (1H, s)

Figure 2.4. (a) ^{1}H NMR spectra of folic acid.

(b)

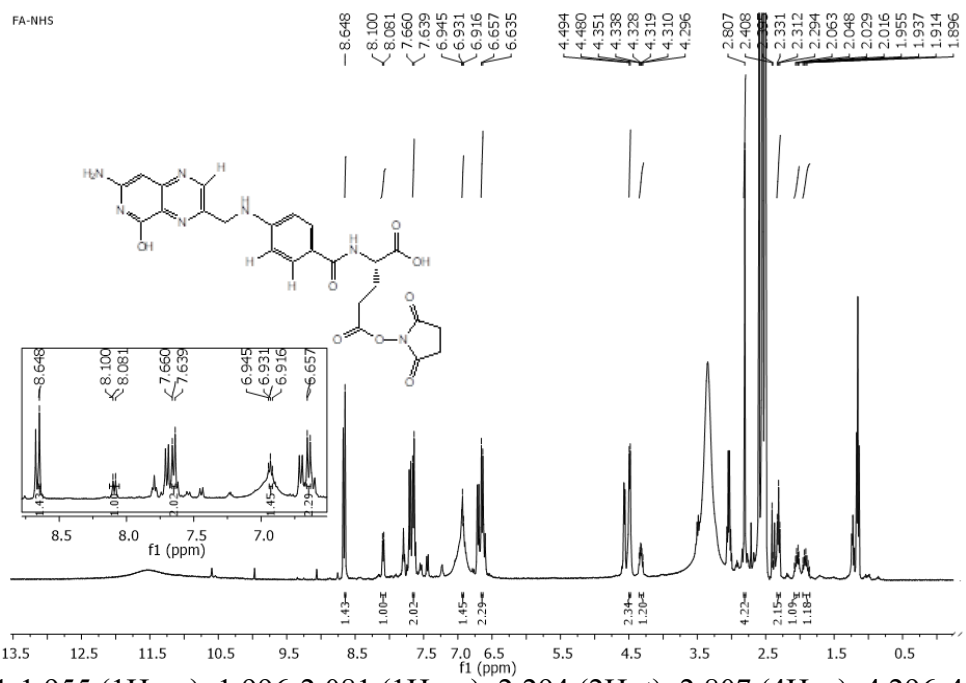

δ 1.861-1.955 (1H, m), 1.996-2.081 (1H, m), 2.294 (2H, t), 2.807 (4H, s), 4.296-4.351 (1H, m), 4.480 (2H, d, *J*= 5.6 Hz), 6.635 (2H, d, *J*= 8.8 Hz), 6.916 (1H, t), 7.639 (2H, d, *J*= 8.4 Hz), 8.081 (1H, d, *J*= 7.6 Hz), 8.648 (1H, s)

Figure 2.4. (b) ^{1}H NMR spectra of activated folic acid.

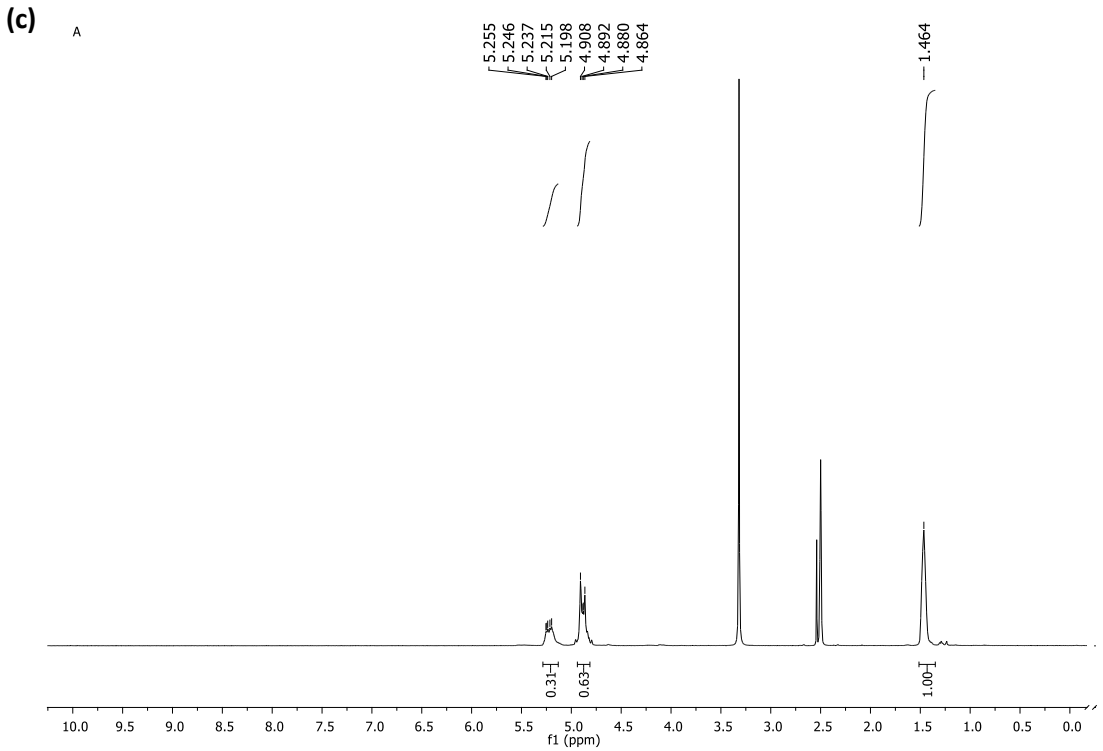

δ 1.464 (s), 4.864 (m), 5.198 (m)

Figure 2.4. (c) ^{1}H NMR spectra of PLGA.

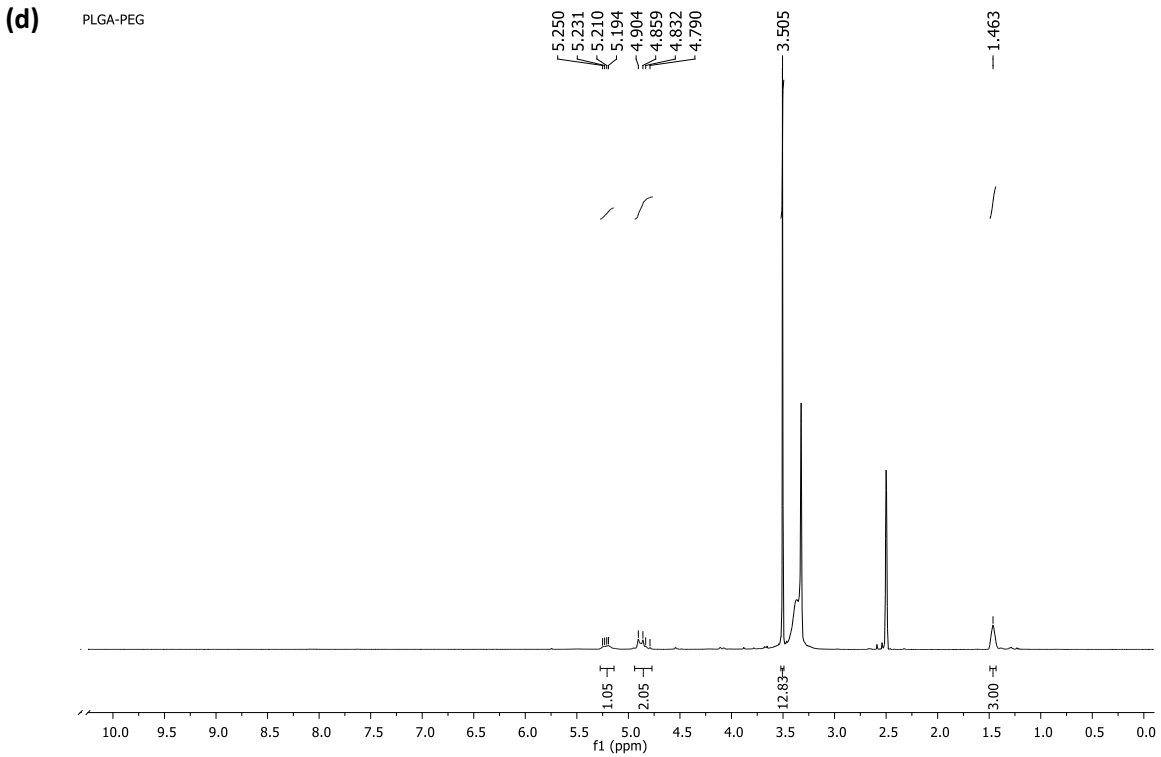

δ 1.463 (s), 3.505 (s), 4.790 (m), 5.194 (m)

Figure 2.4. (d) ^{1}H NMR spectra of PLGA-PEG.

In the ^{1}H NMR spectrum of PLGA-PEG-FA, singlet and two multiplets at δ 1.463, 4.842 and 5.196 are attributed to the methyl, methylene and methine protons of PLGA, respectively. A sharp singlet at δ 3.505 is assigned to the methylene proton of the PEG scaffold. The aromatic protons and pyridine proton of the folic acid moiety show two separate doublets and a singlet in the downfield region at δ 6.661, 7.245 and 8.316, as represented in Figure 2.5. δ 1.463 (s), 3.505 (s), 4.842 (m), 5.196 (m), 6.661 (d, *J*= 8 Hz), 7.245 (d, *J*= 8 Hz), 8.316 (s)

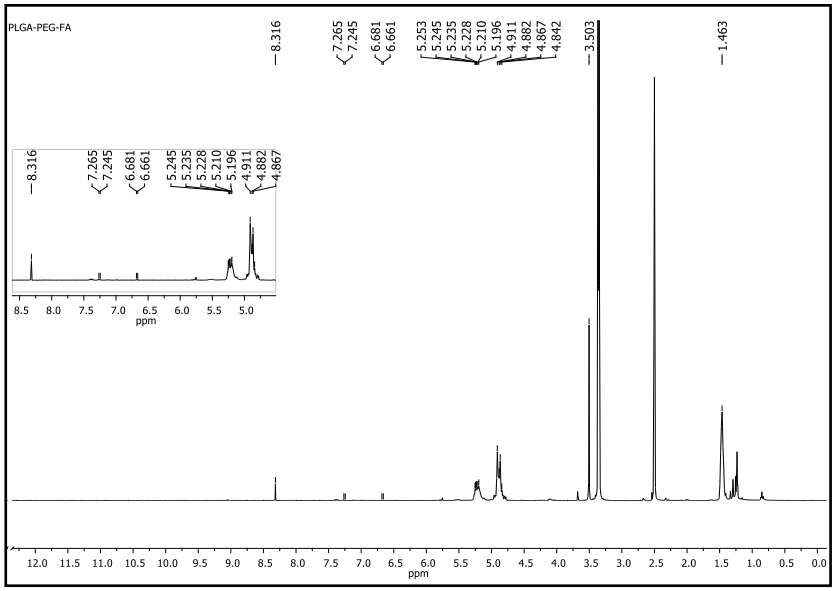

Figure 2.5 ^{1}H NMR spectra of PLGA-PEG-FA.

Additionally, the purity of the isolated PLGA-PEG-FA, which was 88.04% pure, was further checked via HPLC. (Figure 2.6).

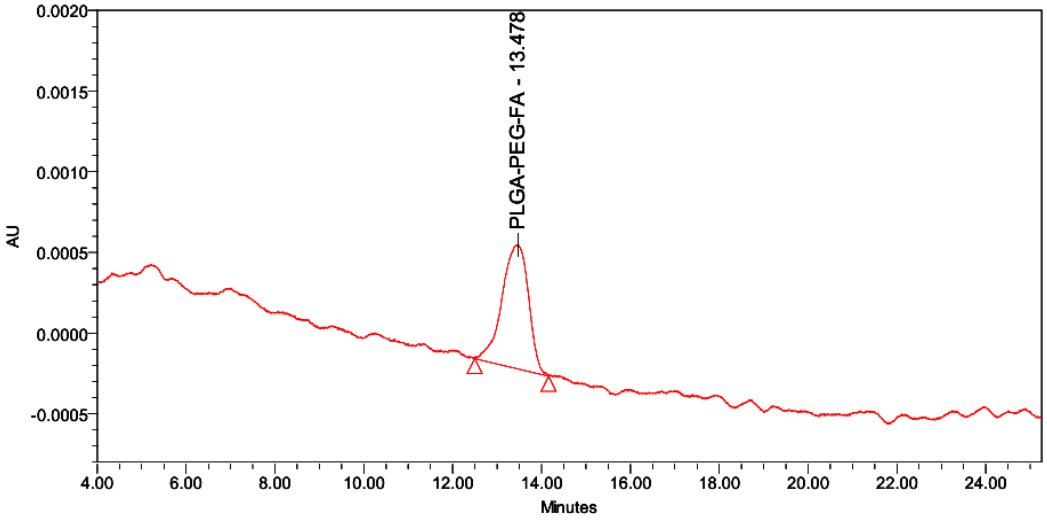

Figure 2.6. HPLC chromatogram confirming the purity of the isolated PLGA-PEG-FA conjugates.

In the UV–visible spectra of folic acid (5), the n→π* transition occurred due to the presence of the electron withdrawing -COOH group, but the transition was restricted after the insertion of the amide group in PLGA-PEG-FA. A hypsochromically shifted new and distinct absorption band appeared at 370 nm in the UV–visible spectrum (Figure 2.7) of PLGA-PEG-FA (6), which clearly indicates the formation of the target compound.

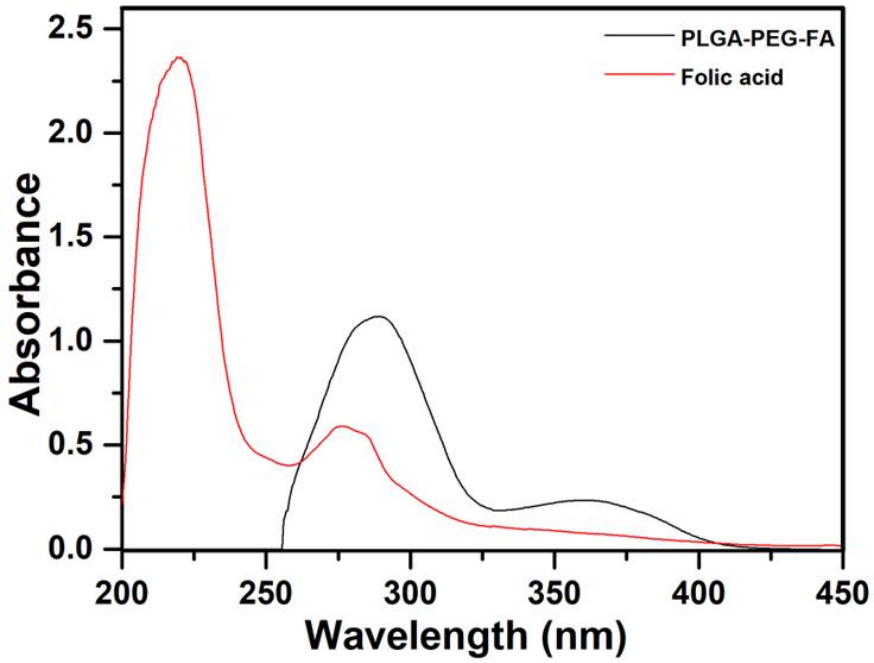

Figure 2.7. UV–visible spectra of folic acid and PLGA-PEG-FA.

2.3.3. Determination of folic acid Conjugation Efficiency

The PLGA-PEG-FA conjugate was analysed for the FA-conjugated. The amount of conjugated FA was determined by comparing the obtained absorbance value with the standard curve. The amount of FA conjugated per 1 mg of PLGA-PEG-FA was 90.99 µg, which is within the optimal range for enhancing tumor targeting through folate receptor-mediated uptake. This conjugation efficiency is consistent with previously reported values for FA-conjugated polymeric systems using DCC/NHS coupling chemistry.(Parvathaneni *et al*., 2023)

2.3.4. Dynamic light scattering confirms the nanosized dimensions of the particles

The nanoparticles were formed via self-assembly of PLGA-PEG-FA copolymers encapsulating 9-Br-Nos via the nanoprecipitation technique (Figure 2.8). The hydrodynamic diameter (H_D) and polydispersity index (PDI) of the PLGA-PEG-FA nanoparticles were found to be 122±8 nm and 0.28, respectively, as shown in Figure 2.9, which indicated that the nanoparticles were within the optimal size range for passive and

active tumor targeting via the EPR effect and folate receptor-mediated endocytosis, respectively. This result revealed a narrow size distribution and high homogeneity of the formulation.

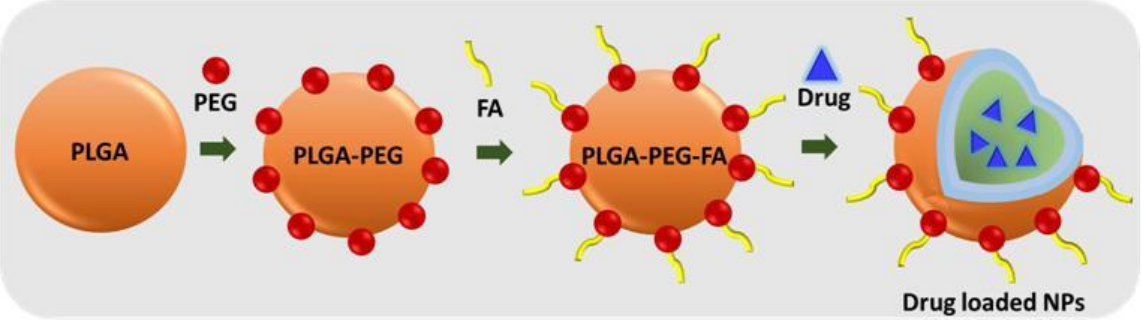

Figure 2.8. Schematic illustration of 9-bromo-noscapine encapsulation with PLGA-PEG-FA nanoparticles forming a targeted drug delivery system. Characterization of PLGA-PEG-FA nanoparticles prepared via the coprecipitation method.

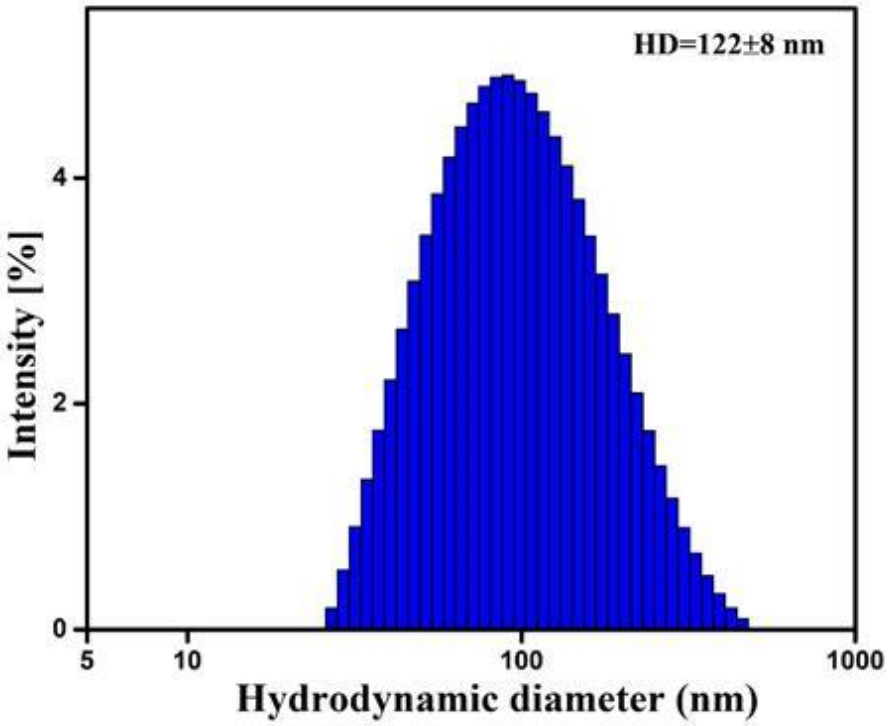

Figure 2.9. Particle size distribution of the nanoparticles obtained via DLS.

2.3.5. Scanning electron microscopy (SEM) revealed the uniform spherical shape of the PPFD nanoparticles

The surface morphology of the PLGA-PEG-FA (PPF) nanoparticles was analysed by scanning electron microscopy. SEM micrographs (Figure 2.10) revealed that spherical and aggregated nanoparticles were obtained via folic acid-conjugated polymeric self-assembly. The relatively uniform size distribution indicates the stability of the nanoparticles.

Furthermore, the smooth surface morphology observed under SEM supports the hypothesis that the drug was either well encapsulated or uniformly dispersed in the polymer matrix.

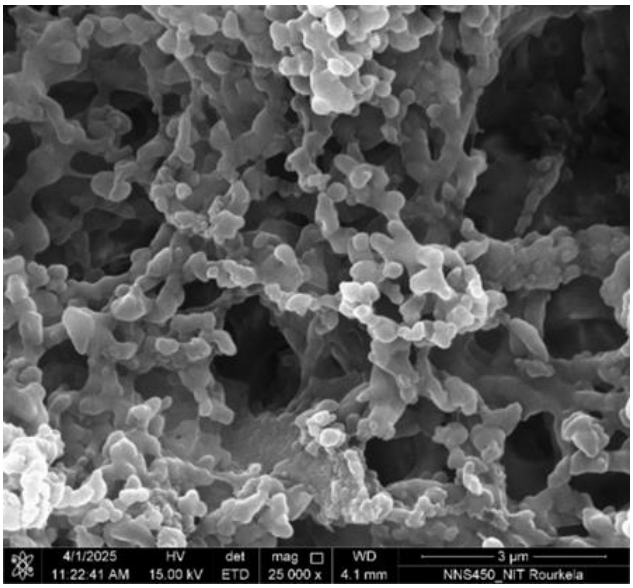

Figure 2.10. SEM image of the 9-Br-Nos-loaded PLGA-PEG-FA nanoparticles.

2.3.6. Enhanced drug loading and high entrapment efficiency of PLGA-PEG-FA nanoparticles

The drug loading and entrapment efficiency of the PLGA-PEG-FA nanoparticles were determined via HPLC analysis. The chromatogram in Figure 2.11 shows a significant drug loading capacity of 9.45% and a drug entrapment efficiency of 94.5%. The high entrapment efficiency can be attributed to the strong affinity between the drug 9-Br-Nos and the polymer PLGA-PEG-FA. This result may also enhance the therapeutic efficacy of the drug 9-Br-Nos while minimizing off-target effects.

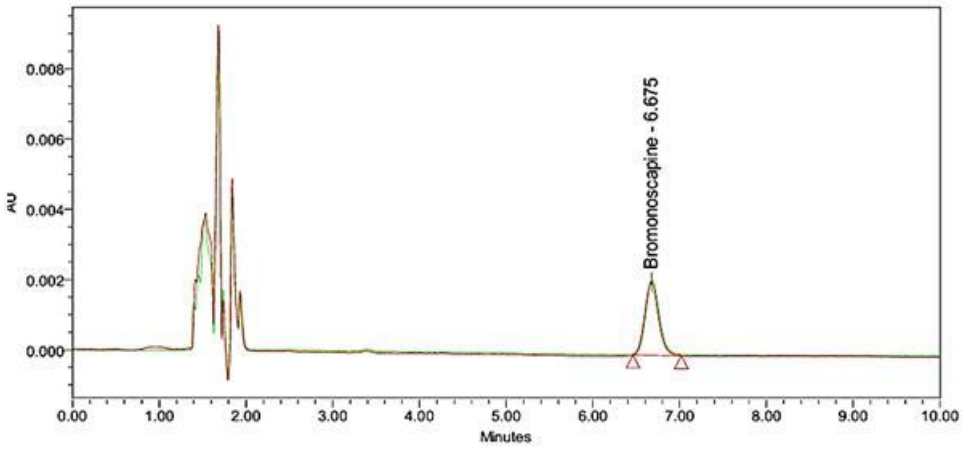

Figure 2.11. Representative HPLC chromatogram illustrating 9-Br-Nos loading and entrapment efficiency in PLGA-PEG-FA nanoparticles.

2.3.7. 9-Br-Nos showed sustained drug release behavior from PLGA-PEG-FA nanoparticles at physiological pH

The *in vitro* drug release study from the PLGA-PEG-FA nanoparticles and the free drug 9-Br-Nos was conducted in PBS (pH 7.4) under constant stirring. The cumulative drug release profile revealed initially burst release which was then followed by a sustained release profile, as shown in Figure 2.12. The burst release of free 9-Br-Nos, accounting for approximately 100% of the total drug within 2 h, may be due to the rapid diffusion of the drug absorbed on the surface of the nanoparticles. However, in the case of the PPFD, the initial phase of burst release occurred, after which a decrease in the release rate occurred, resulting in a cumulative release of 60% over 72 hrs. The controlled release of 9-Br-Nos from the nanoparticles has the potential to provide prolonged therapeutic action. Several release models, such as zero-order, first-order, Higuchi's square root, and Korsmeyer–Peppas models, were fitted to analyse the cumulative drug release. The model that provides a correlation coefficient value ($R^2 = 0.9718$) close to unity was considered the order of release. As shown in Table 2.1, following the initial burst release, the PPFD nanoparticles followed the Higuchi model, indicating that drug release primarily involved diffusion and then a combination of diffusion and degradation in the later phase. (Jain *et al*., 2012)

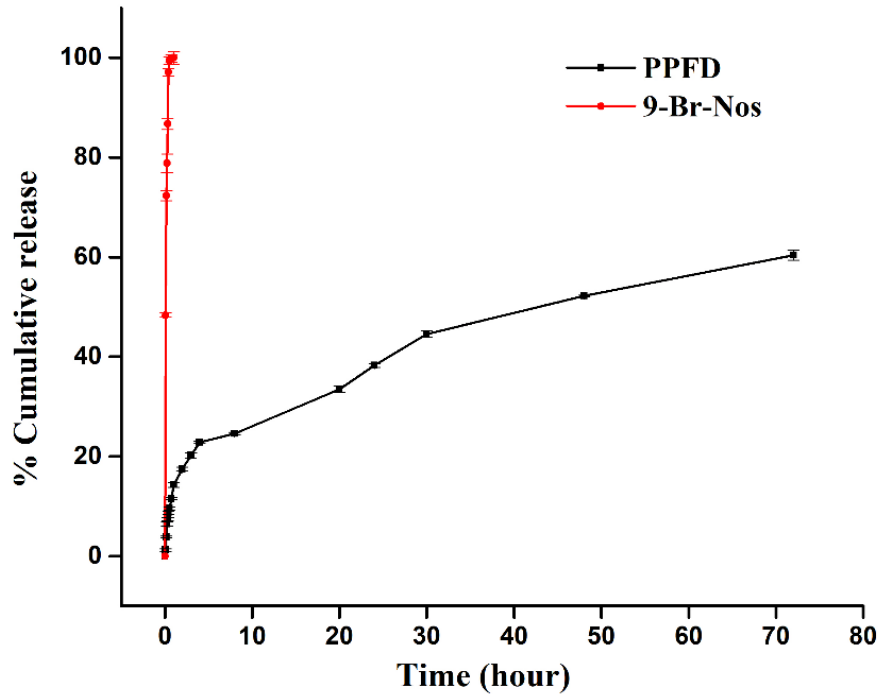

Figure 2.12. *In vitro* release profile of 9-Br-Nos from PLGA-PEG-FA nanoparticles in PBS (pH~7.4) at 37°C.

Table 2.1. Correlation coefficient values obtained by fitting the *in vitro* drug release data to different kinetic models.

Release kinetics model	Correlation coefficient (R^2)
Zero-order	0.86
First-order	0.9315
Higuchi	0.9718
Hixson–Crowell model	0.9102

2.3.8. Compared with the PLGA nanoparticles, the Coumarin-6-loaded PLGA-PEG-FA nanoparticles showed enhanced cellular uptake

Coumarin-6, a hydrophobic fluorescent dye commonly used as a model compound for tracing cellular nanoparticles uptake, was effectively encapsulated into PLGA-PEG-FA polymer matrix to evaluate their cellular internalization efficiency. The cellular uptake of the coumarin-6 loaded PPFD nanoparticles in MDA-MB-231 breast cancer cells was assessed via fluorescence microscopy, as shown in Figure 2.13(a). These findings suggested that the coumarin-6 loaded PLGA-PEG-FA nanoparticles were internalized by the cells and localized around the nuclear region, where the blue fluorescence (DAPI) stains the nucleus and the green fluorescence (coumarin-6) represents the nanoparticles. The results revealed a significantly greater fluorescence intensity in the cells treated with PPFD nanoparticles than in those treated with PD nanoparticles. The difference in fluorescence intensity suggests that folic acid conjugation in the nanoparticles facilitates more efficient cellular uptake in breast cancer cells. Furthermore, the quantitative analysis (Figure 2.13(b)) by one-way ANOVA also revealed that the fluorescent intensity of active targeting group (PPFD) was significantly higher than that of the non-targeting (PD) as well as the control group ($P<0.0001$). The increased uptake of the PLGA-PEG-FA nanoparticles can be attributed to folate groups as folate receptors are overexpressed in MDA-MB-231 cancer cells which ultimately promotes receptor-mediated endocytosis. Such targeted delivery not only improves cellular uptake but also increases the therapeutic index of the encapsulated drug by promoting selective accumulation in cancer cells while minimizing off-target effects in healthy tissues.

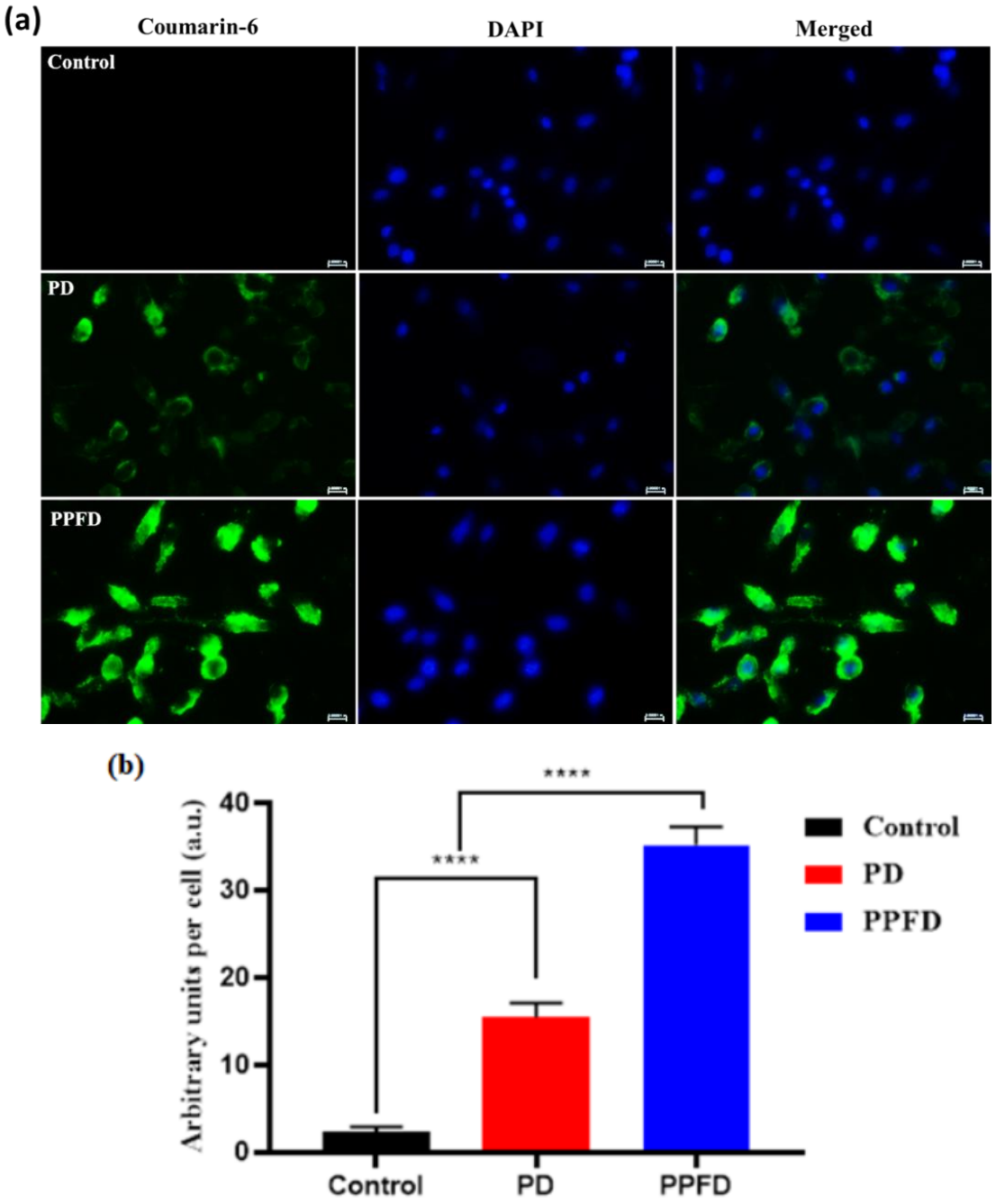

Figure 2.13. Cellular uptake of Coumarin-6-loaded PLGA (w/o folic acid) and PLGA-PEG-FA (w/folic acid) nanoparticles. (a) Representative fluorescence images of MDA-MB-231 cells incubated with Coumarin-6 (C6) nanoparticles for 4 h. Blue represents nuclear staining (DAPI), and green represents C6. Green fluorescence was observed in the cytoplasm, suggesting nanoparticle uptake. Scale bar: 10 μm. (b) Quantitative analysis of the cellular uptake efficiency of the different groups was performed via one-way ANOVA (****P<0.0001 compared with the control group).

2.3.9. Compared with the 9-Br-Nos-loaded PLGA-PEG-FA nanoparticles and free 9-Br-Nos, the 9-Br-Nos-loaded PLGA-PEG-FA nanoparticles showed improved cytotoxicity in MDA-MB-231 and MCF-7 cells

The cytotoxic effects of drug-loaded PLGA-PEG-FA nanoparticles, drug-loaded PLGA nanoparticles, and the free drug 9-Br-Nos were evaluated in MDA-MB-231 and MCF-7 breast cancer cells and revealed a dose-dependent decrease in cell viability in both cell lines, as shown in Figure 2.14. In the MDA-MB-231 cells shown in Figure 2.14(a), the PLGA-PEG-FA nanoparticles presented the greatest cytotoxicity, with an IC_{50} value of 31.27 µg/mL, followed by the PLGA nanoparticles (93.81 µg/mL) and 9-Br-Nos (230.1 µg/mL). Similarly, in MCF-7 cells, as shown in Figure 2.14(b), the IC_{50} values for the PLGA-PEG-FA nanoparticles, PLGA nanoparticles, and 9-Br-Nos were 213.3, 95.54, and 38.81 µg/mL, respectively. The superior result in the case of the PLGA-PEG-FA nanoparticles is attributed to folic acid-mediated receptor targeting, which enhances drug uptake and hence cytotoxicity. However, the PLGA nanoparticles were less effective than the PLGA-PEG-FA nanoparticles were, and the free drug displayed the lowest cytotoxicity because of its poor solubility and limited cellular internalization. The addition of folic acid for targeted delivery greatly enhanced cytotoxicity, notably in MDA-MB-231 cells with high expression of folate receptors. However, the effectiveness observed in MCF-7 cells despite their low receptor levels highlights the efficacy of the drug delivery system.(Monteiro *et al*., 2020)

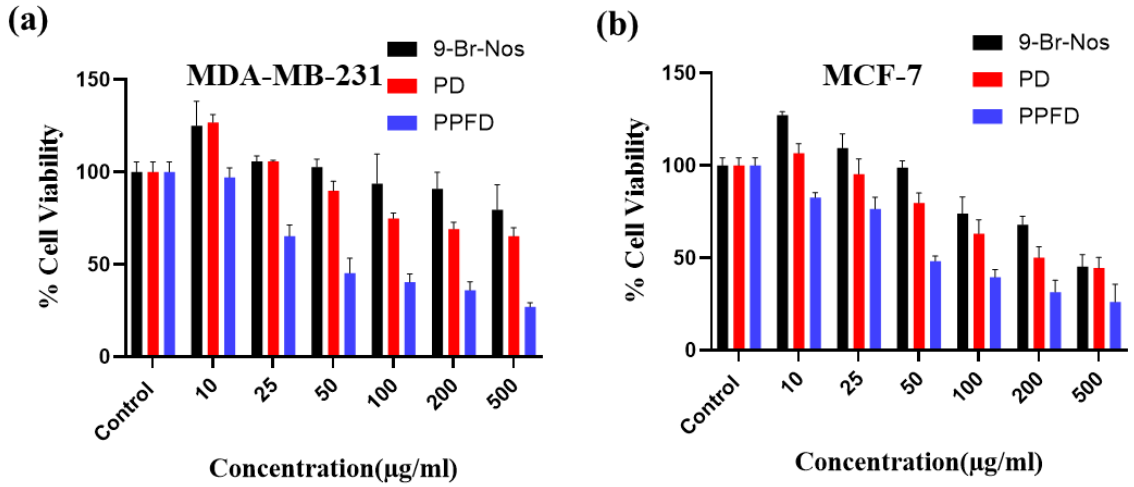

Figure 2.14. (a) Cytotoxic effects of free 9-Br-Nos, PD, and PPFD on MDA-MB-231 and (b) MCF-7 cells. Cell viability was determined by the MTT assay.

2.3.10. 9-Br-Nos-loaded PLGA-PEG-FA nanoparticles induce prominent apoptotic changes with chromatin condensation and nuclear fragmentation

Hoechst 33342 staining revealed (Figure 2.15(a)) distinct differences in nuclear morphological changes between cells treated with 9-Br-Nos and those treated with the drug-loaded PLGA-PEG-FA nanoparticles. The cells treated with the PPFD exhibited pronounced apoptotic features, including intense chromatin condensation and significant nuclear fragmentation ($F_{2,15}$=101.8, P<0.001), as represented in Figure 2.15(b). However, the cells treated with free 9-Br-Nos presented moderate nuclear changes, whereas the control cells subjected to no treatment presented evenly stained nuclei and a healthy morphology. The enhanced apoptotic activity observed in the PPFD-treated group highlights the potential of the nanoparticle formulation to improve drug delivery, cellular uptake, and therapeutic efficacy compared with those of the free drug.

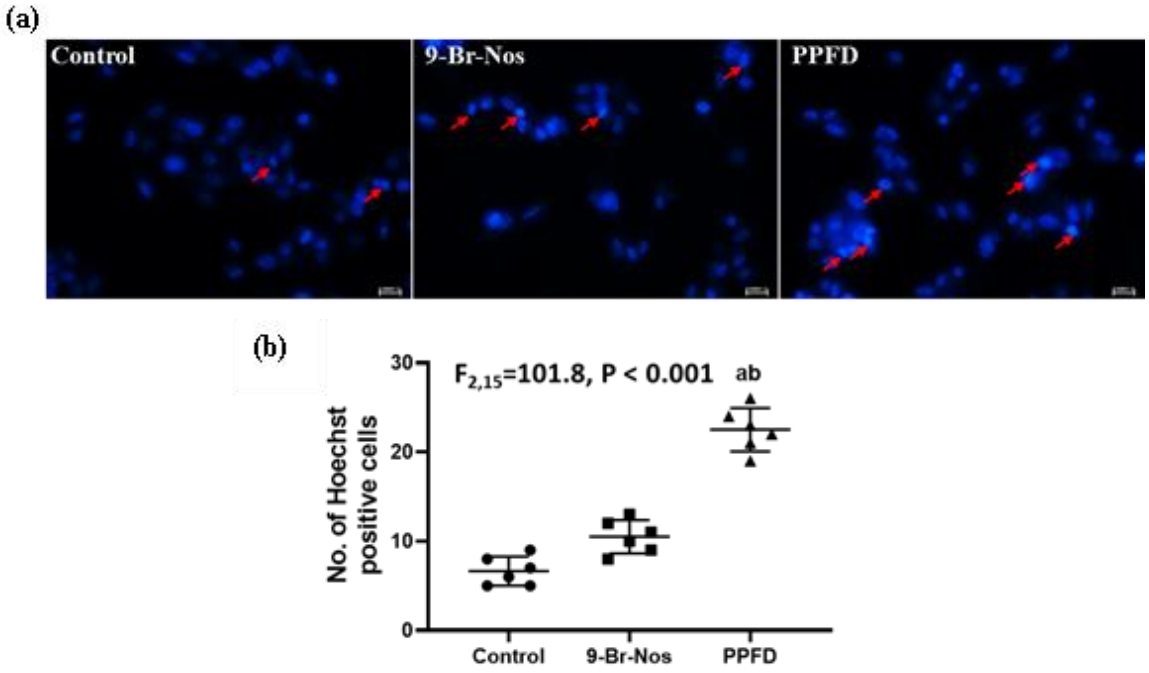

Figure 2.15. (a) Representative 40x image of MDA-MB-231 cells after Hoechst 33342 staining. Arrowheads depict Hoechst-positive cells; scale bar: 10 µm. The graph shows the number of Hoechst-positive cells. (b) Data are presented as the means ± SDs (n=6) and were analysed via one-way ANOVA. 'a' indicates $p < 0.001$ compared to the control group, and 'b' indicates $p < 0.001$ compared with free drug, 9-Br-Nos group.

2.3.11. Compared with the free drug 9-Br-Nos, PPFD increased the apoptotic potential by significantly altering the mitochondrial membrane potential

The mitochondrial membrane potential (MMP) was evaluated via JC-1 dye to study the effects of 9-Br-Nos and PPFD on mitochondrial integrity and apoptosis (Figure 2.16(a)).

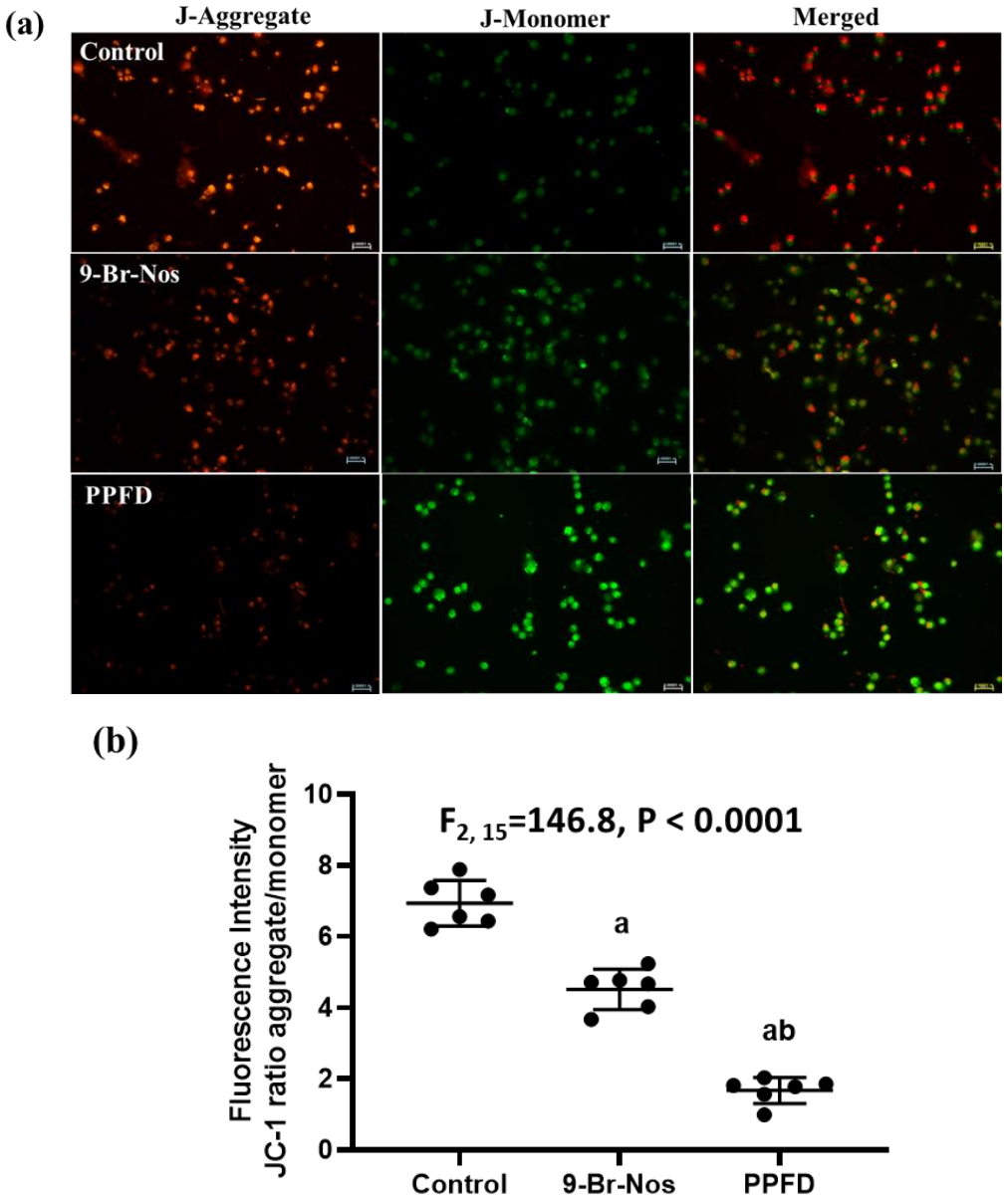

Figure 2.16. (a) Representative fluorescence images of JC-1 staining showing ΔΨm in MDA-MB-231 cells treated with free 9-Br-Nos and PPFD nanoparticles. Red fluorescence (JC-1 aggregates) indicates intact mitochondria, whereas green fluorescence (JC-1 monomers) indicates depolarized mitochondria. (b) Quantitative analysis of JC-1 aggregate/monomer fluorescence intensity ratio. The data are presented as the mean ± SDs, (n = 6) and were analysed via one-way ANOVA. 'a' indicates $p < 0.0001$ compared with the control group, and 'b' indicates $p < 0.0001$ compared with the 9-Br-Nos group.

In untreated control cells, JC-1 dye predominantly formed aggregates within healthy mitochondria, which resulted in strong red fluorescence and a low green/red fluorescence ratio, indicating an intact MMP. However, compared with control cells, which presented partial mitochondrial depolarization, cells treated with 9-Br-Nos presented a moderate increase in the green/red fluorescence ratio. However, the cells treated with the PPFD presented a significant increase in green/red fluorescence ratio, suggesting high membrane depolarization ($F_{2,15}$=146.8, P<0.0001), as shown in Figure 2.16(b). This result indicates greater disruption of mitochondrial function and triggered apoptosis in the PPFD-treated group than in control and free drug. These findings emphasize the enhanced therapeutic efficacy of PPFD in activating apoptotic pathways by disrupting mitochondrial function.

2.3.12. Compared with 9-Br-Nos, PPFD results in increased ROS-mediated apoptotic activity by promoting increased oxidative stress and activation of the apoptotic pathway

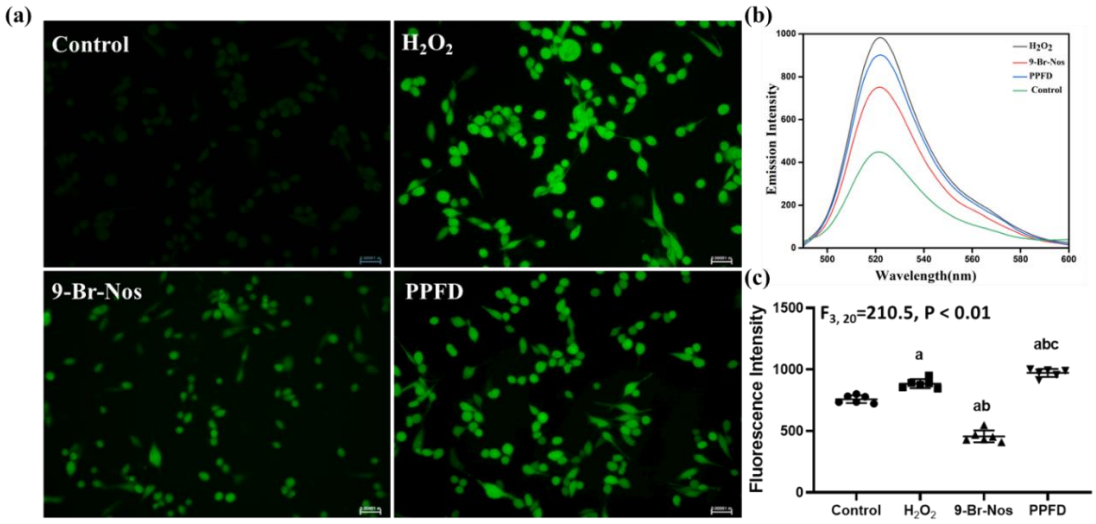

Figure 2.17. (a) Intracellular reactive oxygen species (ROS) levels in MDA-MB-231 cells detected via DCFH-DA staining after treatment with free 9-Br-Nos and PPFD nanoparticles. (b) Fluorescence emission spectra of the treated cells indicating ROS generation. (c) Graph depicting the fluorescence intensity. The data are presented as the means ± SDs (n = 6) and were analysed via one-way ANOVA. 'a' indicates $p < 0.01$ compared with the control group, 'b' indicates $p < 0.01$ compared with the H_2O_2 group, and 'c' indicates $p < 0.01$ compared with the 9-Br-Nos group.

Reactive oxygen species (ROS) play important roles in cellular signalling and are hence responsible for the induction of apoptosis. The generation of ROS was assessed in cells treated with PPFD, 9-Br-Nos, and hydrogen peroxide (H_2O_2) as a positive control. H_2O_2 resulted in the highest level of ROS generation, confirming the effectiveness of the positive

control for oxidative stress. The ROS level was significantly greater in the PPFD-treated cells than in those treated with free 9-Br-Nos, as indicated by the green fluorescence in Figure 2.17(a). This was further validated by fluorescence emission spectra, where the control group showed minimal fluorescence emission, H_2O_2 significantly increased the emission intensity, and 9-Br-Nos resulted in a moderate increase in ROS (Figure 2.17(b)). However, PPFD-induced ROS generation was significantly greater than that induced by the free drug. These differences were also statistically significant at $F_{3,20}=210.5$, $P<0.01$ (Figure 2.17(c)). The elevated ROS levels in PPFD-treated cells correlated with increased mitochondrial dysfunction, disruption of the membrane potential, and activation of apoptotic pathways, including caspase activation. These results highlight the importance of ROS in mediating the cellular response to both the PPFD and 9-Br-Nos, with a greater effect observed for the PPFD in terms of apoptosis induction.

2.3.13. Disintegration of tumor spheroids following treatment with 9-Br-Nos and PPFD nanoparticles

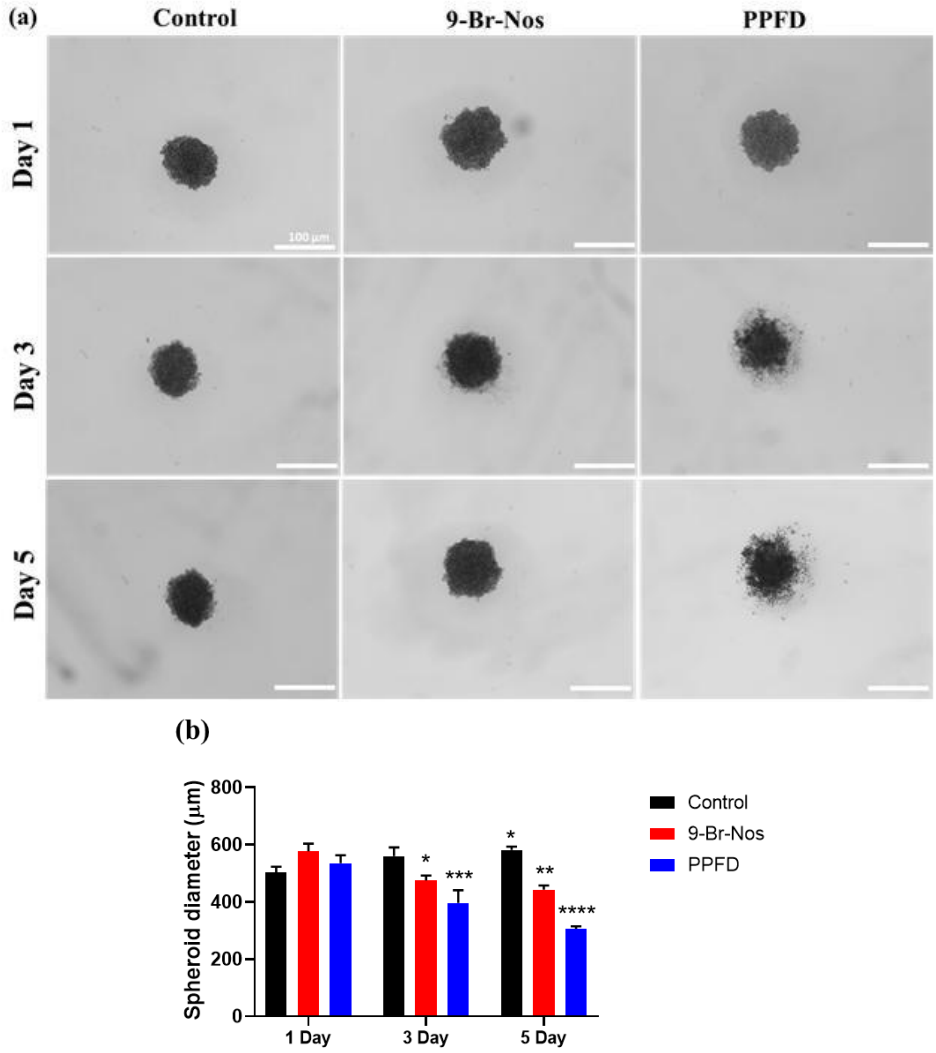

Figure 2.18. (a) Representative spheroid images of MDA-MB-231 cells treated with 9-Br-Nos and PPFD nanoparticles showing morphological changes and structural disruption. Quantification was performed via ImageJ software (mean±SD, n=6). (b) Differences between treatment groups were evaluated via two-way ANOVA, and statistically significant differences are indicated by * $p < 0.05$, ** $p < 0.01$, *** $p < 0.001$, and **** $p < 0.0001$.

Three-dimensional tumor spheroids are well-established *in vitro* models that closely mimic the structural and physiological characteristics of *in vivo* tumors. The structural disruption of the tumor spheroids was assessed following treatment with 9-Br-Nos and PPFD nanoparticles. In the untreated control group, there was a statistically significant and gradual increase in spheroid diameter, i.e., from 503.22 μm on day 1 to 581.93 μm on day 5, whereas treatment with free 9-Br-Nos resulted in partial disintegration, with spheroids showing a moderate reduction in average size from 576.89 μm on day 1 to 443.05 μm on day 5. In contrast, spheroids treated with PPFD nanoparticles exhibited a significant reduction in spheroid size on day 5, i.e., from 534.90 μm to 306.34 μm (Figure 2.18(a) and (b)). This result indicated that the PPFD nanoparticles were markedly more effective than 9-Br-Nos in disrupting 3D tumor spheroids. Incorporating this nanoparticle delivery system may offer enhanced therapeutic outcomes by effectively overcoming the penetration barriers associated with solid tumors.

2.3.14. Western blot analysis of apoptotic proteins in 9-Br-Nos and PPFD nanoparticle-treated MDA-MB-231 cells reveals the activation of apoptotic pathways

Western blot analysis of apoptotic proteins revealed distinct differences among the PPFD nanoparticle, 9-Br-Nos, and control treatments. In PPFD-treated cells, there was a significant increase in the expression of the proapoptotic proteins Bax and Cleaved caspase-3, along with a marked reduction in expressing the antiapoptotic protein Bcl-2, which indicated increased induction of apoptosis. In contrast, 9-Br-NOS treatment resulted in moderate upregulation of Cleaved caspase-3 and Bax, with a slight decrease in Bcl-2, which was associated with a decreased apoptotic response compared with that in the PPFD nanoparticle-treated group. On the other hand, control cells presented no significant changes in the expression of these apoptotic markers, confirming the specificity of the apoptotic response in the treated groups (Figure 2.19(a) and (b)). These findings suggest that the PPFD is more effective than 9-Br-Nos in activating apoptotic pathways, which highlights its potential as a more potent therapeutic agent for inducing apoptosis. The

significant upregulation of apoptotic markers in PPFD-treated cells underscores its potential as a more potent and efficient therapeutic candidate for promoting apoptosis in cancer cells.

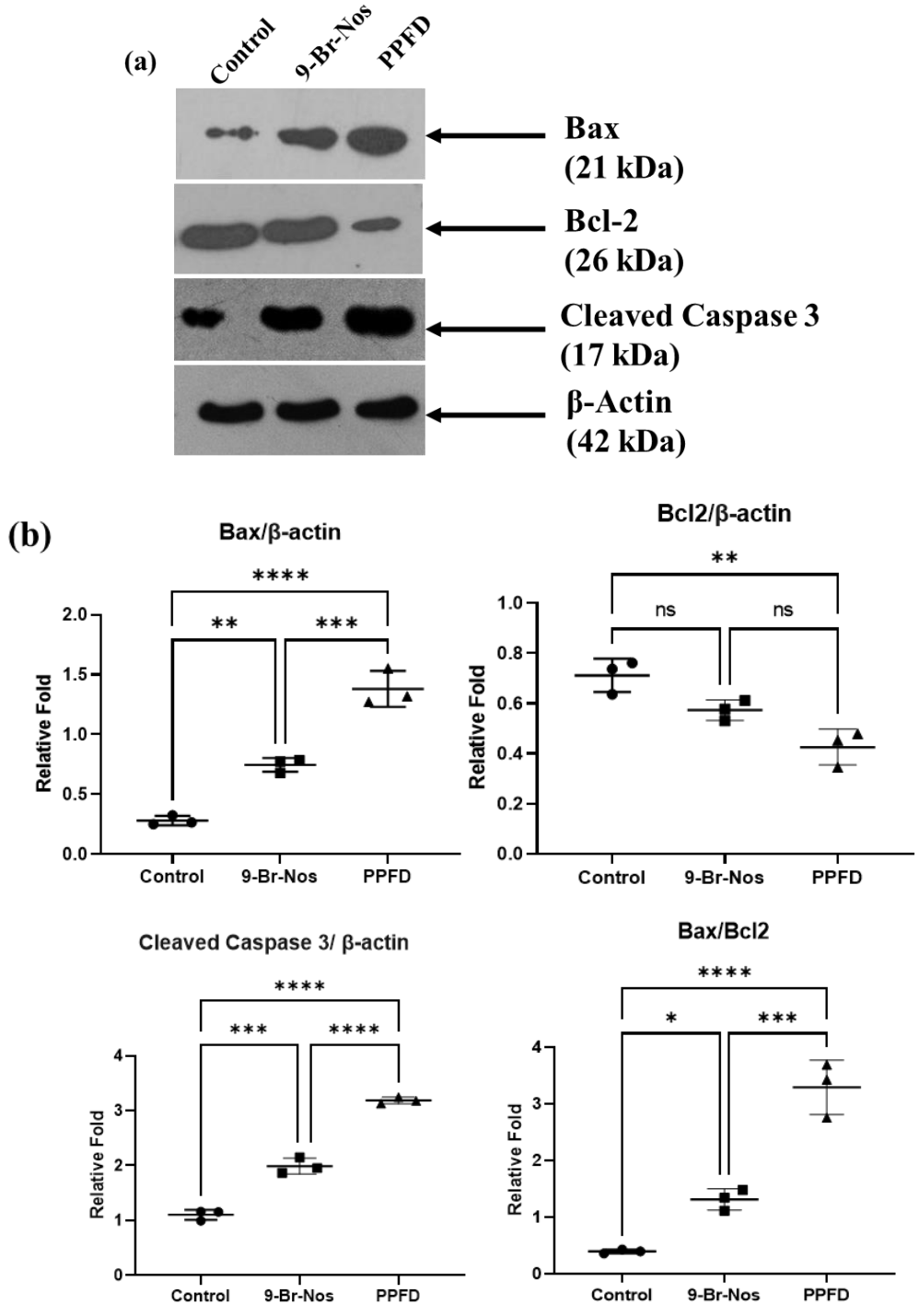

Figure 2.19. (a) Representative Western blot images and quantitative analyses of relative protein expression. MDA-MB-231 cells were treated with 9-Br-Nos and PPFD for 48 hours. (b) Differences between treatment groups were evaluated via ANOVA, and statistically significant differences are indicated by * $p < 0.05$ and ** $p < 0.01$.

2.3.15. *In vivo* assessment of Acute and Subacute Toxicity in rats administered with 9-Br-Nos and PPFD nanoparticles

The acute oral toxicity of the free drug and PPFD nanoparticles were evaluated in Wistar rats in accordance with OECD guidelines. A single dose of the test compounds were administered to the rats, which were then observed over a 14-day period for any mortality, behavioural changes, body weight fluctuations, or signs of organ-specific toxicity. No deaths or significant adverse clinical symptoms were detected in any treatment group during the observation period. For the subacute toxicity assessment, the free drug and PPFD nanoparticles were administered orally on a daily basis for 28 days. Animals were closely monitored for any clinical abnormalities, changes in body weight, food and water consumption, hematological and biochemical parameters, and histopathological alterations. No signs of toxicity or mortality were observed throughout the duration of treatment. A consistent increase in body weight was observed across all treatment groups, suggesting normal physiological and metabolic activity. Data on body weight (Table 2.2), as well as food and water intake (Table 2.3), were recorded accordingly.

Table 2.2. Body weights (in gram) of rats treated with the free drug i.e. 9-Br-Nos and PPFD nanoparticles at a daily dose of 500 mg/kg body weight for 28 days revealed no abnormal weight gain/loss compared to untreated normal group.

Days	Body weight (grams)		
	Control	9-Br-Nos	PPFD
1	241.627±0.884	241.128±0.934	241.413±0.844
7	244.2±1.174	243.298±1.022	244.055±1.498
14	246.488±0.877	246.645±0.976	245.929±0.563
21	247.802±0.418	248.177±0.594	247.796±0.432
28	249.507±0.941	250.492±0.611	250.307±0.855

Table 2.3. Food intake (in gram) and water intake (in mL) of rats treated with the free drug i.e. 9-Br-Nos and PPFD nanoparticles at a daily dose of 500 mg/kg body weight for 28 days revealed no significant deviation between treated and untreated control groups.

	Food intake		
Day	Control	9-Br-Nos	PPFD
1	21.112±1.065	21.131±0.594	21.314±0.531
7	23.909±0.75	23.885±0.415	23.039±1.056
14	25.298±0.371	24.569±0.869	25.294±0.647
21	26.489±0.704	26.529±0.748	26.332±0.85
28	28.55±0.674	28.814±0.544	28.343±0.957

Water intake			
1	20.917±0.418	20.586±0.61	21.001±0.527
7	22.131±0.566	22.086±0.514	22.064±0.551
14	23.414±0.549	23.226±0.551	22.92±0.439
21	24.055±0.317	24.078±0.37	24.1±0.537
28	25.23±0.274	25.101±0.529	25.149±0.647

2.3.16. *In vivo* assessment of Hematological and Biochemical Parameters

The hematological profile of rats subjected to a 28-day subacute toxicity study with free drug and PPFD nanoparticles were analyzed to evaluate the impact of the compounds on blood physiology. Key indicators such as red blood cell (RBC) count, haemoglobin (Hb) concentration, hematocrit (HCT), mean corpuscular volume (MCV), white blood cell (WBC) count, and platelet (PLT) count were measured and compared to those of untreated control animals. No significant changes were observed in RBC count, haemoglobin levels, or hematocrit values, suggesting normal erythropoiesis and no evidence of anemia. Additionally, MCV, mean corpuscular haemoglobin (MCH), and mean corpuscular haemoglobin concentration (MCHC) remained within standard physiological limits, indicating stable red blood cell morphology and haemoglobin content. Total and differential WBC counts (including neutrophils, lymphocytes, monocytes, and eosinophils) did not exhibit any signs of immune suppression or inflammatory response. Platelet counts also remained unaffected, implying no impact on the blood clotting function. Biochemical evaluation revealed no significant alterations in serum glucose, total protein, albumin, globulin, or electrolyte levels (sodium, potassium, calcium, and phosphorus) between the treated and control groups. Liver function markers-alkaline phosphatase (ALP), alanine aminotransferase (ALT), and aspartate aminotransferase (AST)-were within the normal physiological range and showed no meaningful differences between groups. Similarly, kidney function indicators such as serum urea and creatinine remained stable and comparable to controls. The findings are presented in Tables 2.4 and 2.5.

Table 2.4: Hematological parameters of rats administered 9-Br-Nos and PPFD nanoparticles daily at a dose of 500 mg/kg body weight for 28 days showed no notable differences compared to the untreated control group.

Parameter	Control	9-Br-NOS	PPFD
white blood cell count (WBC (10^3/L))	6.893±0.396	7.161±0.339	7.188±0.582
Neutrophils (Neu# (10^3/L))	5.813±0.689	5.734±0.824	5.052±0.886
Lymphocytes (Lym# (10^3/L))	2.155±0.905	2.55±1.051	2.379±0.822
Monocytes (Mon# (10^3/L))	1.44±0.268	1.382±0.302	1.447±0.21
Eosinophils (Eos# (10^3/L))	0.656±0.282	0.721±0.217	0.456±0.285
Basophil (Bas# (10^3/L))	0.545±0.334	0.474±0.187	0.62±0.274

NLR	2.052±0.693	2.442±0.587	2.239±0.807
PLR	1.356±0.243	1.48±0.239	1.506±0.203
red blood cell count (RBC (10^{12}/L))	5.99±0.556	6.085±0.496	5.643±0.511
Hemoglobin (HGB (g/dL))	16.127±1.165	15.964±1.462	15.737±1.428
HCT	45.69±4.443	46.736±3.274	46.852±3.2
MCV (fL)	81.405±3.089	80.728±3.346	80.449±2.791
MCH (pg)	30.213±3.011	30.374±2.696	29.6±1.826
MCHC (g/L)	33.671±0.84	34.167±1.159	33.56±1.251
RDW-CV	12.713±1.369	15.237±1.206	13.072±0.765
RDW-SD (fL)	43.28±3.104	46.233±3.693	46.447±2.419
platelet count (PLT (10^3/L))	153.134±2.262	156.999±3.977	156.079±3.037
PCT (mL/L)	1.698±0.287	1.409±0.289	1.768±0.222

Table 2.5: Serum biochemical parameters in rats administered 9-Br-Nos and PPFD nanoparticles daily at a dose of 500 mg/kg body weight for 28 days showed no significant differences compared to the untreated control group.

Parameter	**Control**	**9-Br-NOS**	**PPFD**
Glucose (GLU)	97.86±3.13	100.86±6.1	111.66±6.67
Albumin (ALB)	2.53±0.58	3.18±0.41	2.81±0.33
Urea (UREA)	31.46±8.21	43.18±3.1	28.24±3.65
Creatinine (CREA)	0.85±0.29	0.66±0.33	0.96±0.2
Cholesterol (CHOL)	144.6±8.54	119.53±9	163.38±8.43
Triglycerides (TG)	101.37±5.84	98.45±5.13	94.66±7.8
Alanine Transaminase (ALT)	86.01±5.58	53.88±4.48	65.06±2.02
Aspartate Aminotransferase (AST)	30.74±4.69	36.55±4.53	27.92±7.12
Total Protein (TP)	6.17±0.6	6.13±0.56	6.13±0.28
Magnesium (MG)	7.37±1.33	4.6±1.18	5.92±0.98
Phosphorus (PHOS)	10.14±0.42	9.99±1.57	7.59±2.25
Calcium (CA)	0.23±0.06	0.86±0.43	0.25±0.05
Direct Bilirubin (DBIL)	0.49±0.16	0.2±0.29	0.48±0.17
Total Bilirubin (TBIL)	65.45±7.1	56.55±16.1	45.61±7.91
High-density Lipoprotein (HDL)	4.92±1.41	5.95±1.92	7.21±0.84
Gamma-glutamyl Transferase (GGT)	184.24±3.81	160.36±4.73	162.91±4.68
Alkaline Phosphatase (ALP)	97.86±3.13	100.86±6.1	111.66±6.67

2.3.17. Histopathological alterations in vital organs did not significantly change after the administration of the free drug 9-Br-Nos or PPFD nanoparticles

Vital organs, which includes the heart, liver, kidneys, brain, and lungs, were examined via hematoxylin and eosin (H&E) staining and Hoechst 33342 staining to assess morphological alterations and chromatin condensation after administration of the PPFD nanoparticles.

The results revealed no significant morphological changes in any of the vital organs (Figure 2.20(a)). Compared with normal animals, brain tissue has no intact neuronal structure. There were no changes in cardiac muscle fibres, acidophilic cytoplasm, or centrally located nuclei in the hearts of the treated animals. The lung tissue contained normal alveoli. The kidney showed normal glomeruli, proximal and distal convoluted tubules, and blood vessels in the treated animals. Histology of the liver revealed no changes in the hepatic lobular architecture, and hepatocytes were observed in the treated group. Furthermore, Hoechst staining (Figure 2.20(b)) revealed no significant increase in chromatin condensation or nuclear fragmentation in any of the organs. Additionally, quantitative analysis revealed no significant difference in the number of Hoechst-positive cells between the control and treated groups (t_8=0.072, P>0.05).

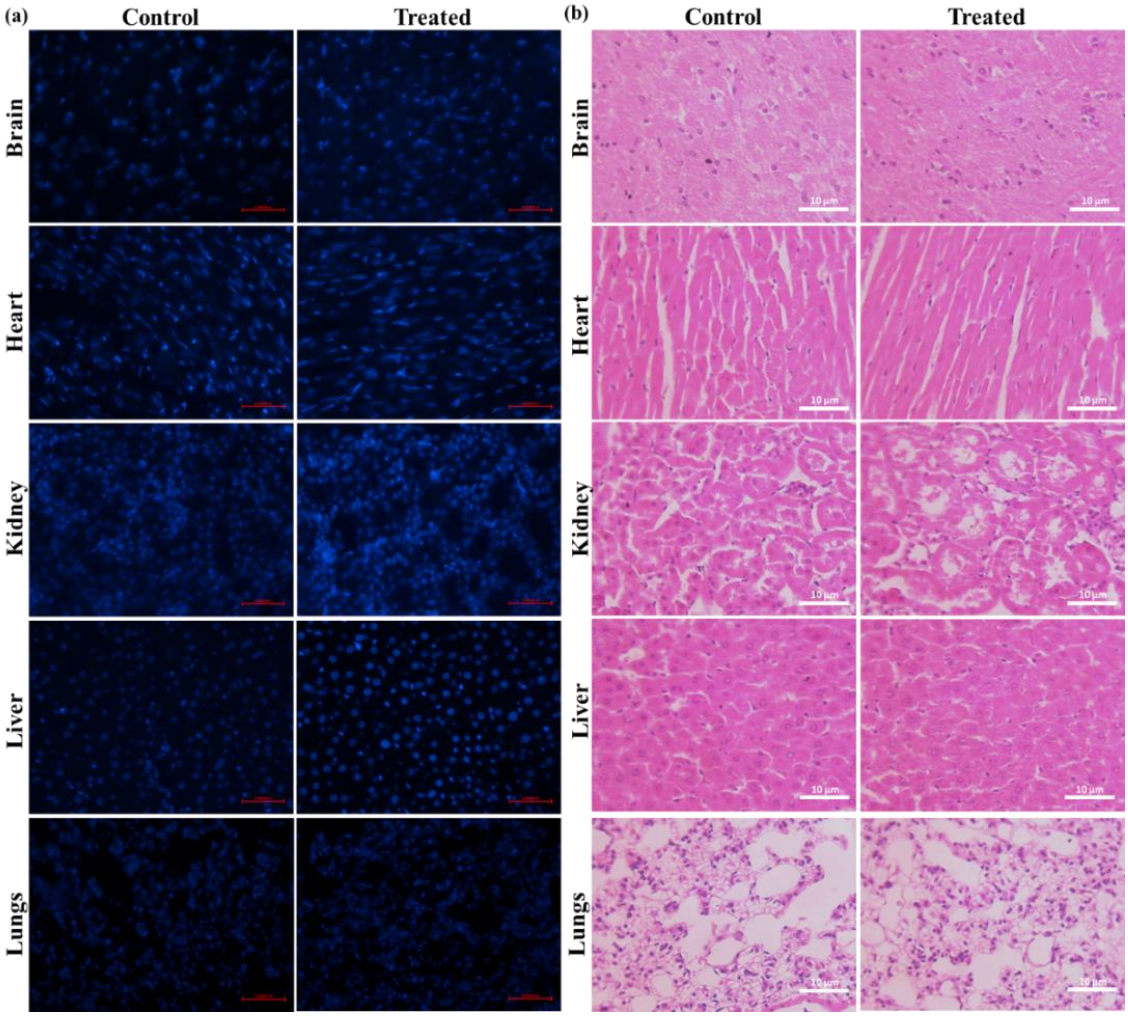

Figure 2.20. (a) Fluorescence images showing Hoechst 33342-stained sections of vital organs. (b) Representative histological images of major organs (heart, brain, kidney, liver, and lungs) stained with hematoxylin and eosin (H&E).

2.3.18. Pharmacokinetic analysis reveals enhanced systemic retention and bioavailability of PPFD nanoparticles compared with those of free 9-Br-Nos

In this study, the quantification of both the free drug 9-Br-Nos and the PPFD nanoparticles was performed via UHPLC-QTOF/MS (Figure 2.22). A calibration curve for 9-Br-Nos was established across a concentration range of 10 ng/mL-250 ng/mL from the MRM chromatogram (Figure 2.21).

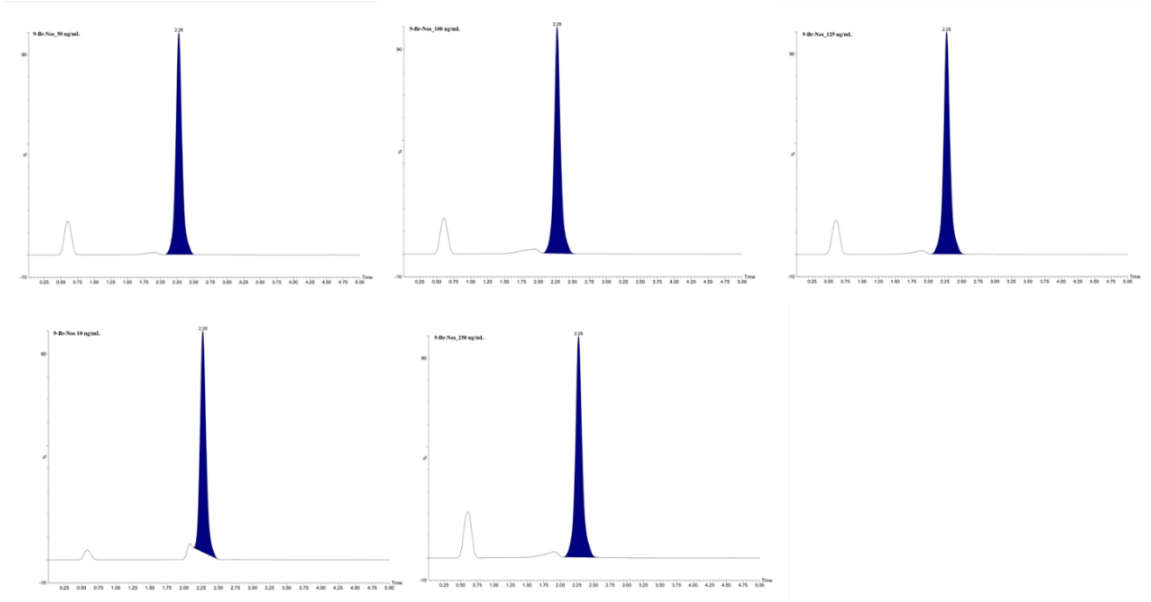

Figure 2.21. Chromatogram showing the separation of 9-Br-Nos at various concentrations (10-250 ng/mL) via UHPLC-QTOF MS.

The pharmacokinetic analysis using plasma samples collected at different time intervals was used to evaluate various pharmacokinetic parameters, including the maximum plasma concentration (Cmax), time to reach maximum concentration (Tmax), area under the plasma concentration–time curve (AUC), half-life ($t_{1/2}$), and clearance (CI) of both 9-Br-Nos and the nanoparticles, as shown in Table 2.6. The results revealed that, compared with 9-Br-Nos, PPFD nanoparticles presented a significantly greater Cmax, indicating an increased plasma drug concentration at 2 hours post-administration. The AUC of the PPFD was also very high, which indicates increased systemic exposure and improved bioavailability. On the other hand, the Tmax value for the nanoparticle-treated group was slightly longer, which corresponds to a controlled and sustained release mechanism that allows prolonged drug circulation. Furthermore, the increased t1/2, i.e., approximately 26 hours in the case of the PPFD, indicates slower metabolism and reduced elimination, which contribute to prolonged therapeutic activity in plasma. Additionally, the clearance rate of PPFD was lower than that of 9-Br-Nos, supporting the theory of extended systemic

retention in plasma (Figure 2.23). These findings highlight the limitations of 9-Br-Nos over PPFD nanoparticles, which may be responsible for hindering their therapeutic potential.

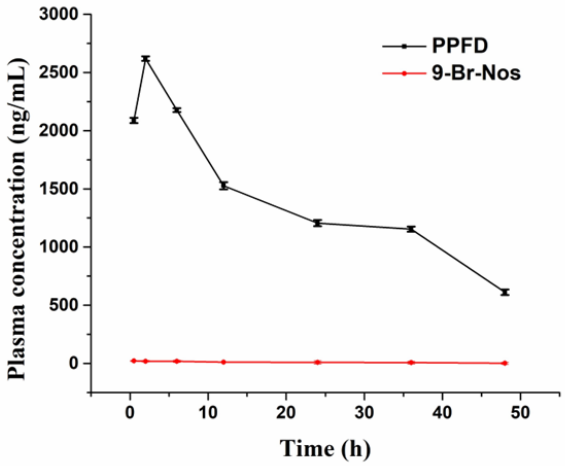

Figure 2.22. MRM chromatograms showing plasma concentrations at different time points (0.5 h, 2 h, 6 h, 12 h, 24 h, 36 h, and 48 h) following oral administration of the free 9-Br-Nos and PPFD nanoparticles.

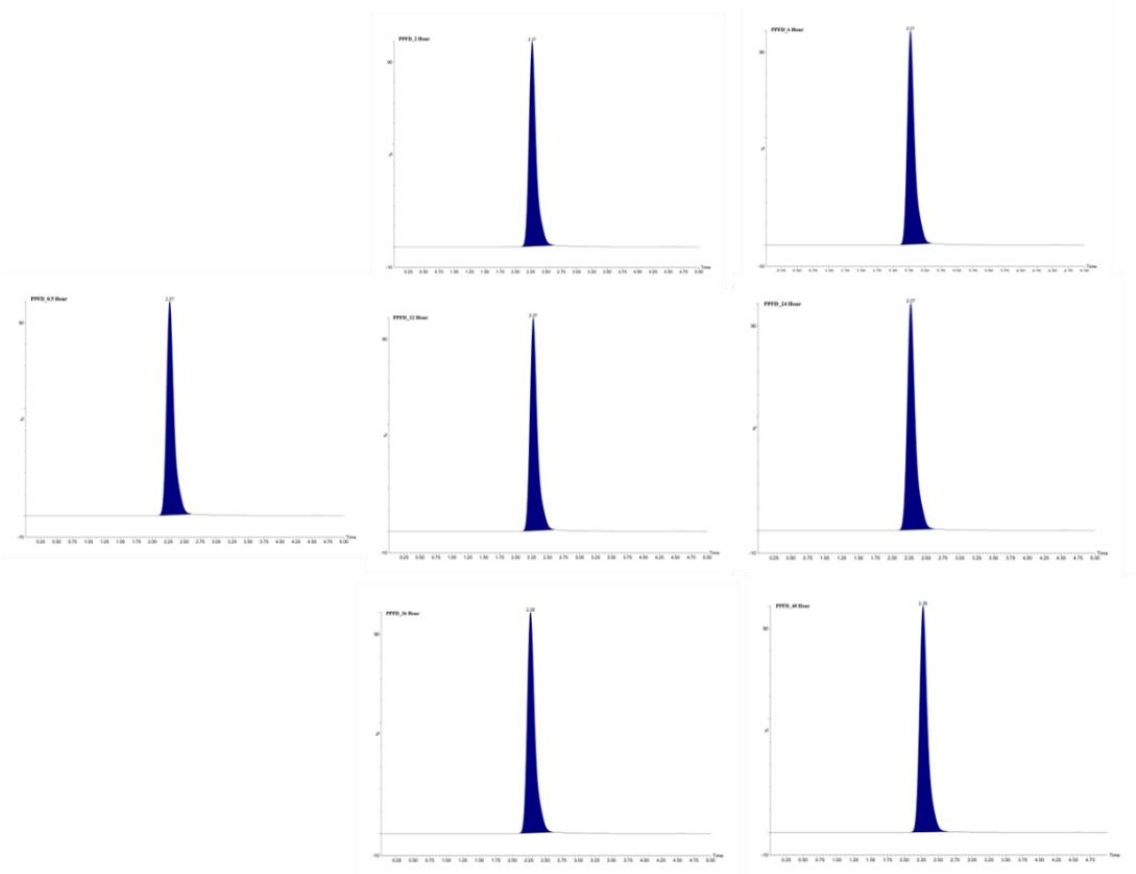

Figure 2.23. Mean plasma concentration versus time plot of free 9-Br-Nos and PPFD nanoparticles in SD rats following oral administration (mean ± SD, n=3).

Table 2.6. Pharmacokinetic parameters (mean ± SD, n=3) of the free drugs 9-Br-Nos and PPFD following oral administration.

Pharmacokinetic parameters	9-Br-Nos	PPFD
C_{max} (μg/mL)	0.021±0.41	2.62.85±0.74
T_{max} (hr)	0.5±0.76	2.00±0.63
AUC_{0-t} (μg hr/mL)	11.03±14.32	1118.70±24.91
$AUC_{0-\infty}$ (μg hr/mL)	480.56±61.37	665.10±78.35
CL (mL/hr/kg)	1.74±0.67	0.14±0.44
Vd (mL)	37.8±11.02	5.17±38.34
$t_{1/2}$ (hr)	15.06±3.28	26.57±5.72

C_{max}: maximum plasma concentration, T_{max}: time to reach maximum plasma concentration, AUC: the area under the concentration–time curve, CL: clearance, Vd: volume of distribution, $t_{1/2}$: half-time.

2.3.19. Tumor Volume Reduction Following Treatment with PPFD nanoparticle in the MDA-MB-231 Xenograft Model

nude mice bearing MDA-MB-231 human breast cancer xenografts were administered with 9-Br-Nos loaded PLGA-PEG-FA nanoparticles at a daily oral dosage of 150 mg/kg body weight. Tumor progression was closely monitored, and a notable decrease in tumor volume was observed in the treated groups compared to the untreated controls (Figure 2.24 (a)). By day 30 post-tumor implantation, the average tumor volume in the 9-Br-Nos treated mice had reduced to 1660 mm^3, and in PPFD nanoparticle it was reduced to 1182 mm^3, whereas the tumors in the control group expanded significantly, reaching an average volume of 3152 mm^3. Upon completion of the experiment, tumors were excised and weighed. Tumor weights in the control group ranged between 23.4 g and 28.5 g, with an average of 25.22 g. In contrast, the 9-Br-Nos treated group displayed the residual tumor mass ranged between 20.3 g and 12.7 g, with an average of 19.05g, whereas, in PPFD nanoparticles treated group the tumor weight varies between 18.1 g and 2.7 g, having an average of 10.13 g indicating a substantial inhibition in tumor growth. The tumor-suppressive activity of the drug loaded nanoparticle showed statistical significance ($p < 0.001$). Furthermore, no noticeable weight loss was detected in the treated animals throughout the study duration, highlighting the compound's potent antitumor activity without apparent systemic toxicity (Figure 2.24 (b)).

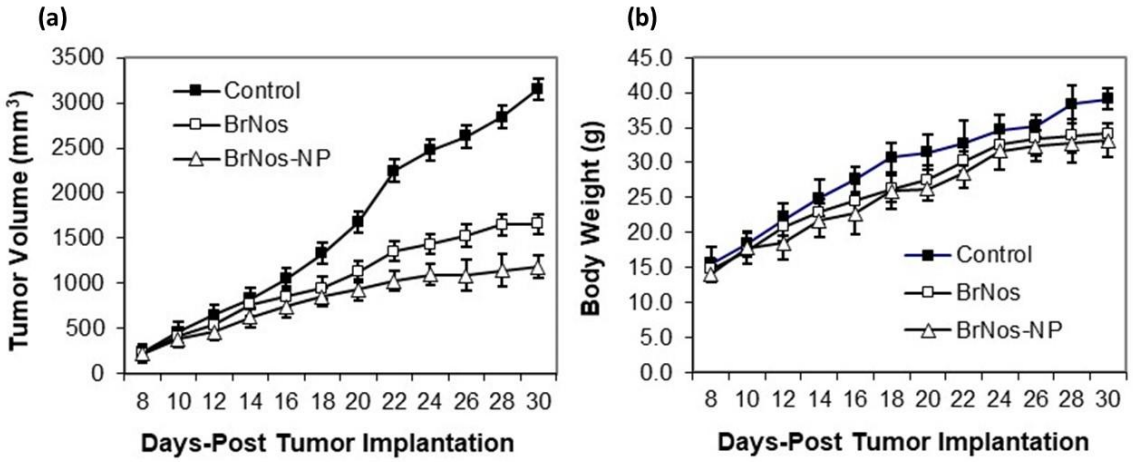

Figure 2.24. (a) Development of growing tumors in human MDA-MB-231 xenograft mice treated with 9-Br-Nos and PPFD nanoparticles. The growth of the tumors was considerably reduced compared with that of the untreated group. (b) Effects of 9-Br-Nos and PPFD nanoparticles on the body weights of the mice. There were no significant differences in body weight between the control and treated groups.

2.4. Conclusion

In summary, we have introduced a novel folate-targeted nanoparticle drug delivery system based on PLGA-PEG-FA for the efficient delivery of 9-Br-Nos, which has limited bioavailability and poor water solubility as a tubulin-binding anticancer agent. This nanoformulation effectively combines the advantages of biodegradable polymers, PEGylation for prolonged circulation, and folic acid-mediated targeting to enhance selective uptake by cancer cells overexpressing folate receptors, thus increasing the therapeutic index and minimizing off-target effects. The resulting 9-Br-Nos-loaded PLGA-PEG-FA nanoparticles presented desirable physiochemical characteristics, including a nanoscale size suitable for passive tumor targeting via the enhanced permeability and retention (EPR) effect, high drug encapsulation efficiency, and a sustained release profile over an extended period of time. These features are critical for maintaining therapeutic drug concentrations at the tumor site while minimizing systemic exposure. *In vitro* studies revealed enhanced cytotoxicity and cellular uptake in folate receptor-overexpressing cancer cells, whereas *in vivo* and toxicity assessments revealed good biocompatibility with no significant damage or systemic toxicity in any of the vital organs. Notably, pharmacokinetic evaluation revealed improved bioavailability with an extended half-life and higher drug concentration in plasma than those of the free drug. This approach effectively overcomes key limitations, such as poor solubility and stability, thereby improving the therapeutic efficacy and safety of the drug.

CHAPTER-3

Potent therapeutic efficacy of 9-Bromo-Noscapine against Breast Cancer Cells via enhanced bioavailability of the Noscapine-Cyclodextrin inclusion complex

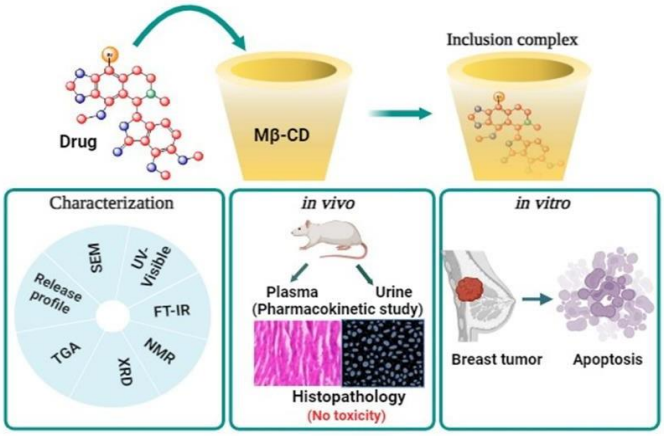

Graphical Abstract. Schematic illustration of the synthesis, characterization, *in vitro* and *in vivo* evaluation of the 9-Br-Nos-Mβ-CD inclusion complex.

ABSTRACT

The poor bioavailability and low therapeutic indices of conventional cancer therapeutics hinder their efficacy despite their promising anticancer potential. This study presents an improved solubility and enhanced drug delivery system against breast cancer by complexing bromo-noscapine (9-Br-Nos) with methyl-β-cyclodextrin (Mβ-CD). After the inclusion complex was synthesized, it was characterized using ultraviolet–visible (UV–Vis) spectroscopy, proton nuclear magnetic resonance (^{1}H NMR), Fourier-transform infrared spectroscopy (FT-IR), X-ray diffraction (XRD), scanning electron microscopy (SEM), and thermogravimetric analysis (TGA). In addition, the arrangement of the drug molecules within the Mβ-CD cavity was confirmed by molecular docking and molecular dynamic simulations. The drug release profile, bioavailability and anticancer activity of the complex were also evaluated *in vitro*. Moreover, the toxicity and metabolic clearance kinetics were assessed *in vivo.* Furthermore, to explore the molecular mechanism of the anticancer activity of the 9-Br-Nos-Mβ-CD inclusion complex, FITC-annexin V apoptosis assay and western blot analysis were conducted to explore the enhanced apoptotic cell death and the modulation of cancer-related proteins in breast cancer cells. In summary, this report demonstrated that the Noscapine–Cyclodextrin inclusion complex enhances the anticancer potential of 9-Br-Nos by modulating its bioavailability and persistence in breast cancer cells.

Keywords: 9-Bromo-Noscapine; Methyl-β-Cyclodextrin; Inclusion complex; Breast cancer; Apoptosis.

3.1. Introduction

Breast cancer is the most common malignancy among women, with an estimated 2.3 million new cases in 2020, representing 11.7% of all cancer cases worldwide. (Heer *et al*., 2020; Sung & Kim, 2020) Studies indicate that there will be more than 2 million breast cancer cases by 2030 globally. Consequently, early diagnosis and treatment play important roles in the survival of patients. Conventional breast cancer therapies such as surgery, chemotherapy, radiation, and hormone-based treatments have significantly improved patient outcomes. (Jun Wang & Wu, 2023) However, their long-term effectiveness is frequently hindered by certain limitations, such as poor drug selectivity, systemic toxicity, and multidrug resistance. However, the efficiencies of most cytotoxic drugs are also reduced because of their low solubility caused by their hydrophobic nature. (Jabbarzadeh Kaboli *et al*., 2014) This poor aqueous solubility makes it difficult for the drugs to be absorbed into the bloodstream and effectively reach the tumor-targeting site. Therefore, higher concentrations of chemotherapeutic drugs must be administered during treatment. (Anand *et al.*, 2023) This not only increases the risk of systemic toxicity but also may contribute to variable patient responses and treatment failure. (Madan *et al*., 2014; Memisoglu-Bilensoy *et al*., 2005; Santos *et al.*, 2017; Szente & Szejtli, 1999)

Noscapine, a naturally occurring benzylisoquinoline alkaloid derived from opium poppy (*Papaver somniferum*), has gained significant attention for its anticancer potential because of its ability to selectively bind to tubulin and interfere with microtubule dynamics without exerting cytotoxic effects on normal cells. (Čermák *et al*., 2020) Breast cancer is characterized by a high proliferative index and frequent mitotic activity, making it particularly susceptible to agents that target microtubule dynamics. (Testa *et al.*, 2020) By modulating microtubule polymerization, noscapine disrupts mitotic spindle assembly, leading to cell cycle arrest at the metaphase stage and the subsequent activation of apoptotic pathways. Compared with parent noscapine, 9-bromo-noscapine (9-Br-Nos) has a distinct effect on tubulin polymerization in breast cancer cells (i.e., 5–40-fold greater effects). (Karna *et al*., 2012) It halts the progression of the cell cycle during mitosis at a lower concentration than native noscapine does, promoting the sequential development of multipolar spindles and leading to apoptotic cell death. Considerable research has emphasized the preclinical effectiveness of this approach, as demonstrated in various xenograft models, including breast cancer. (Verma *et al.*, 2006) Despite its promising therapeutic characteristics, the clinical application of 9-Br-Nos is limited because of its weak solubility in water (0.35 × 10-3 g/ml) and hence limited bioavailability in systemic circulation. (Mangolim et al., 2014) This limitation requires the use of higher

concentrations of drugs during treatment, which can lead to increased potential side effects. The development of an ideal drug delivery carrier is crucial to address these challenges by reducing conventional dosages while maintaining drug efficacy. (Mukherjee et al., 2024)

One promising approach to address this challenge is the use of drug delivery carriers that can improve aqueous solubility and reduce systemic toxicity. Accordingly, identifying the best drug delivery carrier that can lower the standard dosage of chemotherapeutic drugs and destroy cancerous cells without hindering their efficiency is essential. Among various carriers, including liposomes, nanoparticles, and polymeric micelles, cyclodextrins have emerged as a favourable class of drug delivery agent because of their biocompatibility and ability to form noncovalent inclusion complexes with hydrophobic drug molecules. (Real et al., 2021) Specifically, methyl-β-cyclodextrin (Mβ-CD) has been proven to be the most efficient carrier owing to its larger cavity size and higher aqueous solubility (>2000 mg/L). (Szente & Szejtli, 1999) Mβ-CD modifies the physical, chemical, and biological characteristics of guest molecules by forming inclusion complexes in both solid and solution states. (Madan et al., 2014; Memisoglu-Bilensoy et al., 2005; Santos et al., 2017) Most notably, it improves the physicochemical properties of hydrophobic drugs in aqueous solutions and thereby enhances their solubility to facilitate targeted drug delivery.

To overcome these limitations of the poor solubility of the drug, there is a need to develop delivery systems that can enhance the solubility and systemic availability of 9-Br-Nos while maintaining its anticancer potency. Herein, we report a comprehensive study on the synthesis and characterization of an inclusion complex of 9-Br-Nos with Mβ-CD on the basis of spectral and analytical analysis. In silico modelling of the 9-Br-Nos-Mβ-CD inclusion complex and molecular simulation (Mu et al., 2022; Mukne & Nagarsenker, 2004) were performed to examine the dynamics and predict the relative binding affinities. The toxicity of the drug and the complex in vital organs was assessed in vivo, and its pharmacokinetic properties were analyzed via LC–MS/MS to determine the bioavailability of the drug. (Abbas et al., 2022) After the toxicity and bioavailability of the synthesized drug were verified, its in vitro antitumor activity was tested against the MCF-7 and MDA-MB-231 breast cancer cell lines. Additionally, the induction of apoptosis was examined via flow cytometry, whereas western blot analysis was conducted to assess the expression of molecular apoptotic marker proteins.

3.2. Materials and methods

3.2.1. Chemicals and reagents

Methyl-β-cyclodextrin (Mβ-CD) (MW 1331.37 g/mol) was commercially sourced (Sigma–Aldrich, ≥98% purity), while bromo-noscapine (9-Br-Nos) was chemically synthesized from noscapine as mentioned previously. (Aneja *et al.*, 2006) Briefly, 9-Br-Nos was synthesized using natural α-noscapine as the starting material. A suspension of natural α-noscapine (4.0 g, 9.7 mmol) in 15 mL of 48% hydrobromic acid was prepared and allowed to stir at room temperature. Fifty mL of freshly prepared saturated bromine water was added dropwise while being constantly stirred for approximately one hour until an orange precipitate started to develop. The reaction mixture was again stirred for approximately 30 minutes to confirm that the reaction was completed. A 25% aqueous ammonia solution was then used to neutralize the reaction mixture to pH 10. The product was then extracted with chloroform (3×25 mL), dried over anhydrous sodium sulfate and concentrated under reduced pressure. Finally, the crude residue was purified by silica gel chromatography via ethyl acetate:hexane (3:7), and pure 9-Br-Nos (4.3 g, 90%) was produced. All the other chemicals and reagents were obtained from Sigma–Aldrich unless otherwise mentioned.

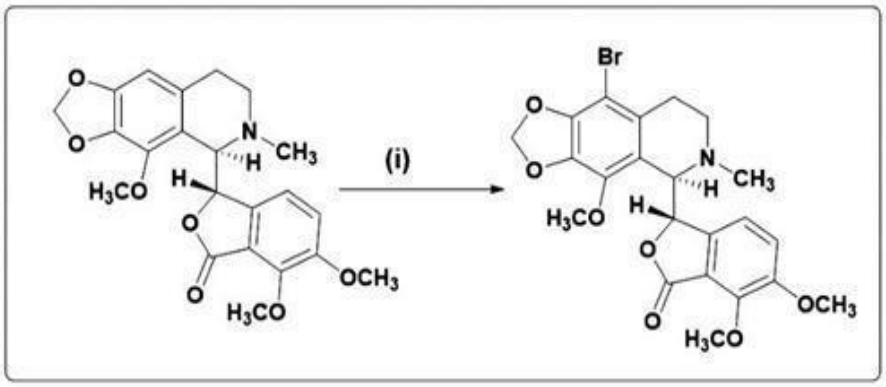

Reaction Scheme 1: Synthesis of 9-Bromo-Noscapine

3.2.2. Cell culture

MCF-7 and MDA-MB-231 breast cancer cell lines (passage number 23) (NCCS, Pune) were maintained in a humidified CO_2 incubator at 37°C with 5% CO_2. Dulbecco's Modified Eagle Medium (DMEM) (Gibco BRL, UK), Fetal Bovine Serum (FBS) (Gibco BRL, UK), 10X phosphate buffer saline (Gibco BRL, UK), 0.003% trypsin, 0.25% EDTA (Gibco BRL, UK), 10 mg/mL penicillin/streptomycin solution (Sigma–Aldrich), and DMSO (HIMEDIA) were used in this study for cell culture and treatment. The cells were grown in DMEM supplemented with 10% FBS and 1% penicillin/streptomycin and subcultured at a confluency of 70–80% with trypsin-EDTA.

All procedures were performed within a Class A2 biosafety cabinet following standard aseptic protocols. Cell line authentication was performed by NCCS via short tandem repeat (STR) profiling using commercially available AmpFLSTR™ Identifiler™ Plus PCR Amplification Kit from the applied biosystem. Additionally, mycoplasma testing was conducted using hoechst staining/PCR method to ensure contamination-free cultures.

3.2.3. Preparation of the 9-Br-Nos-Mβ-CD complex

The preparation of methyl-β-cyclodextrin (Mβ-CD) and 9-Br-Nos inclusion complex was performed at a 1:1 molar ratio according to the previously reported coprecipitation method, as represented in Figure 3.1(A) and (B). (Jing Wang *et al*., 2011) One equivalent of Mβ-CD **(1)** (150 mg, 0.1 mmol) was dissolved in 2 ml of distilled water at 50°C. Simultaneously, one equivalent of 9-Br-Nos **(2)** (56.67 mg, 0.1 mmol) was dissolved in 0.5 ml methanol and gradually added to an aqueous solution of Mβ-CD **(1)** with continuous stirring at 50°C for 24 hours. After the inclusion complex **(3)** was formed, the precipitate was filtered, washed with 5 mL of methanol:water (30:70) three times and then vacuum-dried. The yield of the target inclusion complex **(3)** was 71%.

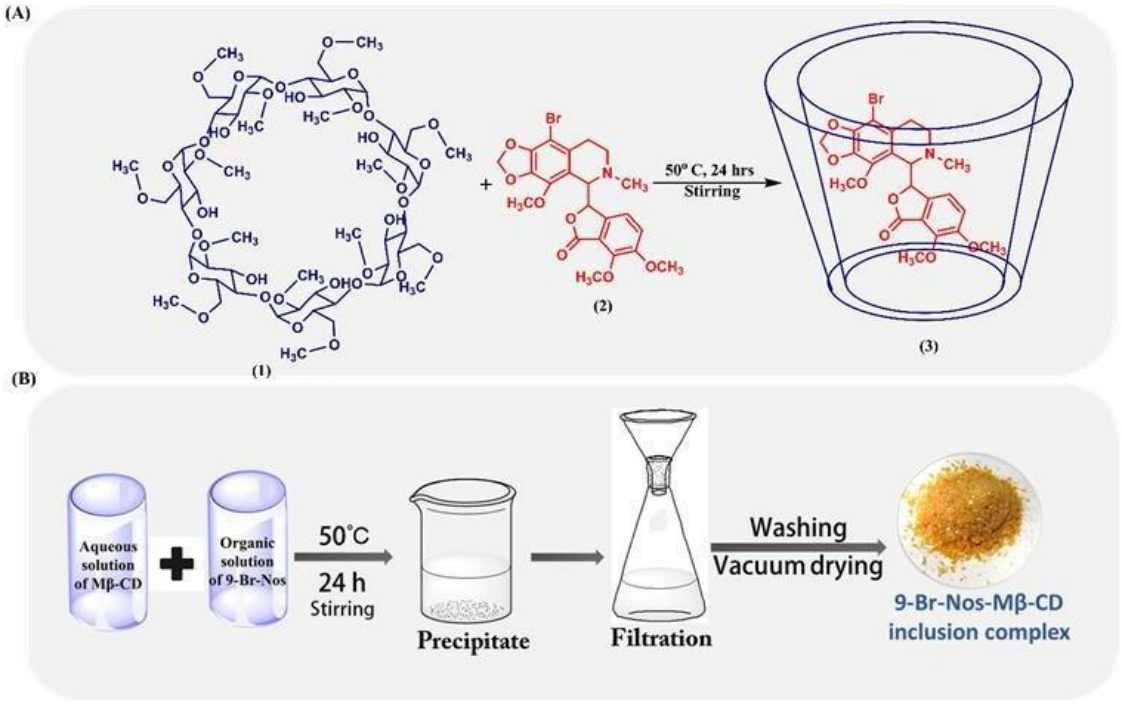

Figure 3.1. (A) Synthetic scheme of 9-Br-Nos-loaded Mβ-cyclodextrin. (B) Synthesis of the 9-Br-Nos-Mβ-CD inclusion complex via the coprecipitation method.

3.2.4. Molecular docking and molecular dynamic simulation

The molecular structures of Mβ-cyclodextrin and 9-Br-Nos were built via ChemDraw. The structures were imported into the maestro (Schrödinger-2023 LLC, NY, Schrödinger Release 2023-2) environment, and energy was minimized by Macromodel (Schrödinger-2023 LLC, NY, Schrödinger Release 2023-2) with OPLS 2005 as a force field and the PRCG algorithm (energy gradient of 0.001). Finally, the different conformations of 9-Br-Nos were generated using Ligprep (Schrödinger-2023 LLC, NY, Schrödinger Release 2023-2). Mβ-cyclodextrin was considered the receptor, and 9-Br-Nos was considered the ligand in the molecular docking experiments. Molecular docking was conducted for the inclusion of 9-Br-Nos in the Mβ-cyclodextrin complex using "Extra Precision" (XP) mode of Glide docking (Schrödinger-2023 LLC, NY, Schrödinger Release 2023-2) according to previously described methods. (Dandawate *et al*., 2012; Friesner *et al*., 2004; Halgren *et al*., 2004; Naik *et al*., 2011; Sravani *et al*., 2023) Briefly, the inclusion complex of Mβ- cyclodextrin was defined by creating a concentric grid box using Glide grid-receptor generation program (Schrödinger-2023 LLC, NY, Schrödinger Release 2023-2). It consists of an inner grid box with dimensions of 12 Å × 12 Å × 12 Å and an outer grid box with dimensions of 24 Å × 24 Å × 24 Å. The inner grid box represents the centroid of the bound ligand, whereas the outer grid box accommodates all the atoms of the ligand. The grid box of the above dimension was sufficient to place the Mβ-CD inclusion complex. Moreover, the ligand 9-Br-Nos was docked within the inclusion complex and was not rejected by the docking algorithm. A van der Waals radius scaling factor of 0.4 was applied, with partial charges capped at an absolute value of 0.25. For further analysis, the docked complex of Mβ-CD and 9-Br-Nos was selected on the basis of having the lowest docking score. (Patel *et al*., 2021; Ray *et al*., 2022; Yan *et al*., 2017) The docking score of 9-Br-Nos was calculated via the Glide XPscore.

A molecular dynamics simulation was performed to investigate the orientation of 9-Br-Nos within Mβ-CD using the Amber 16 suite. The docked complex with the lowest minimum docking score was considered for the MD simulation. Both Mβ-CD and 9-Br-Nos were processed using a general Amber force field (GAFF) through the Antechamber program. (Pearlman *et al*., 1995) The atomic point charges were determined by the AM1-BCC charge model. With the use of the tleap tool of the Amber 16 and ACPYPE applications, ligand internal coordinates and topologies were created. The default parameters were selected for the MD simulation of the co- complex structure of Mβ-CD and 9-Br-Nos to elucidate the mode of interaction between the molecules. Initially, 500 ps of NVT at 300 K was run, followed by NPT running while keeping the position

restrictions of 10 kcal/Å2 and a Parrinello-Rahman barostat with a reference pressure of 1 bar. Furthermore, a 100 ns simulation was run after equilibration, keeping 2 fs of a time step to evaluate the stability of the inclusion complex. The particle–mesh Ewald method (PME) was taken into consideration for long-range electrostatic interactions, keeping van der Waals and short-range electrostatics both at a cut-off range of 10 Å. Bonds were limited by the SHAKE algorithm. (Ryckaert et al., 1977) The temperature of the system was considered by the modified Berendsen thermostat. At every 20 ps, the atomic coordinates were taken into consideration. The trajectories for the root mean square deviation (RMSD) and radius of gyration (Rg) were analyzed and plotted by GRACE software. (Goga et al., 2012; Lee et al., 2016) Two methods, the Poisson–Boltzmann (PB) approach and the generalized Born (GB) approach, were employed to calculate the electrostatic component of the binding energy for each conformation. (H. Wang & Laughton, 2007)

3.2.5. Characterization of the inclusion complex

9-Br-Nos, Mβ-CD, and the 9-Br-Nos–Mβ-CD inclusion complex were characterized using a range numerous analytical and stoichiometric methods. First, the stoichiometry of the complex was evaluated using Job's plot method and the phase solubility analysis. Further, UV–visible spectroscopy (double beam spectrophotometer-UV 3200 (LABINDIA)) was employed to confirm the inclusion complex formation by monitoring different changes in the absorbance in the UV-Visible region at wavelengths ranging between 200 and 800 nm. Also, the surface morphology was assessed via a scanning electron microscope (Carl Zeiss (Ultra plus)) operated at 15 kV, which also represents the inclusion complex formation. Structural interactions were further analyzed by using Fourier transform infrared (FT-IR) spectroscopy (Bruker, ALPHA II, scan range 4000–550 cm^{-1}). Proton Nuclear Magnetic Resonance (^1H NMR) spectroscopy was also conducted in DMSO-d6 using a Bruker 400 MHz spectrometer to validate the host-guest interaction between the drug molecule and Mβ-CD. Crystallinity changes for the 9-Br-Nos–Mβ-CD inclusion complex was investigated through X- ray diffraction (XRD) analysis (PANalytical Empyrean XRD), and the thermal stability of the samples was evaluated using Thermogravimetric Analysis (Shimadzu TGA-50H, heating rate 10°C per min under nitrogen and compared to that of the free drug as well as Mβ-CD.

3.2.5.1. Determination of the stoichiometry of the inclusion complex

The stoichiometry of the host (Mβ-CD)-guest (9-Br-Nos) inclusion complex was determined by Job's method (continuous variation method) by using UV-Visible spectroscopy. This method was employed to confirm the 1:1 stoichiometry of the complex. A series of solutions containing Br-Nos and Mβ-CD were prepared, with the molar fraction of Br-Nos varying from 0 to 1. The Job plot was then generated by plotting $\Delta A \times R$ against R, where ΔA is the difference in absorbance between the 9-Br-Nos without and with Mβ-CD and R = [9-Br-Nos]/([9-Br-Nos] + [Mβ-CD]) at 311 nm.

3.2.5.2. Phase solubility study

Phase solubility investigations were conducted following the procedure outlined by Higuchi and Connors in 1965. (Malli *et al*., 2018; Saokham *et al.*, 2018) An excess amount of Br-Nos (8 mg)/Mβ-CD was added to 5 ml of distilled water to prepare supersaturated solutions of different concentrations ranging from 0 to 10 mM. These mixtures were then placed in a shaker incubator for 72 h at 25°C. Once equilibrium was established, the solution was subsequently filtered, and a small portion of the filtrate was extracted and analysed for 9-Br-Nos at 311 nm employing a UV–visible spectrophotometer. The phase solubility patterns were generated by plotting the solubility of Br-Nos against the concentration of Mβ-CD (n=3). The apparent stability constant, denoted as Kc, for the complex formed between 9-Br-Nos and Mβ-CD could be computed by considering the slope and intercept of the linear segment of the phase solubility curve, following the equation:

$Kc = \text{slope}/S_0 (1\text{-slope})$, where S_0 represents is solubility of drug in absence of Mβ-CD.

3.2.5.3. UV–Vis spectrophotometric study

Five milligrams of 9-Br-Nos was dissolved in methanol and Mβ-CD, and the 9-Br-Nos-Mβ-CD complex were diluted in distilled water. The absorption spectra were scanned using a double beam spectrophotometer-UV 3200 (LABINDIA) at wavelengths ranging between 200 and 800 nm.

3.2.5.4. Scanning electron microscopy (SEM)

Scanning electron microscopy (SEM) was used to evaluate the morphology of the 9-Br-Nos, Mβ-CD, and 9-Br-Nos-Mβ-CD inclusion complexes. A 10 µL volume of each sample was deposited onto SEM stubs equipped with copper tape. The stubs were then subjected to drying in a vacuum desiccator at room temperature for approximately 12 hours, followed by 120 seconds of gold coating to make the samples electrically conductive. The resulting images were captured using a Carl Zeiss (Ultra plus) scanning

electron microscope (SEM).

3.2.5.5. FT-IR Spectroscopy

FTIR spectra were recorded for solid samples of 9-Br-Nos, Mβ-CD and the 9-Br-Nos-Mβ- CD inclusion complex via a Fourier transform infrared spectrometer (Bruker, ALPHA II) in ATR mode. Measurements were performed in the scanning range of 4000–550 cm^{-1}.

3.2.5.6. ^{1}H NMR spectroscopy

^{1}H NMR spectra were obtained on a Bruker Ultra shield 400 MHz NMR spectrometer. Mβ-CD, 9-Br-Nos, and the 9-Br-Nos-Mβ-CD inclusion complex were dissolved in DMSO-d_6. Chemical shifts were reported in ppm, with tetramethylsilane (TMS) used as the internal standard.

3.2.5.7. Powder X-ray diffraction (PXRD) study

Powder XRD patterns for 9-Br-Nos, Mβ-CD, and the 9-Br-Nos-Mβ-CD inclusion complex were recorded by using a PANalytical Empyrean XRD.

3.2.5.8. Thermal-gravimetric analysis (TGA)

Thermal characterization of the Mβ-CD, 9-Br-Nos, and 9-Br-Nos-Mβ-CD inclusion complex using TGA was performed via a Shimadzu TGA-50H instrument at a heating rate of 10°C/min under a nitrogen atmosphere. The samples were then placed in a platinum pan and heated from 26°C to 600°C at 100 mL/minute flow rate.

3.2.6. *In vitro* drug release profile

To investigate the drug release profile of 9-Br-Nos from the Mβ-CD cavity, the release medium was prepared with distilled water containing 0.05% Tween 80. This concentration of Tween 80 ensures adequate solubilization of 9-Br-Nos while maintaining physiological relevance and minimizing interference with release kinetics. The release study was conducted by dispersing 5 mg of free drug and 50 mg of the inclusion complex in 25 mL of the release medium and stirring at 200 rpm. At specific time intervals of 5, 10, 15, 30, 45, 60, 90, 120, 180, 240, and 300 minutes, 2 mL aliquots were withdrawn, and the removed volume was replaced with an equal volume of fresh release medium to maintain the sink condition throughout the study. Each experiment was performed in triplicate, and the data are presented as the means±SDs. Statistical analysis was performed using two- way ANOVA followed by Tukey's multiple comparison test. The release of 9-Br-Nos was quantified using a UV–vis spectrophotometer (UV 3200, LAB INDIA) at a wavelength of 311 nm. (Yang *et al*., 2022) Furthermore, the *in vitro* release data were analyzed by using various kinetic models, including zero-order (Q =

K_0t), first-order ($\ln Q = \ln Q_0 - K_1t$), Higuchi ($Q = K_Ht^{1/2}$), and Korsmeyer–Peppas ($\ln Q = n\ln t + \ln K_P$) models, to understand the drug release mechanism from the inclusion complex, where Q denotes the percentage of drug released at a given time (t). K_0, K_1, K_H, and K_P correspond to the rate constants for the zero-order, first-order, Higuchi, and Korsmeyer–Peppas models, respectively. The parameter n represents the release exponent, which characterizes the mechanism of drug release. The best-fitting model was determined by comparing the correlation coefficient (R^2) values for each model.

3.2.7. *In vivo* pharmacokinetic and toxicity study by UHPLC-Q-TOF/MS analysis

Three male Sprague–Dawley (SD) rats (250 ± 20 g) were acclimatized for 7 days and then housed in metabolic cages one day prior to the experiment. A 12-hour light–dark cycle (12-hour light cycle from 8:00 AM–8:00 PM and a 12-hour dark cycle from 8.00 PM to 8.00 AM) was maintained. Food pellets (Lipton Pvt. Ltd., India), and water was provided ad libitum. The temperature and humidity of the animal facility were maintained at 25±2°C and 55±5%, respectively. (Baitharu *et al*., 2014) The animals were administered a single oral dose of the 9-Br-Nos-Mβ-CD inclusion complex at a concentration of 6.5 µg/mL through oral gavage. Blood samples (250 µL) were collected by puncturing the retro-orbital venous plexus using a glass capillary tube at 6, 12, 24, and 48 hours after drug administration. These samples were then centrifuged at 4000 rpm for 10 minutes to separate the plasma, which was then stored at -80°C until pharmacokinetic analysis. Urine samples were also collected at the same time points (i.e., 6, 12, 24, and 48 hours post-administration) using metabolic cages for the pharmacokinetic study. All the samples were analysed for the quantification of 9-Br-Nos using UHPLC-Q-TOF/MS. After completion of the study, the rats were anaesthetized with isoflurane followed by transcardial perfusion with ice-cold phosphate-buffered saline (PBS) to remove blood from the tissues before vital organs such as the brain, heart, liver, lungs, and kidneys were isolated and subsequently fixed with 4% paraformaldehyde in PBS. All the experimental procedures and protocols followed in the present study were approved by the Institutional Animal Ethics Committee of Sambalpur University, Odisha vide approval letter no. SU/BTBI/IAEC/2023/06.

3.2.7.1. Sample preparation

The plasma and urine samples were brought to room temperature and then redissolved. To do this, 100 µL of the sample was added to 300 µL of a 1:1 methanol:acetonitrile mixture in an Eppendorf tube. The mixture was vortexed for 2 minutes, sonicated in an ice–water bath for 2 minutes, and then centrifuged at 15,000 rpm for 10 minutes to separate the proteins. The supernatant was carefully collected into a new tube, after which the proteins were left behind. The samples were then desiccated at 25 °C (room temperature). Before analysis, the dried samples were redissolved in 1.5 mL of methanol, vortexed for 2–3 minutes, sonicated for 15 minutes, and centrifuged at 15,000 rpm for 10 minutes. Finally, the samples were filtered, and 10 µL was injected for UHPLC-Q-TOF/MS analysis. The data are presented as the means ± SDs (n=3). Statistical analysis was performed using an unpaired t test between the 9-Br-Nos-treated and inclusion complex- treated groups.

3.2.7.2. Instrumentation and chromatographic conditions for UHPLC-Q-TOF/MS analysis

The analysis was performed on a Xevo G3 QToF Waters Corporation (MA, USA) with Acquity UPLC I Class Plus and MassLynx software (Waters Corporation, USA). The data were processed through MassLynx software (Waters Corporation, USA). The separation was carried out using an Acquity UPLC HSS T3 column (100 × 2.1 mm, 1.8 µm) (Waters Corporation, USA). The column was maintained at 40°C, and the sample temperature was maintained at 15°C during the analysis. The elution was carried out in positive mode [ES+] at a flow rate of 0.4 ml/min using a gradient mobile phase, 0.1% formic acid in water (solvent A), and 0.1% formic acid in acetonitrile (solvent B). The volume ratio of solvent B was changed as follows: 20% B for 0–0.5 min, 20–40% B for 0.5–1.5 min, 40–95% B for 1.5–2.5 min, 95% B for 2.5–3.75 min, 95–20% B for 3.75–0.8 min, and 20% B for 3.8–5.0 min. A total of 10 µL of the standard solution of different concentrations (10 ng/mL, 50 ng/mL, 100 ng/mL, 125 ng/mL, 250 ng/mL) was injected, and the chromatographs were recorded for 5 min. Furthermore, 10 µL of the sample solution (plasma and urine) was injected, and the chromatographs were recorded for 5 min. The acquisition method in LC-HRMS was performed via an optimized MRM method where the MS parameters were as follows: ionization type-ESI, mode-Tof-MRM, acquisition time 5 min, mass range (m/z) 100−550 m/z, where the 9-Br-Nos set mass was kept at 492.03 m/z, with the target daughter ion at 297.97 m//z, collision energy 30 eV, cone

voltage 40 V, capillary voltage 3.0 kV, source temperature 130°C, desolvation temperature 500°C, cone gas flow 50 L/h, desolvation gas flow 800 L/h.

3.2.7.3. Hematoxylin and eosin (H&E) staining for morphological analysis

The isolated heart, liver, kidney, brain, and lung tissues were subsequently fixed with paraformaldehyde solution (4% PFA) for 24 hours, followed by dehydration via a graded series of alcohol. The dehydrated tissues were treated with xylene to remove alcohol and embedded in molten paraffin wax to prepare blocks. The paraffin blocks were subsequently sectioned via a semiautomated circular microtome (Leica) to prepare sections with a thickness of 4 µm. The tissue sections were mounted on slides for hematoxylin and eosin (H&E) staining. The stained slides were subsequently visualized and micrographed via a light microscope with a Nikon ECLIPSE Ts2R imaging system.

3.2.7.4. Chromatin condensation of rat tissues by Hoechst staining

Following the methodology described in previous studies, (Baitharu *et al*., 2014) we assessed chromatin condensation as an indicator of apoptotic cell death using Hoechst 33342 staining. Tissue samples from the heart, liver, kidney, brain, and lung were fixed in 4% paraformaldehyde for 16 hours. The samples then underwent a series of processes, including washing, dehydration, and paraffin embedding, followed by sectioning into thin slices. Specifically, 10-µm-thick tissue sections were treated with 0.1% Triton in PBS to enable permeabilization and then stained with Hoechst 33342 (1.5 µg/ml) in light protected condition at room temperature for 15 minutes. After being rinsed gently with 0.1 M PBS, the sections were mounted with glycerol. Chromatin condensation was assessed using a Nikon ECLIPSE Ts2R fluorescence microscope with a blue filter and DAPI staining. The data are presented as the means ± SDs (n=6). Statistical analysis was performed using an unpaired t test between the control and treated groups.

3.2.8. *In vitro* cytotoxicity assay

Cell viability was determined via a colorimetric MTT assay. The breast cancer cells (MDA-MB-231 and MCF-7) were seeded at a density of 5,000 cells/well in complete growth medium in 96-well plates and incubated for 24 hours. The cells were then incubated with different concentrations of 9-Br-Nos and the 9-Br-Nos-MβCD inclusion complex (1–50 µg/mL) for 48–72 h before adding MTT reagent. Then, fresh solution of MTT (0.5 mg/mL in 1XPBS) was added to each single well of the 96-well plates. The plate was incubated in a CO_2 incubator for another 3-4 hours. Finally, the

cells were dissolved in 100 µL of DMSO and then analyzed in a microplate reader (Bio-Rad iMark™ Microplate Absorbance Reader) at 570 nm. The untreated cells were used as a negative control for evaluating cytotoxicity. Three independent experiments performed in triplicate were used for the calculations, and statistical analysis was performed via two-way ANOVA followed by Tukey's multiple comparison test.

3.2.9. Chromatin condensation of breast cancer cells by Hoechst staining

MDA-MB-231 and MCF-7 cells were treated for 24 hours with various concentrations (half of the IC_{50}) of 9-Br-Nos and its inclusion complex. Following treatment, the cells were washed three times with phosphate-buffered saline (1X PBS) and fixed in 100% ice-cold methanol for 15 minutes. After fixation, the cells were washed again three times with PBS and stained with Hoechst 33342 (1 µg/mL) for 15 minutes to visualize the nuclei using fluorescence microscopy (Nikon ECLIPSE Ts2R). [Das 2023] Data are presented as the means ± SDs (n=6), and statistical significance was determined using one-way ANOVA followed by Tukey's post hoc test.

3.2.10. Expression of cleaved caspase 3, Bax and p-JNK in MDA-MB-231 cells by western blotting

MDA-MB-231 breast cancer cells were treated with the 9-Br-Nos-MβCD inclusion complex for 48 hours, while untreated cells were used as a negative control. Total cellular proteins were extracted using lysis buffer containing 20 mM Tris-HCl (pH 8.0), 1 mM EDTA, 0.5 mM EGTA, 0.1% sodium deoxycholate, 150 mM NaCl, 0.1% IGEPAL and 10% glycerol. Additionally, the lysis buffer contained a protease inhibitor cocktail (PIC) from Roche, PhosStop (Roche) and 1 mM PMSF. The mixtures were then centrifuged at 12,000 rpm for 25 minutes, after which the supernatants were collected, and the total protein concentration was measured using a BCA kit. Fifty micrograms of protein from each sample were separated on a 10% SDS–PAGE gel and transferred onto a polyvinylidene difluoride (PVDF) membrane (Bio-Rad, USA) using a Bio-Rad Trans-Blot® SD Semi-Dry Transfer Cell. The membrane was blocked for 1 hour at room temperature with 5% nonfat milk. The samples were then incubated at 4°C overnight with the appropriate primary antibody. The primary antibodies used in this study were β-actin (~42 kDa, 1:1000, CST #4967S, MA, USA), Bax (~20 kDa, CST #2772S, MA, USA), cleaved caspase 3 (~17 kDa, 1:1000, CST #9661S, MA, USA), and p-JNK (~54 kDa, 1:1000, CST #9251S, MA, USA). The membranes were then washed three times with 1X PBS/PBST followed by a 1-hour incubation at room temperature with horseradish peroxidase-conjugated secondary antibodies (1:5000, Promega #W4011).

Finally, the PVDF membranes underwent a similar washing step, and the signal was detected using a chemiluminescent peroxidase substrate kit. Densitometric analysis of the captured signal blot was performed with ImageJ software, and the results are expressed as a percentage of the control. All the experiments were repeated three times, and statistical analysis was performed via one-way ANOVA followed by Tukey's post hoc test.

3.2.11. Apoptosis detection by Annexin-V-FITC

In cancer cells apoptosis was assessed using the Annexin-V-FITC assay with an apoptosis detection kit (Sigma-Aldrich) following the manufacturer's protocol. MDA-MB-231 cells were seeded at a density of 50,000 cells/well in a 6-well culture plate and incubated for 24 hours. The cells were then treated with the IC_{50} concentrations of the free drug 9-Br-Nos and the inclusion complex for 48 hours, with untreated cells serving as controls. The cells were then washed with PBS and trypsinized, and the cell pellets were resuspended in 100 µL of 1X binding buffer containing 5 µL of Annexin V-FITC and 5 µL of PI, followed by incubation at room temperature for 20 minutes in the dark. The samples were analysed via a flow cytometer (CytoFLEX Flow Cytometer, Beckman Coulter). Viable cells (Annexin V^-/PI^-), early apoptotic cells (Annexin V^+/PI^-), late apoptotic/necrotic cells (Annexin V^+/PI^+) and late necrotic cells (Annexin V^-/PI^+) were identified, and their percentages were determined. (Muhammad Nadzri *et al*., 2013) All the experiments were repeated three times, and statistical analysis was performed using one-way ANOVA followed by Tukey's post hoc test.

3.2.12. Statistical analysis

The statistical significance of all experimental groups was assessed using one-way ANOVA followed by post hoc analysis using Newman–Keuls post hoc test and Student's t test. A p value of less than 0.05 was considered indicative of a significant difference. The data are expressed as the mean ± standard deviation for $n \geq 3$. The cell viability (IC_{50}) of both cancer cells, MDA-MB-231 and MCF-7 was calculated by non-linear curve fitting using software GraphPad Prism version 8.0.2.

3.3. Results and Discussion

3.3.1. *In silico* molecular modelling and molecular dynamic simulation

Molecular docking provides valuable insights into the binding mode between 9-Br-Nos and Mβ-CD. The ligand, 9-Br-Nos was docked within the Mβ-CD inclusion complex, and the docking energy was found to be -5.0 kcal/mol, indicating a weak interaction between them. The most likely binding configuration was determined, which revealed a 1:1 binding interaction between 9-Br-Nos and Mβ-CD, with the drug fitting snugly within the pocket, as illustrated in Figure 3.2(A). To gain a better understanding of the mode of interaction of 9-Br-Nos within the Mβ-CD inclusion complex and the stability of the complex, molecular dynamic simulation is a useful computational approach. A 100 ns molecular dynamics simulation study was conducted to observe the stability of the binding complex of 9-Br-Nos and Mβ-CD. To assess the system's stability, two primary parameters are employed: the root-mean-square deviation (RMSD) and the radius of gyration (Rg). The RMSD plot vs. time quantifies the extent of displacement among atoms or different groups over time and is typically a key indicator of the stability of the system. The relatively low fluctuation in the RMSD (Figure 3.2(B)) of the binding complex of 9-Br-Nos and Mβ-CD after 30 ns indicates the stability of the system. Conversely, Rg serves as a metric to gauge structural compaction in certain entities, such as proteins, polymers, and micelle formations. After approximately 30000 picosecond simulations, the binding complex of 9-Br-Nos and Mβ- CD remained stable (Figure 3.2(C)). To correctly calculate the binding free energy between 9-Br-Nos and Mβ-CD, we used the MM-PBSA method. For this purpose, from the last 2 ns, 1000 snapshots of the MD trajectory were taken, and the binding free energy between 9-Br-Nos and Mβ-CD was calculated. The predicted binding free energy was found to be -7.18 +/- 6.51 kcal/mol between 9-Br-Nos and Mβ-CD, indicating weak interactions. Furthermore, the mode of interaction between both 9-Br-Nos and Mβ-CD is shown in Figure 3.2(A). The binding of 9-Br-Nos with the Mβ-CD inclusion complex mostly included three weak hydrogen bonding interactions (H-bonding distance > 3.0 Å). The O atom of 9-Br-Nos formed a H-bond with the hydroxyl group of Mβ-CD, which has a bond length of 3.25 Å, and the methoxy oxygen of 9-Br-Nos formed a H-bond with the hydrogen of Mβ-CD, which has a bond length of 3.28 Å. These findings provide valuable insights into potential complex formation and various characterizations that lay the groundwork for further experimental stages.

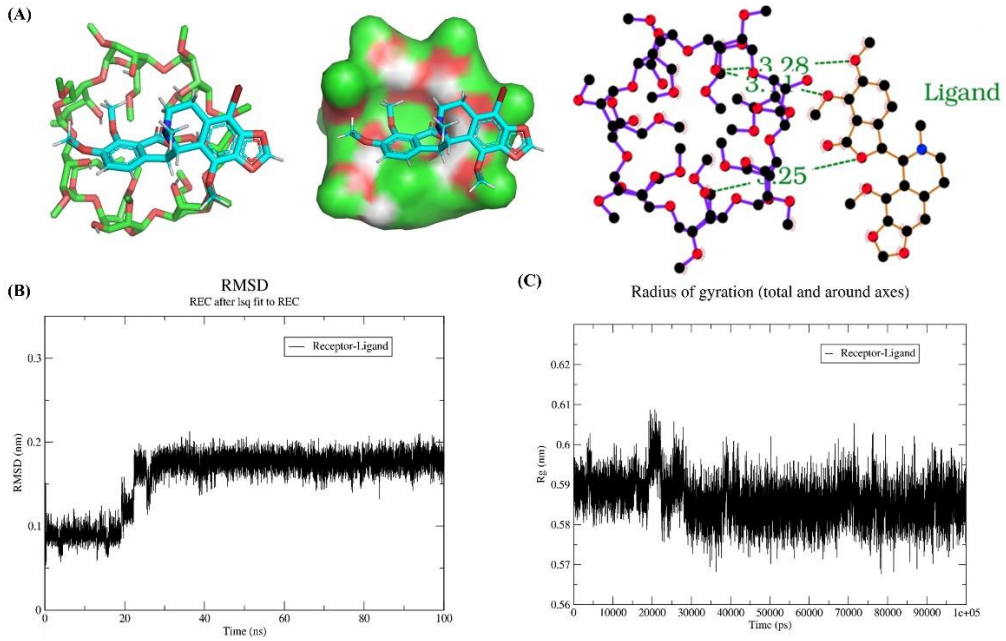

Figure 3.2. (A) The binding poses of the inclusion compound predicted by docking (from left to right 3D view, pocket view, and 2D view) of IC, and the 2D view represents the binding of 9-Br-Nos with the Mβ-CD inclusion complex, which includes three weak hydrogen bonding interactions (H-bonding distance > 3.0 Å). The O atom of 9-Br-Nos formed a H-bond with the hydroxyl group of Mβ-CD, which has a bond length of 3.25 Å, and the methoxy oxygen of 9-Br-Nos formed a H-bond with the hydrogen of Mβ-CD, which has a bond length of 3.28 Å. (Red: O atom; black: H atom; blue: N atom. (B) Diagrams showing the RMSD and radius of gyration and (C) (Rg) in a 100 ns simulation of the 9-Br-Nos-Mβ-CD inclusion complex.

3.3.2. Phase solubility analysis and stoichiometry evaluation

The stoichiometry and apparent stability constant (Kc) between the drug and the host molecule can be determined via Job's plot and phase solubility studies, respectively. In Job's method, equimolar solutions of 9-Br-Nos and Mβ-CD were mixed in varying mole fractions by maintaining a constant total concentration, and a plot was constructed by plotting the difference in absorbance against the mole fraction. Figure 3.3(A) shows that a 1:1 binding stoichiometry was observed for the inclusion complex, as the maximum peak was at R = 0.5. Similarly, Figure 3.3(B) shows the phase solubility diagram for inclusion complex formation between 9-Br-Nos and Mβ-CD. The solubility of the drug increases linearly in aqueous solution with increasing concentrations of Mβ-CD, which is classified as the A_L type. The A_L type corresponds to a linear phase-solubility diagram, which represents a linear relationship between the concentration of a dissolved drug and the

amount of Mβ-CD added to the solution. The stability constant, $K_{1:1,}$ was calculated from a linear equation with a slope value of 0.0422 and an intercept of 0.354 was 114.1 M^{-1}, which represented moderate binding affinity between 9-Br-Nos and Mβ-CD. These values suggested that the inclusion complex formed between 9-Br-Nos and Mβ-CD was stable. Additionally, as the slope value was less than unity, the ratio between the host and the drug molecule was 1:1. (Araujo *et al.*, 2009)

3.3.3. Characterization of the inclusion complex

3.3.3.1. UV–visible spectroscopy

The UV–visible spectra of Mβ-CD, 9-Br-Nos, and the 9-Br-Nos-Mβ-CD inclusion complex were measured separately in MeOH and are shown in Figure 3.3(C). In the spectrum of Mβ-CD (a), no absorbance peak was observed, which indicates that it did not absorb UV light within this region. An absorbance maximum at approximately 311 nm was observed in the spectrum of the 9-Br-Nos drug molecule (b) due to $\pi \rightarrow \pi^*$ or $n \rightarrow \pi^*$ transitions. However, the spectrum (c) showed increased absorbance at 311 nm (hyperchromic effect), confirming the presence of the drug molecules in the inclusion complex and suggesting successful encapsulation.

3.3.3.2. Scanning electron microscopy (SEM)

To assess the morphological characteristics and confirm complex formation, scanning electron microscopy (SEM) analysis was performed. Changes in surface morphology can provide insight into the physical interactions and successful inclusion of drug molecules within the carrier system. The SEM images shown in Figure 3.3(D) revealed the spherical characteristics of Mβ-CD (panel a), whereas the pure drug 9-Br-Nos depicted clump-like irregularly shaped structures (panel b). However, the SEM image of the complex shown in panel c represents a different crystal-type morphology. This change in the morphology of the inclusion complex and the formation of a new solid phase indicates a departure from the spherical shape of Mβ-CD and the typical appearance of 9-Br-Nos. Hence, morphological changes may serve as evidence to validate the interactions between 9-Br-Nos and Mβ-CD.

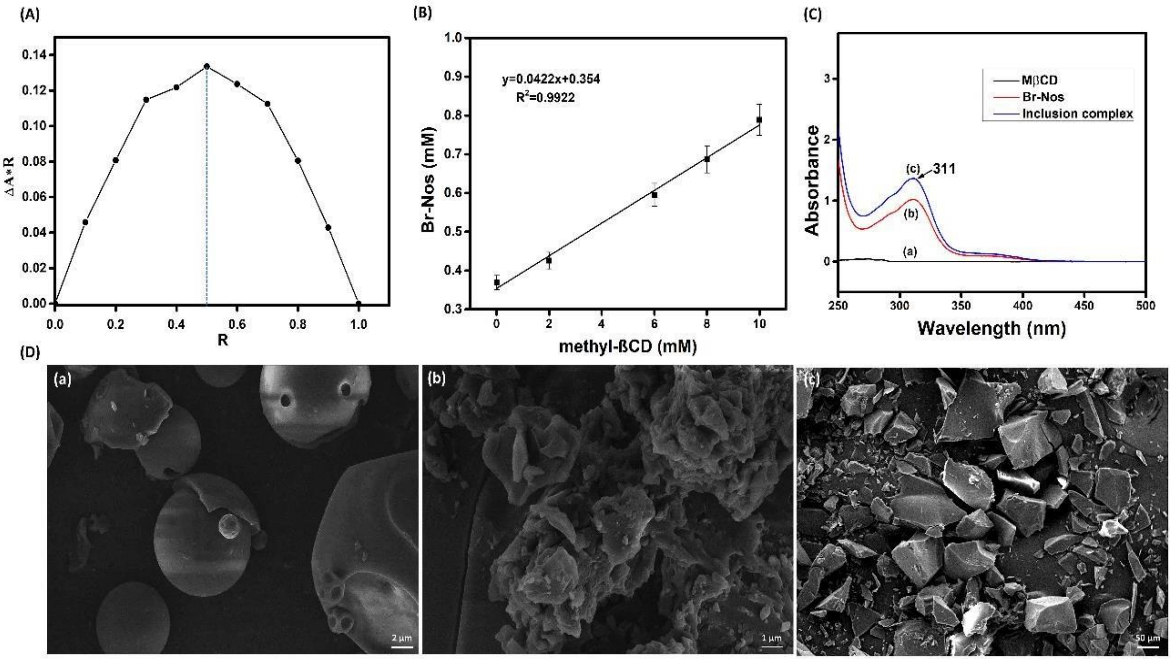

Figure 3.3. (A) Continuous variation plot (Job's plot) for the 9-Br-Nos-Mβ-CD inclusion complex. (B) Phase solubility diagram of the 9-Br-Nos-Mβ-CD binary system in distilled water at 25 °C (y=0.0422x+0.354, R^2=0.9922). The experiments were performed in triplicate (n=3). (C) UV–visible spectra and (D) scanning electron microscopy images of (a) Mβ-CD. (b) Br-Nos and (c) 9-Br-Nos-Mβ-CD inclusion complexes at a magnification factor of 100x.

3.3.3.3. FT-IR spectroscopy

The 9-Br-Nos-Mβ-CD inclusion complex was further characterized through the FT-IR technique. Figure 3.4(A) shows the FT-IR spectra of 9-Br-Nos, Mβ-CD, and the 9-Br-Nos-Mβ-CD inclusion complex. In the FT-IR spectrum of Mβ-CD (depicted in spectrum (a)), the peaks at 3376, 2924 and 1037 cm^{-1} are assigned to the –OH, C–H and C–O stretching frequencies, respectively. The FT-IR spectrum of 9-Br-Nos (b) shows that the peaks at 2945, 1614 and 1032 cm^{-1} are associated with C-H, C=C and C-O stretching, respectively. A distinctive peak at 1751 cm^{-1} was observed for the carbonyl group, confirming the existence of a lactone ring. However, after the formation of the inclusion complex for the 9-Br-Nos complex with Mβ-CD (c), a few identical peaks of individual components were also present in the FT-IR spectrum. Peaks at 3371, 2925, 1750, 1615 and 1032 cm^{-1} were attributed to –OH, C-H, C=O, C=C and C-O functional groups, respectively. This suggested the insertion of drug molecules within the hydrophobic cavity of the cyclodextrin.

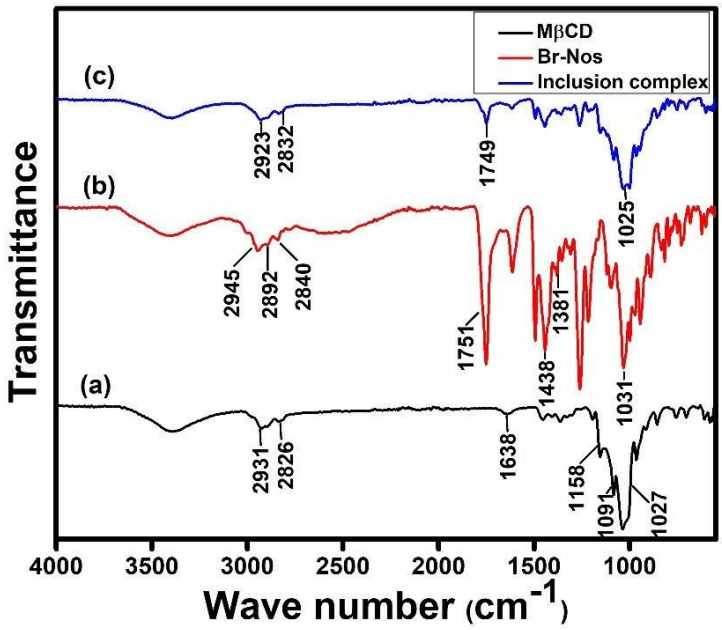

Figure 3.4. (A) FT-IR spectra of Mβ-CD (a), 9-Br-Nos (b), and the 9-Br-Nos-Mβ-CD inclusion complex (c).

3.3.3.4. ^{1}H NMR spectroscopy

The inclusion of 9-Br-Nos as guest molecules in the Mβ-CD cavity was more clearly demonstrated by ^{1}H NMR spectroscopy, as shown in Figure 3.4(B). Two sharp peaks at δ 3.837 ppm and 6.076 ppm for 9-Br-Nos shifted to δ 3.841 ppm and 6.084 ppm, respectively, after the inclusion complex formed. The chemical shift values (Table 3.1) of the outer surface protons of Mβ-CD, i.e., H-1, H-2, H-4, and H-6, slightly moved upfield. However, a significant change was observed in the chemical shifts of the inner H-3 and H- 5 protons, with a greater upfield shift observed for H-3 than for H-5. Although both protons were located inside the cyclodextrin cavity, H-3 was positioned near the wider rim. These chemical shift changes suggest that the drug preferentially enters the cyclodextrin cavity from the wide side, indicating a directional mode of the inclusion. Hence, we hypothesize that the guest molecule interacts noncovalently with the hydrophobic cavity of Mβ-CD, resulting in an increase in the electron density in the cavity. This might create a shielding effect on the H-3 and H-5 protons, which suggests the encapsulation of 9-Br-Nos with the host molecule. (Deng *et al.*, 2018) Additionally, as shown in Figure 3.4B (b), the peaks for 9-Br-Nos appear at 3.10--5.21 ppm, and the protons of Mβ-CD appear near 3.35, 3.81, and 6.05 ppm (Figure 3.4B (c)), whereas the NMR profile of the inclusion complex in Figure 3.4B (a) shows the respective signals of Mβ-CD and signals for the drug (represented by arrows) but at low intensity, which signifies the encapsulation of 9-Br-Nos with the host molecule.

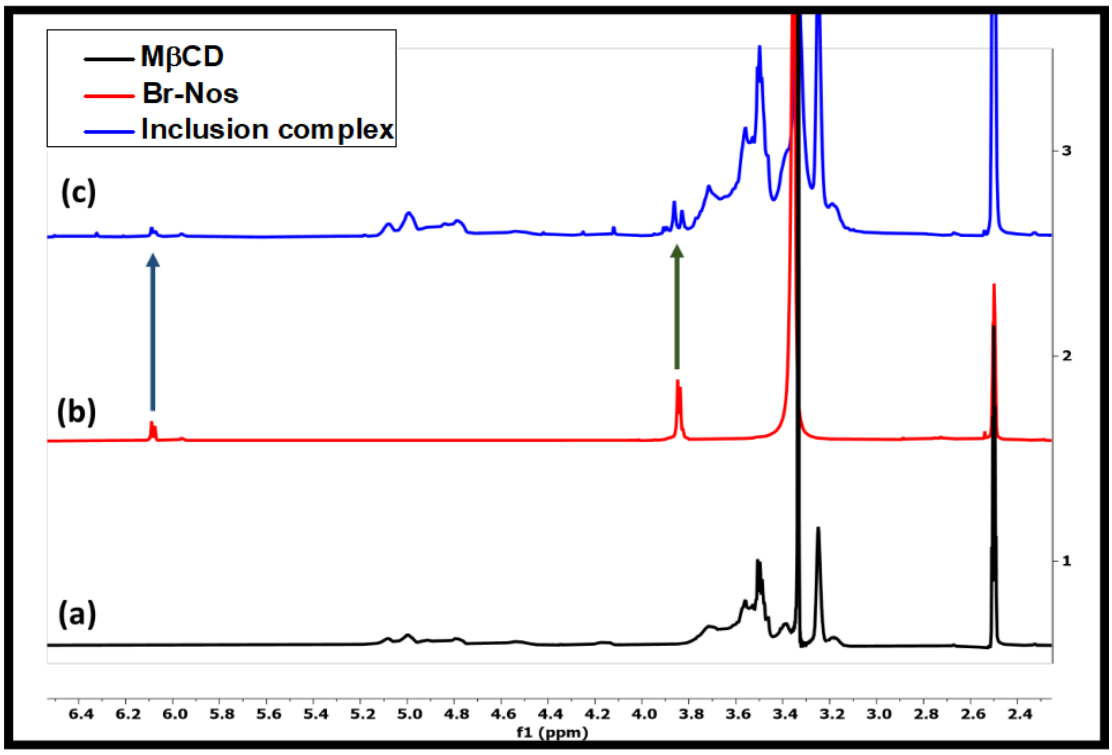

Figure 3.4. (B) ^{1}H NMR spectra of Mβ-CD (a), 9-Br-Nos (b), and the 9-Br-Nos-Mβ-CD inclusion complex (c).

Table 3.1. Chemical shifts of Mβ-CD and the inclusion complex.

	H-1	**H-2**	**H-3**	**H-4**	**H-5**	**H-6**
Mβ-CD (ppm)	4.909(d)	3.529(dd)	4.787(t)	3.489(t)	3.678(m)	3.893(d)
Inclusion Complex (ppm)	4.916 (d)	3.536(dd)	4.833(t)	3.495(t)	3.690(m)	3.901(d)
Δδ (ppm)	0.007	0.007	0.046	0.006	0.012	0.008

3.3.3.5. X-ray diffraction analysis

Powder X-ray diffraction is commonly used to determine the physical state of a drug molecule inside the hollow cavity of a host molecule. The loss of crystallinity of the drug molecules confirmed the formation of the inclusion complex. As shown in Figure 3.4(C), 9-Br-Nos presented sharp peaks at 2θ angles of 10.5, 14.15, 17.36, 21.11, 23.65, 25.97, 27.55, and 29.39, which indicated the crystalline state. However, only two broad peaks

were observed in the spectrum of Mβ-CD at 11.04° and 18.14°, which is consistent with its amorphous state. However, the distinctive sharp peaks of 9-Br-Nos disappeared or weakened in the diffraction spectrum of the inclusion complex. This change suggested a disruption of the long-range crystallinity order of the drug, which can be attributed not only to the incorporation of the drug molecules inside the cavity of Mβ-CD but also to the loss of crystallinity. (Chen *et al*., 2018; Han *et al*., 2020)

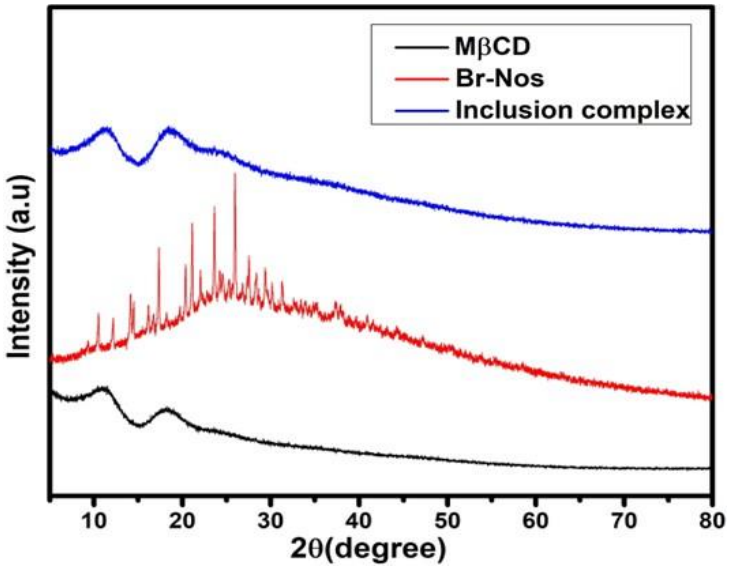

Figure 3.4. (C) X-ray diffractogram of Mβ-CD (a), 9-Br-Nos (b), and the 9-Br-Nos-Mβ-CD inclusion complex (c).

3.3.3.6. Thermogravimetric analysis (TGA)

Thermogravimetric analysis (TGA) and the derivative thermogravimetric (DTG) curves (Figure 3.4D) revealed distinct thermal degradation profiles for Mβ-CD, 9-Br-Nos, and their inclusion complexes. The onset of degradation was observed at 332 °C for Mβ-CD, 225 °C for 9-Br-Nos, and 211 °C for the complex. The DTG curve of Mβ-CD exhibited a single, sharp peak at 384 °C, indicating its maximum degradation rate. In contrast, 9-Br-Nos underwent multiple degradation steps, with the most prominent peak at 249 °C. However, the inclusion complex displayed a broad degradation peak, with a maximum rate at 357 °C, suggesting overlapping thermal events. The offset temperatures of degradation were recorded as 398 °C for Mβ-CD, 326 °C for 9-Br-Nos, and 380 °C for the inclusion complex. The residual masses (%) at the end of thermal decomposition were 6.5% for Mβ-CD, 42.7% for 9-Br-Nos, and 15.2% for the complex. These results indicate that the complex has intermediate thermal stability characteristics between those of pure Mβ-CD and 9-Br-Nos. This study further supports the findings from SEM morphology analysis.

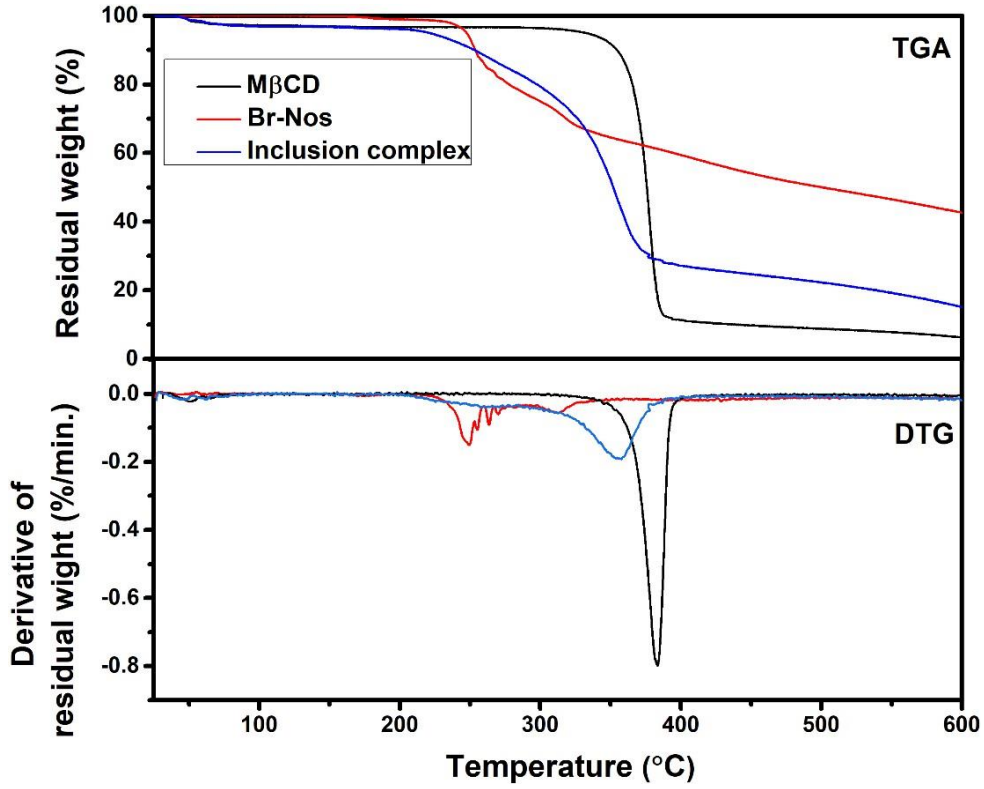

Figure 3.4. (D) TGA and DTG curve of Mβ-CD (a), 9-Br-Nos (b), 9-Br-Nos-Mβ-CD inclusion complex (c).

3.3.4. Cumulative release profile of 9-Br-Nos showing sustained release of the drug

The drug release profiles of 9-Br-Nos and their inclusion complexes are presented in Figure 3.5, which illustrates the cumulative drug release over time. The figure reveals a burst release of 9-Br-Nos, whereas the inclusion complex demonstrated sustained release, reaching 97.28% after 300 min ($p < 0.0001$). The sustained release behavior observed in the inclusion complex can be explained by the molecular encapsulation of the drug within the hydrophobic cavity of Mβ-CD. This encapsulation limits the direct interaction between the drug and the aqueous medium, thereby reducing the rate of dissolution. Moreover, the drug is retained within the cyclodextrin cavity through weak intermolecular forces such as hydrogen bonding and hydrophobic interactions, which further stabilize the complex and contribute to the sustained release profile. This suggests that the formation of the inclusion complex effectively slows the gradual release of 9-Br-Nos, a key factor in improving its efficacy for drug delivery applications. Furthermore, *in vitro* drug release profile of the inclusion complex was analysed via several kinetic models, such as zero-order, first- order, Higuchi, and Korsemeyer–Peppas models. Among these, dissolution exhibited the best fit to the first-order release model, as indicated by the highest correlation coefficient (R^2=0.9152), as represented in Table 3.2. This pattern of drug release aligns with sustained release behaviour, which contributes to prolonged therapeutic efficacy. This release

pattern aligns with previous studies on cyclodextrin-based inclusion complexes, such as the lidocaine/β-cyclodextrin inclusion complex reported by Abou-Okeila *et al*. (2018), (Abou-Okeil *et al*., 2018) which showed a first-order release profile. Another study reported by Yang *et al*. (2021) reported first-order release kinetics of the drug vorinostat from its β-cyclodextrin inclusion complex. (Yang *et al*., 2022)

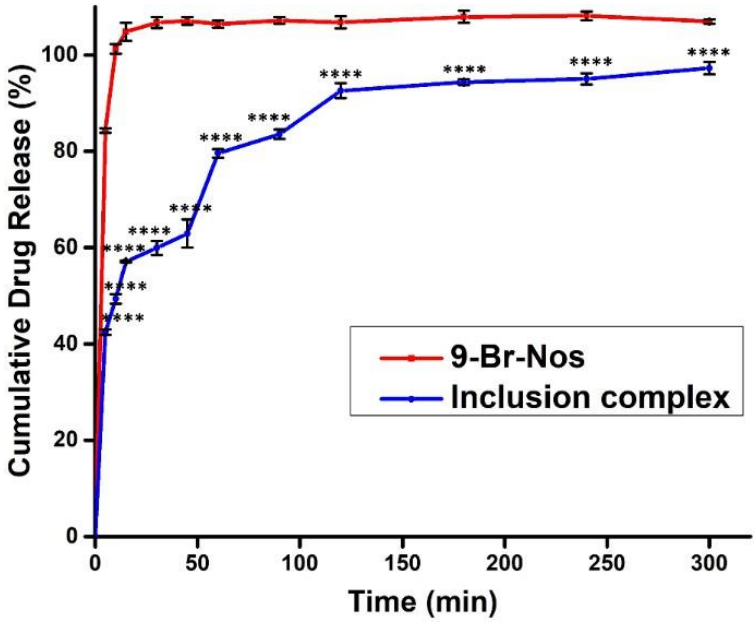

Figure 3.5. Cumulative release profiles of free 9-Br-Nos and 9-Br-Nos from their inclusion complexes (means±SDs, n=3). Two-way ANOVA was used to determine the statistical significance between groups, with **** $p < 0.0001$.

Table 3.2. Kinetics parameters for the release of 9-Br-Nos from the 9-Br-Nos-Mβ-CD inclusion complex.

Models	**Correlation coefficient R^2**
Zero order	0.5921
First-order	0.9152
Higuchi Model	0.8175
Korsmeyer-Peppas Model	0.6584

3.3.5. Evaluation of pharmacokinetic parameters in rats

In this study, quantitative determination of the 9-Br-Nos-Mβ-CD inclusion complex was conducted via UHPLC-Q-TOF/MS analysis. A calibration curve for the free drug (9-Br-Nos) was prepared by measuring concentrations ranging from 10 ng/mL to 250 ng/mL (Figure 3.6).

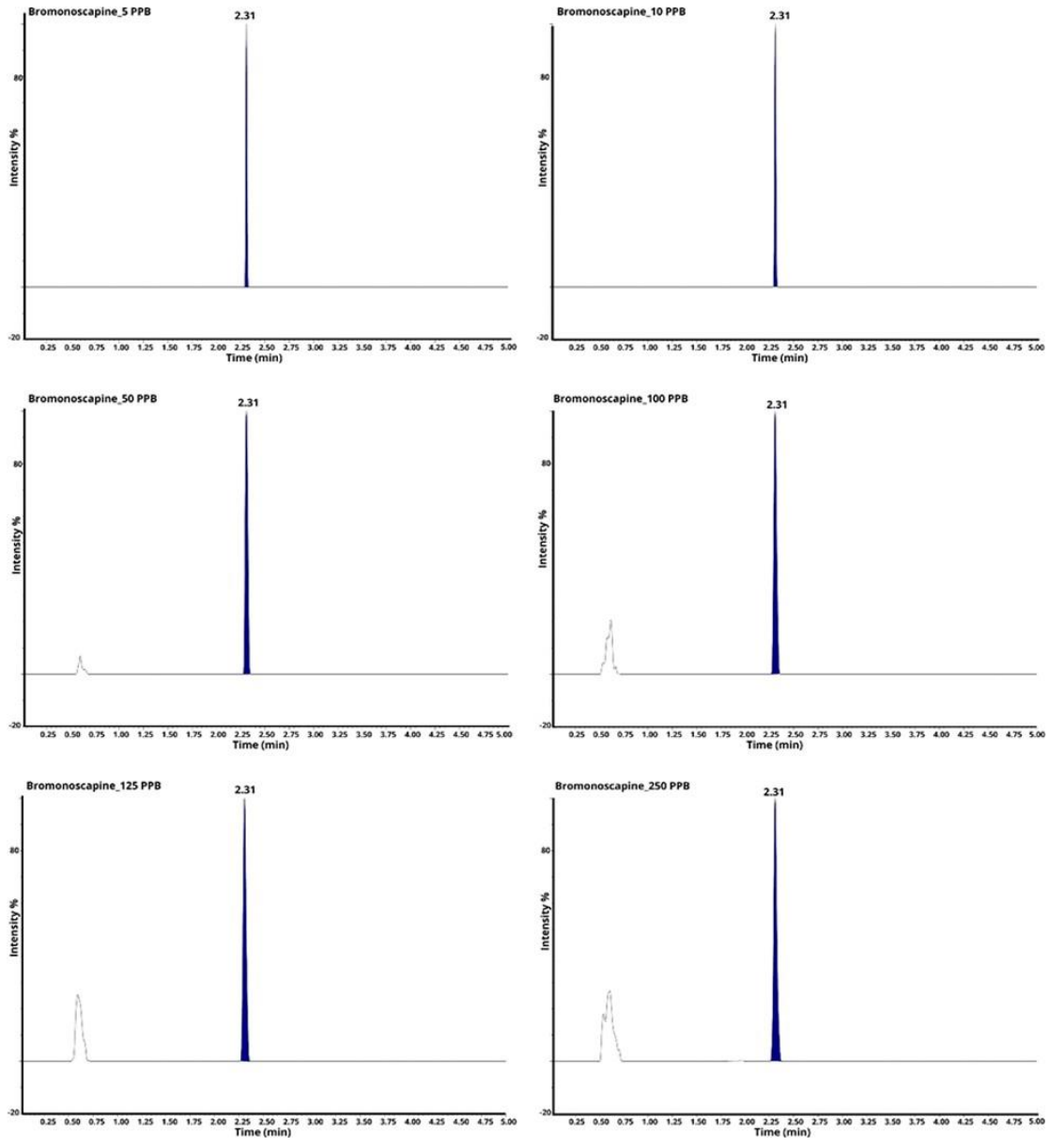

Figure 3.6. Chromatograms showing the separation of 9-Br-Nos at different concentrations via UHPLC-Q-TOF/MS. Each peak corresponds to the elution of 9-Br-Nos at various concentrations (10 ng/mL to 250 ng/mL).

Chromatograms of the plasma and urine samples collected from the rats at different time intervals are presented in Figure 3.7(A) and 3.7(B), respectively. To comprehensively evaluate the biological behavior of the inclusion complex, we analysed its pharmacokinetics and excretion profile (Figure 3.7(D)) and conducted a histopathological study. The mean plasma concentration versus time for the 9-Br-Nos-Mβ-CD complex is shown in Figure 3.7(C), and the pharmacokinetic parameters are detailed in Table 3.3. The present study revealed a higher concentration of 9-Br-Nos in the plasma within 6 hours of administration of the inclusion complex than the significantly lower concentration in the free drug-treated group, i.e., 11.58 ng/mL (t_6=3.311, P<0.05). The higher concentration of the drug was maintained for up to 48 hours following the administration of the inclusion complex, whereas in the free drug-treated group, the plasma concentration decreased significantly within 24 hours, indicating a sustained drug release mechanism. The sustained release mechanism of 9-Br-Nos from the inclusion complex can be attributed to its molecular encapsulation within the hydrophobic cavity of Mβ-CD, which prevents it from burst release. This encapsulation slows the diffusion and absorption of the drug, which results in prolonged retention time in the plasma for up to 48 hours, whereas the free drug 9-Br-Nos was rapidly cleared within approximately 24 hours. This result indicated the increased bioavailability of 9-Br-Nos upon the formation of an inclusion complex. This finding corroborated other studies, such as that of Yao *et al*. (2020), where the pharmacokinetic profile of didymin was evaluated via a cyclodextrin-based inclusion complex. (Yao *et al*., 2020) Similarly, Ye *et al*. (2015) reported improved delivery and controlled release of the poorly water-soluble drug paclitaxel in the form of paclitaxel/dimethyl-β-cyclodextrin inclusion complexes loaded with chitosan nanoparticles. (Y. J. Ye *et al*., 2015) Furthermore, the clearance rate of 9-Br-Nos in the case of the inclusion complex-treated group increased gradually until 48 hours, whereas in the case of the free 9-Br-Nos-administered group, the clearance rate was significantly faster, as evidenced by the lower concentration of drug detected in the urine within 48 hours of administration. This indicated that the complex exhibited low accumulation in the body and relatively rapid excretion *in vivo*. The pharmacokinetic parameters were calculated using Phoenix WinNonlin software. The C_{max} and T_{max} of the inclusion complex in blood plasma were determined to be 18.21 ng/mL and 6 hours, respectively, with a clearance rate of 15.75 mL/hr/kg. Additionally, following oral administration of the 9-Br-Nos-Mβ-CD inclusion complex, the AUC_{0-t} and $AUC_{0-\infty}$ values were 520.11 and 1094.29 ng/h, respectively, whereas the half-life was calculated to be 45.8 hours, indicating a greater volume of distribution than that of 9-Br-Nos. These findings suggest

that the described analytical approach is effective for assessing the pharmacokinetics of 9-Br-Nos in rats and may be applicable to other *in vivo* models. Moreover, the creation of the 9-Br-Nos-Mβ-CD inclusion complex significantly increased the oral bioavailability of 9-Br-Nos.

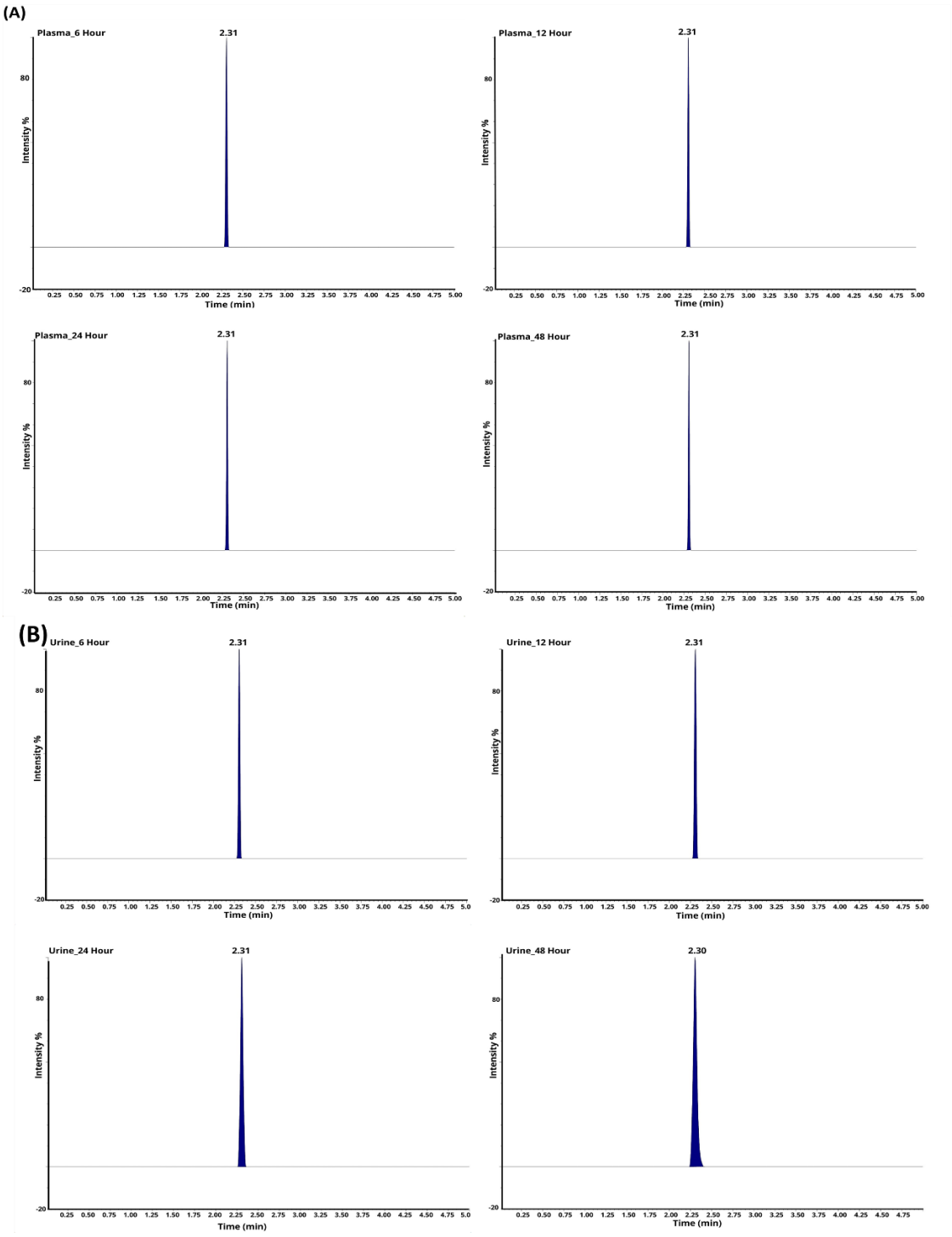

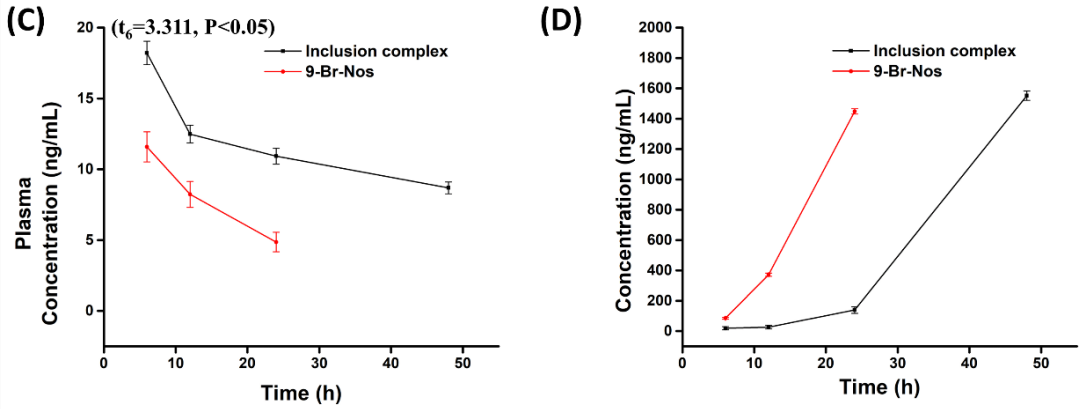

Figure 3.7. Chromatograms showing the separation of 9-Br-Nos at different concentrations via UHPLC-Q-TOF/MS. (A) MRM chromatograms of the plasma concentration over time following oral administration of the 9-Br-Nos-Mβ-CD complex at 6, 12, 24, and 48 h. (B) MRM chromatograms of urine concentration with time following oral administration of the 9-Br-Nos-Mβ-CD complex at 6, 12, 24, and 48 h. (C) Plasma concentration–time plot and (D) Urine concentration-time plot of 9-Br-Nos and its inclusion complex after oral delivery in SD rats (mean± SD, n=3). The data revealed a significant difference (t_6=3.311, P<0.05) in the bioavailability of 9-Br-Nos in free drug- and inclusion complex-treated rats.

Table 3.3. Pharmacokinetic parameters (means± SDs, n=3) of the inclusion complexes.

Pharmacokinetic parameters	**9-Br-Nos**	**9-Br-Nos-Mβ-CD inclusion complex**	**p value**
C_{max} (ng/mL)	11.58±1.06	18.21±1.82	<0.0001
T_{max} (hr)	6.00±1.56	6.00±0.86	>0.05
AUC_{0-t} (ng hr/mL)	217.92±18.22	520.11±25.66	<0.0001
$AUC_{0-\infty}$ (ng hr/mL)	319.97±71.07	1094.29±90.18	<0.0001
CL (mL/hr/kg)	37.92±1.07	15.75±0.94	<0.0001
Vd (mL/kg)	796.37±51.82	1040.34±78.23	<0.01
$t_{1/2}$ (hr)	14.55±2.82	45.80±4.5	<0.0001

C_{max}: Maximum plasma concentration, T_{max}: Time to reach maximum plasma concentration, AUC_{0-t}: Area under the concentration–time curve from time 0 to t, $AUC_{0-\infty}$: Area under the concentration–time curve from time 0 to ∞, CL: Clearance, Vd: Volume of distribution, $t_{1/2}$: Half-time

3.3.6. Histopathological alteration in vital organs following administration of the 9-Br-Nos-Mβ-CD inclusion complex using H&E staining and Hoechst staining

Vital organs, such as brain, heart, liver, kidney, and lung tissues, were stained with hematoxylin & eosin and Hoechst 33342 to assess morphological alterations and chromatin condensation following 48 hours of administration of the 9-Br-Nos-Mβ-CD complex. The results of the present study revealed no significant morphological alterations in any of the vital organs studied, as indicated by H&E staining (Figure 3.8(A)). Histological analysis of cardiac muscle in the heart tissue of the control and inclusion complex-treated groups revealed no significant alterations in the morphology of cardiomyocytes. The cross-striated muscle cells presented prominent central nuclei with junctions between cells called intercalated discs. Additionally, no enhanced cytoplasmic vacuolization or myofibrillar loss was observed in either group, as shown in a and b. Similarly, in c and d, the morphological features of nerve cells in the cortical tissue of both the control and treated groups were not significantly different. The circular cell body and intact nucleus indicated normal cellular morphology with no pycnosis. or neuronal loss following the administration of the inclusion complex. In the kidneys, the morphology of the nephrons in both the treated and control groups was similar, with no significant glomerular/tubular renal atrophy. Tubular epithelial cells were also circular and dense in population in both groups, as shown in e and f. The liver parenchyma cells, sinusoids and morphology of Kupffer cells were not markedly different between the control and treated groups. Additionally, no significant neutrophil infiltration or necrosis was observed in either group (g and h). Morphological analysis of lung tissue from both groups also revealed no significant alterations in the micromorphology of the alveoli. Furthermore, no significant congestion of pulmonary capillaries with erythrocytes was noted in any of the groups. Furthermore, no alveolar septal thickening or hypercellularity was observed in either the control or treated groups (i and j). (Abbas *et al.*, 2022) No significant differences in the number of Hoechst-positive cells in any of the vital organs were observed 48 hours after administration of the 9-Br-Nos-Mβ-CD complex compared with the control group, as represented in Figure 3.8(B) and 3.8(C) (t_8=0.114, P>0.05). In summary, our study revealed that the 9-Br-Nos-Mβ-CD inclusion complex is not toxic to any of the vital organs, even at relatively high concentrations (6.5 μg/mL). In support of our findings, several reports have indicated that the parent molecule noscapine, even at 1.5–3 mg/mL, and several derivatives showing potent anticancer activities have been reported to cause no significant morphological changes in any of the vital organs. (Ke *et al*., 2000)

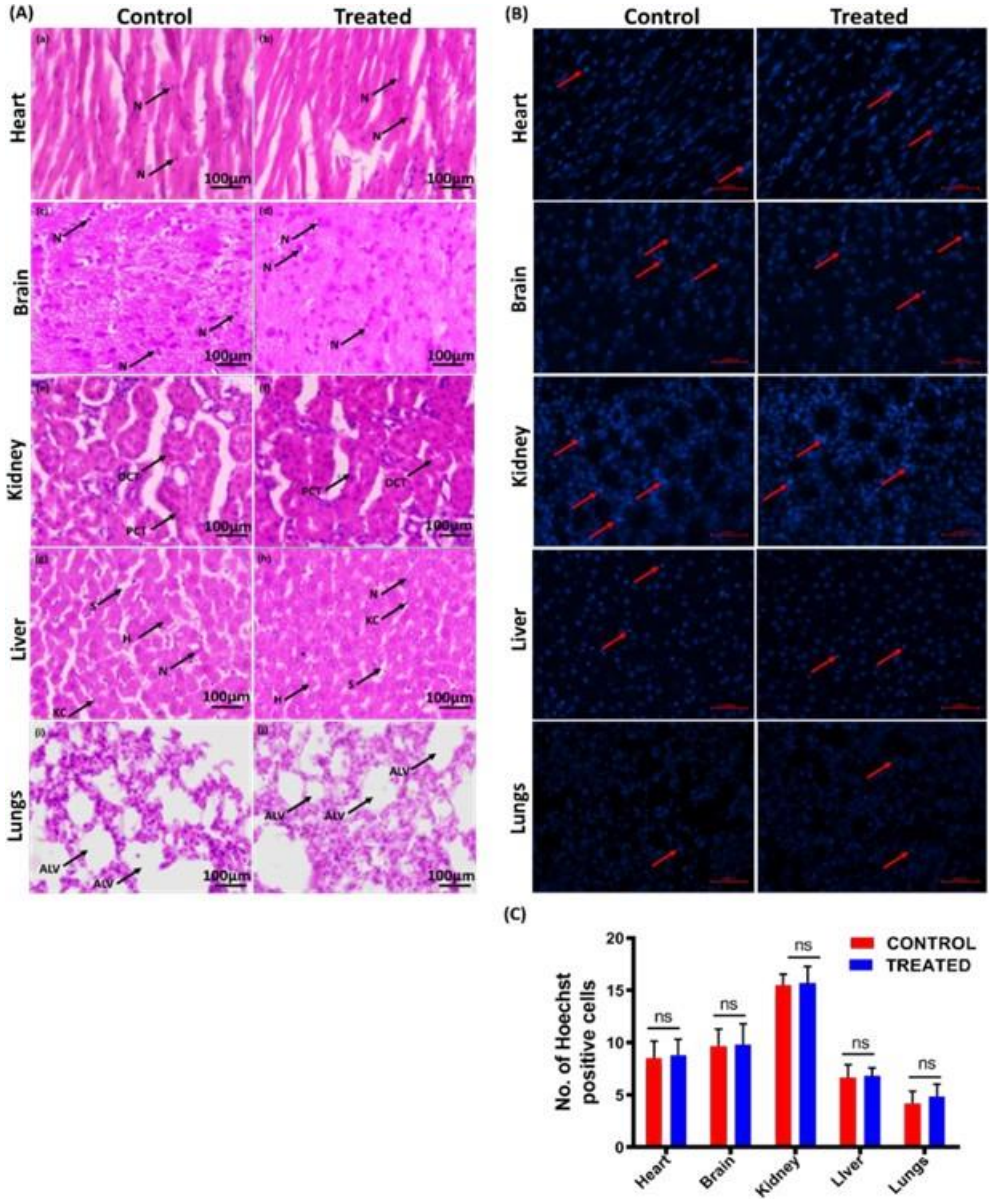

Figure 3.8. (A) Representative images of tissues from vital organs (heart, brain, kidney, liver, and lungs) after H&E staining (magnification: 40x; scale bar: 100 µm), where N: nuclei, PCT: proximal convoluted tubule, DCT: distal convoluted tubule, S: sinusoid, H: hepatocyte, KC: Kupffer cell, and ALV: alveoli. (B) Representative images of tissues from vital organs (heart, brain, kidney, liver, and lungs) after Hoechst 33342 staining (magnification: 40x; scale bar: 50 µm). (C) Graph depicting alterations in the number of Hoechst-positive cells following 9-Br-Nos-Mβ-CD inclusion complex treatment in rats. Student's t test was performed, and values are expressed as the means ± SEMs ($t_8 = 0.114$, $P > 0.05$, n=3), where ns represents no significant differences in any of the vital organs.

3.3.7. Assessment of cell viability via the MTT assay

The MTT assay was used to assess the viability of the synthesized inclusion complex of 9-Br-Nos with Mβ-CD, along with the free drug, on MDA-MB-231 and MCF-7 breast cancer cells. The cells were then treated with range of concentrations (1–100 µg/mL) of both the free drug and the inclusion complex. The results, presented in Figure 3.9, highlight significant differences in efficacy. As depicted in Figure 3.9(A), the inclusion complex exhibited a notably lower IC_{50} value of 12.87 µg/mL in MDA-MB-231 cells than the substantially higher IC_{50} value of approximately 200 µg/mL for the free drug. Similarly, in MCF-7 cells (Figure 3.9B), the inclusion complex demonstrated a low IC_{50} value of 13.07 µg/mL, which was markedly lower than the free drug's IC_{50} value of approximately 150 µg/mL (*$p<0.05$, **$p<0.01$, ***$p<0.001$, ****$p<0.0001$ compared with the control group and #$p<0.05$, ##$p<0.01$, ###$p<0.001$, ####$p<0.0001$ compared with the drug-treated groups). Furthermore, comprehensive statistical analysis revealed that the inclusion complex had a significantly greater cytotoxic effect on breast cancer cell lines at lower concentrations. Since weakly basic drugs ionize in acidic media, they remain undissociated at neutral or basic pH values, allowing them to passively diffuse. 9-Br-Nos is a weakly basic drug that requires a basic medium to remain in its unionized state for better absorption. Thus, the inclusion complex formation with Mβ-CD improved the solubility, thereby resulting in sustained release compared with that of the pure drug. (Bomzan *et al*., 2021) Consistent with the findings from the drug release study, the inclusion complex facilitated better absorption of 9-Br-Nos across different concentrations *in vitro*, thereby enhancing the inhibitory effect of 9-Br-Nos on cancer cell proliferation at IC_{50} values significantly lower than those of the free drug. (Ren *et al.*, 2019) This suggested that the inclusion complex enhanced the diffusion of 9-Br-Nos across the cell membrane, as the drug remained in a soluble and unionized state at neutral pH.

3.3.8. Assessment of chromatin condensation in cancer cells via Hoechst staining

Hoechst staining was conducted to observe nuclear morphological changes, identifying characteristic features such as chromatin condensation and nuclear fragmentation, which serve as preliminary markers of apoptosis. In normal, healthy cells, the nuclei typically (K. Ye *et al.*, 1998) exhibit a spherical shape with evenly distributed DNA. However, in the apoptotic process, DNA condensation occurs. Therefore, the nuclear condensation serves as a distinguishing feature, allowing for the differentiation between apoptotic cells and either type of healthy cells.

Our study revealed that treatment with 9-Br-Nos and the 9-Br-Nos- Mβ-CD inclusion complex induced chromatin condensation in both MDA-MB-231 and MCF-7 cells after 24 hours (Figure 3.9(C)). The apoptotic MDA-MB-231 cells ($F_{2,15}$=75.67, P < 0.0001) and MCF-7 cells ($F_{2,15}$ =99.79, P < 0.0001) presented highly condensed and fragmented nuclei, as shown in Figure 3.9(D) & 3.9(E). The number of Hoechst-positive cells among the control cells and the cells treated with only 9-Br-Nos was significantly lower (p < 0.01) than that among the cells treated with the inclusion complex (p < 0.0001). This result validated the results from the previous MTT assay, which revealed apoptotic changes such as chromatin condensation and nuclear fragmentation in both types of cancer cells treated with the 9-Br-Nos-Mβ-CD inclusion complex.

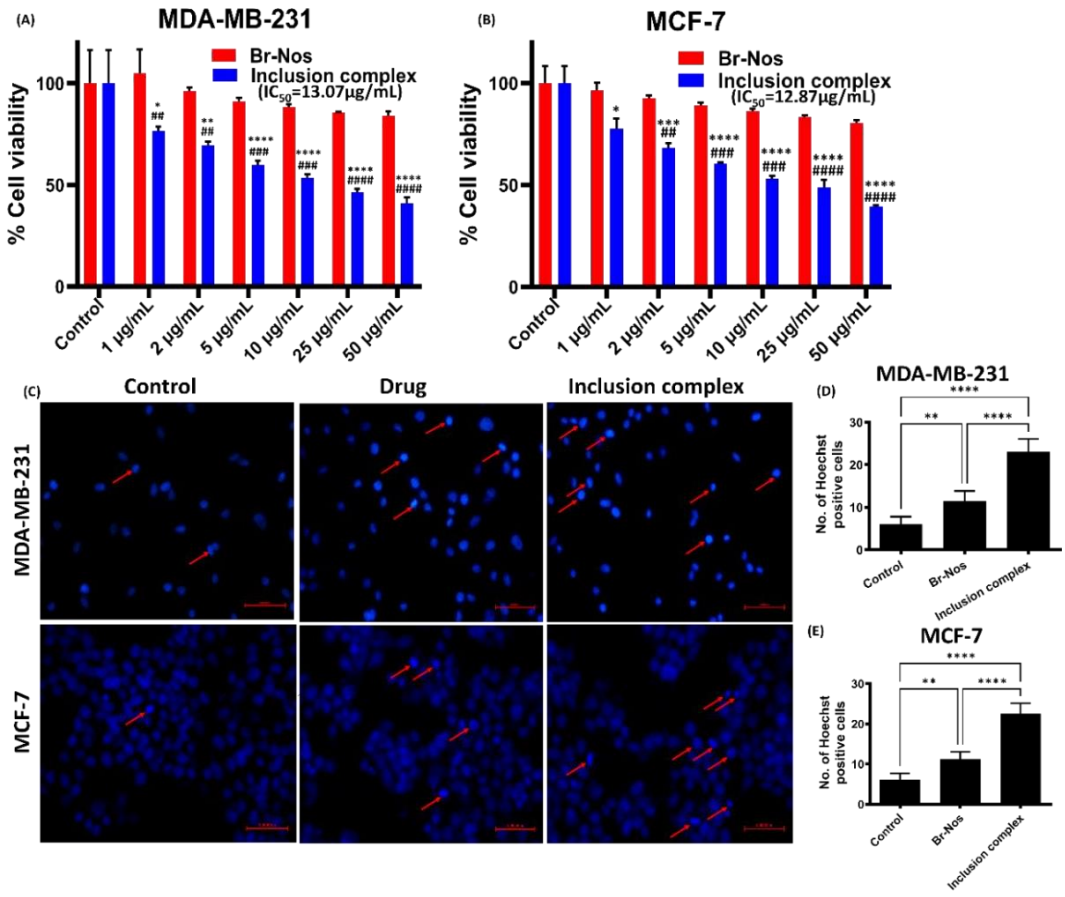

Figure 3.9. (A) Cytotoxicity of 9-Br-Nos (IC_{50}: 12.87 µg/mL) and inclusion complex (IC_{50}:~ 200 µg/mL) in MDA-MB-231 and (B) MCF-7 (IC_{50}: 12.87 µg/mL for 9-Br-Nos and for inclusion complex IC_{50}:~ 150 µg/mL) breast cancer cells. The cells were treated with 9-Br-Nos and the inclusion complex for 48 h. Cell growth was evaluated via the MTT assay. The data are expressed as the means ± SDs. *p<0.05, **p<0.01, ***p<0.001, ****p<0.0001 compared with the control group and #p<0.05, ##p<0.01, ###p<0.001, ####p<0.0001 compared with the drug-treated groups. Chromatin condensation by Hoechst staining. (C) Representative image (n=6) of MDA-MB-231 and MCF-7 cells after

Hoechst 33342 staining. Arrowheads depict the cells that are Hoechst positive; magnification and scale bar: 40x corresponds to 50 µm in different experimental groups. (D) Graph depicting alterations in the number of Hoechst-positive cells (n=6) following 9-Br-Nos and 9-Br-Nos-Mβ-CD inclusion complex treatment in MDA-MB-231 cells and (E) MCF-7 cells. The values are expressed as the means ± SEMs. One-way ANOVA was used to determine the statistical significance of differences between groups, with **p<0.01 and **** p< 0.0001.

3.3.9. The 9-Br-Nos-MβCD inclusion complex increased the expression of cleaved caspase-3, p-JNK, and bax in MDA-MB-231 cells

Western blot analysis revealed that both 9-Br-Nos and their inclusion complexes increased the expression of proapoptotic proteins, such as cleaved caspase-3, phospho-c-Jun N-terminal kinase (p-JNK), and bax, in MDA-MB-231 cells (Figure 3.10(A)). Cleaved caspase-3 is a critical executioner caspase in the apoptotic process. Its activation leads to the cleavage of various substrates involved in cell survival and proliferation, ultimately driving the cell to undergo programmed death. The increase in cleaved caspase-3 expression observed upon treatment with the 9-Br-Nos-Mβ-CD inclusion complex indicated the activation of the intrinsic apoptotic pathway and suggested that this compound may promote apoptosis in MDA-MB-231 cells, as indicated in Figure 3.10(B) ($p < 0.0001$). This finding is consistent with previous studies indicating that various proapoptotic agents can enhance caspase-3 activation, contributing to the cytotoxic effects observed in cancer cells. Additionally, the upregulation of p-JNK in response to the inclusion complex indicates that the JNK signalling pathway may play an essential role in mediating the apoptotic effects ($p < 0.0001$). This finding implies the involvement of stress-activated mitogen-activated protein kinase (MAPK) signalling in mediating drug-induced apoptosis. The phosphorylation of JNK has been linked to both apoptosis and cell survival, with the ultimate outcome depending on the cellular context and chemotherapeutic stress. (Yu *et al.*, 2004) The observed increase in p-JNK suggested that the 9-Br-Nos-MβCD inclusion complex may activate this pathway, which in turn could contribute to the promotion of apoptosis in MDA-MB-231 cells (Figure 3.10(C)). The JNK pathway also contributes to apoptosis by promoting the transcription of proapoptotic genes such as Bax. Moreover, the overexpression of Bax, which is a proapoptotic member of the Bcl-2 family, further supports the proapoptotic effects of the inclusion complex. Bax is known to facilitate the permeabilization of the outer membrane of mitochondria, which releases cytochrome c, which binds to Apaf-1 to form the apoptosome and activates caspase 9. Activated caspase-9 subsequently cleaves and activates the downstream

executioner caspase, caspase-3, which causes proteolytic degradation of cellular components, ultimately leading to apoptosis. (Garrido *et al*., 2006) The increased expression of Bax suggested that the 9-Br-Nos-MβCD inclusion complex may induce mitochondria-mediated apoptosis in these cells ($p < 0.0001$), as represented in Figure 3.10(D). Taken together, these protein expression changes suggest that the 9-Br-Nos-MβCD inclusion complex affects MDA-MB-231 cells by activating multiple intrinsic proapoptotic pathways, including the caspase cascade, the JNK signalling pathway, and mitochondrial dysfunction, ultimately leading to programmed cell death. These results provide promising evidence that the 9-Br-Nos-MβCD inclusion complex may serve as a potential therapeutic agent in the treatment of breast cancer, particularly in targeting apoptosis-resistant cancer cells.

3.3.10. Apoptosis analysis by flow cytometry using Annexin V-FITC/PI staining

The induction of apoptotic cell death in breast cancer cells by the drug 9-Br-Nos and its inclusion complex with Mβ-CD was evaluated through FACS analysis. Apoptosis is characterized by changes in the lipid composition of the cell membrane, including the translocation of phosphatidylserine from the inner to the outer leaflet, which can be detected by Annexin V binding. In contrast, the membrane-impermeable fluorescent dye propidium iodide (PI) only enters cells during late apoptosis, when membrane integrity is compromised. The percentages of MDA-MB-231 cells in early and late apoptosis are shown in Figure 3.10(E). Owing to a lack of solubility and bioavailability, 60.97% of the apoptotic cells (early and late apoptotic) were found with the free drug 9-Br-Nos, whereas the percentage of apoptotic cells significantly increased to 92.9% when the cells were treated with the 9-Br-Nos-Mβ-CD inclusion complex ($p< 0.0001$) (Figure 3.10(F)). The substantial increase in the apoptotic population suggests that the inclusion complex of 9-Br-Nos not only improves the solubility of 9-Br-Nos but also enhances their cellular uptake and cell membrane interaction, amplifying apoptotic signalling. This result was consistent with the western blot analysis, where treatment with the 9-Br-Nos-Mβ-CD inclusion complex induced apoptosis in MDA-MB-231 cells by increasing the expression of key proapoptotic markers. Together, these results indicate that the inclusion complex promotes apoptosis through both improved drug delivery and the activation of intrinsic apoptotic pathways.

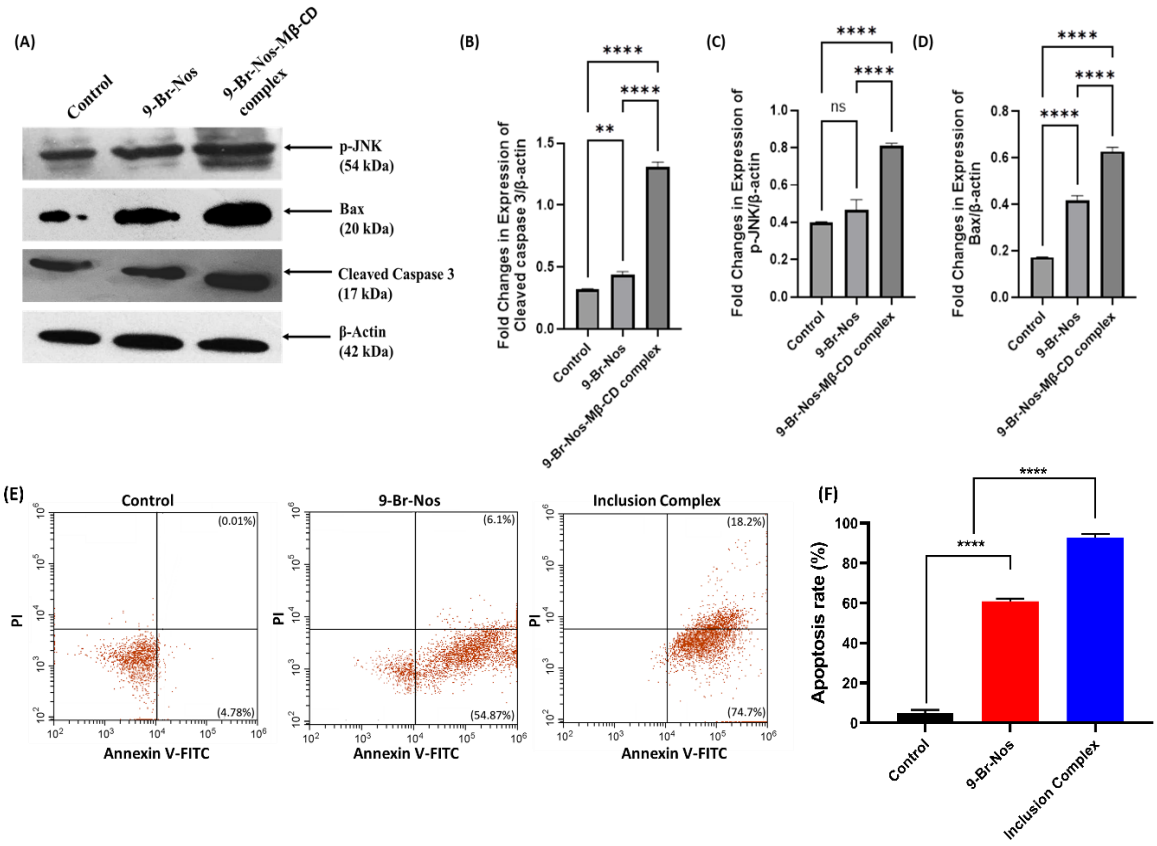

Figure 3.10. (A) Representative Western blot images of cleaved caspase-3, Bax, and p-JNK expression and quantitative evaluation of relative protein expression in MDA-MB-231 cells. MDA-MB-231 cells were treated with 9-Br-Nos-Mβ-CD and 9-Br-Nos for 48 hours. (B, C and D) Differences between treatment groups were assessed via ANOVA, with ** $p < 0.01$ and **** $p < 0.0001$ indicating statistically significant differences. (E) Apoptosis analysis by flow cytometry using Annexin V-FITC/PI staining. Representative scatter plots depict the distribution of cells in different apoptotic stages: live cells (annexin V-/PI-), early apoptotic cells (annexin V+/PI-), late apoptotic/necrotic cells (annexin V+/PI+), and necrotic cells (annexin V-/PI+). The data are shown for the untreated control and treated samples. (F) Quantitative analysis of the percentage of apoptotic MDA-MB-231 cells. One-way ANOVA was used to determine the statistical significance between groups, with **** $p< 0.0001$.

3.4. Conclusion

In summary, we showed the successful encapsulation of 9-Br-Nos within the hydrophobic cavity of Mβ-CD by the formation of an inclusion complex. By utilizing a comprehensive approach that includes computational studies, spectral and analytical techniques, characterization methods, and *in vitro* evaluations, our findings provide robust evidence that cyclodextrin-based inclusion complexes enhance the physicochemical and biological properties of the drug. As compared with the free drug, the inclusion complex exhibited improved solubility, sustained drug release, and notable cytotoxicity against both the MCF-7 and the MDA-MB-231 breast cancer cell lines. Furthermore, promising *in vivo* pharmacokinetic studies in rats revealed prolonged circulation time and efficient elimination through plasma and urine. This study highlighted the significant impact of the inclusion complex on biological processes, suggesting that further *in vivo* investigations into tumor regression could offer critical insights, paving the way for scaling up this technology for breast cancer therapy. With this concept, other hydrophobic drugs could be encapsulated to prepare inclusion complexes for their sustainable delivery. Furthermore, different cavity sizes of cyclodextrin can be used for designing efficient drug delivery systems.

CHAPTER-4

Development of a FA-PLGA-PEG loaded 3-Br-Benzyl-Noscapine nanoparticle for targeted delivery into breast cancer cell lines: chemical synthesis and experimental validation

Abstract

Folate-conjugated PLGA-PEG (FPP) nanocarrier is a promising strategy for targeted delivery of drug to enhanced anticancer efficacy by selective targeting of folate receptors, which are commonly overexpressed in breast cancer cells. In this study, molecular docking and modeling studies were first performed to assess the binding affinity and interaction profile of N-3-Br-benzyl-noscapine with tubulin, confirming its strong potential as a microtubule-interfering agent. The noscapine derivative, N-3-Br-benzyl-noscapine was then encapsulated into FPP nanocarrier by co-precipitation method and evaluated its anticancer potential. DLS analysis of the nanocarrier revealed a hydrodynamic diameter of 155 ± 2 nm and a PDI of 0.27, indicating a uniform nanosize and suitability for tumor targeting via folate receptor-mediated uptake. Further, SEM images revealed aggregated spherical particles with a uniform distribution, suggesting good formulation stability. The cytotoxic potential of the FPP loaded with 3-Br-Bn-Nos was assessed in MDA-MB-231, T47D, and MCF-7 breast cancer cell lines and demonstrated a concentration-dependent reduction in cell viability. Against MDA-MB-231, MCF-7 and T47D cell lines, the IC_{50} values of FPP loaded 3-Br-Bn-Nos were found to be 37.2, 28.9 and 22.7 µg/mL, respectively which were significantly outperforming free 3-Br-Bn-Nos (IC_{50} values were 73.6, 59.8 and 54.1µg/mL, respectively). Cellular studies further revealed improved uptake of 3-Br-Bn-Nos by nanocarrier and disruption of the mitochondrial membrane potential, increased reactive oxygen species (ROS) generation and induction of apoptosis to cancer cells. In addition, a spheroid disintegration assay using a 3D tumor model mimicking the tumor microenvironment revealed partial shrinkage by day 5, with a noticeable but moderate reduction in overall size and density. Furthermore, *in vivo* toxicity assessment was conducted in rats to evaluate the safety of the formulation. Both acute and subacute toxicity studies confirmed that the FPP loaded 3-Br-Bn-Nos was well tolerated at the administered dose and exhibited no significant systemic toxicity.

Keywords: Breast cancer; FA-PLGA-PEG nanocarrier; Folate receptor; N-3-Br-benzyl-noscapine; 3D spheroid.

4.1. Introduction

Advancements in nanomedicine have transformed the landscape of modern pharmacotherapy by offering innovative solutions for drug delivery challenges, particularly in oncology. Among the diverse nanocarrier systems, polymeric nanoparticles (PNs) have garnered significant attention because of their ability to encapsulate hydrophobic drugs, enhance their solubility, provide controlled release, and offer site-specific targeting.(Patra *et al*., 2018; Peer *et al*., 2007) These nanosystems, especially those designed with tunable size and surface characteristics, exploit the enhanced permeability and retention (EPR) effect, allowing for passive accumulation in tumor tissues. (Chehelgerdi *et al*., 2023; He *et al*., 2020) Moreover, surface functionalization with targeting ligands further refines their selectivity, enabling active targeting of tumor-specific biomarkers while minimizing systemic toxicity. (Bajracharya *et al*., 2022)

A well-established example of such a nanocarrier system is poly(lactic-co-glycolic acid) (PLGA), which is functionalized with polyethylene glycol (PEG) and folic acid (FA). This tri-block configuration (FA-PLGA-PEG) offers several advantages: PEG improves the pharmacokinetic profile by evading immune clearance, whereas FA facilitates active targeting via folate receptor-mediated endocytosis, which is particularly relevant in breast and ovarian cancers, where folate receptors are commonly overexpressed. (Chen *et al*., 2017; Makadia & Siegel, 2011; Yoo & Park, 2004) In contrast, these receptors are largely absent in normal tissues, reducing off-target uptake and associated toxicity.

In this study we have selected one of our previously developed halogenated derivatives of the natural alkaloid noscapine i.e. N-3-Br-benzyl-noscapine (3-Br-Bn-Nos) (Figure 4.1) for targeted delivery to cancer cell lines. It has been established as a potent microtubule-targeting agent that induced mitotic arrest and apoptosis, making it a promising candidate for cancer therapy. (Dash *et al*., 2021) However, its poor aqueous solubility and potential systemic toxicity limit its clinical translation (Calaf *et al*., 2024; Kumar *et al*., 2022). While previous approaches, such as cyclodextrin complexation and lipid-based formulations, have been employed to address these limitations in colon and lung cancers, respectively, a folate-targeted polymeric system (FA-PLGA-PEG) has not yet been explored. (Gandhi & Roy, 2023; Madan *et al*., 2010)

To address this gap, the present study focuses on the design, *in silico* molecular modelling, synthesis, and evaluation of PLGA-PEG-FA (FPP) nanoparticles encapsulating 3-BrBn-Nos for targeted breast cancer therapy. The FPP nanocarrier was developed via an emulsion–solvent evaporation technique and optimized for high drug loading, and sustained release. The incorporation of folic acid as a surface ligand aims to increase selective uptake by cancer cells while reducing systemic side effects. This work not only introduces a novel formulation strategy for 3-Br-Bn-Nos but also demonstrates the utility of receptor-mediated nanocarrier systems in enhancing the therapeutic index of poorly soluble anticancer agents.

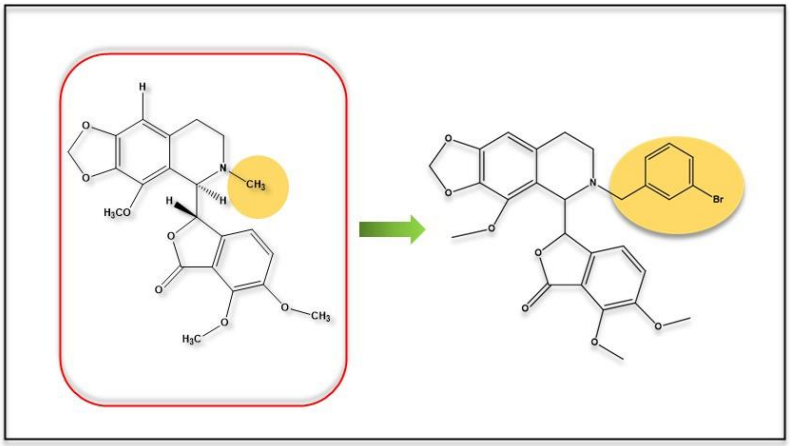

Figure 4.1. Schematic representation of the structural modification of noscapine to obtain 3-bromobenzyl-substituted N-imidazopyridine noscapinoid (3-Br-Bn-Nos).

4.2. Materials and Methods

4.2.1. *In Silico* Evaluation of 3-Br-Bn-Nos as a Tubulin-Binding Anticancer Agent

4.2.1.1. Ligand preparation

The molecular structures of 3-BrBn-Nos were designed using the molecular builder tool in Maestro (version 8.5). These chemical structures were initially energy-minimized in a vacuum environment using Impact (version 5.6, Schrödinger, LLC). Bond orders were properly assigned with the help of LigPrep (version 2.4, Schrödinger, LLC), and preliminary optimization was carried out using the OPLS 2005 force field under default settings. Comprehensive geometrical optimization of the ligands was performed using hybrid density functional theory (DFT), employing the B3LYP functional that integrates Becke's three-parameter exchange with the Lee–Yang–Parr correlation functionals. (Binkley *et al.*, 1980; Gordon *et al.*, 1982; Pietro *et al.*, 1982) These calculations were executed using the 3-21G* basis set. Final geometry optimizations were performed using Jaguar (version 7.7, Schrödinger, LLC).

4.2.1.2. Protein preparation

The crystal structure of the 3-BrBn-Nos-tubulin complex (PDB ID: 6Y6D, resolution 2.20 Å) was utilized for molecular docking and rescoring analysis. Following a thorough inspection and refinement, both chains 'A' and 'B' of the protein were retained in the final configuration. Hydrogen atoms were added using the Maestro interface (version 8.5, Schrödinger, LLC), ensuring the application of a full all-atom representation and the removal of any lone pairs. All water molecules present in the structure were eliminated. Protein preparation was carried out using Schrödinger's Protein Preparation Wizard (PPrep), which follows a multi-step process. Energy minimization was performed using the OPLS 2005 force field and the Polak–Ribiere Conjugate Gradient (PRCG) method. The minimization was halted after reaching either 5,000 iterations or when the energy gradient was reduced below 0.001 kcal/mol. (Santoshi & Naik, 2014)

4.2.1.3. Molecular docking

Glide (version 4.5, Schrödinger, LLC) was employed to perform molecular docking of all ligands into the tubulin receptor structure. (Friesner *et al*., 2004; Halgren *et al*., 2004) The receptor grid was generated by using the grid generation tool, applying a van der Waals scaling factor of 0.4 Å after ensuring that both receptor and ligands were appropriately prepared for docking. Binding site coordinates were defined using SiteMap (version 2.4, Schrödinger, LLC), with the bounding and enclosing boxes centered at the predicted binding site centroid, each with a grid size of 10 Å. Initial docking was carried out using the "standard precision" (SP) method, followed by refinement using the "extra precision" (XP) algorithm within Glide. During the docking process, the van der Waals radii for the ligands were scaled to 0.4 Å. Out of 50,000 initially sampled ligand poses, 4,000 were energy minimized using 1,000 steps of the conjugate gradient method. From this set, the 30 lowest-energy poses were selected based on their Glide docking scores, and the top-ranked conformation for each of the ligand was subsequently selected for further rescoring. (Cross *et al*., 2009)

4.2.1.4. Molecular dynamic simulation

Molecular dynamics (MD) simulations were conducted using GROMACS version 2019.2 to analyze the stability and interactions of the tubulin–noscapinoid complexes, along with associated GTP, GDP, and Mg^{2+} ions. (Abraham *et al*., 2015) The ligand-receptor complexes with the lowest binding energies from docking studies were selected for simulation. The tubulin protein was modeled using the Amber99SB force field, (Hornak et

al., 2006) while the ligands (noscapinoids, GTP, and GDP) were parameterized using the General Amber Force Field (GAFF) through the Antechamber module in Amber 18. Partial atomic charges for the ligands were computed using the AM1-BCC method. (Jakalian *et al*., 2002) Ligand topologies and coordinates were generated using Amber's tleap and ACPYPE tools. The entire system was solvated in a truncated octahedral TIP3P water box, ensuring a 12 Å distance between solute and box edges. (Kumar Pedapati *et al*., 2023) To mimic physiological conditions, the system was neutralized with counterions and set to an ionic strength of 0.15 M. Energy minimization was performed using 10,000 steps of the steepest descent algorithm to eliminate steric clashes. This was followed by a two-step equilibration: a 500 ps constant volume (NVT) simulation at 300 K, then a constant pressure (NPT) phase with position restraints (10 kcal/mol·Å^2) using the Martyna-Tobias-Klein barostat to maintain pressure at 1 bar. A 100 ns production run was then executed with a 2 fs time step. Electrostatic interactions were treated using the Particle Mesh Ewald (PME) method, with a 10 Å cutoff for both van der Waals and short-range electrostatics. All covalent bonds involving hydrogen atoms were constrained using the SHAKE algorithm, (Ryckaert *et al*., 1977) and temperature control was maintained via the Nose-Hoover chain thermostat. System coordinates were saved every 20 ps. Post-simulation analyses, including root mean square deviation (RMSD), and root mean square fluctuation (RMSF), were performed using built-in GROMACS utilities, and the results were visualized with GRACE software. The lowest-energy conformers from the MD trajectory were further analyzed to interpret ligand binding modes.

4.2.1.5. ADME Property prediction

The ADME (absorption, distribution, metabolism, and excretion) properties of 3-Br-Bn-Nos was evaluated using QikProp, which calculates 44 pharmacokinetic descriptors. Any parameters yielding a value of zero were omitted from the analysis. Additionally, the drug-likeness of the compounds was assessed by examining their compliance with Lipinski's Rule of Five, based on the number of violations observed.

4.2.2. Chemicals and reagents

Poly(lactic-co-glycolic acid) (PLGA), polyethylene glycol-bis(amine) (PEG-bis-amine), and folic acid (FA) were used for the synthesis of PLGA-PEG-FA nanocarrier. Coupling agents such as N,N′-dicyclohexylcarbodiimide (DCC) and N-hydroxysuccinimide (NHS) were employed for the conjugation reactions. Solvents, including anhydrous dimethyl sulfoxide (DMSO), anhydrous dichloromethane (DCM) and methanol, were used during

nanoparticle formulation. The viability of the cells was assessed via the 3-(4,5-dimethylthiazol-2-yl)-2,5-diphenyltetrazolium bromide (MTT) assay. All reagents and chemicals were procured from Sigma–Aldrich (USA) unless mentioned otherwise. Throughout the study, deionized and filtered water (Milli-Q Academic®, Millipore, Molsheim, France) was used in all the experimental procedures.

4.2.3. Cell Culture

MCF-7, MDA-MB-231, and T47D breast cancer cell lines (obtained from NCCS, Pune) were cultured at 37°C in a humidified incubator with 5% CO_2. The cell culture utilized Dulbecco's Modified Eagle Medium (DMEM) (Gibco BRL, UK) supplemented with fetal bovine serum (FBS) (Gibco BRL, UK), along with 10X phosphate-buffered saline (PBS) (Gibco BRL, UK), 0.25% trypsin containing 0.003% EDTA (Gibco BRL, UK), and a penicillin/streptomycin solution (10 mg/mL, Sigma–Aldrich). Dimethyl sulfoxide (DMSO) (HIMEDIA) was used for treatment preparation. All the experimental procedures were conducted under sterile conditions inside a Class A2 biosafety cabinet, adhering strictly to aseptic conditions.

4.2.4. Chemical Synthesis of 3-Br-benzyl Noscapine (3-Br-Bn-Nos)

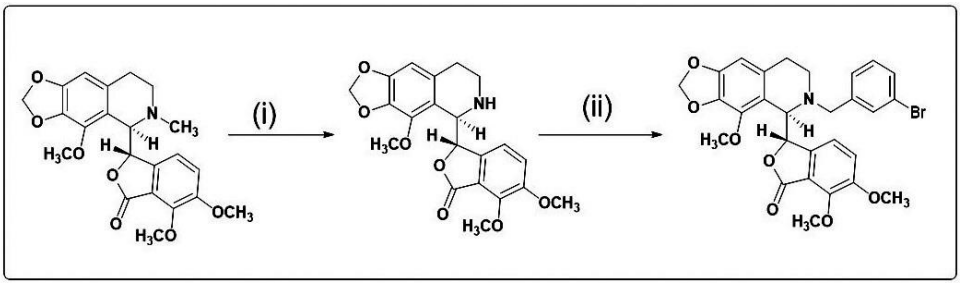

Reaction Scheme: Reaction Conditions: (i) a: m-CPBA, DCM; b: 2 N HCl; C: $FeSO_4.7H_2O$; (ii) 3-Bromo benzyl bromide, KI, K_2CO_3, acetone, RT, 96% yield.

A derivative of Noscapine, 3-Br-benzyl Noscapine was chemically synthesised as reported earlier. (Dash *et al.*, 2021) Briefly the starting solution of Noscapine (200 mg, 0.50 mmol) in acetone (5 mL), was added to potassium carbonate (1.10 mmol), potassium iodide (0.5 mmol) and 3-Bromo-benzyl bromide (0.55 mmol) and stirred at room temperature (RT) for 1 h. The crude reaction mixture was filtered and evaporated under vacuum, water (5 mL) and dichloromethane (2 X 10 mL) were added, and the organic layer was dried over Na_2SO_4 and concentrated under reduced pressure. The crude residue was purified via silica gel column chromatography with hexane/ethyl acetate (70:30) to yield a solid product of 3-Br-Bn-Nos. It was characterised using NMR, HR-MS, FT-IR and UV-Visible spectroscopy

which were included in the supporting material in the appendix (Figure S11-S14). The detailed synthetic scheme is mentioned below.

(S)-3-((R)-6-(3-bromobenzyl)-4-methoxy-5,6,7,8tetrahydro-[1,3]dioxolo[4,5-g]isoquinolin-5-yl)-6,7dimethoxyisobenzofuran-1(3H)-one: Yield: 97%; mp 65°C; [α]D25 = 52.0 (c = 1, Dichloromethane); IR νmax (cm^{-1}): 3503, 2940, 2837, 1759, 1621, 1498, 1387, 1271, 1212, 1039, 891, 785, 695. ^{1}HNMR: (300 MHz, $CDCl_3$): δ 7.40-7.30 (m, 2H), 7.24-7.09 (m, 2H), 6.99 (d, J= 8.30 Hz, 1H), 6.34 (s, 1H), 6.15 (d, J= 8.30 Hz, 1H), 5.95 (s, 2H), 5.66 (d, J= 3.96 Hz, 1H), 4.60 (d, J= 3.96 Hz, 1H), 4.17-4.06 (m, 4H), 4.04 (s, 3H) 3.87, (s, 3H), 3.63 (d, J= 13.78 Hz, 1H), 2.50-2.37 (m, 2H), 2.32-2.19 (m, 1H), 2.07-1.92 (m, 1H). ^{13}CNMR (75 MHz, $CDCl_3$): δ 168.1, 152.2, 148.5, 147.9, 141.5, 140.4, 134.0, 131.8, 131.4, 130.0, 129.7, 127.3, 122.2, 118.1, 117.7, 116.6, 102.4, 100.7, 81.6, 81.1, 62.5, 61.1, 59.5, 59.3, 56.7, 45.4, 26.8. MS (ESI) m/z 568 $[M+H]^+$. HRMS (ESI) Calcd for $C_{28}H_{26}BrNO_7$ $[M+H]^+$: 568.41, found: 568.41.

4.2.5. Synthesis of the FA-PLGA-PEG Nanocarrier

The FA-PLGA-PEG nanocarrier (FPP) was synthesized following a previously established method with minor modifications, as illustrated in Figure 4.2. (El-Hammadi *et al*., 2017; Fasehee *et al*., 2016)

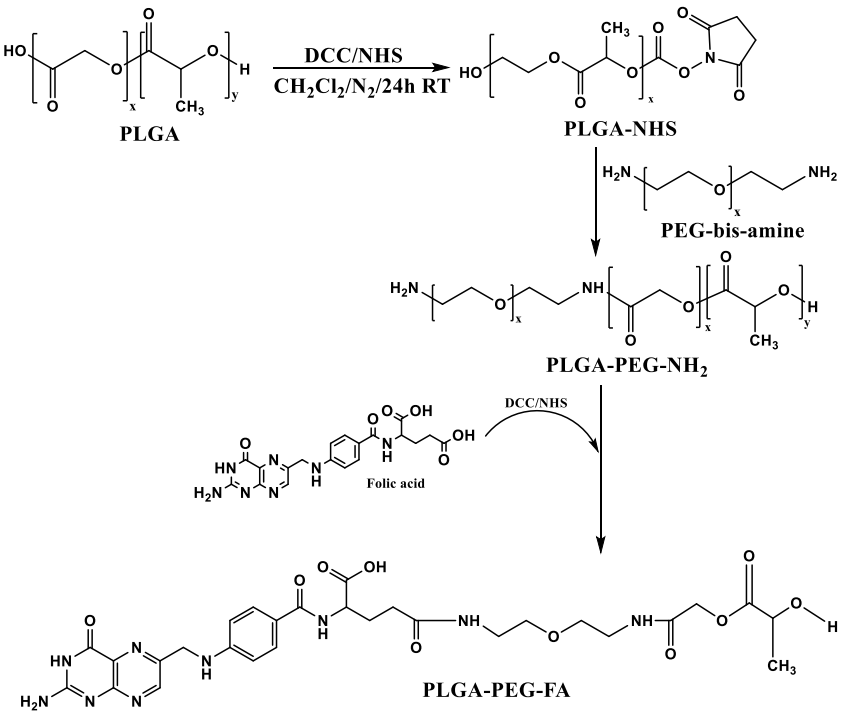

Figure 4.2. Synthetic scheme for the preparation of the FA-PLGA-PEG nanocarrier.

4.2.6. PLGA Activation

PLGA was dissolved in dry dichloromethane (DCM), and N-hydroxysuccinimide (NHS) and N,N′-dicyclohexylcarbodiimide (DCC) were added at a 1:2:2 molar ratio (PLGA:NHS:DCC). The reaction was performed out in an inert argon atmosphere at 25 ℃ (room temperature) for 24 hours with continuous stirring. Upon completion, the reaction mixture was filtered to remove the dicyclohexylurea (DCU) by-product. The filtrate was added drop wise to ice-cold diethyl ether to precipitate the product. The resulting solid was washed multiple times with a chilled 1:1 mixture of ether and methanol to separate any unreacted NHS. The activated PLGA was collected and vacuum-dried.

4.2.7. PEG Conjugation to Activated PLGA

The NHS-activated PLGA was redissolved in dry DCM and then added drop wise to a separately prepared solution of PEG-bis(amine) in DCM. A 1:3 molar ratio (PLGA:PEG) was used to minimize the formation of undesired triblock structures. The reaction proceeded under an argon atmosphere at room temperature for 24 hours with gentle stirring. The resulting mixture was precipitated in chilled methanol. The copolymer PLGA-PEG-NH_2 was purified by repeated methanol washes, followed by vacuum drying.

4.2.8. Folic Acid Activation

Folic acid was reacted with NHS and DCC at a 1:2:2 molar ratio in anhydrous DMSO, with a catalytic amount of triethylamine. The reaction was carried out overnight under an argon atmosphere in the absence of light. After filtration to remove DCU, the activated folic acid was precipitated in ice-cold anhydrous ether, washed, and vacuum-dried to obtain the NHS-activated folic acid derivative.

4.2.9. Coupling of Folic Acid to PLGA-PEG

NHS-activated folic acid was dissolved in dry DMSO and added drop wise to a stirred solution of PLGA-PEG-NH_2 in DMSO, maintaining a 1:1 molar ratio (FA: PLGA-PEG-NH_2). The reaction was then allowed to continued for 24 hours at room temperature under an inert atmosphere under light-protected conditions. After completion, the product was precipitated in ice-cold diethyl ether, filtered, and washed repeatedly to remove unreacted components. The resulting FPP nanocarrier was vacuum-dried and stored under desiccation until further use.

4.2.10. Loading of 3-Br-Bn-Nos onto FPP Nanocarrier

3-Br-Bn-Nos was loaded onto FPP nanocarrier via the nanoprecipitation technique. Briefly, 50 mg of the FPP nanocarrier and 5 mg of 3-Br-Bn-Nos (maintaining a 10% drug-to-polymer ratio) were co-dissolved in 5 mL of acetone. This organic phase was slowly introduced into 25 mL of aqueous solution of 1% (w/v) polyvinyl alcohol (PVA), followed by probe sonication at 37% amplitude for 1 minute, with 10-second ON/OFF pulse cycles. The emulsion was then stirred at 500 rpm for 6 hours to facilitate complete evaporation of the acetone. After evaporation, the dispersion was sonicated once more time and then centrifuged at 20,000 rpm for 45 minutes at 4 °C. The resulting nanoparticle pellet was washed three times with deionized water and subsequently lyophilized. The FPP-loaded 3-Br-Bn-Nos nanoparticle was prepared in triplicate for consistency.

4.2.11. Structural and Chemical Characterization of FPP-loaded 3-Br-Bn-Nos Nanoparticle

4.2.11.1. Particle Size Determination via Dynamic Light Scattering (DLS)

To determine the particle size of the nanoparticle, the FPP-loaded 3-Br-Bn-Nos was diluted in deionized water and subjected to ultrasonication in a bath sonicator. The measurements were carried out at 25 °C using a Litesizer DLS 500 instrument. Each sample was evaluated through 30 measurement runs, each performed in triplicate. The average hydrodynamic diameter and polydispersity index (PDI) were calculated.

4.2.11.2. Morphological Analysis by Scanning Electron Microscopy (SEM)

The surface characteristics, size distribution, and morphology of the FPP-loaded 3-Br-Bn-Nos nanoparticle was analyzed using field-emission scanning electron microscopy (FE-SEM; JEOL JSM-6480 LV). The samples were adhered to aluminium stubs using conductive carbon tape, followed by gold sputter coating under an argon atmosphere (SC 7620, Quorum Technologies, UK). Imaging was performed at an accelerating voltage of 10 kV with a working distance of 4.1 mm under high vacuum conditions.

4.2.11.3. Drug Encapsulation Efficiency

The drug loading capacity of the FPP nanocarrier was assessed by quantifying the amount of 3-Br-Bn-Nos remaining in the supernatant after centrifugation of the nanoparticle dispersion. This unbound drug amount was subtracted from the total amount of drug initially used. All measurements were conducted in triplicate using a validated UV–Vis

spectrophotometric method at a wavelength of 309 nm. The encapsulation efficiency was calculated using the following formula:

$$EE\ (\%) = ((\text{Total Drug loaded} - \text{Free Drug})/\text{Total Drug loaded}) \times 100$$

4.2.11.4. *In Vitro* Drug Release Study

Drug release profiles of the FPP nanocarrier was investigated in phosphate-buffered saline (PBS, pH ~7.4). The FPP-loaded 3-Br-Bn-Nos (5 mg each) nanoparticle was suspended in 20 mL of PBS and stirred continuously at 150 rpm at 37 °C. At selected intervals (ranging from 5 minutes to 48 hours), 2 mL of the medium was collected and replaced with fresh PBS to maintain sink conditions. The drug concentration was measured spectrophotometrically at 312 nm. (Jusu *et al*., 2021)

4.2.12. *In Vitro* Cytotoxicity Assay

An MTT assay was employed to evaluate the cytotoxic effects of the free 3-Br-Bn-Nos and FPP-loaded 3-Br-Bn-Nos nanoparticle on the MDA-MB-231, MCF-7 and T47D breast cancer cell lines. The cells were plated in 96-well plates at 5000 cells/well and allowed to attach for 24 hours. Then the cells were treated with the test samples at different concentrations (5, 10, 50, 75, and 100 µg/mL) for 48–72 hours. MTT reagent (0.5 mg/mL) was added, and the mixture was incubated for 4 hours. Then, the formazan crystals were dissolved in DMSO, and the absorbance was measured at 570 nm. Untreated cells served as negative controls.

4.2.13. Nuclear Morphology Assessment by Hoechst 33342

MDA-MB-231 cells was treated with IC_{50} concentrations of 3-Br-Bn-Nos and FPP-loaded 3-Br-Bn-Nos for 24 hours. The cells were washed with PBS, fixed in 100% ice-cold methanol for 15 minutes, and then stained with Hoechst 33342 (1 µg/mL) for 15 minutes. Fluorescent nuclear changes were examined under a Nikon ECLIPSE Ts2R microscope. (Ponselvi Induja *et al*., 2018)

4.2.14. Mitochondrial Membrane Potential (MMP) Evaluation Using JC-1

JC-1 dye was used to assess changes in the mitochondrial membrane potential (MMP). The cells were treated with IC_{50} concentration of 3-Br-Bn-Nos and FPP-loaded 3-Br-Bn-Nos for 24 hours. Following treatment, the cells were washed, stained with 5 µM JC-1 for 30 minutes at 37°C, and imaged. Red (J-aggregates) and green (monomers) fluorescence was quantified to assess mitochondrial depolarization using a Nikon ECLIPSE Ts2R microscope.

4.2.15. ROS Generation Assay Using DCF-DA

Reactive oxygen species (ROS) within the cells were quantified using DCF-DA. A 10 mM DCF-DA stock in DMSO was diluted to a working concentration of 20 µM. MDA-MB-231 cells treated with IC_{50} concentrations of 3-Br-Bn-Nos and FPP-loaded 3-Br-Bn-Nos for 12 hours were incubated with 20 µM DCF-DA for 30 minutes at 37°C. Fluorescence was visualized via microscopy and quantified with a Hitachi F-7000 spectrofluorometer after lysis. (Kim & Xue, 2020)

4.2.16. 3D Spheroid Disintegration Assay

To mimic *in vivo* tumor microenvironments, MDA-MB-231 cells (1×10^3 cells/well) were seeded in ultralow attachment 96-well round-bottom plates. The plates were subsequently centrifuged at 1000 rpm for 10 minutes and incubated for 7–10 days to form compact spheroids. The spheroids were then treated with 3-Br-Bn-Nos and FPP-loaded 3-Br-Bn-Nos. The medium was replaced every 48 hours. The spheroids were observed over 5 days for disintegration and size reduction using a Nikon inverted phase-contrast microscope. Spheroid size was quantified using ImageJ.

4.2.17. Acute Toxicity Evaluation in Rats

To determine the acute oral toxicity of 3-Br-Bn-Nos and FPP-loaded 3-Br-Bn-Nos, a single dose of varying concentrations (250, 500, 1000, 2000, or 5000 mg/kg body weight) was administered to Wistar rats. The animals were divided into six groups (6 per group), and each group received one of the designated doses orally. The rats were monitored continuously for signs of toxicity or mortality over a period of 14 days. The total number of deaths in each group was recorded at the end of the observation period, in accordance with OECD Guideline No. 425 (2022).

4.2.18. Subacute Toxicity Assessment of 3-Br-Bn-Nos and FPP-loaded 3-Br-Bn-Nos Nanoparticle

For subacute toxicity evaluation, Wistar rats were randomly distributed in to three groups of six animals each (n = 6). The Group-1 was the control and treated with 1% saline water. Group-2 and Group-3 were the treated groups and were administrated with 3-Br-Bn-Nos and FPP-loaded 3-Br-Bn-Nos nanoparticle orally at a dose of 500 mg/kg body weight per day for 28 consecutive days following OECD guidelines. During this period, the animals were observed daily for any signs of illness, behavioural abnormalities, or mortality. Parameters such as body weight, food consumption, and water intake were recorded

throughout the study. All the experimental procedures and protocols followed in the present study were approved by the Institutional Animal Ethics Committee of Sambalpur University, Odisha vide approval letter no. 25/12/217-CPCSEA.

4.2.19. Haematological and Biochemical Analysis

At the end of the subacute study, the animals were anaesthetized via mild isoflurane followed by cervical dislocation. Blood samples were collected via cardiac puncture. A complete blood count (CBC) was performed via an automated hematology analyser (Byovet). For biochemical analysis, the serum was separated by centrifuging the blood at 5000 rpm for 10 minutes via an Eppendorf 5810r centrifuge. Various biochemical markers, including glucose (GLU), albumin (ALB), urea, creatinine (CREA), cholesterol (CHOL), triglycerides (TG), SGPT, SGOT, total protein (TP), HDL, and alkaline phosphatase (ALP), were measured using an automated biochemical analyser (Byovet Smart-5DX) with standard diagnostic kits.

4.2.20. Histopathological Examination via H&E Staining

Histological evaluation was conducted on major organs such as the brain, heart, liver, and kidneys collected from rats to identify any potential toxic effects. The tissues were fixed in 10% neutral buffered formalin, dehydrated through a graded alcohol series, cleared with xylene, and embedded in paraffin. Sections (3.5 μm thick) were cut from the paraffin blocks and stained with hematoxylin and eosin (H&E) following standard protocols. The stained sections were examined microscopically using a Nikon ECLIPSE Ts2R inverted microscope to observe histopathological alterations.

4.3. Results and Discussion

4.3.1. Molecular Docking and MD Simulation Analysis

The lead compound, noscapine, along with its derivative (3-Br-Bn-Nos), was docked on the known noscapinoid binding site on tubulin using the Glide XP algorithm. The binding affinities were calculated using the Glide XP scoring function. Compared to noscapine, which exhibited a docking score of –2.897 kcal/mol, the 3-BrBn-Nos derivative exhibited a docking score of –4.897 kcal/mol demonstrated stronger binding interactions. The noscapinoid, 3-Br-Bn-Nos was well docked at the interface of α- and β- tubulin as represented in Figure 4.3 (a). Binding interaction analysis through LigPlot revealed distinct interaction patterns for the ligands, attributed to the presence of substituted functional groups (Figure 4.3(b)). 3-BrBn-Nos showed the most favorable binding profile, engaging in hydrogen bonds with key residues such as Gln 247 (B), Leu 248 (B), Val 355 (B), Pro

245 (B), Gly 246 (B) (bond length: 2.78 Å). In addition, numerous hydrophobic interactions were identified between 3-Br-Bn-Nos and it's respective binding site residues, as detailed in Appendix Table S1. Furthermore, 3-BrBn-Nos formed extensive hydrophobic contacts with the surrounding amino acid residues as well. To further assess the complex stability, 100 ns molecular dynamics simulations were conducted on the docked complexes of noscapine and 3-Br-Bn-Nos. Analyses of RMSD indicated that the complex remained stable after 5 ns simulation time (Figure 4.4a). To assess residue-level flexibility throughout the molecular dynamics (MD) simulation, the root mean square fluctuations (RMSF) of the Cα atoms were computed (Fig. 4.4b). Residues with higher RMSF values exhibited greater flexibility. The ligand Br-Bn-Nos remained stably bound to tubulin during the entire simulation period. The five ligand–tubulin complexes with the lowest total energy, selected from the MD trajectory, were used to generate an average structure for binding analysis. 3-Br-Bn-Nos was found to fit well within the tubulin binding pocket, specifically localizing at the interface between the α- and β-tubulin subunits, suggesting stable and favorable binding.

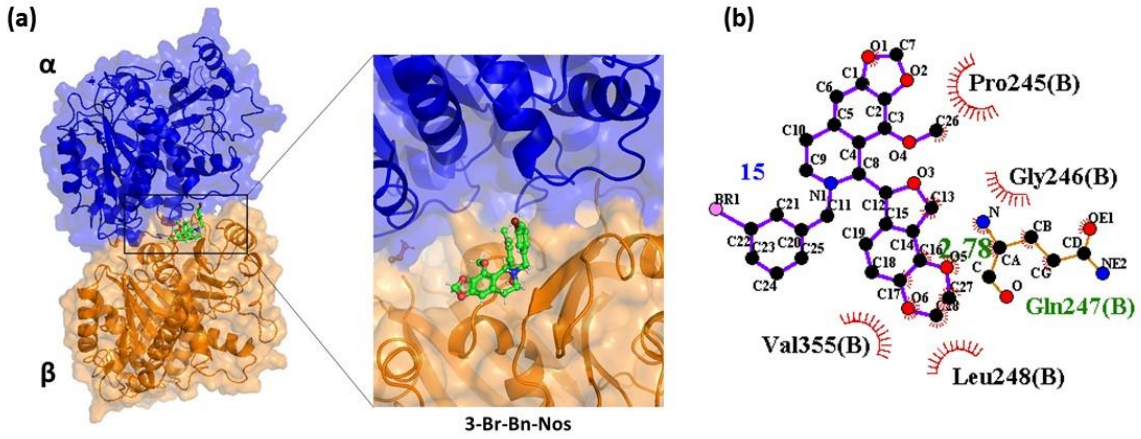

Figure 4.3. (a) The newly designed 3-Br-Bn-Nos was well accommodated inside the noscapine binding site at the interface of α- and β- tubulin. The binding site is represented as micromodel surface according to α- and β- tubulin (α- tubulin in blue colour and β-tubulin in brown colour). (b) 2D LigPlot representation of the molecular interaction between 3-Br-Bn-Nos and the target protein binding site. Hydrogen bonds were depicted as dashed green lines with corresponding the bond lengths (in Å), while hydrophobic interactions are indicated by red arcs with radial spokes pointing toward the interacting residues.

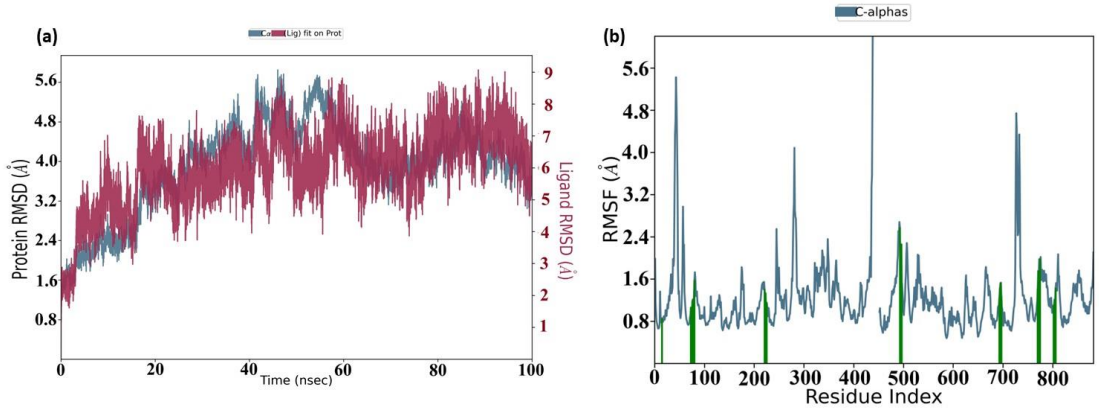

Figure 4.4. Representative molecular dynamics (MD) simulation plots for tubulin and its complex with 3-Br-Bn-Nos over 100 ns. (a) Root mean square deviation (RMSD) plots showing the structural stability of Cα atoms of tubulin alone and in complex with 3-BrBn-Nos. (b) Root mean square fluctuation (RMSF) plots representing the residue-wise flexibility of tubulin in the bound state with 3-Br-Bn-Nos.

4.3.2. ADME Property Prediction

The absorption, distribution, metabolism, and excretion (ADME) properties of 3-Br-Bn-Nos was assessed using the QikProp tool. Key descriptors analyzed included molecular weight (MW), solvent-accessible surface area (SASA), partition coefficients such as QPlogPo/w (octanol/water), QPlogPoct (octanol/gas), and QPlogPw (water/gas), as well as polarizability (QPlogrz). Other parameters included QPlogBB (brain/blood partitioning), QPlogHERG (HERG K^+ channel inhibition potential), QPlogKp (skin permeability), QPlogKhsa (human serum albumin binding), and predicted permeability through Caco-2 and MDCK cell lines (QPPCaco and QPPMDCK), which model intestinal absorption and blood–brain barrier permeability, respectively. Additionally, drug-likeness was assessed through Lipinski's Rule of Five. While the ADME characteristics varied among the compounds, all tested molecules complied with Lipinski's rule, suggesting favorable pharmacokinetic and drug-like properties (Table 4.1).

Table 4.1. QikProp was used to determine the ADME properties of noscapine and 3-Br-Bn-Nos. These molecules are associated with all the ADME parameters.

	ADME Screening	3-Br-Bn-Nos	Noscapine	Recommended values
1	MW	568.41	413.42	130-725
2	SASA	815.667	597.02	300-1000
3	Accpt HB	10.950	8.75	2.0-20.0
4	QPpolrz	56.090	39.09	13.0-70.0
5	QPlogPoct	26.236	17.81	8.0-35
6	QPlogPw	13.819	10.08	4.0-45.0
7	QPlogPo/w	3.081	1.79	-2.0-6.5
8	QPlogHERG	-6.513	-4.42	Below -5.0
9	QPPCaco	94.110	777.7	< 25 poor > 500 great
10	QPlogBB	-0.925	0.33	-3.0-1.2
11	QPPMDCK	42.545	417.06	< 25 poor >500 great
12	QPlogKp	-4.906	-3.95	-8.0- -1.0
13	QPlogKhsa	0.060	-0.49	-1.5-1.5
14	Rule of Five (No. of violations)	1	3	Maximum is 4

4.3.3. Physicochemical Characterization of FPP-loaded 3-Br-Bn-Nos Nanoparticle

4.3.3.1. Particle Size and Morphology

DLS analysis revealed a hydrodynamic diameter of 155 ± 2 nm and a PDI of 0.27 for the FPP-loaded 3-Br-Bn-Nos nanoparticle, indicating a uniform nanosize and suitability for tumor targeting via both the EPR effect and folate receptor-mediated uptake. SEM images (Figure 4.5(a)) revealed aggregated spherical particles with a uniform distribution, suggesting good formulation stability.

4.3.3.2. Entrapment Efficiency

UV–visible spectroscopic analysis revealed a high drug entrapment efficiency of 98.7% of FPP nanocarrier. This finding suggests a strong interaction between 3-Br-Bn-Nos and FPP, which may enhance delivery efficiency and therapeutic potential.

4.3.3.3. *In Vitro* Drug Release

Drug release in PBS (pH 7.4) revealed that free 3-Br-Bn-Nos was rapidly released (~100% within 2 h), whereas FPP-loaded 3-Br-Bn-Nos nanoparticle exhibited a sustained release pattern with ~65% drug release over 72 h (Figure 4.5(b)).

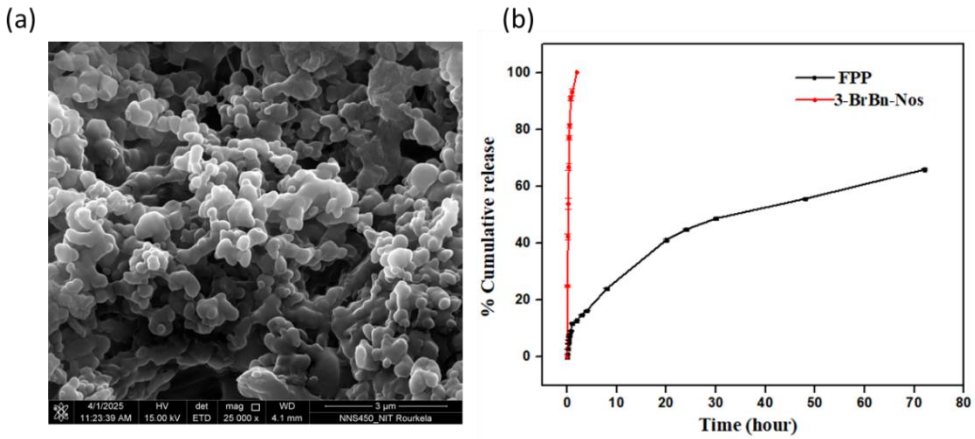

Figure 4.5. (a) Representative SEM image of FPP-loaded 3-Br-Bn-Nos nanoparticles. (b) *In vitro* release profile of 3-Br-Bn-Nos from FPP nanocarrier vs. free 3-Br-Bn-Nos release in PBS (pH 7.4).

4.3.4. FPP Nanocarrier Increased the Cytotoxicity of 3-Br-Bn-Nos

The cytotoxic potential of the FPP-loaded 3-Br-Bn-Nos was assessed in three different breast cancer cell lines such as MDA-MB-231, T47D, and MCF-7. The cytotoxicity effect was demonstrated in a dose-dependent manner (Figure 4). The IC_{50} value using MDA-MB-231 for FPP-loaded 3-Br-Bn-Nos was found to be 37.2 µg/mL which is significantly outperformed compared to free 3-Br-Bn-Nos with IC_{50} of 73.6 µg/mL (Figure 4.6 (a)). Similarly, against MCF-7 the IC_{50} value for FPP-loaded 3-Br-Bn-Nos was found to be 28.9 µg/mL compared to free 3-Br-Bn-Nos with IC_{50} of 59.8 µg/mL, (Figure 4.6 (b)). In the case of T47D, the IC_{50} value of FPP-loaded 3-Br-Bn-Nos was 22.7 µg/mL in comparison to the free 3-Br-Bn-Nos with IC_{50} value of 54.1 µg/mL (Figure 4.6 (c)). The improvement in IC_{50} value for FPP-loaded 3-Br-Bn-Nos is attributed primarily to folate receptor-mediated targeting and greater cellular uptake of the drug.

4.3.5. FPP-loaded 3-Br-Bn-Nos Triggered Cellular Alterations Leading to Apoptosis

Hoechst 33342 staining (Figure 4.6 (d)) revealed clear differences in nuclear morphology among the treatment groups. The cells exposed to the FPP-loaded 3-Br-Bn-Nos displayed prominent apoptotic features, such as intense chromatin condensation and marked nuclear fragmentation. In contrast, cells treated with free 3-Br-Bn-Nos presented only moderate nuclear alterations, whereas untreated control cells presented uniformly stained nuclei with a healthy, intact morphology. The pronounced apoptotic effects by the FPP-loaded 3-Br-Bn-Nos treated cells suggested that the nanoparticle system significantly enhances the intracellular delivery and antitumour activity of 3-Br-Bn-Nos compared to the free drug.

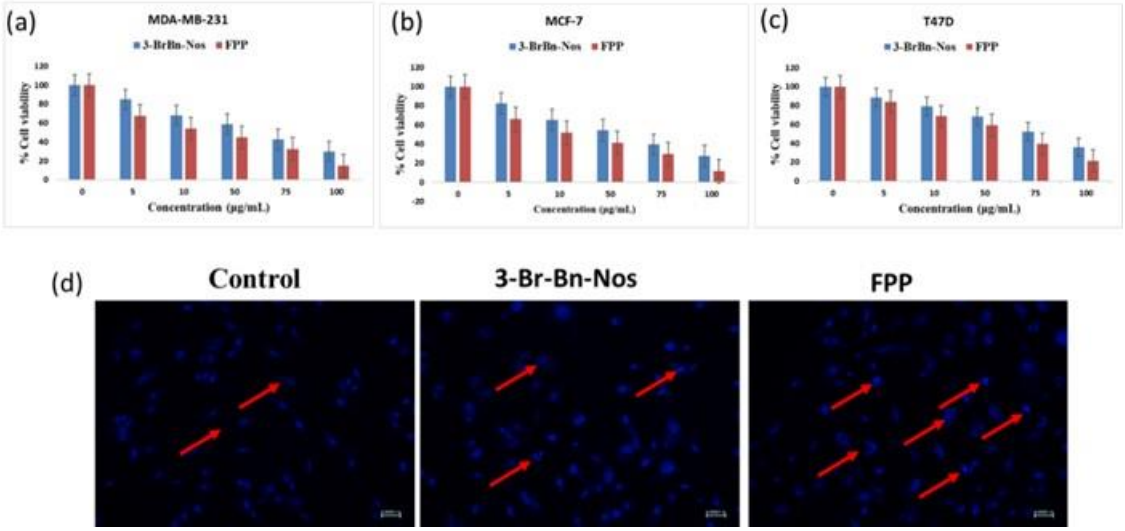

Figure 4.6. Dose-dependent cytotoxic effects of 3-Br-Bn-Nos and FPP-loaded 3-Br-Bn-Nos on (a) MDA-MB-231, (b) MCF-7 and (c) T47D breast cancer cell lines. Cell viability was assessed using the MTT assay after 48 h of treatment at various concentrations (0–100 µM). The data are presented as the means ± SDs (n = 3). (d) Representative Hoechst 33342 staining images of MDA-MB-231 cells showing nuclear condensation and fragmentation in treated cells, indicating the induction of apoptosis following exposure to the free drug and FPP-loaded 3-Br-Bn-Nos.

4.3.6. FPP-loaded 3-Br-Bn-Nos Induced Greater Mitochondrial Membrane Depolarization Than Free 3-Br-Bn-Nos

The effects of FPP-loaded 3-Br-Bn-Nos on the mitochondrial membrane potential (MMP) compared to free 3-Br-Bn-Nos was assessed using JC-1 staining (Figure 4.7(a)). In untreated control cells, JC-1 primarily formed red fluorescent aggregates within healthy mitochondria, indicating preservation of the MMP and a low green/red fluorescence ratio. Treatment with 3-Br-Bn-Nos led to a moderate increase in the green/red fluorescence ratio, signifying partial depolarization of the mitochondrial membrane. In contrast, cells exposed to FPP-loaded 3-Br-Bn-Nos presented a significant increase in the green/red fluorescence ratio, reflecting a substantial decrease in the MMP. These findings suggest that FPP-loaded 3-Br-Bn-Nos causes a more pronounced disruption of mitochondrial function, thereby enhancing apoptosis more effectively than both the control and the free drug. Overall, these data support the superior proapoptotic activity of FPP-loaded 3-Br-Bn-Nos through mitochondrial destabilization.

4.3.7. FPP-loaded 3-Br-Bn-Nos Results in Greater ROS-Mediated Apoptotic Activity Compared to 3-Br-Bn-Nos

Reactive oxygen species (ROS) are crucial mediators of intracellular signalling and are key drivers of apoptosis. The production of intracellular ROS was evaluated in cells treated with FPP-loaded 3-Br-Bn-Nos and 3-Br-Bn-Nos. Cells treated with FPP-loaded 3-Br-Bn-Nos showed markedly higher green fluorescence compared to those treated with 3-Br-Bn-Nos, indicating increased ROS production (Figure 4.7(b)). The increased ROS production was associated with increased mitochondrial damage, loss of membrane potential, and activation of apoptosis-related pathways, including caspase signalling. These findings underscore the pivotal role of ROS in driving apoptosis and highlight the enhanced proapoptotic efficacy of FPP-loaded 3-Br-Bn-Nos over the free drug.

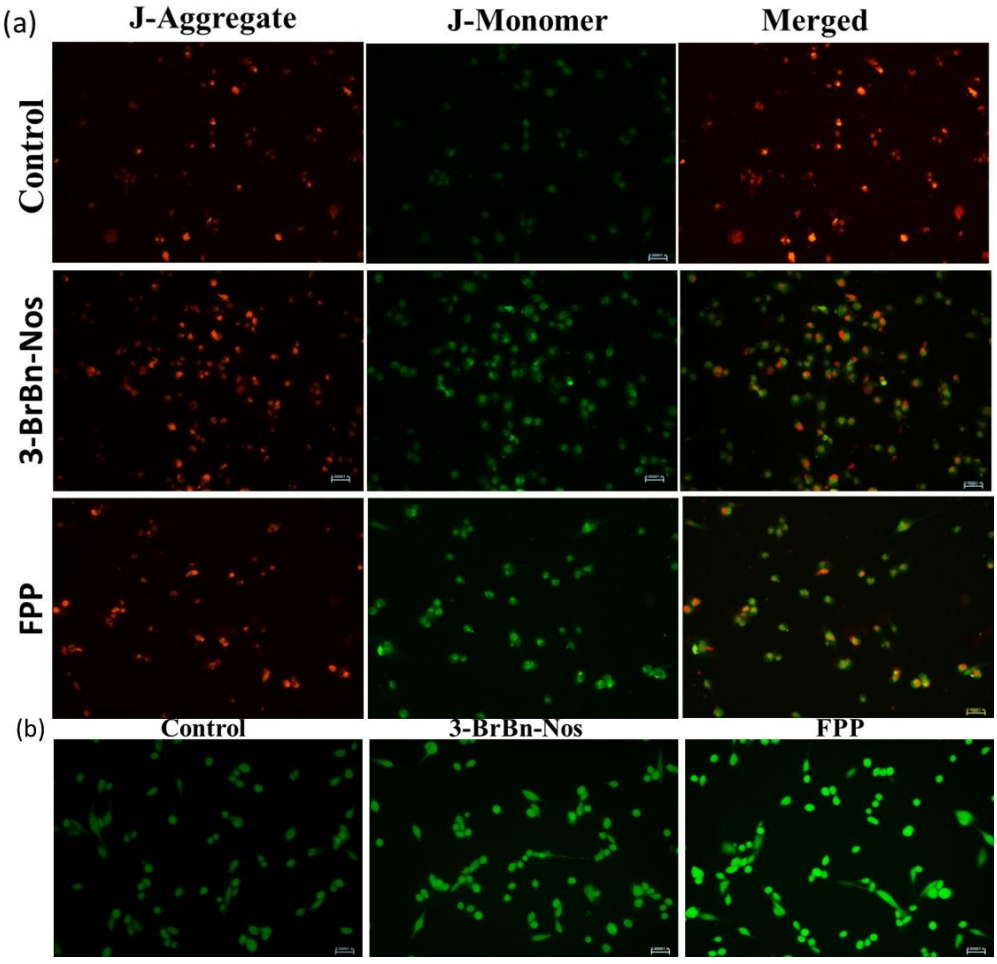

Figure 4.7. Representative fluorescence images showing (a) the mitochondrial membrane potential (MMP) in MDA-MB-231 cells as assessed by JC-1 staining. A decrease in the red/green fluorescence ratio indicates MMP disruption after treatment with 3-Br-Bn-Nos and its nanoparticle formulation (FPP). (b) ROS generation in MDA-MB-231 cells visualized by DCFDA staining, where increased green fluorescence reflects elevated ROS levels (n=3).

4.3.8. Disruption of Tumor Spheroids Following Treatment With 3-Br-Bn-Nos and FPP-loaded 3-Br-Bn-Nos Nanoparticles

The ability of 3-Br-Bn-Nos and FPP-loaded 3-Br-Bn-Nos nanoparticles to disrupt 3D tumor spheroids was visually examined over a 5-day period. The images depicted a clear contrast in spheroid morphology across treatment groups. In the control group, the spheroids retained their dense and compact structure from day 1 to day 5, showing no signs of structural disintegration. Upon treatment with 3-Br-Bn-Nos, the spheroids exhibited partial shrinkage by day 5, with a noticeable but moderate reduction in overall size and density. In stark contrast, FPP-loaded 3-Br-Bn-Nos treated spheroids displayed substantial disintegration and loss of structural integrity by day 5, with a visibly smaller and more fragmented core than the other groups did (Figure 4.8). These observations support the enhanced therapeutic potential of FPP nanoparticles in effectively disrupting the tumor spheroid architecture compared with the free drug after 5 days of administration.

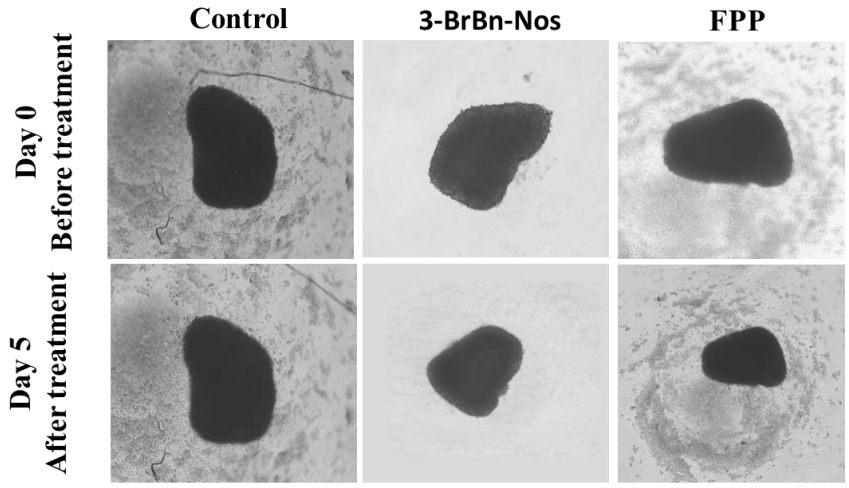

Figure 4.8. Representative phase-contrast images show the structural integrity of the tumor spheroids following treatment with 3-Br-Bn-Nos and FPP-loaded 3-Br-Bn-Nos nanoparticles for 5 days. Untreated spheroids served as controls.

4.3.9. Acute and Subacute Toxicity of 3-Br-Bn-Nos and FPP-loaded 3-Br-Bn-Nos in Rats

The acute oral toxicity of 3-Br-Bn-Nos and its FPP nanoformulation was evaluated in Wistar rats according to OECD guidelines. A single dose of each test substance was administered, and the animals were observed over a 14-day period for any signs of mortality, behavioural changes, body weight variation, or organ-related toxicity. No mortality or significant behavioural abnormalities were detected in any of the treatment groups, including the control, during the observation period. For the subacute toxicity

assessment, the rats received daily oral doses of 3-Br-Bn-Nos, FPP-loaded 3-Br-Bn-Nos or vehicle (control) for 28 consecutive days. The animals were closely monitored for clinical symptoms; changes in body weight; food and water intake; as well as haematological, biochemical, and histopathological parameters. No treatment-related mortality or observable toxicity symptoms were reported throughout the study duration. All treated groups, including the control, presented a progressive increase in body weight, suggesting preserved metabolic and physiological functions. Detailed measurements of body weight (Table 4.2), food and water consumption (Table 4.3) were documented to support these findings.

Table 4.2. Body weights (in grams) of rats treated with the control, 3-Br-Bn-Nos, and FPP-loaded 3-Br-Bn-Nos nanoparticle at a daily dose of 500 mg/kg body weight for 28 days.

	Body weight (grams)		
Days	**Control**	**3-Br-Bn-Nos**	**FPP-loaded 3-Br-Bn-Nos**
1	241.174±1.097	241.177±0.589	241.803±0.595
7	244.041±1.12	243.363±1.301	243.857±0.97
14	246.055±0.995	246.373±0.786	246.823±0.874
21	247.871±0.529	247.832±0.474	248.238±0.443
28	249.607±0.9	249.275±1.026	249.314±0.839

Table 4.3. Food (in grams) and water intake (in mL) of rats treated with the control, 3-Br-Bn-Nos, or its nanoparticle formulation (FPP) at a daily dose of 500 mg/kg body weight for 28 days.

	Food intake		
Day	**Control**	**3-Br-Bn-Nos**	**FPP-loaded 3-Br-Bn-Nos**
1	21.461±0.442	22.311±0.821	20.958±0.961
7	23.509±0.913	23.434±0.911	23.715±0.943
14	24.696±0.448	24.903±0.368	25.087±0.333
21	26.203±0.665	26.901±0.621	25.9±0.71
28	28.817±1.028	28.313±0.815	29.575±0.322
	Water intake		
1	20.809±0.352	20.869±0.656	20.88±0.578
7	22.104±0.689	21.718±0.482	21.49±0.319
14	23.132±0.596	22.9±0.651	22.592±0.333
21	24.08±0.427	24.219±0.481	24.613±0.336
28	24.762±0.477	25.473±0.344	25.27±0.221

4.3.10. Haematological and Biochemical Parameters Following Treatment with 3-Br-Bn-Nos and FPP-loaded 3-Br-Bn-Nos

A 28-day subacute toxicity study was conducted to assess the hematological and biochemical effects of 3-Br-Bn-Nos and FPP-loaded 3-Br-Bn-Nos nanoparticle in rats. Parameters such as RBC count, hemoglobin (Hb), hematocrit (HCT), MCV, WBC count,

and platelet levels were evaluated. No significant changes were observed in RBC, Hb, HCT, or red cell indices (MCV, MCH, MCHC), indicating normal erythropoiesis and red blood cell morphology. The WBC and differential leukocyte counts remained within physiological limits, suggesting that there was no immune suppression or inflammatory response. The platelet counts also revealed no adverse effects on coagulation. Biochemical analyses revealed no significant differences in serum glucose, total protein, albumin, globulin, or electrolytes (Na^+, K^+, Ca^{2+}, P) between the treated and control groups. Liver enzymes (ALP, ALT, AST) remained within normal ranges, indicating no hepatotoxicity. Similarly, renal function markers (urea and creatinine) were not abnormal. The results are presented in Table 4.4 and Table 4.5.

Table 4.4. The haematological parameters of the rats treated with 3-Br-Bn-Nos and FPP-loaded 3-Br-Bn-Nos at a daily dose of 500 mg/kg body weight for 28 days showed no significant differences compared to the untreated control group.

Parameter	Control	3-Br-Bn-Nos	FPP-loaded 3-Br-Bn-Nos
White blood cell count (WBC) (10^3/L)	6.575±0.863	6.756±0.285	6.478±0.38
Neutrophils (Neu#) (10^3/L)	5.642±0.889	6.061±0.792	5.629±0.498
Lymphocytes (Lym#) (10^3/L)	2.262±0.918	2.46±0.477	2.512±0.767
Monocytes (Mon#) (10^3/L)	1.604±0.332	1.351±0.201	1.257±0.308
Eosinophils (Eos#) (10^3/L)	0.594±0.304	0.306±0.272	0.477±0.267
Basophil (Bas#) (10^3/L)	0.429±0.34	0.508±0.146	0.589±0.245
NLR	2.515±0.987	2.72±0.691	2.456±0.851
PLR	1.244±0.529	1.163±0.102	1.443±0.258
red blood cell count (RBC) (10^{12}/L)	5.864±0.578	5.782±0.503	5.921±0.487
Hemoglobin (HGB) (g/dL)	15.823±1.755	14.741±1.45	14.694±1.150
HCT	44.067±3.428	43.43±4.412	45.453±3.559
MCV (fL)	82.048±3.042	80.949±2.69	81.452±3.440
MCH (pg)	31.689±1.645	31.729±1.479	31.780±2.864
MCHC (g/L)	33.724±0.469	33.23±0.852	34.135±1.133
RDW-CV	12.907±0.799	12.438±1.412	13.340±1.551
RDW-SD (fL)	44.111±2.543	40.976±4.145	42.817±2.521
platelet count (PLT) (10^3/L)	155.659±2.545	153.616±2.735	155.514±1.366
PCT (mL/L)	1.407±0.293	1.542±0.363	1.705±0.343

Table 4.5. The serum biochemical parameters of the rats treated with 3-Br-Bn-Nos and FPP-loaded 3-Br-Bn-Nos at a daily dose of 500 mg/kg body weight for 28 days showed no significant alterations compared to the untreated control group.

Parameter	Control	3-Br-Bn-Nos	FPP-loaded 3-Br-Bn-Nos
Glucose (GLU)	77.792±1.556	77.042±2.021	77.240±1.523
Albumin (ALB)	4.175±0.626	3.875±0.681	3.578±0.644
Urea (UREA)	18.555±2.4	18.484±2.294	18.768±2.243
Creatinine (CREA)	1.365±0.231	1.385±0.261	1.580±0.312
Cholestrol (CHOL)	165.36±11.02	140.907±27.472	142.79±23.46
Triglycerides (TG)	49.85±4.43	47.206±4.538	48.006±4.238
Alanine Transaminase (ALT)	16.86±4.731	15.801±4.548	15.568±3.723
Aspartate Aminotransferase (AST)	6.995±2.632	5.59±2.771	5.550±2.672
Total Protein (TP)	7.277±0.653	7.186±0.693	7.434±0.524
Magnesium (MG)	2.453±0.245	2.481±0.31	2.834±0.573
Phosphorus (PHOS)	4.542±0.807	5.002±1.036	5.487±1.12
Calcium (CA)	10.769±0.371	10.551±0.795	10.09±0.65
Direct Bilirubin (DBIL)	0.572±0.255	0.518±0.27	0.545±0.773
Total Bilirubin (TBIL)	0.595±0.195	0.685±0.134	0.597±0.211
High-density Lipoprotein (HDL)	38.724±1.568	38.69±1.168	38.672±1.303
Gamma-glutamyl Transferase (GGT)	4.454±3.011	4.763±2.427	4.543±2.781
Alkaline Phosphatase (ALP)	107.343±2.615	106.776±1.968	105.96±1.864

4.3.11. Histopathological Evaluation of Vital Organs via Hematoxylin & Eosin (H & E) Staining

Histopathological assessment of vital organs, including the brain, heart, kidneys, lungs, and liver, was carried out after 28 days of daily oral treatment with 3-Br-Bn-Nos and FPP-loaded 3-Br-Bn-Nos at 500 mg/kg. Tissue sections from treated rats were compared with those from control animals to evaluate any structural alterations (Figure 4.9). The brain tissue exhibited intact neuronal architecture without signs of neurotoxicity. Cardiac sections revealed well-preserved myocardial fibres, indicating that there were no cardiotoxic effects. Kidney histology revealed normal glomeruli and tubules, suggesting preserved renal function. Similarly, liver sections maintained their lobular structure, with no signs of inflammation, necrosis, or fatty changes. Overall, no significant histopathological abnormalities were observed in the treated groups, supporting the safety and biocompatibility of 3-Br-Bn-Nos and FPP-loaded 3-Br-Bn-Nos at the tested dose.

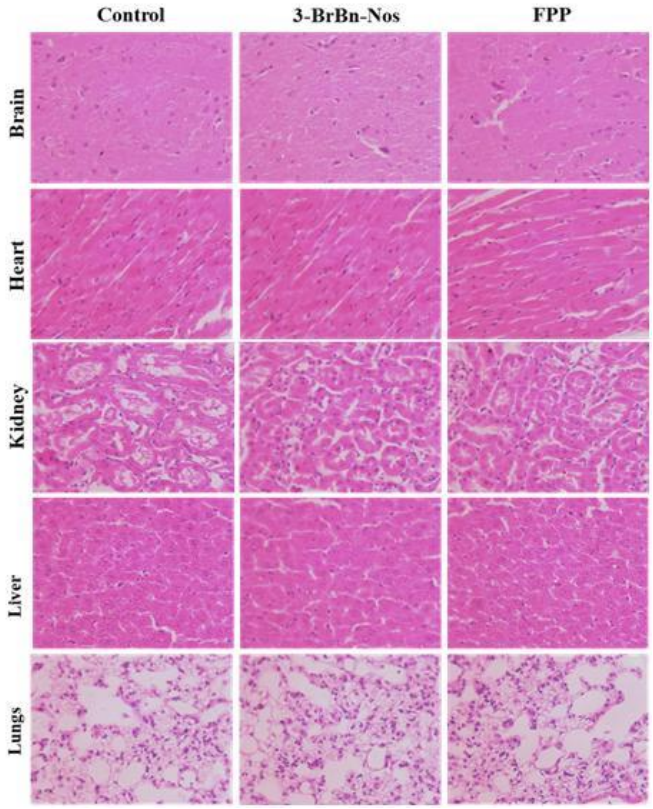

Fig. 4.9. Representative histological sections of major organs (heart, brain, kidney, liver, and lungs) were stained with hematoxylin and eosin (H&E) and observed at 40x magnification.

4.4. Conclusion

The present study highlights the potential of 3-bromo-benzyl noscapine (3-Br-Bn-Nos) as an effective anticancer agent and demonstrates that its therapeutic performance is significantly improved through folate-targeted polymeric nanoparticle (FPP) delivery. Despite its inherent poor aqueous solubility, the nanoformulation enabled better solubility, enhanced cellular uptake, and a marked reduction in the IC_{50} across the tested cancer cell lines while sparing normal cells. Mechanistic studies revealed the induction of apoptosis, mitochondrial dysfunction, and ROS generation in cancer cells, which was supported by the results of morphological and functional assays. Additionally, 3D spheroid disintegration assays further confirmed its potency in a more physiologically relevant model. The *in vivo* evaluation confirmed that FPP did not induce any significant hematological, biochemical, or histopathological abnormalities, confirming its safety. Overall, this study establishes 3-Br-Bn-Nos-loaded FPP as a promising and biocompatible anticancer formulation with improved bioavailability and targeted therapeutic efficacy.

CHAPTER-5

Rational Design, Chemical Synthesis, and Anticancer Activity of Novel Noscapine-Based Tubulin Inhibitors for Breast Cancer Therapy

Abstract

Breast cancer is one of the most prevalent malignancy among women worldwide, often necessitating the development of various novel chemotherapeutics with enhanced efficacy and safety. Noscapine, a tubulin-binding alkaloid with a favourable safety profile, is promising as an anticancer agent but is limited by low potency and aqueous solubility. To overcome these challenges, two novel noscapine derivatives, **13** and **14,** were synthesized and computationally validated via molecular docking and molecular dynamics simulations, confirming their strong binding affinities with tubulin. *In vitro* cytotoxicity assays revealed that compound **13** exhibited superior anticancer activity across T47D, MDA-MB-231, and MCF-7 breast cancer cell lines and significantly reduced cell viability compared with other derivatives. Apoptotic induction was confirmed by Hoechst 33342 and AO/EtBr dual staining, with compound **13** showing pronounced nuclear fragmentation and chromatin condensation. JC-1 staining revealed a notable decrease in the red/green fluorescence ratio, indicating the loss of the mitochondrial membrane potential. DCFDA staining revealed robust ROS generation. Cell migration assays at 24 and 48 h revealed significant inhibition by compound **13**, while 3D spheroid disintegration assays on days 3 and 5 further confirmed its tumor-inhibitory potential. *In vivo* acute and subacute toxicity studies in rats (500 mg/kg for 28 days) revealed no significant alterations in hematological, biochemical, or histopathological parameters compared with those of the controls. Overall, compound **13** demonstrated potent anticancer efficacy and a favourable safety profile, supporting its potential for further preclinical development.

Keywords: Noscapine, Breast cancer, Microtubule-targeting agents, Apoptosis, *In vivo* toxicity.

5.1. Introduction

Cancer remains one of the foremost global health challenges, with breast cancer being the most commonly diagnosed malignancy among women worldwide. (Arnold *et al*., 2022) These challenges have intensified the search for novel anticancer agents that are not only effective but also safer and more selective.

Noscapine, a naturally occurring benzylisoquinoline alkaloid derived from *Papaver somniferum* (opium poppy), has emerged as a promising lead compound for this purpose. (Vadhel *et al*., 2023) Unlike classical microtubule-targeting agents such as paclitaxel or vincristine, noscapine exerts its anticancer activity by modulating microtubule dynamics without altering the overall polymer mass. (Altinoz *et al*., 2019) This subtle interference leads to mitotic arrest and subsequent apoptotic cell death, suggesting a distinct mechanism with reduced toxicity. (Wordeman & Vicente, 2021) Importantly, noscapine does not cause depolymerization of microtubules, which is typically associated with the neurotoxicity of many traditional agents. In addition to its mitotic effects, noscapine disrupts mitochondrial function, increases oxidative stress, and impairs cellular integrity features that collectively contribute to its cytotoxic potential. (Landen *et al*., 2002)

Although noscapine possesses several desirable attributes, including oral bioavailability and a favourable safety profile, its clinical utility is restricted by moderate potency and limited aqueous solubility. These drawbacks have motivated the synthesis of structurally modified derivatives aimed at enhancing biological efficacy and overcoming pharmacokinetic limitations.(Dash *et al.*, 2023) In this context, the present study focuses on two novel noscapine derivatives, such as compound **13** and **14**, which were developed through strategic chemical modifications intended to improve tubulin interactions, cellular uptake, and anticancer activity.

This chapter provides a comprehensive assessment of the newly synthesized noscapine derivatives, combining computational modelling with biological evaluations to determine their potential as improved anticancer candidates. The findings aim to guide future preclinical development by identifying compounds with both enhanced therapeutic efficacy and acceptable safety profiles.

5.2. Materials and methods

5.2.1. Rational design and synthesis of noscapine derivatives

A variety of noscapine derivatives have been synthesized in previous studies, many of which are undergoing different stages of preclinical and clinical testing. In our further

attempts to develop additional derivative of Noscapine with improved biological efficacy, we conjugated the 1,3,4-thiadiazole) benzamide derivatives to the scaffold structure. This is because the 1,3,4-thiadiazole) benzamide derivatives have been reported for their cytotoxicity against various cancer cell types such as prostate (PC-3) and breast cancer **(**MCF-7 and MDA-MB-231 breast cancer**)** and colon cancer (Janowska *et al.*, 2022). Therefore, this functional group has been substituted in the native noscapine scaffold to develop a new derivative of the noscapine, that is 2-bromo-5-methoxy-N-(5-((4-(((S)-5-methoxy-1-((R)-4-methoxy-6-methyl-5,6,7,8-tetrahydro-[1,3]dioxolo[4,5-g]isoquinolin-5-yl)-3-oxo-1,3-dihydroisobenzofuran-4-yl)oxy)butyl)thio)-1,3,4-thiadiazol-2-yl)benzamide **(13)**. Similarly, coumarins are naturally occurring benzopyrone compounds with various biological activity. When modified with a nitro group, this group of compounds have anticancer activity mainly because it disrupts microtubule formation (Zhang and Xu, 2019). Therefore, 6-nitro coumarin functional group has been substituted to the scaffold to generate a new derivative of noscapine, that is 3-(((R)-5-((S)-4,5-dimethoxy-3-oxo-1,3 dihydroisobenzofuran-1-yl)-4-methoxy-7,8dihydro-[1,3]dioxolo[4,5-g]isoquinolin-6(5H)-yl)methyl)-5-nitro-1H-isochromen-1-one **(14)**. Both the derivatives of Noscapine were used for molecular docking to determined their binding affinity with αβ-tubulin dimmer. (Janowska *et al.*, 2022; Zhang & Xu, 2019)

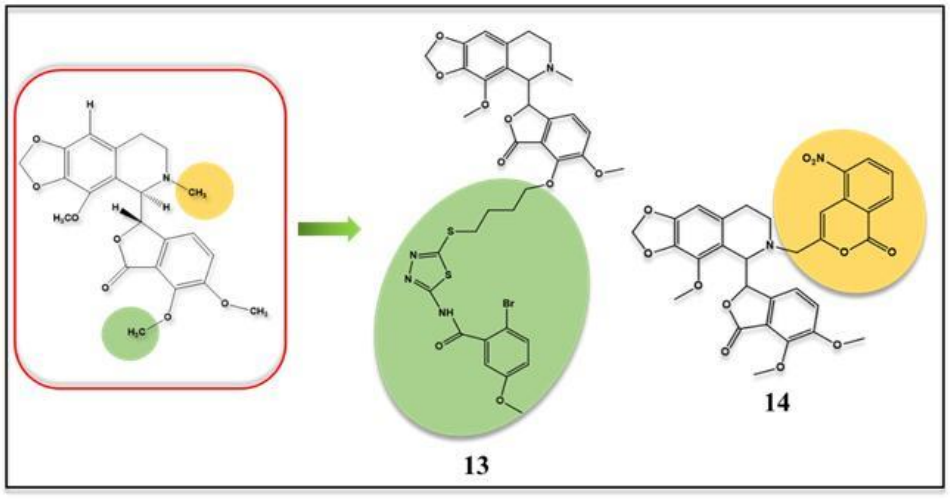

Figure 5.1. Molecular structure of newly developed Noscapine derivatives (**13** and **14**) by substituting different functional groups on the noscapine scaffold.

5.2.2. Protein Preparation

The X-ray crystallographic structure of the noscapine–tubulin protein complex (PDB ID: 646D, resolution 3.58 Å) was employed for molecular docking and rescoring studies. (Oliva *et al.*, 2020) After carefully inspecting and refining the structure, both the 'A' and 'B' chains of the protein were preserved in the final complex. Hydrogen atoms were added

automatically using the Maestro interface (version 8.5, Schrödinger, LLC), ensuring the absence of lone pairs and the application of an explicit all-atom model. All water molecules were excluded from the structure. The final preparation of the protein was carried out using Schrödinger's multistep protein preparation tool (PPrep). The resulting complex was then subjected to energy minimization using the OPLS 2005 force field in combination with the Polak-Ribiere Conjugate Gradient (PRCG) algorithm. The minimization process was terminated upon reaching either 5,000 steps or when the energy gradient fell below 0.001 kcal/mol.

5.2.3. Ligand Preparation

The molecular structures of the noscapinoids **(13 and 14)** were constructed using the molecular builder in Maestro (version 8.5). These structures were then energy minimized in vacuum using Impact (version 5.6; Schrödinger, LLC). Appropriate bond orders were assigned to each compound using LigPrep (version 2.4, Schrödinger, LLC), followed by initial optimization with the OPLS 2005 force field using default parameters. The full geometrical optimization of the ligand structures was conducted using hybrid density functional theory (DFT) with the B3LYP functional, which combines Becke's three-parameter exchange and the Lee-Yang-Parr correlation functionals. (Becke, 1993; Lee *et al.*, 1988) The calculations employed the 3-21G* basis set. (Binkley *et al.*, 1980; Gordon *et al.*, 1982; Pietro *et al.*, 1982) Geometrical optimizations of the ligands were conducted using Jaguar (version 7.7, Schrödinger, LLC).

5.2.4. Molecular Docking of Ligands

Glide (version 4.5, Schrödinger, LLC) was used to docked **13 and 14** onto the tubulin receptor. (Friesner *et al*., 2004; Halgren *et al*., 2004) The receptor grid file was created using the grid receptor generation tool with van der Waals scaling of 0.4 Å after ensuring that the proteins and ligands were in the proper shape for docking. The bounding and enclosing boxes were then created with a grid box size of 10 Å, at the centroid of the tubulin-predicted binding sites using SiteMap, version 2.4, Schrödinger, LLC. The ligands were first docked using the "standard precision" approach, followed by refinement with the "extra precision" Glide algorithm. During docking, the van der Waals radius of the ligands was scaled to 0.4 Å. From an initial pool of 50,000 sampled poses, 4,000 underwent energy minimization using 1,000 steps of the conjugate gradient method. Among these conformations, the 30 lowest-energy conformations were selected for further evaluation on

the basis of their Glide docking scores. Ultimately, the best single conformation of every ligand was chosen for additional rescoring.

5.2.5. Molecular dynamic simulation

Molecular dynamics (MD) simulation was performed using GROMACS version 2019.2 to study the complex formed between tubulin and the noscapinoids, along with GTP, GDP, and magnesium ions. (Abraham *et al*., 2015) Docked conformations exhibiting the lowest binding energies were selected for the simulation. The protein was parameterized using the Amber99SB force field (Hornak *et al.*, 2006), whereas the GTP, GDP, and noscapinoids were processed using the General Amber Force Field (GAFF) via the Antechamber module from Amber 18. Atomic partial charges for the ligands were assigned using the AM1-BCC method. (Jakalian *et al*., 2002) Ligand topologies and coordinates were generated using Amber's tleap tool and ACPYPE. (Sousa Da Silva & Vranken, 2012) The solvated system was placed in a truncated octahedral box with a 12 Å buffer between the solute and box edges, using TIP3P water molecules. (Kumar Pedapati *et al*., 2023) To simulate physiological conditions, the system was neutralized and adjusted to an ionic strength of 0.15 M with counterions. Energy minimization was carried out using 10,000 steps of the steepest descent algorithm to remove steric clashes. Equilibration involved a 500 ps NVT run at 300 K followed by an NPT ensemble with positional restraints of 10 kcal/mol·Å², using the Martyna-Tobias-Klein barostat to maintain pressure at 1 bar. A 100 ns production run was subsequently conducted with a 2 fs time step. Long-range electrostatic interactions were computed using the Particle Mesh Ewald (PME) method, with a 10 Å cut-off applied to both van der Waals and short-range electrostatic interactions. Bond constraints were applied using the SHAKE algorithm, (Ryckaert *et al.*, 1977) and temperature regulation was maintained with Nose-Hoover chain thermostat. Atomic coordinates were recorded every 20 ps. Trajectory analyses were performed for the root mean square deviation (RMSD), and root mean square fluctuation (RMSF) were performed using GROMACS tools, with the plots generated in GRACE. The representative derived structures with the lowest total energy from the trajectory were used to elucidate the ligand binding mechanisms.

5.2.6. Predictive binding affinity using MM-PBSA technique

The binding free energies of noscapinoids (**13**, and **14)** were estimated using the Molecular Mechanics Poisson–Boltzmann Surface Area (MM-PBSA) method. (Kollman *et al*., 2000) From the final 10 ns of the MD simulation, 500 snapshots were extracted at 20 ps intervals

to calculate the average predicted binding free energy (ΔG_bind pred) using the MM-PBSA tool as per the following equation:

$$\Delta G_{bind,pred} = \Delta G_{complex} - [\Delta G_{Rec} + \Delta G_{lig}]$$

The total Gibbs free energy (G) was computed as:

$$G = E_{gas} + G_{sol} - TS$$

$$E_{gas} = E_{int} + E_{ele} + E_{vdw}$$

$$G_{sol} = G_{PB(GB)} + G_{sol-np}$$

$$G_{sol-np} = \gamma SAS$$

where E_gas is the gas-phase energy, consisting of internal energy (E_int), electrostatic energy (E_ele), and van der Waals energy (E_vdw). G_sol is the solvation free energy, comprising both polar (G_PB) and nonpolar (G_sol-np) components. G_sol-np represents the nonpolar solvation energy, which is calculated as γ × SASA (solvent-accessible surface area), with γ set at 0.0072 kcal/mol. The polar solvation energy (G_PB) includes contributions from electrostatic interactions (E_ele) and the Poisson–Boltzmann calculations. Owing to their strong binding affinities toward tubulin, favourable docking scores, and superior predicted free energies compared with those of the parent compound, both the derivatives of Noscapine were selected for chemical synthesis and further experimental validation.

5.2.7. Binding affinity prediction using MM-GBSA calculation

Prime MM-GBSA is used to calculate the binding free energy between a ligand and its receptor. This method integrates molecular mechanics energy from the OPLS force field (EMM), a polar solvation term based on the surface generalized Born (GSGB) model, and a nonpolar solvation term (G_{NP}). The total binding free energy was calculated using the following equation:

$$\Delta G_{bind} = G_{complex} - (G_{protein} + G_{ligand})$$

$$G = E_{MM} + G_{SGB} + G_{NP}$$

The G_{NP} component accounts for the nonpolar solvent-accessible surface area and van der Waals contributions. The docked complexes were further refined using the local minimization option in Prime (version 2.2, Schrödinger). Energy calculations were performed using the OPLS 2005 force field in combination with the GBSA continuum

solvation model, as described previously. (Bag *et al*., 2010) During minimization, protein residues located more than 12 Å from the ligand binding site were held rigid.

5.2.8. ADME Property Prediction

The ADME (absorption, distribution, metabolism, and excretion) profiles of noscapinoids **13** and **14** were predicted using QikProp, which analyzes 44 different pharmacokinetic parameters. Parameters with a value of zero were excluded from the analysis. The compounds were further assessed on the basis of the number of violations of Lipinski's Rule of Five.

5.2.9. Chemical synthesis of noscapine derivatives

Both the Noscapine derivatives were chemically synthesized using the parent compound, noscapine, as the starting material. The synthesis process was particularly challenging, labor intensive, and time consuming because of the presence of a highly reactive C–C bond between the isoquinoline and isobenzofuranone rings, which is sensitive to strongly acidic and basic conditions. Nevertheless, by carefully selecting appropriate solvents and optimizing the reaction conditions, we were able to preserve the integrity of these labile bonds during synthesis. Each reaction was monitored using thin-layer chromatography (TLC) on precoated silica gel plates and visualized under UV light. Both the intermediates and final products were structurally confirmed through ^{1}H and ^{13}C NMR spectroscopy in $CDCl_3$ using AVANCE spectrometers operating at 300, 400, and 500 MHz. High-resolution mass spectra were acquired using an ESI source on the QSTAR XL hybrid MS/MS system (Applied Biosystems/MDS Sciex, Foster City, USA), supported by IICT, Hyderabad. All reactions were performed under magnetic stirring in an oven-dried glassware. Analytical TLC on silica gel GF254 plates was routinely used to monitor progress. Visualization was performed under 254 nm UV light, followed by PMA staining and characterization of non-UV-active compounds. The solvents were evaporated under vacuum and gently heated at 35 °C in water bath. For column chromatography, fine silica gel (less than 200 mesh) was employed. The columns were packed with a hexane slurry and calibrated with the appropriate solvent system before the compound was loaded as a concentrated solution or solid. Elution was aided by pressure using an air pump. Unless otherwise mentioned, reported yields correspond to pure compounds confirmed by chromatography and spectroscopy. The compound structures and nomenclature were assigned using ChemBioDraw Ultra 14.0. Melting points were determined via a Fischer–Johns apparatus and are uncorrected. Analytical HPLC (SPD-M20A, Shimadzu) with an ODS column and

gradient elution (acetonitrile–water) confirmed the purity of the compounds (>96%) prior to biological testing. FT-IR spectra were recorded using neat liquids or KBr pellets, with absorption bands reported in cm^{-1}. NMR data were acquired in appropriate solvents using 300 MHz (Bruker) and 500 MHz (Varian) instruments, with tetra methyl silane (TMS) as an internal reference or residual solvent peaks as secondary references. Chemical shifts are reported in δ (ppm), and signal multiplicities are denoted as s (singlet), d (doublet), t (triplet), q (quartet), br (broad), and m (multiplet, for unresolved signals). ^{13}C NMR spectra were obtained using a 75 MHz spectrometer. High-resolution mass spectrometry (HRMS) was performed using ESI-QTOF. Optical rotations were measured at 25 °C using a Rudolph Digipol 781 polarimeter. Commercial solvents such as hexane, dichloromethane (CH_2Cl_2), and ethyl acetate (EtOAc) were used without any further purification. Natural α-noscapine was procured from Sigma-Aldrich and used as received. The synthetic routes for both the noscapine derivatives are illustrated in the following reaction schemes.

Chemical Synthesis of compound 13:

Natural α-noscapine was treated with sodium azide (NaN_3) and sodium iodide (NaI) in DMF at elevated temperatures (135–140 °C) for 4 hours. This reaction led to the demethylation of the 7-methoxy group of noscapine. In the next step, the intermediate was subjected to alkylation using 2-bromo-N-(5-((4-bromobutyl)thio)-1,3,4-thiadiazol-2-yl)-5-methoxybenzamide in the presence of potassium carbonate (K_2CO_3) as base in DMF at 50 °C for 4 hours. The detailed synthetic scheme was mentioned below. The reaction resulted in the desired noscapine–thiadiazole (compound **13)** hybrid compound with a yield of 92%.

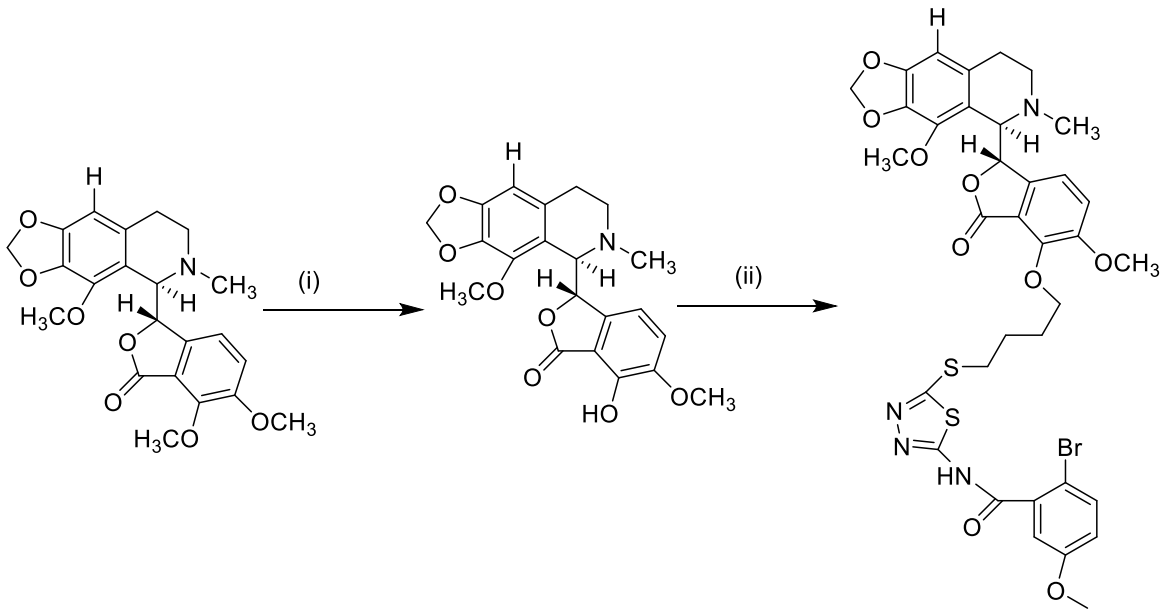

Reaction Scheme 1. Synthesis of compound **13**.

Reaction Conditions: (i) NaN_3/NaI, DMF, 4 h, 135–140 ºC, 75% (ii) 2-bromo-N-(5-((4-bromobutyl)thio)-1,3,4-thiadiazol-2-yl)-5-methoxybenzamide/K_2CO_3/DMF, 50 ºC, 4 h, 92% yield.

2-bromo-5-methoxy-N-(5-((4-(((S)-5-methoxy-1-((R)-4-methoxy-6-methyl-5,6,7,8-tetrahydro-[1,3]dioxolo[4,5-g]isoquinolin-5-yl)-3-oxo-1,3-dihydroisobenzofuran-4-yl)oxy)butyl)thio)-1,3,4-thiadiazol-2-yl)benzamide (13): Yield: 95%; mp 65 °C; $[\alpha]_D^{25}$ = 52.0 (c = 1, Dichloromethane); IR νmax (cm^{-1}): 3343, 2927, 2849, 1755, 1615, 1496, 1387, 1263, 1212, 1035, 891, 790, 689. ^{1}H NMR (300 MHz, $CDCl_3$): δ 7.52 (d, *J*= 8.30 Hz, 1H), 7.22 (s, 1H), 6.91 (d, *J*= 8.30 Hz, 1H), 6.82 (d, J= 8.30 Hz, 1H), 6.30 (s, 1H), 6.02 (d, *J*= 8.30 Hz, 1H), 5.91 (s, 2H), 5.04 (d, *J* = 4.72 Hz, 1H), 4.38 (d, *J* = 4.72 Hz, 1H), 4.20 (m, 2H), 4.01 (s, 3H), 3.86 (s, 6H), 3.28 (t, 2H), 2.54 (m, 1H), 2.51 (s, 3H), 2.39 (t, 2H), 1.91 (m, 6H). ^{13}C NMR (75 MHz, $CDCl_3$):168.0, 165.2, 160.6, 159.7, 158.7, 152.4, 148.3, 146.4, 140.9, 140.3, 135.0, 134.5, 133.9, 131.9, 120.4, 119.1,118.0, 117.7, 116.8, 114.9, 110.3, 102.2, 100.7, 81.6, 73.8, 60.7, 59.3, 56.6, 55.6, 49.8, 46.1, 33.4, 28.8, 27.8, 25.5. HRMS (ESI) m/z 799.1102 $[M+H]^+$; (Calcd: 798.1029 for $C_{35}H_{35}BrN_4O_9S_2$). The ^{1}H-NMR, ^{13}C-NMR and mass spectra (ESI and HR-MS) of the final product were included as supporting material in the appendix (Figure S1-S5).

Chemical Synthesis of compound 14:

(S)-6,7-dimethoxy-3-((R)-4-methoxy-5,6,7,8-tetrahydro[1,3]dioxolo[4,5-g]isoquinolin-5 yl) isobenzofuran-1(3H)-one: To a stirred solution of natural α-noscapine (2.0 g, 4.84 mmol) in dichloromethane (15 mL), meta-chloroperbenzoic acid (mCPBA, 1.66 g, 9.7 mmol) was added in portions at 0 °C. The reaction mixture was then continuously stirred at room temperature for 1 hour. After completion, it was diluted with dichloromethane (20 mL), and excess oxidant was quenched using 15 mL of 1 M aqueous sodium bisulfite. The organic layer was separated, dried over anhydrous sodium sulfate, and concentrated under reduced pressure. The resulting residue was dissolved in methanol (20 mL), acidified to pH 1.0 using 2N HCl, stirred for 5 minutes, and filtered. The filtrate was evaporated under vacuum, and the residue was redissolved in dichloromethane (20 mL), dried over sodium sulfate, filtered, and concentrated to obtain the pale yellow solid α-noscapine N-oxide hydrochloride salt. This intermediate was then dissolved in methanol (20 mL), and ferrous sulfate heptahydrate ($FeSO_4 \cdot 7H_2O$, 2.69 g, 9.68 mmol) was added. The mixture was stirred at room temperature for 12 hours. After concentration, the residue was basified to pH 10 using 25% aqueous ammonia and extracted with dichloromethane (3 × 10 mL). The combined organic extracts were dried over sodium sulfate and evaporated. The crude

product was purified by column chromatography on triethylamine-treated silica gel, using ethyl acetate:hexane (3:7 and 2:3) as the eluent, to afford compound as a white solid (0.92 g, 48% yield). mp 170°C; [α]D 25= -105.6 (c=1, methanol), Yield: 48%; IRν_{max} (cm^{-1}): 3360, 2942, 1759, 1624, 1501, 1280, 1119, 1074, 1042, 1023, 932, 796, 679. ^{1}H NMR (300 MHz, $CDCl_3$): δ 6.94 (d, *J* = 8.30 Hz, 1H), 6.33 (s, 1H), 5.99-5.89 (m, 4H), 4.85 (d, *J*=4.53 Hz, 1H), 4.09 (s, 3H), 4.07 (s, 3H), 3.85 (s, 3H), 2.69-2.58 (m, 1H), 2.54-2.42 (m, 1H), 2.36-2.23 (m, 1H), 2.22-2.09 (m, 1H). ^{13}C NMR (75MHz, $CDCl_3$) δ 168.5, 152.1, 148.3,147.8, 141.0, 140.4, 134.1, 131.9, 119.6, 118.3, 117.5, 116.9, 103.1, 100.7, 20.6, 62.2, 59.4, 56.6, 52.7, 39.5, 29.7. HRMS (ESI) $[M+H]^+$: m/z 400.1391, (Calcd 399.1318 for $C_{21}H_{21}NO_7$).

3-(((R)-5-((S)-4,5-dimethoxy-3-oxo-1,3-dihydroisobenzofuran-1-yl)-4-methoxy-7,8-dihydro-[1,3]dioxolo[4,5-g]isoquinolin-6(5H)-yl)methyl)-5-nitro-1H-isochromen-1-one: The target compound was synthesized by N-alkylation of the intermediate using 3-(bromomethyl)-5-nitro-1H-isochromen-1-one as the electrophilic coupling partner in the presence of triethylamine (TEA) as a base. The reaction mixture was stirred at room temperature for 4 hours, affording the N-substituted noscapine derivative in excellent yield (96%). The detailed of the synthetic scheme was mentioned below. The structure of the final compound was confirmed by spectral analysis, including ^{1}H NMR (300 MHz), ^{13}C NMR (75 MHz), and HRMS, and the data are provided in the appendix as supporting information.

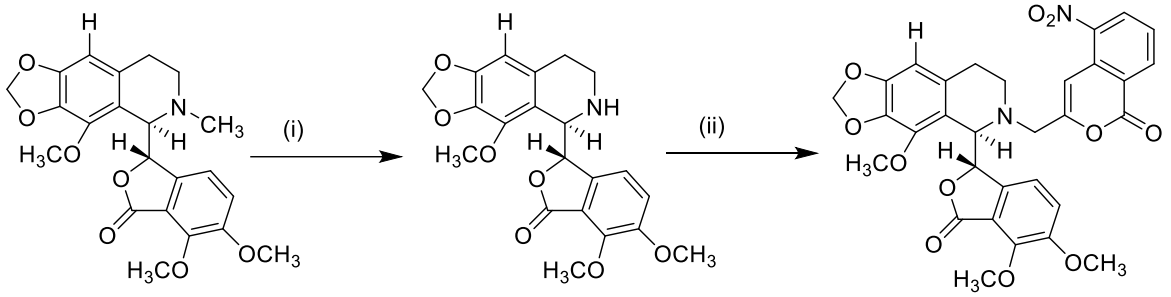

Reaction Scheme 2. Synthesis of compound **14**.

Reaction Conditions: (i) a: m-CPBA, DCM; b: 2N HCl; c: $FeSO_4.7H_2O$; (ii) 3-(bromomethyl)-5-nitro-1H-isochromen-1-one, TEA, RT, 4h, 96% yield.

3-(((R)-5-((S)-4,5-dimethoxy-3-oxo-1,3-dihydroisobenzofuran-1-yl)-4-methoxy-7,8-dihydro-[1,3]dioxolo[4,5-g]isoquinolin-6(5H)-yl)methyl)-5-nitro-1H-isochromen-1-one (14): Yield: 97%; mp 65 °C; $[\alpha]_D^{25}$ = 52.0 (c = 1, Dichloromethane); IR νmax (cm^{-1}): 2941, 2844, 1739, 1613, 1457, 1393, 1278, 1208, 1088, 901, 790, 685. ^{1}H NMR (300 MHz, $CDCl_3$): δ 8.56(d, *J*= 8.30 Hz, 1H), 8.40(d, *J*= 8.30 Hz, 1H), 7.51-7.60(m, 1H), 7.15

(s, 1H), 7.02 (d, *J*= 8.30 Hz, 1H), 6.38 (s, 1H), 6.18 (d, *J*= 8.30 Hz, 1H), 5.88 (s, 2H), 5.61 (d, *J*= 4.72 Hz, 1H), 4.78 (d, *J*= 4.72 Hz,1H), 4.02 (s,3H), 3.98 (s, 3H), 3.87 (s, 3H), 3.81 (s, 2H), 2.80-2.86 (m, 1H), 2.58-2.64 (m, 1H), 2.47-2.56 (m, 1H), 2.18-2.29 (m, 1H). ^{13} C NMR (75 MHz, $CDCl_3$): 167.7, 160.4, 159.2, 152.3, 148.6, 147.8, 143.8, 140.4, 140.3, 135.5, 134.1, 131.5, 131.3, 131.1, 126.9, 122.3, 119.5, 118.6, 117.5, 116.5, 102.4, 100.8, 98.1, 81.8, 62.0, 59.4, 59.3, 58.8, 56.7, 47.1, 28.1. HRMS (ESI) $[M+H]^+$: m/z 603.1609, (Calcd 602.1537 for $C_{31}H_{26}N_2O_{11}$). The FT-IR, UV-visible, ^{1}H-NMR, ^{13}C-NMR and mass spectra (ESI and HR-MS) of the final product were included as supporting material in the appendix (Figure S6-S10).

5.2.10. Cell culture and reagents

The natural compound used in this study, noscapine, was procured from Sigma–Aldrich. All other reagents and cell culture media were also obtained from Sigma. The human breast cancer cell lines MDA-MB-231, MCF-7, and T47D were sourced from the National Centre for Cell Science (NCCS), Pune, Maharashtra, India. The cells were cultured in DMEM or RPMI medium supplemented with 10% fetal bovine serum (FBS), along with epidermal growth factor (EGF, 100 µg/mL), insulin (10 µg/mL), hydrocortisone (1 µg/mL), and 1% antibiotic. The cells were maintained in a humidified incubator at 37 °C with 5% CO_2.

5.2.10.1. *In vitro* assessments of the cytotoxicity of the designed compounds in breast cancer cells

The antiproliferative activity of the two noscapine derivatives was evaluated using MTT assay [3-(4,5-dimethylthiazol-2-yl)-2,5-diphenyltetrazolium bromide] in the three different breast cancer cell lines, MCF-7, MDA-MB-231, and T47D. The cancer cells (5000 cells per well) were seeded into 96-well plates and allowed to adhere for 24 hours. Post-attachment, the cells were treated with varying concentrations of noscapine derivatives. Treatments were carried out in complete growth medium for 48 to 72 hours. To assess cell viability, 10 µL of MTT solution (5 mg/mL) was added to each well, and the mixture was incubated for 3–4 hours at 37 °C. The resulting formazan crystals were then dissolved in DMSO, and the absorbance was recorded at 570 nm using a microplate reader (Bio-Rad). The IC_{50} values, which represent the concentration required to inhibit 50% cell viability, were calculated by using the GraphPad Prism 10.4.2.

5.2.10.2. Acridine Orange & Ethidium bromide (EtBr) staining

Apoptotic changes in MDA-MB-231 cells following treatment with noscapinoids were evaluated using dual staining with acridine orange (AO) and ethidium bromide (EtBr), followed by fluorescence microscopy. MDA-MB-231 cells were seeded onto 6-well culture plates and treated with the IC_{50} concentrations of the noscapinoids, and noscapine for 72 hours. After treatment, the cells were washed twice with cold PBS, fixed with 4% paraformaldehyde (PFA) solution and stained with a mixture of AO and EtBr in PBS. The stained cells were immediately observed under a fluorescence microscope (Nikon Eclipse Ts2R-FL), where live cells displayed uniform green fluorescence, early apoptotic cells presented bright green nuclei with condensed chromatin, late apoptotic cells presented orange to red fluorescence with nuclear fragmentation, and necrotic cells appeared deep red due to membrane disruption. (Kasibhatla *et al*., 2006)

5.2.10.3. Nuclear morphological evaluation by Hoechst staining

Changes in the morphology of the nucleus in response to treatment with noscapinoids were assessed using Hoechst staining followed by fluorescence microscopy. Briefly, MDA-MB-231 cells were cultured in 6-well plates and treated with noscapinoids, and noscapine at the IC_{50} concentration for 72 hours. After treatment, the cells were washed twice with ice-cold PBS and fixed with 4% paraformaldehyde (PFA). The fixed cells were then stained with Hoechst 33342 (1 µg/mL) and imaged using an inverted fluorescence microscope (Nikon Eclipse Ts2R-FL). Apoptotic cells were identified by characteristic nuclear features such as chromatin condensation, membrane blebbing, and the presence of apoptotic bodies.

5.2.10.4. Reactive oxygen species (ROS) generation by DCFDA

The increase in intracellular ROS is a latent characteristic that damage organelles, lipid membranes, and nucleic acids, ultimately leading to the death of cancer cells. By oxidatively converting the sensitive fluorescent probe, 2',7'-dichlorofluorescence-diacetate (DCFH-DA) in to fluorescent probe 2',7'-dichlorofluorescein (DCF), the intracellular ROS levels can be ascertained. MDA-MB-231 cells were treated with an IC_{50} concentration of noscapinoids, and noscapine for 48 hours in 6-well plates that were covered with glass. Additionally, the cells were then resuspended in DCFH-DA (10 µM; Molecular Probes Inc., Invitrogen) after being washed with PBS, after which they were allowed to sit at room temperature for 30 minutes in the dark. A Nikon Eclipse Ts2R-FL inverted fluorescence microscope was used for visualization.

5.2.10.5. Measurement of the mitochondrial membrane potential (ΔΨm)

The effects of the derivatives of noscapine, and noscapine on the potential of the mitochondrial membrane were assessed using JC-1 dye on a 6-well plate and exposed to the IC_{50} of the drugs for 48 hours. The samples were then stained with JC-1 (10 µg/ml) for 10 minutes, followed by washing with PBS at room temperature. After staining, the cells were subjected to two PBS washes before being observed at 400x magnification using a Nikon Eclipse Ts2R-FL inverted fluorescence microscope. In healthy cells, JC-1 forms J-aggregates that exhibit strong red fluorescence (higher ΔΨm), with excitation and emission at 560 nm and 595 nm, respectively. In apoptotic cells, JC-1 exists as a monomer and displays strong green fluorescence (lower ΔΨm), with excitation and emission at 485 nm and 535 nm, respectively.

5.2.10.6. Cell migration assay

The migration potential of MDA-MB-231 breast cancer cells upon treatment with noscapine derivatives was assessed using the wound healing assay. MDA-MB-231 cells were seeded in 6-well plates at a density of 3×10^5 cells per well and allowed to grow until a confluent monolayer formed. A uniform scratch (wound) was then created in the monolayer using a sterile 200 µL pipette tip. The wells were gently washed with phosphate-buffered saline (PBS) to remove detached cells and debris. The cells were then treated with noscapine derivatives (**13** and **14**) at IC_{50} concentrations, and an untreated control. Images of the wound area were recorded at 0, 24, and 48 hours using a phase-contrast inverted microscope. The experiment was performed in triplicate.

5.2.10.7. Three-dimensional (3D) spheroid disintegration assay

To assess the effects of noscapinoids in a 3D tumor-like structure, the 3D spheroid disintegration assay was performed. It offers a physiologically appropriate *in vivo* tumor microenvironment. Briefly, MDA-MB-231 cells were seeded in 96-well round-bottom plates with ultralow attachment (Corning) that contained 100 µl of whole medium at a density of 1×10^3 cells per well. For cell aggregation, the plate was centrifuged for 10 minutes at 1000 rpm. The mixture was then incubated for 7–10 days at 37 °C with 5% CO_2 to enable the formation of compact 3D spheroids. They were then treated with noscapinoids, and noscapine after the spheroids formed, and the untreated cells were used as a control. Every two days, new media was added to replace the spent media. After that, the treatments were given in triplicate, and over the course of five days, the spheroids were examined under a Nikon inverted phase-contrast microscope for morphological changes such as changes in spheroid integrity, diameter reduction, and disintegration.

5.2.11. *In vivo* antitumour efficacy against breast tumour xenograft model

Female BALB/c athymic nude mice aged 8--10 weeks were selected for the study. Each mouse was subcutaneously implanted in the anterior flank with approximately 1×10^6 MDA-MB-231 human breast adenocarcinoma cells suspended in 0.2 mL of phosphate-buffered saline (PBS). After a period of 7 to 10 days, when the tumors became palpable, compounds **13** and **14** were administered through oral gavage. The mice were randomly divided into two groups of five animals each. Group 1 was the untreated control and received acidified water (pH 4.0), while Group 2 and Group 3 were treated with compounds **13** and **14** with a dose of 150 mg/kg body weight per day. Tumor growth was observed and measured every other day following previous procedures. (Tomayko & Reynolds, 1989) All the animals were sacrificed on the 30th day, when there was a significant increase in tumor volume in the control group. The tumor volumes in both the treated as well as control groups were measured according to the procedure described above. The animal ethical approval for this study (Approval No. NIP/04/2022/PC/476) was obtained from the Institutional Animal Ethics Committee (IAEC) of the NIPER, Hyderabad.

5.2.12. Acute toxicity studies (Rodent-Rat)

Single doses of different concentrations, such as 250, 500, 1000, 2000 and 5000 mg/kg, of the noscapine derivatives (**13** and **14**) were administered orally to six groups, with six animals in each group (n=6). The rats were placed under observation for 14 days, after which the number of dead rats was recorded (OECD Test No. 423, 2008).

5.2.13. Subacute toxicity study of the noscapine derivatives using rats

Wistar rats were randomly divided into two groups with six animals in each group (n=6). The Noscapine derivatives (**13** and **14**) were administered orally with a daily dose of 500 mg/kg body weight for 28 days following the repeated oral toxicity test (OECD Test No. 408, 2008). The animals were observed daily to detect death or abnormal clinical signs. Body weight, water intake and food intake were recorded for 28 days.

5.2.14. Haematology and biochemical parameters of the animals in the treated and untreated groups

The animals were anaesthetized using mild anaesthesia (isoflurane) followed by cervical dislocation, and the blood was collected by cardiac puncture. Blood cell parameters were analysed via a CBC analyser (ByoVet). The collected blood was then centrifuged for 10 min at 5000 rpm (Eppendorf 5810r) for serum separation to study biochemical parameters

such as GLU, ALB, UREA, CREA, CHOL, TG, SGPT, SGOT, TP, HDL, ALP, etc., via an automated biochemical analyser (Byovet, Smart-5DX) with their respective standard kits.

5.2.15. *In vivo* histopathological analysis by hematoxylin and eosin (H&E) staining

Hematoxylin and eosin (H&E) staining of tissue sections from the brain, heart, liver, and kidneys of rats (n=6) treated with noscapinoids was used for histopathological analysis to assess toxicity in vital organs. The collected organs were fixed with 10% neutral buffer formalin. Then, the samples were subjected to dehydration and rehydration, cleaned with xylene, and finally embedded in paraffin (Medimas, India). A 3.5 µm thick paraffin section from each block was stained with hematoxylin & eosin (H&E) (Desouki *et al.*, 2015) to look over the autolytic changes in the tissue. A Nikon ECLIPSE Ts2R microscope was then used to view the stained tissue samples.

5.3. Results and Discussion

5.3.1. Molecular modelling

It was demonstrated that both *in vitro* and *in vivo* noscapine and its derivatives interact with the tubulin and modulate microtubule dynamics. These compounds are known to bind at the interface of α- and β-tubulin subunits. To determine the binding affinity of newly developed Noscapine derivatives **13** and **14** with tubulin heterodimer, the compounds were docked by Glide XP. The binding affinity with respect to docking score for both the molecules was found to be -5.485 (compound **13**) and -5.418 kcal/mol (compound **14**), suggesting strong binding affinity compared to that of Noscapine (docking score is -2.575 kcal/mol). Similarly, the docking energy for **13 and 14** was found to be -97.358 and -72.571 kcal/mol (Table 5.1). Further, the binding mode of **13 and 14** with the tubulin heterodimer was determined by LigPlot and included in Figure 5.2. Both the noscapine derivatives, **13** and **14** were found to be well accommodated inside the binding cavity (Figure 5.2 (a) and (b)) at the interface between α- and β- tubulin. Further, the LigPlot diagrams illustrate the distinct interaction profiles of **13 and 14** with tubulin residues. As shown in Figure 5.2(c) and (d), the interactions at the binding site include several hydrogen bonds and hydrophobic contacts, contributing to the overall binding stability. (Wallace *et al.*, 1995)

Table 5.1. Molecular docking results (Glide XPscore) and the relevant energy parameters of the designed noscapine derivatives with tubulin.

Ligands	Compound Structure	Glide Score (kcal/mol)	Glide Emodel (kcal/mol)
Noscapine	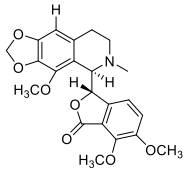	-2.575	-27.655
13	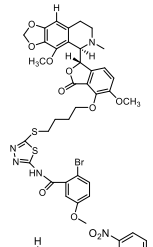	**-5.485**	**-97.358**
14	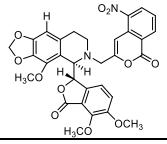	**-3.418**	**-72.571**

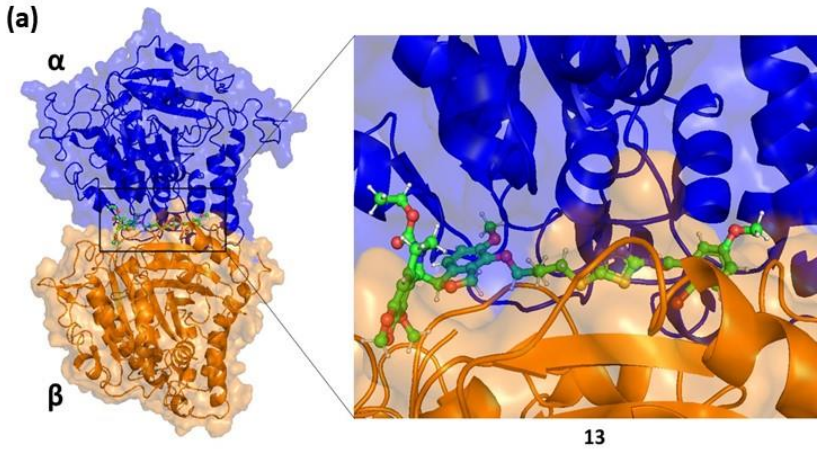

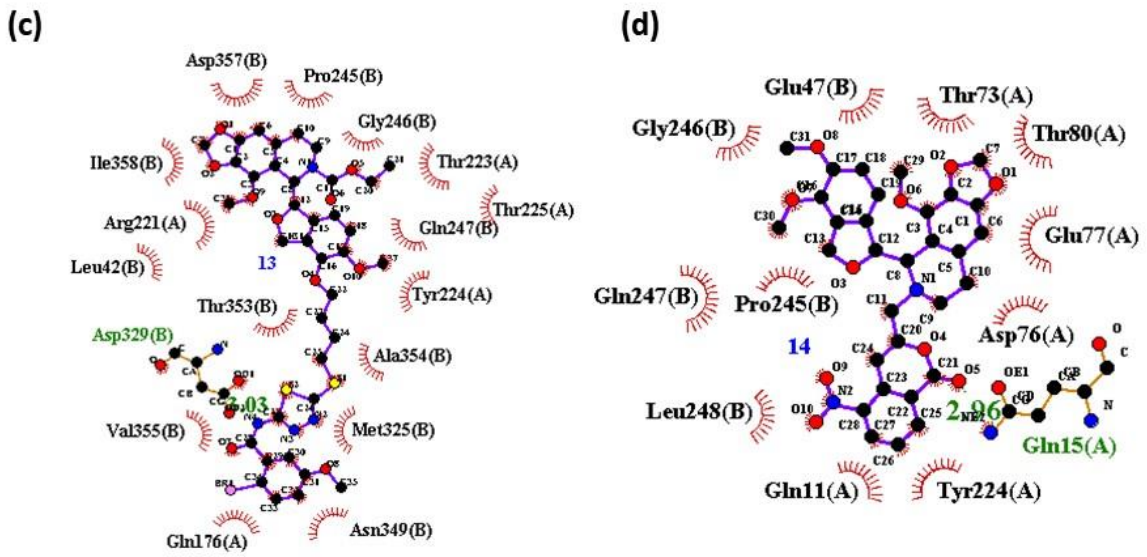

Figure 5.2. (a) The newly designed noscapinoids **13** and (b) **14** were well accommodated inside the noscapine binding site at the interface of α- and β- tubulin. (where, α-tubulin is represented in blue and β- tubulin in brown colour micromodel surface). Two-dimensional representation of the interaction between the binding site residues of tubulin and (c) **13** and (d) **14**. The dashed line represents hydrogen bonds, and the numbers indicate the hydrogen bond lengths in A^0. Hydrophobic interactions are shown as arcs with radical spokes. The figure was created using LIGPLOT.

The amino acids of the binding site involved in the binding of compound **13** were Asp 329 (B), Leu 42 (B), Arg 221 (A), Ile 358 (B), Asp 357 (B), Pro 245 (B), Gly 246 (B), Thr 223 (A), Thr 225 (A), Gln 247 (B), Tyr 224 (A), Ala 354 (B), Met 325 (B), Asn 349 (B), Gln 176 (A), and Val 355 (B). Binding of this noscapine derivative with tubulin involved hydrogen bonds with a bond length of 3.03 A^0. In the case of compound **14** binding with tubulin, the amino acids involved were Gln 15 (A), Tyr 224 (A), Gln 11 (A), Leu 248 (B), Gln 247 (B), Pro 245 (B), Gly 246 (B), Glu 47 (B), Thr 73 (A), Thr 80 (A), Glu 77 (A), and Asp 76 (A). The hydrogen bond involved in the binding of compound **14** and tubulin was 2.96 A^0. Moreover, a substantial number of hydrophobic interactions were observed in the binding of the two noscapine derivatives with their respective binding site residues, as detailed in Appendix Table S2.

5.3.2. Molecular dynamic simulation of the complex

The interaction of noscapinoids and tubulin was investigated through molecular dynamics (MD) simulations for 100 ns. Simulations were carried out for each tubulin-noscapinoid complex individually. To assess the stability of these systems, the root mean square deviation (RMSD) of the Cα atoms was calculated across all simulation frames. After the

equilibration phase, the RMSD values showed minimal fluctuations, and all systems remained stable beyond 20 ns of simulation (Figure 5.3a, and b). Additionally, the root mean square fluctuation (RMSF) of Cα atoms was analysed to evaluate residue-level flexibility throughout the simulation. Residues displaying higher RMSF values were interpreted as more flexible (Figure 5.4a, and b). All the noscapinoids maintained stable binding with tubulin for the entire duration of the MD run. Furthermore, the five tubulin–noscapinoid complexes with the lowest total energy from the simulation trajectories were selected to generate average structures for detailed binding mode analysis.

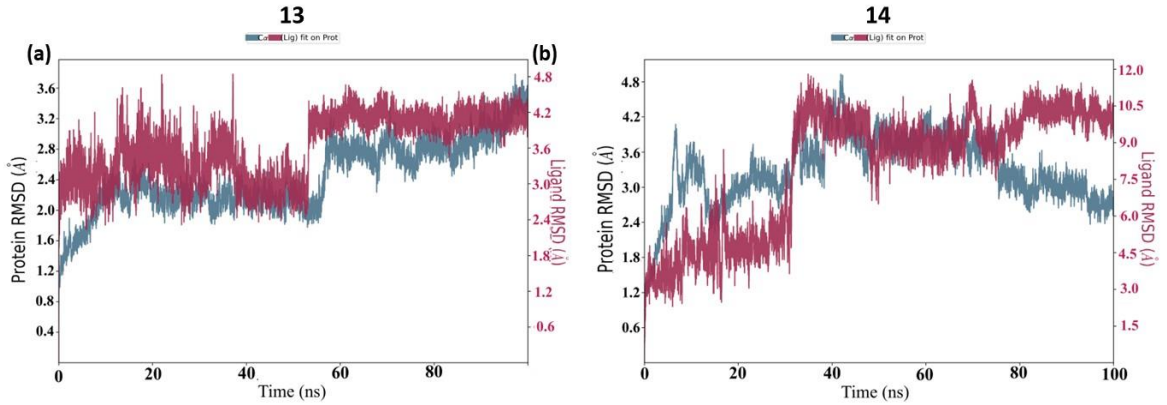

Figure 5.3. Representative figures of the root mean square deviations (RMSDs) of the Cα carbon atoms of tubulin only and in complex with compounds (a) **13** and (b) **14** during 100 ns of MD simulation.

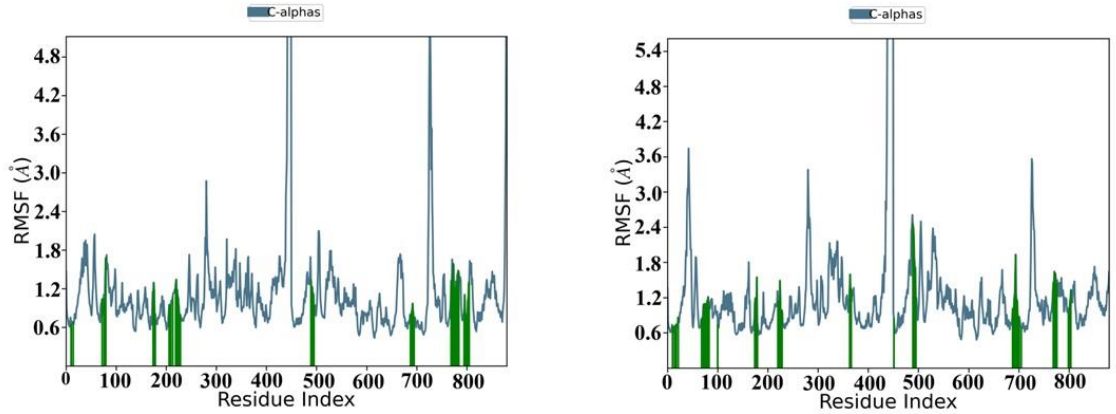

Figure 5.4. Representative figures of the root mean square fluctuation (RMSF) of the residues of tubulin in the bound form of the ligand compounds (a) **13** and (b) **14** with the tubulin heterodimer.

5.3.3. ADME Attribute Analysis

The ADME properties of native noscapine and its derivatives (compounds **13** and **14**) were evaluated using QikProp. The key parameters analysed included the molecular weight (MW), total solvent-accessible surface area (SASA), octanol/water partition coefficient

(QPlogPo/w), octanol/gas partition coefficient (QPlogPoct), water/gas partition coefficient (QPlogPw), polarizability (QPlogrz), brain/blood partition coefficient (QPlogBB), IC50 for HERG K^+ channel inhibition (QPlogHERG), skin permeability (QPlogKp), human serum albumin binding prediction (QPlogKhsa), and predicted permeability across Caco-2 and MDCK cell monolayers (QPPCaco and QPPMDCK, respectively). Caco-2 cells mimic the intestinal barrier, whereas MDCK cells represent the blood–brain barrier. To evaluate drug-likeness, the compliance of the compounds with Lipinski's Rule of Five was also evaluated. Notably, noscapine and its derivatives exhibited distinct ADME profiles but met the criteria of Lipinski's rule, indicating favourable drug-like characteristics (Table 5.2).

Table 5.2. QikProp was used to determine the ADME properties of noscapine and its derivatives (**13** and **14)**. These molecules are associated with all the ADME parameters.

	ADME Screening	**13**	**14**	**Noscapine**	**Recommended values**
1	MW	799.708	602.552	413.42	130-725
2	SASA	1151.177	741.050	597.02	300-1000
3	Accpt HB	13.200	7.450	8.75	2.0-20.0
4	QPpolrz	75.845	50.277	39.09	13.0-70.0
5	QPlogPoct	34.122	20.976	17.81	8.0-35
6	QPlogPw	16.449	9.518	10.08	4.0-45.0
7	QPlogPo/w	7.545	4.884	1.79	-2.0-6.5
8	QPlogHERG	-7.340	-6.106	-4.42	Below -5.0
9	QPPCaco	1046.869	1380.138	777.7	< 25 poor > 500 great
10	QPlogBB	-1.227	0.592	0.33	-3.0-1.2
11	QPPMDCK	3149.266	2055.244	417.06	< 25 poor >500 great
12	QPlogKp	-1.334	-2.779	-3.95	-8.0- -1.0
13	QPlogKhsa	1.237	0.579	-0.49	-1.5-1.5
14	Rule of Five (No. of violations)	3	2	3	Maximum is 4

5.3.4. Synthesis and spectral characterization of noscapine derivatives

The synthetic scheme used to prepare the two noscapine derivatives, **13** and **14,** were illustrated in Schemes 1 and 2. These compounds were obtained using the parent noscapine as the starting material. The synthesized noscapinoids were characterized by ^{1}H NMR, ^{13}C NMR, FT-IR, ESI-MS, and UV-spectroscopic analyses (represented in the supporting material (Figure S1-S10)).

5.3.5. Increased antiproliferative activity of Noscapine derivatives in breast cancer cells

The cytotoxic efficacy of the two noscapine derivatives **13** and **14** was assessed using MTT assays in different breast cancer cell lines, MCF-7 (estrogen receptor-positive), MDA-MB-231 (triple negative), and T-47D (also estrogen receptor-positive). Figure 5.5 clearly showed that both derivatives induced cytotoxic effects in a dose-dependent manner; however, the extent of response varied between the compounds and across different cell lines. Among the cell lines, MCF-7 (blue) and MDA-MB-231 (red) exhibited significantly increased sensitivity to compound **13**, as shown by their low IC_{50} values of 5.731 µM and 6.609 µM, respectively. In contrast, T-47D cells (black) were much more resistant to compound **13**, with an IC_{50} value of 62.05 µM, indicating a reduced cytotoxic response, as shown in Figure 5.5 (a). Similarly, compound **14** exhibited strong cytotoxic activity in both MCF-7 and MDA-MB-231 cell lines, with IC_{50} values of 9.611 µM and 11.01 µM, respectively, whereas T-47D cells were considerably less sensitive to compound **14**, with an IC_{50} value of 54.78 µM, suggesting moderate resistance (Figure 5.5 (b)). These findings suggested that both compounds were highly effective in inhibiting cell proliferation in both MCF-7 and MDA-MB-231 cells, whereas the viability of T-47D cells remained relatively high even at intermediate concentrations, dropping below 50% at only highest tested dose (100 µM). In summary, compounds **13** and **14** were more effective against MDA-MB-231 and MCF-7 cancer cells but had limited effects on T47D cells. Overall, MDA-MB-231 cells were indicating greater effectiveness of these derivatives against aggressive breast cancer subtypes.

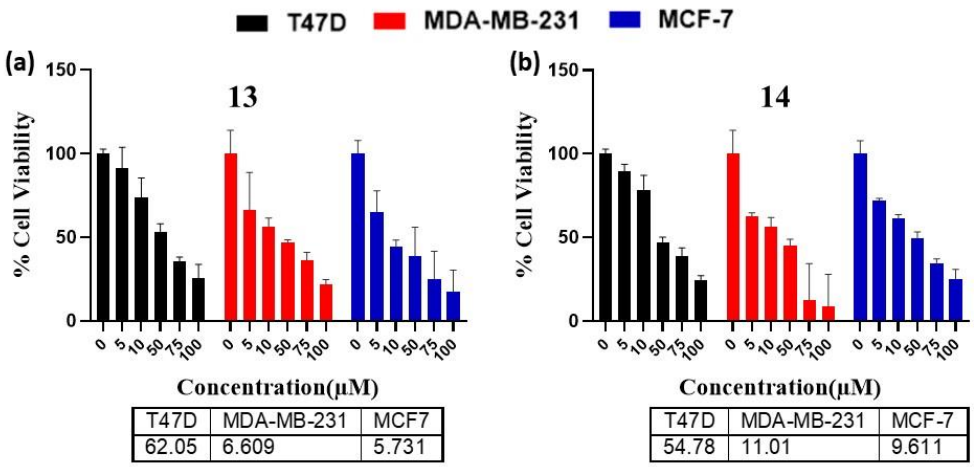

T47D	MDA-MB-231	MCF7
62.05	6.609	5.731

T47D	MDA-MB-231	MCF-7
54.78	11.01	9.611

Figure 5.5. Dose-dependent cytotoxic effects of noscapine derivatives (a) **13** and (b) **14** on breast cancer cell lines (T47D, MDA-MB-231, and MCF-7). Cell viability was assessed via the MTT assay after 48 h of treatment at various concentrations (0–100 µM). The data are presented as the means ± SDs (n=3).

5.3.6. Assessment of nuclear morphological changes by Hoechst 33342 staining

Hoechst 33342 staining was used to study the nuclear morphological alterations induced by treatment with the two noscapine derivatives in breast cancer cells. The fluorescence microscopy images in Figure 5.6 clearly indicate distinct nuclear features across the control and treated groups. In the untreated control group, the nuclei appeared uniformly stained with an intact, round morphology, indicating healthy, viable cells. In contrast, cells treated with compounds **13** and **14** exhibited prominent nuclear condensation and fragmentation. The red arrows point to condensed and fragmented nuclei, confirming the onset of apoptotic processes. Compared with the control treatment, the treatments with compounds **13** and **14** led to a significant increase in the number of intensely stained cells and fragmented nuclei. These results collectively indicate that the noscapine derivatives induced apoptosis in breast cancer cells through nuclear disintegration. These findings are consistent with prior reports highlighting the ability of noscapinoids to destabilize microtubules and initiate programmed cell death. The marked nuclear condensation observed in the treated groups confirms the cytotoxic nature of the derivatives and their potential efficacy as anticancer agents.

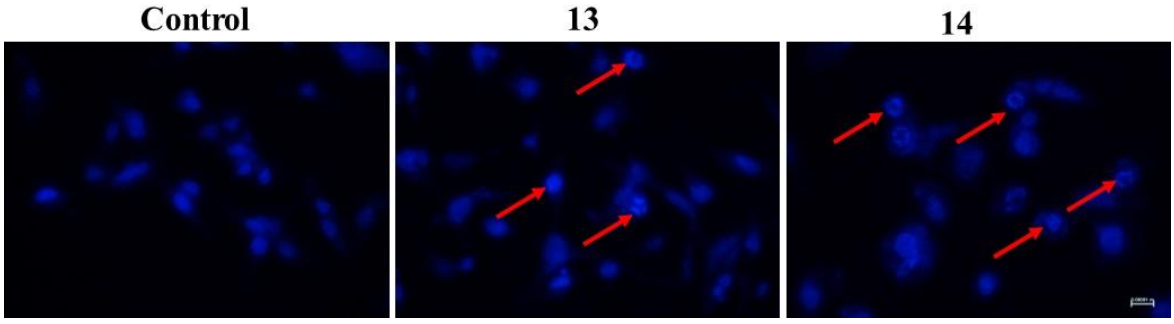

Figure 5.6. Representative Hoechst 33342-stained images of MDA-MB-231 cells induced with noscapine derivatives (**13** and **14**). Untreated cells were used as control.

5.3.7. Assessment of apoptotic morphology using AO/EtBr dual staining

The AO/EtBr dual-staining assay was used to analyze the mode of cell death induced by the noscapine derivatives in MDA-MB-231 breast cancer cells. As shown in Figure 5.7, untreated control cells presented uniformly green nuclei, indicating viable cells with intact membranes. In contrast, the treated cells displayed distinct morphological changes, including chromatin condensation and nuclear fragmentation, characterized by orange to reddish nuclei. Notably, cells treated with compound **13** displayed the most prominent apoptotic morphology, including condensed and fragmented nuclei with intense orange/red staining, suggesting that this compound has the strongest apoptotic effect among the tested

derivatives. Compound **14** also induced visible apoptotic features, although to a slightly lesser extent, with fewer apoptotic cells evident. These changes are indicative of early and late apoptosis, respectively, caused by the loss of membrane integrity and EtBr intercalation. The intensity and distribution of red/orange fluorescence increased progressively across the treated groups, suggesting a dose-dependent apoptotic effect of the compounds. The merged images further confirmed the apoptotic phenotype by revealing prominent orange-stained nuclei in the treated cells. These findings collectively revealed that the compounds induce apoptotic cell death in MDA-MB-231 breast cancer cells, as visualized by the differential uptake of acridine orange and ethidium bromide.

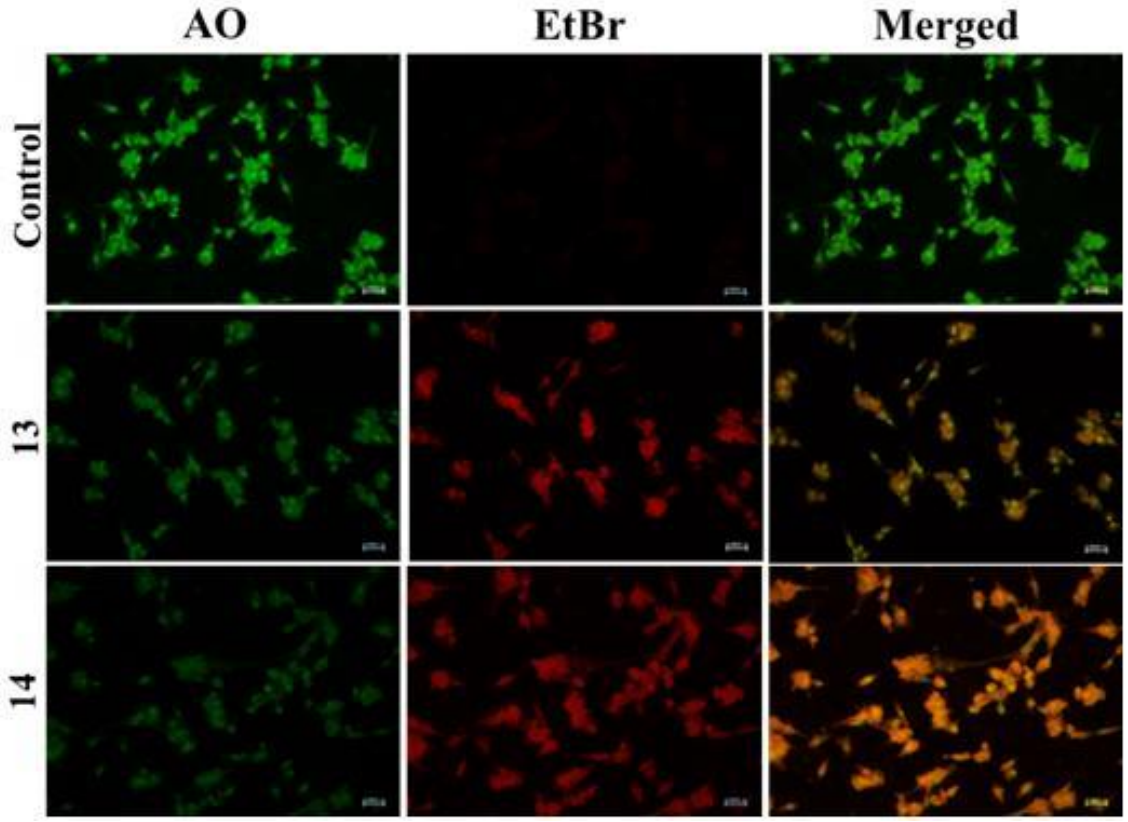

Figure 5.7. Representative AO/EtBr dual-staining images of MDA-MB-231 breast cancer cells treated with noscapine derivatives. The cells were treated with compounds **13** and **14** for 24 hours and stained with acridine orange (AO) and ethidium bromide (EtBr) to assess the nuclear morphology and mode of cell death. Untreated cells were used as controls.

5.3.8. Assessment of mitochondrial membrane potential induced by Noscapine derivatives using JC-1 fluorescence imaging

A JC-1 staining assay was used to evaluate the mitochondrial membrane potential ($\Delta\Psi m$) in MDA-MB-231 breast cancer cells, following the treatment with compounds **13** and **14**. As shown in Figure 5.8, in untreated control cells, intense red fluorescence was observed,

which is indicative of JC-1 aggregates in polarized, healthy mitochondria. This was reflected in a high red/green fluorescence ratio, indicating intact mitochondrial function. In contrast, treatment with compound **13** caused a significant reduction in red fluorescence and a substantial increase in green fluorescence, resulting in a strong decrease in ΔΨm. Consequently, a significantly reduced red/green fluorescence ratio was observed, confirming severe mitochondrial depolarization. Compound **14** also led to a decrease in red fluorescence and an increase in green fluorescence intensity, resulting in a moderately decreased red/green ratio and indicating partial disruption of mitochondrial integrity. The merged images further supported these findings, demonstrating the change from red to green fluorescence. The control cells displayed predominantly red signals in the merged channels, whereas the compound **13**-treated cells presented overall green fluorescence. These qualitative and semiquantitative changes in the red/green fluorescence ratio indicated that among the tested compounds, compound **13** induced the most significant degree of mitochondrial depolarization, followed by compound **14**.

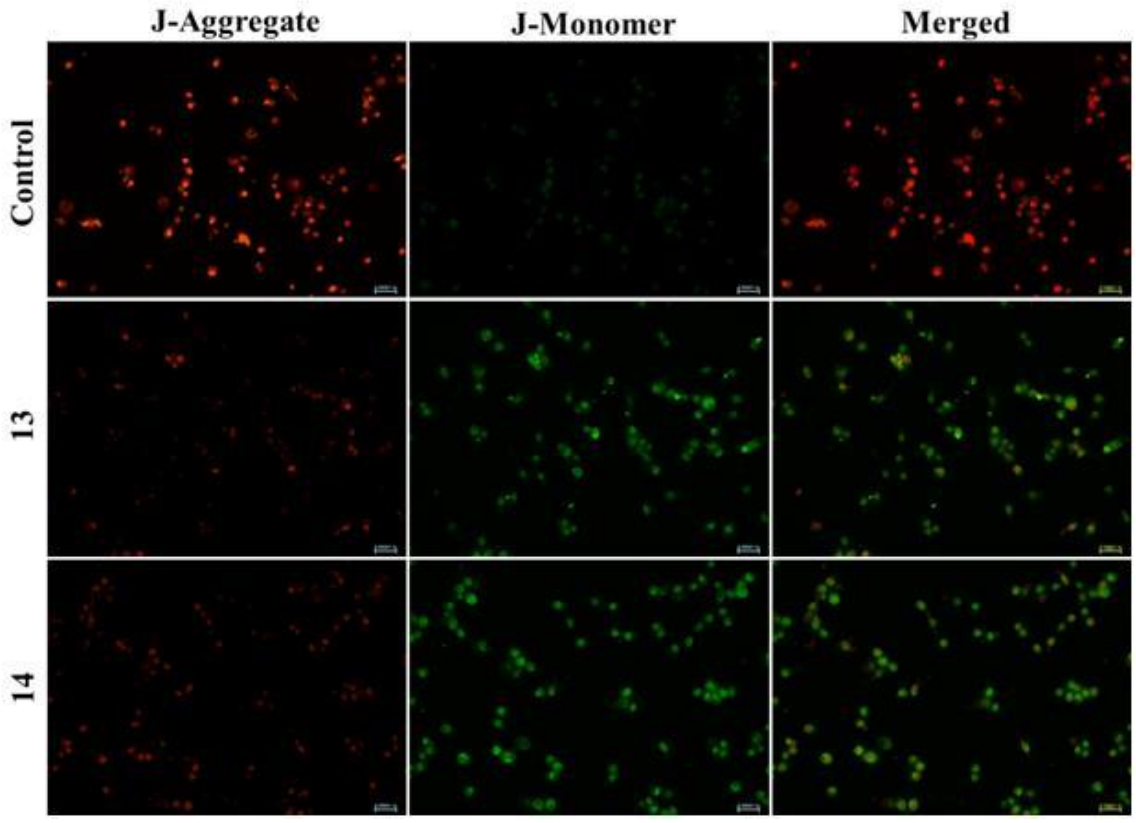

Figure 5.8. JC-1 staining of MDA-MB-231 cells treated with the noscapine derivatives compound **13** and **14** to assess the mitochondrial membrane potential. Red fluorescence indicates JC-1 aggregates in polarized mitochondria, whereas green fluorescence represents JC-1 monomers in depolarized mitochondria. Merged images show the overlay of the red and green channels. Images are representative of three independent experiments.

5.3.9. Evaluation of Oxidative Stress (Reactive oxygen species-ROS generation) in MDA-MB-231 Cells via DCFDA Staining

The Reactive oxygen species (ROS) levels in MDA-MB-231 cancer cells were assessed using DCFDA staining, as visualized through green fluorescence (Figure 5.9). The control group displayed minimal fluorescence, indicating baseline ROS levels in untreated cells. In contrast, cells treated with the noscapine derivatives presented variable intensities of green fluorescence, which correlated with increased intracellular ROS production. Among the treated groups, compound **13** presented the most intense green fluorescence, suggesting robust induction of oxidative stress. Compounds **13** and **14** exhibited moderate and relatively low fluorescence, respectively. These observations suggested that compound **13** triggers a significant increase in ROS, likely contributing to its cytotoxic effects through oxidative damage-mediated apoptosis in breast cancer cells. Elevated ROS generation is consistent with mitochondrial dysfunction and complements the findings from JC-1 and nuclear staining assays.

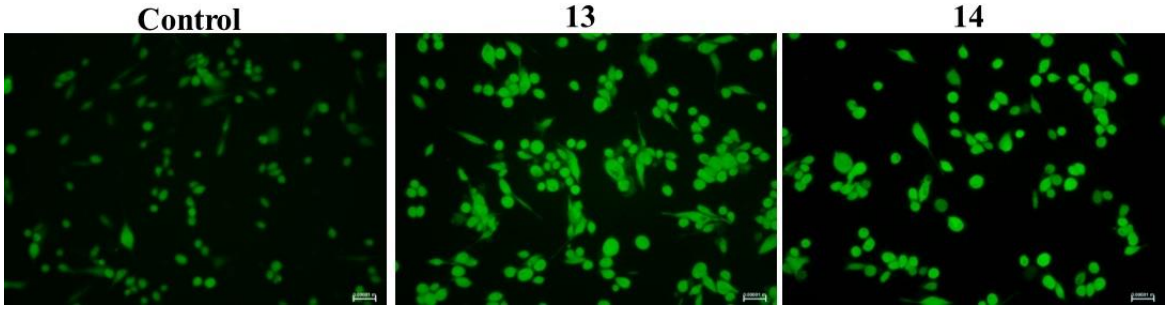

Figure 5.9. Representative fluorescence microscopy images of MDA-MB-231 cells stained with DCFDA to assess intracellular reactive oxygen species (ROS) generation following treatment with compounds **13** and **14,** including the control. The fluorescence images revealed green fluorescence, which is indicative of the level of ROS.

5.3.10. Inhibition of MDA-MB-231 Breast Cancer Cell Migration by Noscapine Derivatives

The effects of noscapine derivatives on cell migration were evaluated in MDA-MB-231 cells using a wound healing assay for 24 and 48 hours, as represented in Figure 5.10. In the untreated control group, progressive wound closure was observed, with substantial migration at both time points. Among the test compounds, **13** demonstrated the strongest inhibition, maintaining a significantly wider wound gap at both 24 and 48 hours, indicating potent suppression of cell migration. Compared with compound 13, compound **14** showed moderate inhibition at 24 hours, with partial closure by 48 hours. The time-dependent

analysis further supported the sustained antimigratory activity of both noscapine derivatives, suggesting their potential role in preventing cancer cell metastasis.

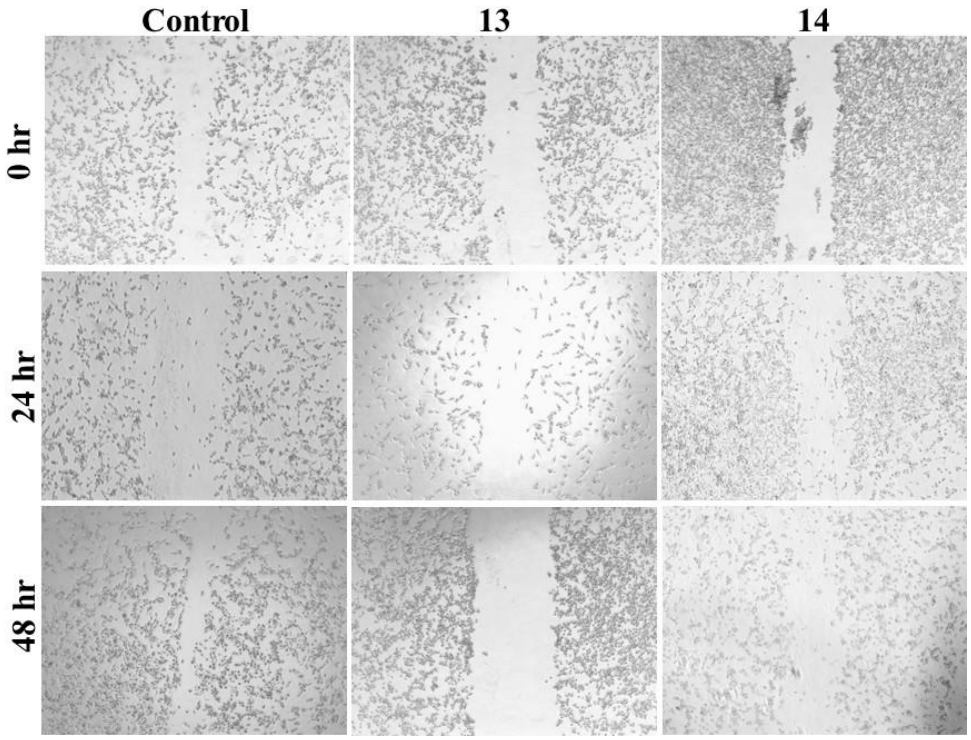

Figure 5.10. Wound healing assay to assess the effects of noscapine derivatives on MCF-7 cell migration at 24 and 48 hours. The cells were treated with compounds **13** and **14,** and left untreated (control). Images were captured at 0, 24, and 48 hours to monitor wound closure. The remaining wound area reflects the extent of migration inhibition.

5.3.11. Evaluation of 3D Spheroid Disintegration by Noscapine Derivatives

The antitumour activity of the noscapine derivatives was further evaluated in a 3D spheroid disintegration model, which closely mimics *in vivo* tumor architecture and cellular interactions. MDA-MB-231 cells were cultured into compact spheroids, and after the spheroids formed, they were treated with compounds **13 and 14**, as represented in Figure 5.11. The untreated control spheroids retained their dense, spherical morphology, indicating continued viability and structural integrity. Among the test compounds, **13** induced the most pronounced spheroid disintegration by Day 5, with visible loss of compactness and clear signs of cellular dispersal. In contrast, compound **14** had also significant effects, with the spheroids remaining relatively intact. These morphological observations suggest that the compound **13** has superior activity in disrupting multicellular tumor spheroids, likely through mechanisms involving the inhibition of cell–cell adhesion and the induction of apoptosis. This 3D model provides more physiologically relevant

insight into the antitumour behavior of the compound and supports its potential as a lead compound for further development.

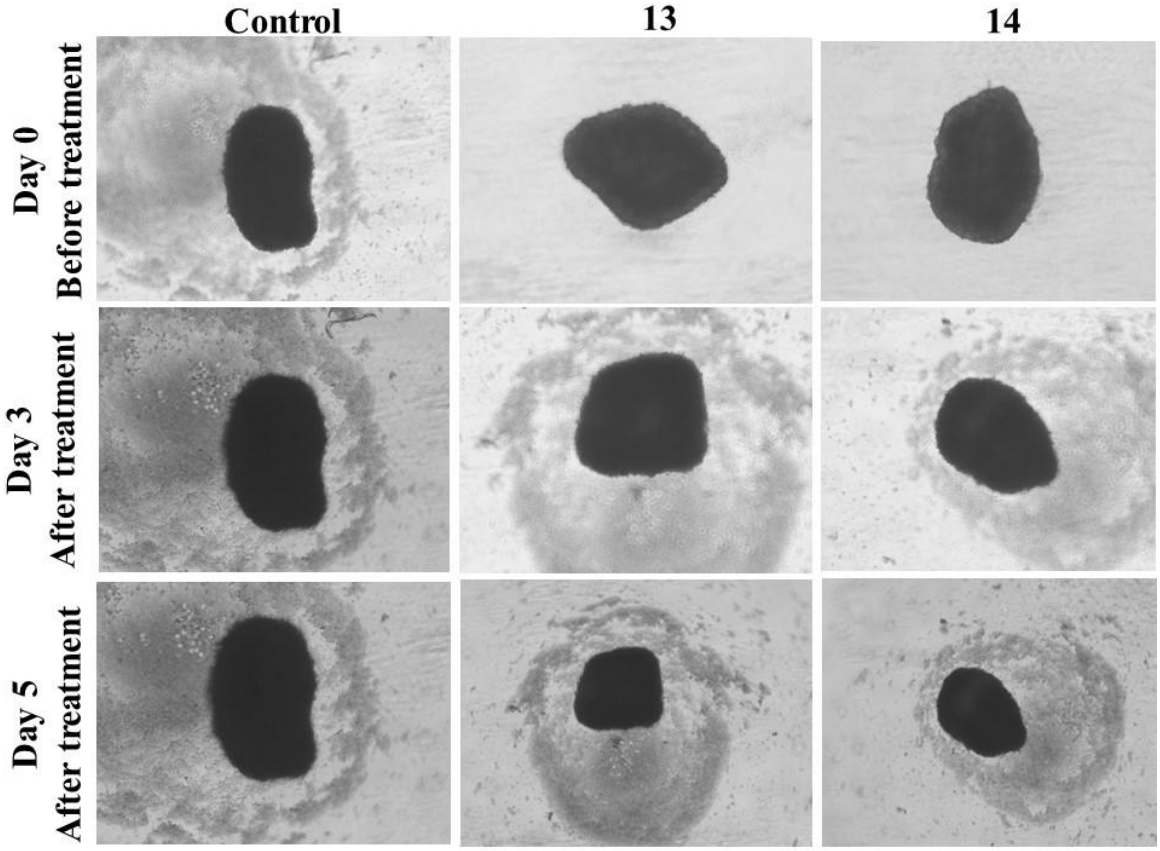

Figure 5.11. Representative images of MDA-MB-231 3D spheroids captured on days 3 and 5 after treatment with noscapine derivatives (compounds **13** and **14**), and the untreated control. An assay was performed to observe the changes in spheroid morphology and integrity. Images were acquired via an inverted phase-contrast microscope.

5.3.12. Reduction in tumor volume with the treatment of noscapine derivatives in the MDA-MB-231 xenograft model

Nude mice bearing MDA-MB-231 human breast tumors were treated with compounds **13** and **14**, which are potent noscapine derivatives, at a daily oral dose of 150 mg/kg body weight. Tumor regression was then systematically observed, and a marked reduction in volume of tumor was noted in the treated group compared with the untreated controls (Figure 5.12 (a)). By day 30 post-implantation, the average tumor volume in treated mice with compound 13 had decreased to 1200 mm^3, whereas the control group presented a significantly larger tumor size of 3030 mm^3. Similarly in case of mice treated with compound 14 for 30 days the volume has reduced to 1660 mm^3, compared to the control group with tumor size 2630 mm^3. At the end of the study, the tumors were removed and

weighed. The tumor masses in the control group ranged from 18.7 to 35.8 g, with a mean weight of 28.7 g. In contrast, only minimal tumor masses (~2.7 g with compound **13** and 3.5 g with compound **14**) were detectable in the treated groups after 30 days of treatment, indicating significant suppression of tumor progression. This inhibitory effect of the compounds on tumor growth was statistically significant ($p < 0.001$). Additionally, there was no significant weight loss observed in the treated mice throughout the study, suggesting the therapeutic efficacy of the compound without causing any systemic toxicity (Figure 5.12 (b)).

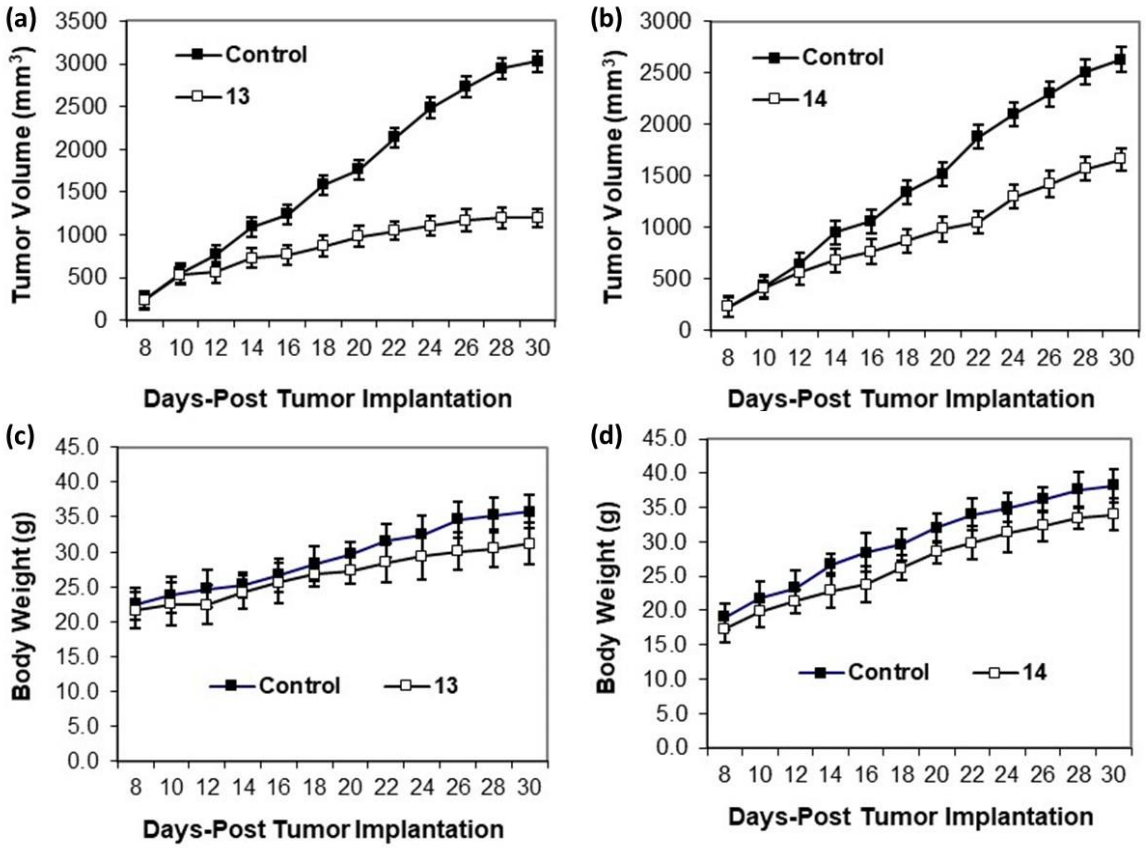

Figure 5.12. (a) Development of tumor growth in human MDA-MB-231 xenograft mice treated with compound **13** and **14**. The growth of the tumors was considerably reduced compared with that of the untreated group. (b) Effects of noscapinoids (**13** and **14**) on the body weights of the mice. There were no significant differences in body weight between the control and treated groups.

5.3.13. Evaluation of the Acute and Subacute Toxicity of Noscapine Derivatives in Rats

The acute oral toxicity of the noscapine derivatives was assessed in Wistar rats following the OECD Guidelines. The animals were administered a single dose of the test compound and observed for 14 consecutive days for signs of mortality, behavioural abnormalities,

weight changes, or organ-specific toxicity. No mortality or severe adverse clinical signs were observed in any of the treated groups throughout the observation period.

In the subacute toxicity study, daily oral administration of noscapine derivatives was carried out over a 28-day period. The animals were monitored for clinical signs, body weight, food and water intake, hematological and biochemical parameters, and histopathological changes. Throughout the treatment period, no mortality or signs of toxicity were noted. The body weights of the animals in all the treatment groups steadily increased, indicating normal metabolic and physiological functions. Body weight (Table 5.3), water intake and food intake (Table 5.4) were recorded.

Table 5.3. Compared with those of the untreated normal group, the body weights (in grams) of the rats treated with Noscapine derivatives (**13** and **14)** at a daily dose of 500 mg/kg body weight for 28 days revealed no abnormal weight gain/loss.

	Body weight (grams)		
Days	**Control**	**13**	**14**
1	241.668±0.766	241.831±0.541	242.223±0.534
7	243.383±0.885	243.574±1.006	243.577±1.22
14	246.658±0.83	245.947±0.451	246.276±0.644
21	248.378±0.512	248.34±0.294	248.124±0.598
28	249.459±0.859	248.986±0.71	249.798±0.782

Table 5.4. Food intake (in grams) and water intake (in ml) of rats treated with Noscapine derivatives (**13** and **14)** at a daily dose of 500 mg/kg body weight for 28 days revealed no significant differences between the treated and untreated control groups.

Food intake			
Day	**Control**	**13**	**14**
1	20.849±0.627	21.386±0.692	21.686±0.918
7	23.737±0.553	23.467±0.797	23.56±1.1
14	25.011±0.563	24.958±0.589	25.001±0.544
21	26.141±0.573	26.322±0.842	26.544±0.817
28	28.314±0.713	28.81±0.73	28.807±0.798
Water intake			
1	20.971±0.546	20.948±0.67	21.372±0.453
7	21.558±0.43	21.828±0.541	21.544±0.507
14	23.502±0.145	22.994±0.521	23.276±0.659
21	24.488±0.478	24.036±0.678	23.964±0.554
28	25.037±0.637	24.85±0.586	24.848±0.543

5.3.14. *In vivo* evaluation of haematological and biochemical parameters following treatment with noscapine derivatives

The hematological profile of rats treated with noscapine derivatives (**13** and **14**) over a 28-day subacute toxicity study was evaluated to study the effects of the compounds on blood physiology. The key parameters, such as red blood cell count (RBC), hemoglobin concentration (Hb), hematocrit (HCT), mean corpuscular volume (MCV), white blood cell count (WBC), and platelet count (PLT), were measured and compared to those of control animals. No statistically significant alterations were observed in the RBC, Hb, or HCT levels, indicating the absence of anaemia or impaired erythropoiesis. Similarly, the MCV, MCH, and MCHC values remained within normal physiological ranges, suggesting stable red cell morphology and hemoglobin content. Total WBC counts and differential leukocyte counts (neutrophils, lymphocytes, monocytes, eosinophils) did not indicate any signs of immunosuppression or inflammation. The platelet counts were also unaltered, indicating that there was no adverse impact on coagulation function.

Table 5.5. The blood parameters of the rats treated with Noscapine derivatives (**13** and **14**) at a daily dose of 500 mg/kg body weight for 28 days revealed no significant differences between the treated and untreated control groups.

Parameter	Control	13	14
white blood cell count (WBC (10^3/L))	6.755±0.368	7.025±0.447	6.871±0.59
Neutrophils (Neu# (10^3/L))	5.246±0.988	6.002±0.924	5.926±0.785
Lymphocytes (Lym# (10^3/L))	2.161±0.819	2.189±0.733	2.856±0.819
Monocytes (Mon# (10^3/L))	1.406±0.233	1.362±0.25	1.679±0.302
Eosinophils (Eos# (10^3/L))	0.495±0.303	0.383±0.319	0.473±0.283
Basophil (Bas# (10^3/L))	0.427±0.3	0.428±0.348	0.672±0.184
NLR	3.145±0.789	2.357±1.011	2.573±0.698
PLR	1.424±0.259	1.623±0.263	1.451±0.288
red blood cell count (RBC (10^{12}/L))	6.264±0.585	5.901±0.491	6.121±0.472
Hemoglobin (HGB (g/dL))	15.238±1.657	15.646±1.19	15.994±1.119
HCT	45.088±3.284	43.835±4.377	46.743±4.159
MCV (fL)	82.084±3.042	84.106±1.608	81.15±3.213
MCH (pg)	30.986±2.679	30.2±2.492	31.387±2.468
MCHC (g/L)	33.427±1.169	34.045±0.744	34.778±1.039
RDW-CV	13.007±0.997	12.511±0.96	13.876±1.617
RDW-SD (fL)	45.611±2.465	44.622±3.051	43.178±3.941
platelet count (PLT (10^3/L))	157.489±3.545	153.565±1.834	156.714±1.446
PCT (mL/L)	1.447±0.313	1.731±0.103	1.604±0.333

Additionally, the biochemical analysis revealed no significant differences in the serum glucose, total protein, albumin, globulin, or electrolyte levels, such as sodium, potassium, calcium, and phosphorus, between the control and treated groups. Similarly, in the liver function test, ALP, ALT, and AST levels were within the normal range and did not significantly differ between the control group and the treated group. Furthermore, kidney function indicators, such as serum urea and creatinine, did not differ from those of the control group. The results are presented in Tables 5.5 and 5.6.

Table 5.6. The blood biochemistry parameters of rats treated with Noscapine derivatives (**13** and **14**) at a daily dose of 500 mg/kg body weight for 28 days revealed no significant differences between the treated and untreated control groups.

Parameter	Control	13	14
Glucose (GLU)	78.792±1.957	77.804±2.046	76.544±1.465
Albumin (ALB)	4.193±0.726	3.959±0.522	3.672±0.5
Urea (UREA)	18.519±2.7	18.423±2.353	16.784±1.414
Creatinine (CREA)	1.395±0.242	1.574±0.214	1.446±0.327
Cholestrol (CHOL)	168.363±18.016	154.313±33.618	159.877±26.966
Triglycerides (TG)	50.95±5.4	53.113±3.69	50.612±5.806
Alanine Transaminase (ALT)	17.68±5.371	19.666±4.194	14.075±3.454
Aspartate Aminotransferase (AST)	7.955±2.622	3.851±1.778	4.669±3.275
Total Protein (TP)	7.779±0.641	6.888±0.843	7.917±0.849
Magnesium (MG)	2.433±0.263	2.566±0.412	2.574±0.266
Phosphorus (PHOS)	4.422±0.905	5.253±1.093	4.289±0.416
Calcium (CA)	10.679±0.481	10.816±0.806	10.383±0.722
Direct Bilirubin (DBIL)	0.562±0.252	0.56±0.276	0.543±0.349
Total Bilirubin (TBIL)	0.572±0.292	0.432±0.215	0.443±0.297
High-density Lipoprotein (HDL)	38.427±1.585	37.905±1.641	39.04±1.095
Gamma-glutamyl Transferase (GGT)	4.153±3.013	5.813±3.348	6.064±2.576
Alkaline Phosphatase (ALP)	107.11±2.561	104.893±3.595	107.157±2.215

5.3.15. Histopathological evaluation of vital organs via hematoxylin & eosin (HE) staining

Histopathological evaluation of vital organs such as the brain, heart, kidneys, and liver was conducted to assess potential organ-specific toxicity following daily oral administration of noscapine derivatives (**13** and **14**) at a dose of 500 mg/kg body weight for 28 consecutive

days. Tissues from treated animals were compared with those from untreated controls to detect any microscopic alterations (Figure 5.13). The brain sections of treated rats displayed preserved neuronal architecture without signs of neurodegeneration, edema, or inflammatory infiltration, indicating that there were no neurotoxic effects. Cardiac tissue showed intact myocardial fibres with acidophilic cytoplasm and centrally located nuclei, with no evidence of fibrosis, myocyte degeneration, or cellular infiltration, suggesting preserved cardiac integrity. Renal sections exhibited normal histoarchitecture, with well-defined glomeruli, proximal and distal convoluted tubules, and intact vasculature, suggesting that renal function was unaltered by the treatment. Liver tissue retained its hepatic lobular organization, with healthy hepatocytes showing no signs of necrosis, steatosis, or inflammation, confirming hepatoprotective tolerance at the administered dose. Collectively, these histopathological findings confirm that the tested noscapine derivatives did not cause significant structural or morphological damage to major organs under subacute exposure conditions, supporting their *in vivo* safety and biocompatibility at therapeutic dose levels.

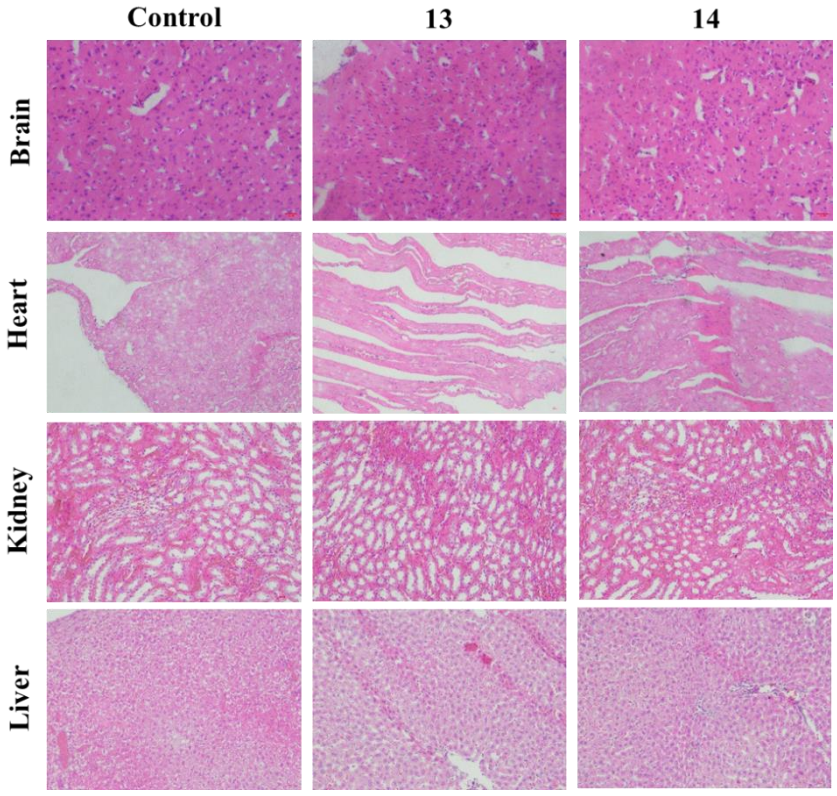

Figure 5.13. Representative histopathology of major organs in rats following subacute oral administration of noscapine derivatives (**13** and **14)** at a dose of 500 mg/kg body weight. Sections of the brain, heart, kidneys, and liver were stained with hematoxylin and eosin (H&E) and observed via light microscopy at 40x magnification.

5.4. Conclusion

In summary, this study highlights the potential of structurally modified noscapine derivatives, specifically compounds **13** and **14**, as promising anticancer agents for the treatment of breast cancer. By leveraging strategic chemical modifications, these derivatives demonstrated enhanced interactions with tubulin, as confirmed through molecular docking and molecular dynamics simulations. The computational findings were supported by *in vitro* assays, which revealed superior cytotoxic activity, increased apoptotic induction, elevated ROS generation, and mitochondrial dysfunction in hormone receptor-positive breast cancer cells compared with the parent compound. Furthermore, their ability to disrupt 3D tumor spheroids and inhibit cell migration underscores their therapeutic potential beyond monolayer cultures. The acute and subacute toxicity studies in rodent models confirmed an acceptable safety profile, reinforcing their potential for further preclinical development. Overall, this integrated approach combining computational modelling with biological evaluation offers valuable insight into the design and therapeutic potential of noscapine-based anticancer compounds, paving the way for future translational research in targeted breast cancer therapy

CONCLUSION

The current study was designed to improve the therapeutic efficacy and the bioavailability of noscapine and its derivatives through advanced drug delivery systems and molecular modifications. Beginning with the formulation and characterization of 9-bromo-noscapine (9-Br-Nos) inclusion complexes and nanoparticle-based systems, the work evolved through in-depth *in vitro*, *in vivo*, and *in silico* investigations. The findings collectively demonstrated the advantages of nanocarrier systems and noscapine structural analogues for improved anticancer performance and safety. Initially, a molecular docking and 100 ns molecular dynamics (MD) simulation study revealed a stable 1:1 inclusion complex formation between 9-Br-Nos and methyl-β-cyclodextrin (Mβ-CD). Weak interactions such as hydrogen bonding (bond lengths >3.0 Å) and a binding energy of -7.18 ± 6.51 kcal/mol supported the feasibility of complex formation. Structural stability throughout the simulation, supported by low RMSD fluctuation and consistent radius of gyration (Rg), further confirmed complex stability in solution. The pharmacokinetics of the inclusion complex in rats demonstrated a significantly improved profile over the free drug. The 9-Br-Nos-Mβ-CD complex possessed a higher Cmax, longer half-life ($t_{1/2}$ = 45.8 h), and sustained drug release up to 48 hours, unlike the rapid clearance seen with free 9-Br-Nos within 24 hours. These improvements are attributable to molecular encapsulation by Mβ-CD, which delayed drug release and absorption. Safety evaluations, including histopathological analysis (H&E staining) and Hoechst staining of normal cells, confirmed that the inclusion complex caused no significant toxicity. Parallelly, PLGA-PEG-FA (PPFD) nanoparticles loaded with 9-Br-Nos were synthesized to achieve tumor-targeted delivery via folate receptor-mediated endocytosis. These nanoparticles showed superior cytotoxicity compared to both PLGA nanoparticles and free 9-Br-Nos in MDA-MB-231 and MCF-7 cells, with IC_{50} values indicating significantly higher potency. Apoptotic induction was confirmed by nuclear condensation (Hoechst), mitochondrial depolarization (JC-1), and ROS generation (DCFDA). Flow cytometry analysis showed a notable increase in apoptotic cells 92.9% in the PPFD-treated group compared to 60.97% with the free drug. Western blot results further confirmed upregulation of pro-apoptotic markers (Bax, Cleaved Caspase-3) and downregulation of anti-apoptotic Bcl-2. Pharmacokinetic data supported improved bioavailability and systemic retention of PPFD nanoparticles, with prolonged half-life (~26 hours), enhanced AUC, and reduced clearance rate. Histopathology of major organs confirmed safety post-administration. These results highlighted the superiority of the PPFD formulation in both efficacy and biocompatibility. Building on these outcomes, the study was extended to evaluate three novel noscapine derivatives-KS-RT-130, KS-rRP-134, and KS-N-3-Br-Benzyl-developed to

further enhance anticancer activity. These derivatives were synthesized and structurally confirmed via NMR, IR, and mass spectrometry. Their cytotoxicity activity was assessed in three breast cancer cell lines (MCF-7, MDA-MB-231, and T47D), along with the normal breast epithelial cell line MCF-10A to evaluate selectivity. Among the derivatives, KS-RT-130 exhibited the highest potency, particularly against MDA-MB-231 cells, while showing minimal toxicity to MCF-10A, indicating its selective action on cancer cells. Mechanistic studies using Hoechst and AO/EtBr staining confirmed apoptosis induction. JC-1 and DCFDA assays further supported mitochondrial dysfunction and elevated ROS levels as contributing mechanisms. Wound healing and 3D spheroid assays demonstrated the anti-migratory and spheroid-disrupting effects of these derivatives, with KS-RT-130 showing the strongest performance. The tumor regression using *in vivo* xenograft model with MDA-MB-231 revealed significant tumor volume reduction upon treatment with the derivatives, without causing systemic toxicity. Acute and subacute toxicity studies in rats supported the safety of these compounds, with no significant changes in hematological, biochemical, or histopathological parameters. In conclusion, the work successfully demonstrated the benefits of both drug delivery approaches (cyclodextrin and PLGA-PEG-FA nanoparticles) and structural modification strategies for improving noscapine's therapeutic profile. The inclusion complex and PPFD nanoparticles both enhanced bioavailability, sustained release, and anticancer efficacy while ensuring biocompatibility. Among the synthesized derivatives, KS-RT-130 emerged as the most promising candidate, showing strong, selective anticancer activity and a favorable safety profile. This comprehensive evaluation lays a strong foundation for future preclinical development of noscapine-based anticancer therapies, particularly focusing on derivative optimization and targeted delivery systems.

REFERENCES

1. Abdipour, H., Abbasi, F., Nasiri, M., Ghamkhari, A. & Ghorbani, M. (2024). Multifunctional microbubbles comprising poly(lactic-co-glycolic acid), chitosan, polyethylene glycol, and folic acid for targeted cancer therapy. *Journal of Drug Delivery Science and Technology*, *94*. https://doi.org/10.1016/j.jddst.2024.105469
2. Adepu, S. & Ramakrishna, S. (2021). Controlled drug delivery systems: Current status and future directions. In *Molecules* (Vol. 26, Issue 19). https://doi.org/10.3390/molecules26195905
3. Anand, U., Dey, A., Chandel, A. K. S., Sanyal, R., Mishra, A., Pandey, D. K., De Falco, V., Upadhyay, A., Kandimalla, R., Chaudhary, A., Dhanjal, J. K., Dewanjee, S., Vallamkondu, J. & Pérez de la Lastra, J. M. (2023). Cancer chemotherapy and beyond: Current status, drug candidates, associated risks and progress in targeted therapeutics. In *Genes and Diseases* (Vol. 10, Issue 4). https://doi.org/10.1016/j.gendis.2022.02.007
4. Aneja, R., Vangapandu, S. N., Lopus, M., Viswesarappa, V. G., Dhiman, N., Verma, A., Chandra, R., Panda, D. & Joshi, H. C. (2006). Synthesis of microtubule-interfering halogenated noscapine analogs that perturb mitosis in cancer cells followed by cell death. *Biochemical Pharmacology*, *72*(4). https://doi.org/10.1016/j.bcp.2006.05.004
5. Aparoy, P., Kumar Reddy, K. & Reddanna, P. (2012). Structure and Ligand Based Drug Design Strategies in the Development of Novel 5- LOX Inhibitors. *Current Medicinal Chemistry*, *19*(22). https://doi.org/10.2174/092986712801661112
6. Arnold, M., Morgan, E., Rumgay, H., Mafra, A., Singh, D., Laversanne, M., Vignat, J., Gralow, J. R., Cardoso, F., Siesling, S. & Soerjomataram, I. (2022). Current and future burden of breast cancer: Global statistics for 2020 and 2040. *Breast*, *66*. https://doi.org/10.1016/j.breast.2022.08.010
7. Barisic, M., Rajendraprasad, G. & Steblyanko, Y. (2021). The metaphase spindle at steady state – Mechanism and functions of microtubule poleward flux. In *Seminars in Cell and Developmental Biology* (Vol. 117). https://doi.org/10.1016/j.semcdb.2021.05.016
8. Baskar, R., Lee, K. A., Yeo, R. & Yeoh, K. W. (2012). Cancer and radiation therapy: Current advances and future directions. In *International Journal of Medical Sciences* (Vol. 9, Issue 3). https://doi.org/10.7150/ijms.3635
9. Bratton, S. B. & Salvesen, G. S. (2010). Regulation of the Apaf-1-caspase-9 apoptosome. In *Journal of Cell Science* (Vol. 123, Issue 19). https://doi.org/10.1242/jcs.073643
10. Bucur, P., Fülöp, I. & Sipos, E. (2022). Insulin Complexation with Cyclodextrins—A Molecular Modeling Approach. *Molecules*, *27*(2). https://doi.org/10.3390/molecules27020465
11. Cai, S. S., Li, T., Akinade, T., Zhu, Y. & Leong, K. W. (2021). Drug delivery carriers with therapeutic functions. In *Advanced Drug Delivery Reviews* (Vol. 176). https://doi.org/10.1016/j.addr.2021.113884
12. Calaf, G. M., Crispin, L. A. & Quisbert-Valenzuela, E. O. (2024). Noscapine and Apoptosis in Breast and Other Cancers. In *International Journal of Molecular Sciences* (Vol. 25, Issue 6). https://doi.org/10.3390/ijms25063536
13. Cheung, A., Bax, H. J., Josephs, D. H., Ilieva, K. M., Pellizzari, G., Opzoomer, J., Bloomfield, J., Fittall, M., Grigoriadis, A., Figini, M., Canevari, S., Spicer, J. F., Tutt, A. N. & Karagiannis, S. N. (2016). Targeting folate receptor alpha for cancer treatment. In *Oncotarget* (Vol. 7, Issue 32). https://doi.org/10.18632/oncotarget.9651

14. Cho, H., Gao, J. & Kwon, G. S. (2016). PEG-b-PLA micelles and PLGA-b-PEG-b-PLGA sol–gels for drug delivery. *Journal of Controlled Release*, *240*. https://doi.org/10.1016/j.jconrel.2015.12.015
15. Chu, D. T., Nguyen, T. T., Tien, N. L. B., Tran, D. K., Jeong, J. H., Anh, P. G., Thanh, V. Van, Truong, D. T. & Dinh, T. C. (2020). Recent progress of stem cell therapy in cancer treatment: Molecular mechanisms and potential applications. In *Cells* (Vol. 9, Issue 3). https://doi.org/10.3390/cells9030563
16. Correia, J. J., Beth, A. H. & Williams, R. C. (1988). Tubulin exchanges divalent cations at both guanine nucleotide-binding sites. *Journal of Biological Chemistry*, *263*(22). https://doi.org/10.1016/s0021-9258(18)38025-6
17. Correia, J. & Lobert, S. (2005). Physiochemical Aspects of Tubulin-Interacting Antimitotic Drugs. *Current Pharmaceutical Design*, *7*(13). https://doi.org/10.2174/1381612013397438
18. DeBono, A., Capuano, B. & Scammells, P. J. (2015). Progress Toward the Development of Noscapine and Derivatives as Anticancer Agents. *Journal of Medicinal Chemistry*, *58*(15). https://doi.org/10.1021/jm501180v
19. Downing, K. H. & Nogales, E. (1998). Tubulin structure: Insights into microtubule properties and functions. *Current Opinion in Structural Biology*, *8*(6). https://doi.org/10.1016/S0959-440X(98)80099-7
20. Duong, V. A., Nguyen, T. T. L. & Maeng, H. J. (2020). Preparation of solid lipid nanoparticles and nanostructured lipid carriers for drug delivery and the effects of preparation parameters of solvent injection method. In *Molecules* (Vol. 25, Issue 20). https://doi.org/10.3390/molecules25204781
21. Elmowafy, M. & Al-Sanea, M. M. (2021). Nanostructured lipid carriers (NLCs) as drug delivery platform: Advances in formulation and delivery strategies. In *Saudi Pharmaceutical Journal* (Vol. 29, Issue 9). https://doi.org/10.1016/j.jsps.2021.07.015
22. Endres, T. K., Beck-Broichsitter, M., Samsonova, O., Renette, T. & Kissel, T. H. (2011). Self-assembled biodegradable amphiphilic PEG-PCL-lPEI triblock copolymers at the borderline between micelles and nanoparticles designed for drug and gene delivery. *Biomaterials*, *32*(30). https://doi.org/10.1016/j.biomaterials.2011.06.064
23. Ferrati, S., Nicolov, E., Bansal, S., Hosali, S., Landis, M. & Grattoni, A. (2015). Docetaxel/2-Hydroxypropyl β -Cyclodextrin Inclusion Complex Increases Docetaxel Solubility and Release from a Nanochannel Drug Delivery System. *Current Drug Targets*, *16*(14). https://doi.org/10.2174/1389450116141511191255 41
24. Franco, P. & De Marco, I. (2021). Preparation of non-steroidal anti-inflammatory drug/β-cyclodextrin inclusion complexes by supercritical antisolvent process. *Journal of CO2 Utilization*, *44*. https://doi.org/10.1016/j.jcou.2020.101397
25. Gabrielli, B., Brooks, K. & Pavey, S. (2012). Defective cell cycle checkpoints as targets for anti-cancer therapies. *Frontiers in Pharmacology*, *3 FEB*. https://doi.org/10.3389/fphar.2012.00009
26. Gardner, M. K., Hunt, A. J., Goodson, H. V. & Odde, D. J. (2008). Microtubule assembly dynamics: new insights at the nanoscale. In *Current Opinion in Cell Biology* (Vol. 20, Issue 1). https://doi.org/10.1016/j.ceb.2007.12.003
27. Goodson, H. V. & Jonasson, E. M. (2018). Microtubules and microtubule-associated proteins. *Cold Spring Harbor Perspectives in Biology*, *10*(6). https://doi.org/10.1101/cshperspect.a022608

28. Graña, X. & Premkumar Reddy, E. (1995). Cell cycle control in mammalian cells: Role of cyclins, cyclin dependent kinases (CDKs), growth suppressor genes and cyclin-dependent kinase inhibitors (CKIs). In *Oncogene* (Vol. 11, Issue 2).
29. Guchelaar, H. J., Ten Napel, C. H. H., de Vries, E. G. E. & Mulder, N. H. (1994). Clinical, toxicological and pharmaceutical aspects of the antineoplastic drug taxol: A review. In *Clinical Oncology* (Vol. 6, Issue 1). https://doi.org/10.1016/S0936-6555(05)80367-X
30. Guidi, L., Cascone, M. G. & Rosellini, E. (2024). Light-responsive polymeric nanoparticles for retinal drug delivery: design cues, challenges and future perspectives. In Heliyon (Vol. 10, Issue 5). https://doi.org/10.1016/j.heliyon.2024.e26616
31. Hruban, R. H., Yardley, J. H., Donehower, R. C. & Boitnott, J. K. (1989). Taxol toxicity. Epithelial necrosis in the gastrointestinal tract associated with polymerized microtubule accumulation and mitotic arrest. *Cancer*, *63*(10). https://doi.org/10.1002/1097-0142(19890515)63
32. Huang, L., Peng, Y., Tao, X., Ding, X., Li, R., Jiang, Y. & Zuo, W. (2022). Microtubule Organization Is Essential for Maintaining Cellular Morphology and Function. In *Oxidative Medicine and Cellular Longevity* (Vol. 2022). https://doi.org/10.1155/2022/1623181
33. Jehn, C. F., Boulikas, T., Kourvetaris, A., Possinger, K. & Lüftner, D. (2007). Pharmacokinetics of liposomal cisplatin (Lipoplatin) in combination with 5-FU in patients with advanced head and neck cancer: First results of a phase III study. *Anticancer Research*, *27*(1 A).
34. Jordan, A., Hadfield, J. A., Lawrence, N. J. & McGown, A. T. (1998). Tubulin as a target for anticancer drugs: Agents which interact with the mitotic spindle. In *Medicinal Research Reviews* (Vol. 18, Issue 4). https://doi.org/10.1002/(SICI)1098-1128(199807)18:4<259::AID-MED3>3.0.CO;2-U
35. Kali, G., Haddadzadegan, S. & Bernkop-Schnürch, A. (2024). Cyclodextrins and derivatives in drug delivery: New developments, relevant clinical trials, and advanced products. In *Carbohydrate Polymers* (Vol. 324). https://doi.org/10.1016/j.carbpol.2023.121500
36. Karlsson, M. O., Dahlström, B. & Neil, A. (1988). Characterization of high-affinity binding sites for the antitussive [3H]noscapine in guinea pig brain tissue. *European Journal of Pharmacology*, *145*(2). https://doi.org/10.1016/0014-2999(88)90230-0
37. Ke, Y., Ye, K., Grossniklaus, H. E., Archer, D. R., Joshi, H. C. & Kapp, J. A. (2000). Noscapine inhibits tumor growth with little toxicity to normal tissues or inhibition of immune responses. *Cancer Immunology Immunotherapy*, *49*(4–5). https://doi.org/10.1007/s002620000109
38. Kerdpol, K., Oo, A., Mahalapbutr, P., Todsaporn, D., Phumphuang, S., Chavasiri, W., Rungrotmongkol, T. & Hannongbua, S. (2023). Improvement of the solubility and anticancer activity of 6,8-dibromochrysin by encapsulation into β-cyclodextrin and its derivatives. *Journal of the Taiwan Institute of Chemical Engineers*, *150*. https://doi.org/10.1016/j.jtice.2023.105029
39. Kleinjung, J. & Fraternali, F. (2014). Design and application of implicit solvent models in biomolecular simulations. In *Current Opinion in Structural Biology* (Vol. 25). https://doi.org/10.1016/j.sbi.2014.04.003
40. Kumar, A., Kumari, K., Singh, S., Bahdur, I. & Singh, P. (2021). Noscapine anticancer drug designed with ionic liquids to enhance solubility: DFT and ADME approach. *Journal of Molecular Liquids*, *325*. https://doi.org/10.1016/j.molliq.2020.115159

41. Lakkireddy, H. R. & Bazile, D. (2016). Building the design, translation and development principles of polymeric nanomedicines using the case of clinically advanced poly(lactide(glycolide))–poly(ethylene glycol) nanotechnology as a model: An industrial viewpoint. In *Advanced Drug Delivery Reviews* (Vol. 107). https://doi.org/10.1016/j.addr.2016.08.012
42. Landen, J. W., Hau, V., Wang, M., Davis, T., Ciliax, B., Wainer, B. H., Van Meir, E. G., Glass, J. D., Joshi, H. C. & Archer, D. R. (2004). Noscapine crosses the blood-brain barrier and inhibits glioblastoma growth. *Clinical Cancer Research*, *10*(15). https://doi.org/10.1158/1078-0432.CCR-04-0360
43. Lara-Gonzalez, P., Pines, J. & Desai, A. (2021). Spindle assembly checkpoint activation and silencing at kinetochores. In *Seminars in Cell and Developmental Biology* (Vol. 117). https://doi.org/10.1016/j.semcdb.2021.06.009
44. Ledermann, J. A., Canevari, S. & Thigpen, T. (2015). Targeting the folate receptor: Diagnostic and therapeutic approaches to personalize cancer treatments. In *Annals of Oncology* (Vol. 26, Issue 10). https://doi.org/10.1093/annonc/mdv250
45. Leonis, G., Christodoulou, E., Ntountaniotis, D., Chatziathanasiadou, M. V., Mavromoustakos, T., Naziris, N., Chountoulesi, M., Demetzos, C., Valsami, G., Damalas, D. E., Tzakos, A. G., Thomaidis, N. S., Karageorgos, V. & Liapakis, G. (2020). Antihypertensive activity and molecular interactions of irbesartan in complex with 2-hydroxypropyl-β-cyclodextrin. *Chemical Biology and Drug Design*, *96*(1). https://doi.org/10.1111/cbdd.13664
46. Ling, S. P., Ming, L. C., Dhaliwal, J. S., Gupta, M., Ardianto, C., Goh, K. W., Hussain, Z. & Shafqat, N. (2022). Role of Immunotherapy in the Treatment of Cancer: A Systematic Review. In *Cancers* (Vol. 14, Issue 21). https://doi.org/10.3390/cancers14215205
47. Lipinski, C. A. (2000). Drug-like properties and the causes of poor solubility and poor permeability. *Journal of Pharmacological and Toxicological Methods*, *44*(1). https://doi.org/10.1016/S1056-8719(00)00107-6
48. Madan, J., Baruah, B., Nagaraju, M., Abdalla, M. O., Yates, C., Turner, T., Rangari, V., Hamelberg, D. & Aneja, R. (2012). Molecular cycloencapsulation augments solubility and improves therapeutic index of brominated noscapine in prostate cancer cells. *Molecular Pharmaceutics*, *9*(5). https://doi.org/10.1021/mp300063v
49. Madan, J., Dhiman, N., Parmar, V. K., Sardana, S., Bharatam, P. V., Aneja, R., Chandra, R. & Katyal, A. (2010). Inclusion complexes of noscapine in β-cyclodextrin offer better solubility and improved pharmacokinetics. *Cancer Chemotherapy and Pharmacology*, *65*(3). https://doi.org/10.1007/s00280-009-1060-3
50. Madan, J., Gundala, S. R., Baruah, B., Nagaraju, M., Yates, C., Turner, T., Rangari, V., Hamelberg, D., Reid, M. D. & Aneja, R. (2014). Cyclodextrin complexes of reduced bromonoscapine in guar gum microspheres enhance colonic drug delivery. *Molecular Pharmaceutics*, *11*(12). https://doi.org/10.1021/mp500408n
51. Mahor, A., Singh, P. P., Bharadwaj, P., Sharma, N., Yadav, S., Rosenholm, J. M. & Bansal, K. K. (2021). Carbon-Based Nanomaterials for Delivery of Biologicals and Therapeutics: A Cutting-Edge Technology. *C*, *7*(1). https://doi.org/10.3390/c7010019
52. Manchukonda, N. K., Naik, P. K., Santoshi, S., Lopus, M., Joseph, S., Sridhar, B. & Kantevari, S. (2013). Rational design, synthesis, and biological evaluation of third generation α-noscapine analogues as potent tubulin binding anti-cancer agents. *PLoS ONE*, *8*(10). https://doi.org/10.1371/journal.pone.0077970

53. Martino, E., Casamassima, G., Castiglione, S., Cellupica, E., Pantalone, S., Papagni, F., Rui, M., Siciliano, A. M. & Collina, S. (2018). Vinca alkaloids and analogues as anti-cancer agents: Looking back, peering ahead. In *Bioorganic and Medicinal Chemistry Letters* (Vol. 28, Issue 17). https://doi.org/10.1016/j.bmcl.2018.06.044
54. Meng, X.-Y., Zhang, H.-X., Mezei, M. & Cui, M. (2012). Molecular Docking: A Powerful Approach for Structure-Based Drug Discovery. *Current Computer Aided-Drug Design*, *7*(2). https://doi.org/10.2174/157340911795677602
55. Mitchell, M. J., Billingsley, M. M., Haley, R. M., Wechsler, M. E., Peppas, N. A. & Langer, R. (2021). Engineering precision nanoparticles for drug delivery. In *Nature Reviews Drug Discovery* (Vol. 20, Issue 2). https://doi.org/10.1038/s41573-020-0090-8
56. Mognetti, B., Barberis, A., Marino, S., Berta, G., De Francia, S., Trotta, F. & Cavalli, R. (2012). In vitro enhancement of anticancer activity of paclitaxel by a Cremophor free cyclodextrin-based nanosponge formulation. *Journal of Inclusion Phenomena and Macrocyclic Chemistry*, *74*(1–4). https://doi.org/10.1007/s10847-011-0101-9
57. Mukhtar, E., Adhami, V. M. & Mukhtar, H. (2014). Targeting microtubules by natural agents for cancer therapy. In *Molecular Cancer Therapeutics* (Vol. 13, Issue 2). https://doi.org/10.1158/1535-7163.MCT-13-0791
58. Naik, P. K., Chatterji, B. P., Vangapandu, S. N., Aneja, R., Chandra, R., Kanteveri, S. & Joshi, H. C. (2011). Rational design, synthesis and biological evaluations of amino-noscapine: A high affinity tubulin-binding noscapinoid. *Journal of Computer-Aided Molecular Design*, *25*(5). https://doi.org/10.1007/s10822-011-9430-4
59. Naik, P. K., Santoshi, S., Rai, A. & Joshi, H. C. (2011). Molecular modelling and competition binding study of Br-noscapine and colchicine provide insight into noscapinoid-tubulin binding site. *Journal of Molecular Graphics and Modelling*, *29*(7). https://doi.org/10.1016/j.jmgm.2011.03.004
60. Newcomb, E. W., Lukyanov, Y., Schnee, T., Ali, M. A., Lan, L. & Zagzag, D. (2006). Noscapine inhibits hypoxia-mediated HIF-1α expression and angiogenesis in vitro: A novel function for an old drug. *International Journal of Oncology*, *28*(5). https://doi.org/10.3892/ijo.28.5.1121
61. Ngan, V. K., Bellman, K., Panda, D., Hill, B. T., Jordan, M. A. & Wilson, L. (2000). Novel actions of the antitumor drugs vinflunine and viaorelbine on microtubules. *Cancer Research*, *60*(18).
62. Niazi, S. K. & Mariam, Z. (2024). Computer-Aided Drug Design and Drug Discovery: A Prospective Analysis. In *Pharmaceuticals* (Vol. 17, Issue 1). https://doi.org/10.3390/ph17010022
63. Osman, M. & Elkady, M. (2017). A prospective study to evaluate the effect of paclitaxel on cardiac ejection fraction. *Breast Care*, *12*(4). https://doi.org/10.1159/000471759
64. Papasozomenos Ch., S., Binder, L. I., Bender, P. K. & Payne, M. R. (1985). Microtubule-associated protein 2 within axons of spinal motor neurons: Associations with microtubules and neurofilaments in normal and β,β'-iminodipropionitrile-treated axons. *Journal of Cell Biology*, *100*(1). https://doi.org/10.1083/jcb.100.1.74
65. Patra, A., Satpathy, S., Naik, P. K., Kazi, M. & Hussain, M. D. (2022). Folate receptor-targeted PLGA-PEG nanoparticles for enhancing the activity of genistein in ovarian cancer. *Artificial Cells, Nanomedicine and Biotechnology*, *50*(1). https://doi.org/10.1080/21691401.2022.2118758
66. Patra, J. K., Das, G., Fraceto, L. F., Campos, E. V. R., Rodriguez-Torres, M. D. P., Acosta-Torres, L. S., Diaz-Torres, L. A., Grillo, R., Swamy, M. K., Sharma, S., Habtemariam, S. & Shin, H. S. (2018). Nano based drug delivery systems: Recent developments and

future prospects. In *Journal of Nanobiotechnology* (Vol. 16, Issue 1). https://doi.org/10.1186/s12951-018-0392-8
67. Payamifar, S. & Poursattar Marjani, A. (2023). A new β-cyclodextrin-based nickel as green and water-soluble supramolecular catalysts for aqueous Suzuki reaction. *Scientific Reports*, *13*(1). https://doi.org/10.1038/s41598-023-48603-6
68. Pearl, M. L., Johnston, C. M., Reynolds, R. K. & Roberts, J. A. (1995). Absence of cumulative bone marrow suppression in heavily pretreated ovarian cancer patients undergoing salvage chemotherapy with paclitaxel. *Oncology (Switzerland)*, *52*(5). https://doi.org/10.1159/000227498
69. Pettit, G. R. (1996). Progress in the discovery of biosynthetic anticancer drugs. In *Journal of Natural Products* (Vol. 59, Issue 8). https://doi.org/10.1021/np9604386
70. Puhalla, S., Bhattacharya, S. & Davidson, N. E. (2012). Hormonal therapy in breast cancer: A model disease for the personalization of cancer care. In *Molecular Oncology* (Vol. 6, Issue 2). https://doi.org/10.1016/j.molonc.2012.02.003
71. Quisbert-Valenzuela, E. O. & Calaf, G. M. (2016). Apoptotic effect of noscapine in breast cancer cell lines. *International Journal of Oncology*, *48*(6). https://doi.org/10.3892/ijo.2016.3476
72. Ramkumar, A., Jong, B. Y. & Ori-McKenney, K. M. (2018). ReMAPping the microtubule landscape: How phosphorylation dictates the activities of microtubule-associated proteins. In *Developmental Dynamics* (Vol. 247, Issue 1). https://doi.org/10.1002/dvdy.24599
73. Ren, L., Yang, X., Guo, W., Wang, J. & Chen, G. (2020). Inclusion complex of docetaxel with sulfobutyl ether β-cyclodextrin: Preparation, in vitro cytotoxicity and in vivo safety. *Polymers*, *12*(10). https://doi.org/10.3390/polym12102336
74. Rowinsky, E. K., Eisenhauer, E. A., Chaudhry, V., Arbuck, S. G. & Donehower, R. C. (1993). Clinical toxicities encountered with paclitaxel (TAXOL®). *Seminars in Oncology*, *20*(4 SUPPL. 3).
75. Santoshi, S., Naik, P. K. & Joshi, H. C. (2011). Rational design of novel anti-microtubule agent (9-azido-noscapine) from quantitative structure activity relationship (QSAR) evaluation of noscapinoids. *Journal of Biomolecular Screening*, *16*(9). https://doi.org/10.1177/1087057111418654
76. Sebak, S., Mirzaei, M., Malhotra, M., Kulamarva, A. & Prakash, S. (2010). Human serum albumin nanoparticles as an efficient noscapine drug delivery system for potential use in breast cancer: Preparation and in vitro analysis. *International Journal of Nanomedicine*, *5*(1). https://doi.org/10.2147/IJN.S10443
77. Shamima Shultana, Kazi M Maraz, Arwah Ahmed, Tanzila Sultana & Ruhul A Khan. (2021). Drug design, discovery and development and their safety or efficacy on human body. *GSC Biological and Pharmaceutical Sciences*, *17*(2). https://doi.org/10.30574/gscbps.2021.17.2.0330
78. Shi, Y., Su, C., Cui, W., Li, H., Liu, L., Feng, B., Liu, M., Su, R. & Zhao, L. (2014). Gefitinib loaded folate decorated bovine serum albumin conjugated carboxymethyl-betacyclodextrin nanoparticles enhance drug delivery and attenuate autophagy in folate receptor-positive cancer cells. *Journal of Nanobiotechnology*, *12*(1). https://doi.org/10.1186/s12951-014-0043-7
79. Sibaud, V., Leboeuf, N. R., Roche, H., Belum, V. R., Gladieff, L., Deslandres, M., Montastruc, M., Eche, A., Vigarios, E., Dalenc, F. & Lacouture, M. E. (2016). Dermatological adverse events with taxane chemotherapy. In *European Journal of Dermatology* (Vol. 26, Issue 5). https://doi.org/10.1684/ejd.2016.2833

80. Siegel, R. L., Miller, K. D., Wagle, N. S. & Jemal, A. (2023). Cancer statistics, 2023. *CA: A Cancer Journal for Clinicians*, *73*(1). https://doi.org/10.3322/caac.21763
81. Slamon, D. J., Leyland-Jones, B., Shak, S., Fuchs, H., Paton, V., Bajamonde, A., Fleming, T., Eiermann, W., Wolter, J., Pegram, M., Baselga, J. & Norton, L. (2001). Use of Chemotherapy plus a Monoclonal Antibody against HER2 for Metastatic Breast Cancer That Overexpresses HER2. *New England Journal of Medicine*, *344*(11). https://doi.org/10.1056/nejm200103153441101
82. Sung, Y. K. & Kim, S. W. (2020). Recent advances in polymeric drug delivery systems. In *Biomaterials Research* (Vol. 24, Issue 1). https://doi.org/10.1186/s40824-020-00190-7
83. Swain, S. M., Shastry, M. & Hamilton, E. (2023). Targeting HER2-positive breast cancer: advances and future directions. In *Nature Reviews Drug Discovery* (Vol. 22, Issue 2). https://doi.org/10.1038/s41573-022-00579-0
84. Tan, H. & Marra, K. G. (2010). Injectable, biodegradable hydrogels for tissue engineering applications. *Materials*, *3*(3). https://doi.org/10.3390/ma3031746
85. Tohme, S., Simmons, R. L. & Tsung, A. (2017). Surgery for cancer: A trigger for metastases. In *Cancer Research* (Vol. 77, Issue 7). https://doi.org/10.1158/0008-5472.CAN-16-1536
86. Tolić, I. M. (2018). Mitotic spindle: kinetochore fibers hold on tight to interpolar bundles. In *European Biophysics Journal* (Vol. 47, Issue 3). https://doi.org/10.1007/s00249-017-1244-4
87. Unnikrishnan, G., Joy, A., Megha, M., Kolanthai, E. & Senthilkumar, M. (2023). Exploration of inorganic nanoparticles for revolutionary drug delivery applications: a critical review. In *Discover Nano* (Vol. 18, Issue 1). https://doi.org/10.1186/s11671-023-03943-0
88. van Gerven, J. M. A., Moll, J. W. B., van den Bent, M. J., Bontenbal, M., van der Burg, M. E. L., Verweij, J. & Vecht, C. J. (1994). Paclitaxel (Taxol) induces cumulative mild neurotoxicity. *European Journal of Cancer*, *30*(8). https://doi.org/10.1016/0959-8049(94)90459-6
89. Vleugel, M., Kok, M. & Dogterom, M. (2016). Understanding force-generating microtubule systems through in vitro reconstitution. In *Cell Adhesion and Migration* (Vol. 10, Issue 5). https://doi.org/10.1080/19336918.2016.1241923
90. Xu, D., Wang, L., Gourevich, D., Kabha, E., Arditti, F., Athamna, M., Cochran, S., Melzer, A. & Gnaim, J. M. (2014). Synthesis and inclusion study of a novel γ-cyclodextrin derivative as a potential thermo-sensitive carrier for doxorubicin. *Chemical and Pharmaceutical Bulletin*, *62*(7). https://doi.org/10.1248/cpb.c13-00950
91. Yam, C. Q. X., Lim, H. H. & Surana, U. (2022). DNA damage checkpoint execution and the rules of its disengagement. In *Frontiers in Cell and Developmental Biology* (Vol. 10). https://doi.org/10.3389/fcell.2022.1020643
92. Yao, Y., Zhou, Y., Liu, L., Xu, Y., Chen, Q., Wang, Y., Wu, S., Deng, Y., Zhang, J. & Shao, A. (2020). Nanoparticle-Based Drug Delivery in Cancer Therapy and Its Role in Overcoming Drug Resistance. In *Frontiers in Molecular Biosciences* (Vol. 7). https://doi.org/10.3389/fmolb.2020.00193
93. Yu, B., Tai, H. C., Xue, W., Lee, L. J. & Lee, R. J. (2010). Receptor-targeted nanocarriers for therapeutic delivery to cancer. In *Molecular Membrane Biology* (Vol. 27, Issue 7). https://doi.org/10.3109/09687688.2010.521200

94. Zenze, M., Daniels, A. & Singh, M. (2023). Dendrimers as Modifiers of Inorganic Nanoparticles for Therapeutic Delivery in Cancer. In *Pharmaceutics* (Vol. 15, Issue 2). https://doi.org/10.3390/pharmaceutics15020398
95. Zhou, J., Gupta, K., Aggarwal, S., Aneja, R., Chandra, R., Panda, D. & Joshi, H. C. (2003). Brominated derivatives of noscapine are potent microtubule-interfering agents that perturb mitosis and inhibit cell proliferation. *Molecular Pharmacology*, *63*(4). https://doi.org/10.1124/mol.63.4.799
96. Ajith, S., Almomani, F., Elhissi, A. & Husseini, G. A. (2023). Nanoparticle-based materials in anticancer drug delivery: Current and future prospects. In *Heliyon* (Vol. 9, Issue 11). https://doi.org/10.1016/j.heliyon.2023.e21227
97. Alserihi, R. F., Mohammed, M. R. S., Kaleem, M., Khan, M. I., Sechi, M., Sanna, V., Zughaibi, T. A., Abuzenadah, A. M. & Tabrez, S. (2021). Development of (-)-epigallocatechin-3-gallate-loaded folate receptor-targeted nanoparticles for prostate cancer treatment. *Nanotechnology Reviews*, *11*(1). https://doi.org/10.1515/ntrev-2022-0013
98. Baitharu, I., Jain, V., Deep, S. N., Shroff, S., Sahu, J. K., Naik, P. K. & Ilavazhagan, G. (2014). Withanolide A prevents neurodegeneration by modulating hippocampal glutathione biosynthesis during hypoxia. *PLoS ONE*, *9*(10). https://doi.org/10.1371/journal.pone.0105311
99. Chen, Jianian, Li, S. & Shen, Q. (2012). Folic acid and cell-penetrating peptide conjugated PLGA-PEG bifunctional nanoparticles for vincristine sulfate delivery. *European Journal of Pharmaceutical Sciences*, *47*(2). https://doi.org/10.1016/j.ejps.2012.07.002
100. Dodda, J. M., Remiš, T., Rotimi, S. & Yeh, Y. C. (2022). Progress in the drug encapsulation of poly(lactic-co-glycolic acid) and folate-decorated poly(ethylene glycol)-poly(lactic-co-glycolic acid) conjugates for selective cancer treatment. In *Journal of Materials Chemistry B* (Vol. 10, Issue 22). https://doi.org/10.1039/d2tb00469k
101. El-Hammadi, M. M., Delgado, Á. V., Melguizo, C., Prados, J. C. & Arias, J. L. (2017). Folic acid-decorated and PEGylated PLGA nanoparticles for improving the antitumour activity of 5-fluorouracil. *International Journal of Pharmaceutics*, *516*(1–2). https://doi.org/10.1016/j.ijpharm.2016.11.012
102. Elmowafy, M., Shalaby, K., Elkomy, M. H., Alsaidan, O. A., Gomaa, H. A. M., Abdelgawad, M. A. & Mostafa, E. M. (2023). Polymeric Nanoparticles for Delivery of Natural Bioactive Agents: Recent Advances and Challenges. In *Polymers* (Vol. 15, Issue 5). https://doi.org/10.3390/polym15051123
103. Fasehee, H., Dinarvand, R., Ghavamzadeh, A., Esfandyari-Manesh, M., Moradian, H., Faghihi, S. & Ghaffari, S. H. (2016). Delivery of disulfiram into breast cancer cells using folate-receptor-targeted PLGA-PEG nanoparticles: In vitro and in vivo investigations. *Journal of Nanobiotechnology*, *14*(1). https://doi.org/10.1186/s12951-016-0183-z
104. Gagliardi, A., Giuliano, E., Venkateswararao, E., Fresta, M., Bulotta, S., Awasthi, V. & Cosco, D. (2021). Biodegradable Polymeric Nanoparticles for Drug Delivery to Solid Tumors. In *Frontiers in Pharmacology* (Vol. 12). https://doi.org/10.3389/fphar.2021.601626
105. Hernández-Giottonini, K. Y., Rodríguez-Córdova, R. J., Gutiérrez-Valenzuela, C. A., Peñuñuri-Miranda, O., Zavala-Rivera, P., Guerrero-Germán, P. & Lucero-Acuña, A. (2020). PLGA nanoparticle preparations by emulsification and nanoprecipitation

techniques: Effects of formulation parameters. In *RSC Advances* (Vol. 10, Issue 8). https://doi.org/10.1039/c9ra10857b

106. Jadhav, V., Roy, A., Kaur, K., Rai, A. K. & Rustagi, S. (2024). Recent advances in nanomaterial-based drug delivery systems. In *Nano-Structures and Nano-Objects* (Vol. 37). https://doi.org/10.1016/j.nanoso.2024.101103
107. Jafari-Gharabaghlou, D., Dadashpour, M., khanghah, O. J., Salmani-Javan, E. & Zarghami, N. (2023). Potentiation of Folate-Functionalized PLGA-PEG nanoparticles loaded with metformin for the treatment of breast Cancer: possible clinical application. *Molecular Biology Reports*, *50*(4). https://doi.org/10.1007/s11033-022-08171-w
108. Jain, S., Rathi, V. V., Jain, A. K., Das, M. & Godugu, C. (2012). Folate-decorated PLGA nanoparticles as a rationally designed vehicle for the oral delivery of insulin. *Nanomedicine*, *7*(9). https://doi.org/10.2217/nnm.12.31
109. Jyoti, K., Kaur, K., Pandey, R. S., Jain, U. K., Chandra, R. & Madan, J. (2015). Inhalable nanostructured lipid particles of 9-bromo-noscapine, a tubulin-binding cytotoxic agent: In vitro and in vivo studies. *Journal of Colloid and Interface Science*, *445*. https://doi.org/10.1016/j.jcis.2014.12.092
110. Lopus, M. & Naik, P. K. (2015). Taking aim at a dynamic target: Noscapinoids as microtubule-targeted cancer therapeutics. In *Pharmacological Reports* (Vol. 67, Issue 1). https://doi.org/10.1016/j.pharep.2014.09.003
111. Madan, J., Baruah, B., Nagaraju, M., Abdalla, M. O., Yates, C., Turner, T., Rangari, V., Hamelberg, D. & Aneja, R. (2012). Molecular cycloencapsulation augments solubility and improves therapeutic index of brominated noscapine in prostate cancer cells. *Molecular Pharmaceutics*, *9*(5). https://doi.org/10.1021/mp300063v
112. Madan, J., Gundala, S. R., Baruah, B., Nagaraju, M., Yates, C., Turner, T., Rangari, V., Hamelberg, D., Reid, M. D. & Aneja, R. (2014). Cyclodextrin complexes of reduced bromonoscapine in guar gum microspheres enhance colonic drug delivery. *Molecular Pharmaceutics*, *11*(12). https://doi.org/10.1021/mp500408n
113. Mitchell, M. J., Billingsley, M. M., Haley, R. M., Wechsler, M. E., Peppas, N. A. & Langer, R. (2021). Engineering precision nanoparticles for drug delivery. In *Nature Reviews Drug Discovery* (Vol. 20, Issue 2). https://doi.org/10.1038/s41573-020-0090-8
114. Monteiro, C. A. P., Oliveira, A. D. P. R., Silva, R. C., Lima, R. R. M., Souto, F. O., Baratti, M. O., Carvalho, H. F., Santos, B. S., Cabral Filho, P. E. & Fontes, A. (2020). Evaluating internalization and recycling of folate receptors in breast cancer cells using quantum dots. *Journal of Photochemistry and Photobiology B: Biology*, *209*. https://doi.org/10.1016/j.jphotobiol.2020.111918
115. Parvathaneni, V., Shukla, S. K. & Gupta, V. (2023). Development and Characterization of Folic Acid-Conjugated Amodiaquine-Loaded Nanoparticles–Efficacy in Cancer Treatment. *Pharmaceutics*, *15*(3). https://doi.org/10.3390/pharmaceutics15031001
116. Patra, A., Satpathy, S., Naik, P. K., Kazi, M. & Hussain, M. D. (2022). Folate receptor-targeted PLGA-PEG nanoparticles for enhancing the activity of genistein in ovarian cancer. *Artificial Cells, Nanomedicine and Biotechnology*, *50*(1). https://doi.org/10.1080/21691401.2022.2118758
117. Perinelli, D. R., Cespi, M., Bonacucina, G. & Palmieri, G. F. (2019). PEGylated polylactide (PLA) and poly (lactic-co-glycolic acid) (PLGA) copolymers for the design of drug delivery systems. In *Journal of Pharmaceutical Investigation* (Vol. 49, Issue 4). https://doi.org/10.1007/s40005-019-00442-2

118. Sung, Y. K. & Kim, S. W. (2020). Recent advances in polymeric drug delivery systems. In *Biomaterials Research* (Vol. 24, Issue 1). https://doi.org/10.1186/s40824-020-00190-7
119. Waheed, S., Li, Z., Zhang, F., Chiarini, A., Armato, U. & Wu, J. (2022). Engineering nano-drug biointerface to overcome biological barriers toward precision drug delivery. In *Journal of Nanobiotechnology* (Vol. 20, Issue 1). https://doi.org/10.1186/s12951-022-01605-4
120. Abbas, Z. S., Sulaiman, G. M., Jabir, M. S., Mohammed, S. A. A., Khan, R. A., Mohammed, H. A. & Al-Subaiyel, A. (2022). Galangin/β-Cyclodextrin Inclusion Complex as a Drug-Delivery System for Improved Solubility and Biocompatibility in Breast Cancer Treatment. *Molecules*, *27*(14). https://doi.org/10.3390/molecules27144521
121. Abou-Okeil, A., Rehan, M., El-Sawy, S. M., El-bisi, M. K., Ahmed-Farid, O. A. & Abdel-Mohdy, F. A. (2018). Lidocaine/β-cyclodextrin inclusion complex as drug delivery system. *European Polymer Journal*, *108*. https://doi.org/10.1016/j.eurpolymj.2018.09.016
122. Anand, U., Dey, A., Chandel, A. K. S., Sanyal, R., Mishra, A., Pandey, D. K., De Falco, V., Upadhyay, A., Kandimalla, R., Chaudhary, A., Dhanjal, J. K., Dewanjee, S., Vallamkondu, J. & Pérez de la Lastra, J. M. (2023). Cancer chemotherapy and beyond: Current status, drug candidates, associated risks and progress in targeted therapeutics. In *Genes and Diseases* (Vol. 10, Issue 4). https://doi.org/10.1016/j.gendis.2022.02.007
123. Aneja, R., Vangapandu, S. N., Lopus, M., Viswesarappa, V. G., Dhiman, N., Verma, A., Chandra, R., Panda, D. & Joshi, H. C. (2006). Synthesis of microtubule-interfering halogenated noscapine analogs that perturb mitosis in cancer cells followed by cell death. *Biochemical Pharmacology*, *72*(4). https://doi.org/10.1016/j.bcp.2006.05.004
124. Araujo, M. V. G. de, Macedo, O. F. L., Nascimento, C. da C., Conegero, L. S., Barreto, L. S., Almeida, L. E., Costa, N. B. da & Gimenez, I. F. (2009). Characterization, phase solubility and molecular modeling of α-cyclodextrin/pyrimethamine inclusion complex. *Spectrochimica Acta - Part A: Molecular and Biomolecular Spectroscopy*, *72*(1). https://doi.org/10.1016/j.saa.2008.09.011
125. Baitharu, I., Jain, V., Deep, S. N., Shroff, S., Sahu, J. K., Naik, P. K. & Ilavazhagan, G. (2014). Withanolide A prevents neurodegeneration by modulating hippocampal glutathione biosynthesis during hypoxia. *PLoS ONE*, *9*(10). https://doi.org/10.1371/journal.pone.0105311
126. Bomzan, P., Roy, N., Sharma, A., Rai, V., Ghosh, S., Kumar, A. & Roy, M. N. (2021). Molecular encapsulation study of indole-3-methanol in cyclodextrins: Effect on antimicrobial activity and cytotoxicity. *Journal of Molecular Structure*, *1225*. https://doi.org/10.1016/j.molstruc.2020.129093
127. Čermák, V., Dostál, V., Jelínek, M., Libusová, L., Kovář, J., Rösel, D. & Brábek, J. (2020). Microtubule-targeting agents and their impact on cancer treatment. In *European Journal of Cell Biology* (Vol. 99, Issue 4). https://doi.org/10.1016/j.ejcb.2020.151075
128. Chen, J., Qin, X., Zhong, S., Chen, S., Su, W. & Liu, Y. (2018). Characterization of curcumin/cyclodextrin polymer inclusion complex and investigation on its antioxidant and antiproliferative activities. *Molecules*, *23*(5). https://doi.org/10.3390/molecules23051179
129. Dandawate, P. R., Vyas, A., Ahmad, A., Banerjee, S., Deshpande, J., Swamy, K. V., Jamadar, A., Dumhe-Klaire, A. C., Padhye, S. & Sarkar, F. H. (2012). Inclusion complex of novel curcumin analogue CDF and β-cyclodextrin (1:2) and its enhanced in vivo

anticancer activity against pancreatic cancer. *Pharmaceutical Research*, *29*(7). https://doi.org/10.1007/s11095-012-0700-1

130. Friesner, R. A., Banks, J. L., Murphy, R. B., Halgren, T. A., Klicic, J. J., Mainz, D. T., Repasky, M. P., Knoll, E. H., Shelley, M., Perry, J. K., Shaw, D. E., Francis, P. & Shenkin, P. S. (2004). Glide: A New Approach for Rapid, Accurate Docking and Scoring. 1. Method and Assessment of Docking Accuracy. *Journal of Medicinal Chemistry*, *47*(7). https://doi.org/10.1021/jm0306430

131. Garrido, C., Galluzzi, L., Brunet, M., Puig, P. E., Didelot, C. & Kroemer, G. (2006). Mechanisms of cytochrome c release from mitochondria. In *Cell Death and Differentiation* (Vol. 13, Issue 9). https://doi.org/10.1038/sj.cdd.4401950

132. Goga, N., Rzepiela, A. J., De Vries, A. H., Marrink, S. J. & Berendsen, H. J. C. (2012). Efficient algorithms for langevin and DPD dynamics. *Journal of Chemical Theory and Computation*, *8*(10). https://doi.org/10.1021/ct3000876

133. Halgren, T. A., Murphy, R. B., Friesner, R. A., Beard, H. S., Frye, L. L., Pollard, W. T. & Banks, J. L. (2004). Glide: A New Approach for Rapid, Accurate Docking and Scoring. 2. Enrichment Factors in Database Screening. *Journal of Medicinal Chemistry*, *47*(7). https://doi.org/10.1021/jm030644s

134. Han, D., Han, Z., Liu, L., Wang, Y., Xin, S., Zhang, H. & Yu, Z. (2020). Solubility enhancement of myricetin by inclusion complexation with heptakis-o-(2-hydroxypropyl)-β-cyclodextrin: A joint experimental and theoretical study. *International Journal of Molecular Sciences*, *21*(3). https://doi.org/10.3390/ijms21030766

135. Heer, E., Harper, A., Escandor, N., Sung, H., McCormack, V. & Fidler-Benaoudia, M. M. (2020). Global burden and trends in premenopausal and postmenopausal breast cancer: a population-based study. *The Lancet Global Health*, *8*(8). https://doi.org/10.1016/S2214-109X(20)30215-1

136. Jabbarzadeh Kaboli, P., Rahmat, A., Ismail, P. & Ling, K. H. (2014). Targets and mechanisms of berberine, a natural drug with potential to treat cancer with special focus on breast cancer. In *European Journal of Pharmacology* (Vol. 740). https://doi.org/10.1016/j.ejphar.2014.06.025

137. Karna, P., Rida, P. C. G., Turaga, R. C., Gao, J., Gupta, M., Fritz, A., Werner, E., Yates, C., Zhou, J. & Aneja, R. (2012). A novel microtubule-modulating agent EM011 inhibits angiogenesis by repressing the HIF-1α axis and disrupting cell polarity and migration. *Carcinogenesis*, *33*(9). https://doi.org/10.1093/carcin/bgs200

138. Ke, Y., Ye, K., Grossniklaus, H. E., Archer, D. R., Joshi, H. C. & Kapp, J. A. (2000). Noscapine inhibits tumor growth with little toxicity to normal tissues or inhibition of immune responses. *Cancer Immunology Immunotherapy*, *49*(4–5). https://doi.org/10.1007/s002620000109

139. Lee, C. J., Liang, X., Wu, Q., Najeeb, J., Zhao, J., Gopalaswamy, R., Titecat, M., Sebbane, F., Lemaitre, N., Toone, E. J. & Zhou, P. (2016). Drug design from the cryptic inhibitor envelope. *Nature Communications*, *7*. https://doi.org/10.1038/ncomms10638

140. Madan, J., Gundala, S. R., Baruah, B., Nagaraju, M., Yates, C., Turner, T., Rangari, V., Hamelberg, D., Reid, M. D. & Aneja, R. (2014). Cyclodextrin complexes of reduced bromonoscapine in guar gum microspheres enhance colonic drug delivery. *Molecular Pharmaceutics*, *11*(12). https://doi.org/10.1021/mp500408n

141. Malli, S., Bories, C., Ponchel, G., Loiseau, P. M. & Bouchemal, K. (2018). Phase solubility studies and anti-Trichomonas vaginalis activity evaluations of metronidazole and methylated β-cyclodextrin complexes: Comparison of CRYSMEB and RAMEB. *Experimental Parasitology*, *189*. https://doi.org/10.1016/j.exppara.2018.04.019

142. Mangolim, C. S., Moriwaki, C., Nogueira, A. C., Sato, F., Baesso, M. L., Neto, A. M. & Matioli, G. (2014). Curcumin-β-cyclodextrin inclusion complex: Stability, solubility, characterisation by FT-IR, FT-Raman, X-ray diffraction and photoacoustic spectroscopy, and food application. *Food Chemistry*, *153*. https://doi.org/10.1016/j.foodchem.2013.12.067
143. Memisoglu-Bilensoy, E., Vural, I., Bochot, A., Renoir, J. M., Duchene, D. & Hincal, A. A. (2005). Tamoxifen citrate loaded amphiphilic β-cyclodextrin nanoparticles: In vitro characterization and cytotoxicity. *Journal of Controlled Release*, *104*(3). https://doi.org/10.1016/j.jconrel.2005.03.006
144. Mu, K., Jiang, K., Wang, Y., Zhao, Z., Cang, S., Bi, K., Li, Q. & Liu, R. (2022). The Biological Fate of Pharmaceutical Excipient β-Cyclodextrin: Pharmacokinetics, Tissue Distribution, Excretion, and Metabolism of β-Cyclodextrin in Rats. *Molecules*, *27*(3). https://doi.org/10.3390/molecules27031138
145. Muhammad Nadzri, N., Abdul, A. B., Sukari, M. A., Abdelwahab, S. I., Eid, E. E. M., Mohan, S., Kamalidehghan, B., Anasamy, T., Ng, K. B., Syam, S., Arbab, I. A., Rahman, H. S. & Ali, H. M. (2013). Inclusion complex of zerumbone with hydroxypropyl-β-Cyclodextrin induces apoptosis in liver hepatocellular HepG2 Cells via caspase 8/BID cleavage switch and modulating Bcl2/Bax ratio. *Evidence-Based Complementary and Alternative Medicine*, *2013*. https://doi.org/10.1155/2013/810632
146. Mukherjee, K., Dutta, P., Dey, S. & Giri, T. K. (2024). Enhancement of the efficacy of synthetic and natural anticancer agents through nanocarrier for colon cancer treatment. *European Journal of Medicinal Chemistry Reports*, *10*. https://doi.org/10.1016/j.ejmcr.2024.100137
147. Mukne, A. P. & Nagarsenker, M. S. (2004). Triamterene-β-cyclodextrin systems: Preparation, characterization and in vivo evaluation. *AAPS PharmSciTech*, *5*(1). https://doi.org/10.1007/bf02830587
148. Naik, P. K., Chatterji, B. P., Vangapandu, S. N., Aneja, R., Chandra, R., Kanteveri, S. & Joshi, H. C. (2011). Rational design, synthesis and biological evaluations of amino-noscapine: A high affinity tubulin-binding noscapinoid. *Journal of Computer-Aided Molecular Design*, *25*(5). https://doi.org/10.1007/s10822-011-9430-4
149. Patel, A. K., Meher, R. K., Reddy, P. K., Pedapati, R. K., Pragyandipta, P., Kantevari, S., Naik, M. R. & Naik, P. K. (2021). Rational design, chemical synthesis and cellular evaluation of novel 1,3-diynyl derivatives of noscapine as potent tubulin binding anticancer agents. *Journal of Molecular Graphics and Modelling*, *106*. https://doi.org/10.1016/j.jmgm.2021.107933
150. Pearlman, D. A., Case, D. A., Caldwell, J. W., Ross, W. S., Cheatham, T. E., DeBolt, S., Ferguson, D., Seibel, G. & Kollman, P. (1995). AMBER, a package of computer programs for applying molecular mechanics, normal mode analysis, molecular dynamics and free energy calculations to simulate the structural and energetic properties of molecules. *Computer Physics Communications*, *91*(1–3). https://doi.org/10.1016/0010-4655(95)00041-D
151. Ray, S., Roy, N., Barman, B. K., Karmakar, P., Bomzan, P., Rajbanshi, B., Dakua, V. K., Dutta, A., Kumar, A. & Roy, M. N. (2022). Synthesis and Characterization of an Inclusion Complex of dl -Aminoglutethimide with β-Cyclodextrin and Its Innovative Application in a Biological System: Computational and Experimental Investigations. *ACS Omega*, *7*(13). https://doi.org/10.1021/acsomega.2c00011
152. Real, D. A., Bolaños, K., Priotti, J., Yutronic, N., Kogan, M. J., Sierpe, R. & Donoso-González, O. (2021). Cyclodextrin-modified nanomaterials for drug delivery:

Classification and advances in controlled release and bioavailability. In *Pharmaceutics* (Vol. 13, Issue 12). https://doi.org/10.3390/pharmaceutics13122131

153. Ren, L., Wang, J. & Chen, G. (2019). Preparation, optimization of the inclusion complex of glaucocalyxin A with sulfobutylether-β-cyclodextrin and antitumor study. *Drug Delivery*, *26*(1). https://doi.org/10.1080/10717544.2019.1568623

154. Ryckaert, J. P., Ciccotti, G. & Berendsen, H. J. C. (1977). Numerical integration of the cartesian equations of motion of a system with constraints: molecular dynamics of n-alkanes. *Journal of Computational Physics*, *23*(3). https://doi.org/10.1016/0021-9991(77)90098-5

155. Santos, P. S., Souza, L. K. M., Araujo, T. S. L., Medeiros, J. V. R., Nunes, S. C. C., Carvalho, R. A., Pais, A. C. C., Veiga, F. J. B., Nunes, L. C. C. & Figueiras, A. (2017). Methyl-β-cyclodextrin inclusion complex with β βcaryophyllene: Preparation, characterization, and improvement of pharmacological activitie. *ACS Omega*, *2*(12). https://doi.org/10.1021/acsomega.7b01438

156. Saokham, P., Muankaew, C., Jansook, P. & Loftsson, T. (2018). Solubility of cyclodextrins and drug/cyclodextrin complexes. In *Molecules* (Vol. 23, Issue 5). https://doi.org/10.3390/molecules23051161

157. Sravani, A. B., Shenoy K, M., Chandrika, B., Kumar B, H., Kini, S. G., Pai K, S. R. & Lewis, S. A. (2023). Curcumin-sulfobutyl-ether beta cyclodextrin inclusion complex: preparation, spectral characterization, molecular modeling, and antimicrobial activity. *Journal of Biomolecular Structure and Dynamics*. https://doi.org/10.1080/07391102.2023.2254409

158. Sung, Y. K. & Kim, S. W. (2020). Recent advances in polymeric drug delivery systems. In *Biomaterials Research* (Vol. 24, Issue 1). https://doi.org/10.1186/s40824-020-00190-7

159. Szente, L. & Szejtli, J. (1999). Highly soluble cyclodextrin derivatives: Chemistry, properties, and trends in development. *Advanced Drug Delivery Reviews*, *36*(1). https://doi.org/10.1016/S0169-409X(98)00092-1

160. Testa, U., Castelli, G. & Pelosi, E. (2020). Breast Cancer: A Molecularly Heterogenous Disease Needing Subtype-Specific Treatments. In *Medical sciences (Basel, Switzerland)* (Vol. 8, Issue 1). https://doi.org/10.3390/medsci8010018

161. Verma, A. K., Bansal, S., Singh, J., Tiwari, R. K., Kasi Sankar, V., Tandon, V. & Chandra, R. (2006). Synthesis and in vitro cytotoxicity of haloderivatives of noscapine. *Bioorganic and Medicinal Chemistry*, *14*(19). https://doi.org/10.1016/j.bmc.2006.05.069

162. Wang, H. & Laughton, C. A. (2007). Molecular modelling methods for prediction of sequence-selectivity in DNA recognition. *Methods*, *42*(2). https://doi.org/10.1016/j.ymeth.2006.09.002

163. Wang, Jing, Cao, Y., Sun, B. & Wang, C. (2011). Physicochemical and release characterisation of garlic oil-β- cyclodextrin inclusion complexes. *Food Chemistry*, *127*(4). https://doi.org/10.1016/j.foodchem.2011.02.036

164. Wang, Jun & Wu, S. G. (2023). Breast Cancer: An Overview of Current Therapeutic Strategies, Challenge, and Perspectives. In *Breast Cancer: Targets and Therapy* (Vol. 15). https://doi.org/10.2147/BCTT.S432526

165. Yan, H. H., Zhang, J. Q., Ren, S. H., Xie, X. G., Huang, R., Jin, Y. & Lin, J. (2017). Experimental and computational studies of naringin/cyclodextrin inclusion complexation. *Journal of Inclusion Phenomena and Macrocyclic Chemistry*, *88*(1–2). https://doi.org/10.1007/s10847-017-0704-x

166. Yang, J., Ma, Y., Luo, Q., Liang, Z., Lu, P., Song, F., Zhang, Z., Zhou, T. & Zhang, J. (2022). Improving the solubility of vorinostat using cyclodextrin inclusion complexes: The physicochemical characteristics, corneal permeability and ocular pharmacokinetics of the drug after topical application. *European Journal of Pharmaceutical Sciences*, *168*. https://doi.org/10.1016/j.ejps.2021.106078
167. Yao, Y., Zhou, Y., Liu, L., Xu, Y., Chen, Q., Wang, Y., Wu, S., Deng, Y., Zhang, J. & Shao, A. (2020). Nanoparticle-Based Drug Delivery in Cancer Therapy and Its Role in Overcoming Drug Resistance. In *Frontiers in Molecular Biosciences* (Vol. 7). https://doi.org/10.3389/fmolb.2020.00193
168. Ye, K., Ke, Y., Keshava, N., Shanks, J., Kapp, J. A., Tekmal, R. R., Petros, J. & Joshi, H. C. (1998). Opium alkaloid noscapine is an antitumor agent that arrests metaphase and induces apoptosis in dividing cells. *Proceedings of the National Academy of Sciences of the United States of America*, *95*(4). https://doi.org/10.1073/pnas.95.4.1601
169. Ye, Y. J., Wang, Y., Lou, K. Y., Chen, Y. Z., Chen, R. & Gao, F. (2015). The preparation, characterization, and pharmacokinetic studies of chitosan nanoparticles loaded with paclitaxel/dimethyl-β-cyclodextrin inclusion complexes. *International Journal of Nanomedicine*, *10*. https://doi.org/10.2147/IJN.S83508
170. Yu, C., Minemoto, Y., Zhang, J., Liu, J., Tang, F., Bui, T. N., Xiang, J. & Lin, A. (2004). JNK Suppresses Apoptosis via Phosphorylation of the Proapoptotic Bcl-2 Family Protein BAD. *Molecular Cell*, *13*(3). https://doi.org/10.1016/S1097-2765(04)00028-0
171. Abraham, M. J., Murtola, T., Schulz, R., Páll, S., Smith, J. C., Hess, B. & Lindah, E. (2015). Gromacs: High performance molecular simulations through multi-level parallelism from laptops to supercomputers. *SoftwareX*, *1–2*. https://doi.org/10.1016/j.softx.2015.06.001
172. Bajracharya, R., Song, J. G., Patil, B. R., Lee, S. H., Noh, H. M., Kim, D. H., Kim, G. L., Seo, S. H., Park, J. W., Jeong, S. H., Lee, C. H. & Han, H. K. (2022). Functional ligands for improving anticancer drug therapy: current status and applications to drug delivery systems. *Drug Delivery*, *29*(1). https://doi.org/10.1080/10717544.2022.2089296
173. Binkley, J. S., Pople, J. A. & Hehre, W. J. (1980). Self-consistent molecular orbital methods. 21. Small split-valence basis sets for first-row elements. *Journal of the American Chemical Society*, *102*(3). https://doi.org/10.1021/ja00523a008
174. Calaf, G. M., Crispin, L. A. & Quisbert-Valenzuela, E. O. (2024). Noscapine and Apoptosis in Breast and Other Cancers. In *International Journal of Molecular Sciences* (Vol. 25, Issue 6). https://doi.org/10.3390/ijms25063536
175. Chehelgerdi, M., Chehelgerdi, M., Allela, O. Q. B., Pecho, R. D. C., Jayasankar, N., Rao, D. P., Thamaraikani, T., Vasanthan, M., Viktor, P., Lakshmaiya, N., Saadh, M. J., Amajd, A., Abo-Zaid, M. A., Castillo-Acobo, R. Y., Ismail, A. H., Amin, A. H. & Akhavan-Sigari, R. (2023). Progressing nanotechnology to improve targeted cancer treatment: overcoming hurdles in its clinical implementation. In *Molecular Cancer* (Vol. 22, Issue 1). https://doi.org/10.1186/s12943-023-01865-0
176. Chen, J., Wu, Q., Luo, L., Wang, Y., Zhong, Y., Dai, H. Bin, Sun, D., Luo, M. L., Wu, W. & Wang, G. X. (2017). Dual tumor-targeted poly(lactic-co-glycolic acid)–polyethylene glycol–folic acid nanoparticles: A novel biodegradable nanocarrier for secure and efficient antitumor drug delivery. *International Journal of Nanomedicine*, *12*. https://doi.org/10.2147/IJN.S136488
177. Cross, J. B., Thompson, D. C., Rai, B. K., Baber, J. C., Fan, K. Y., Hu, Y. & Humblet, C. (2009). Comparison of several molecular docking programs: Pose prediction and

virtual screening accuracy. *Journal of Chemical Information and Modeling*, *49*(6). https://doi.org/10.1021/ci900056c

178. Dash, S. G., Kantevari, S., Pandey, S. K. & Naik, P. K. (2021). Synergistic interaction of N-3-Br-benzyl-noscapine and docetaxel abrogates oncogenic potential of breast cancer cells. *Chemical Biology and Drug Design*, *98*(3). https://doi.org/10.1111/cbdd.13902
179. El-Hammadi, M. M., Delgado, Á. V., Melguizo, C., Prados, J. C. & Arias, J. L. (2017). Folic acid-decorated and PEGylated PLGA nanoparticles for improving the antitumour activity of 5-fluorouracil. *International Journal of Pharmaceutics*, *516*(1–2). https://doi.org/10.1016/j.ijpharm.2016.11.012
180. Fasehee, H., Dinarvand, R., Ghavamzadeh, A., Esfandyari-Manesh, M., Moradian, H., Faghihi, S. & Ghaffari, S. H. (2016). Delivery of disulfiram into breast cancer cells using folate-receptor-targeted PLGA-PEG nanoparticles: In vitro and in vivo investigations. *Journal of Nanobiotechnology*, *14*(1). https://doi.org/10.1186/s12951-016-0183-z
181. Friesner, R. A., Banks, J. L., Murphy, R. B., Halgren, T. A., Klicic, J. J., Mainz, D. T., Repasky, M. P., Knoll, E. H., Shelley, M., Perry, J. K., Shaw, D. E., Francis, P. & Shenkin, P. S. (2004). Glide: A New Approach for Rapid, Accurate Docking and Scoring. 1. Method and Assessment of Docking Accuracy. *Journal of Medicinal Chemistry*, *47*(7). https://doi.org/10.1021/jm0306430
182. Gandhi, S. & Roy, I. (2023). Lipid-Based Inhalable Micro- and Nanocarriers of Active Agents for Treating Non-Small-Cell Lung Cancer. In *Pharmaceutics* (Vol. 15, Issue 5). https://doi.org/10.3390/pharmaceutics15051457
183. Gordon, M. S., Binkley, J. S., Pople, J. A., Pietro, W. J. & Hehre, W. J. (1982). Self-Consistent Molecular-Orbital Methods. 22. Small Split-Valence Basis Sets for Second-Row Elements. *Journal of the American Chemical Society*, *104*(10). https://doi.org/10.1021/ja00374a017
184. Halgren, T. A., Murphy, R. B., Friesner, R. A., Beard, H. S., Frye, L. L., Pollard, W. T. & Banks, J. L. (2004). Glide: A New Approach for Rapid, Accurate Docking and Scoring. 2. Enrichment Factors in Database Screening. *Journal of Medicinal Chemistry*, *47*(7). https://doi.org/10.1021/jm030644s
185. He, Z., Zhang, Y. & Feng, N. (2020). Cell membrane-coated nanosized active targeted drug delivery systems homing to tumor cells: A review. In *Materials Science and Engineering C* (Vol. 106). https://doi.org/10.1016/j.msec.2019.110298
186. Hornak, V., Abel, R., Okur, A., Strockbine, B., Roitberg, A. & Simmerling, C. (2006). Comparison of multiple amber force fields and development of improved protein backbone parameters. In *Proteins: Structure, Function and Genetics* (Vol. 65, Issue 3). https://doi.org/10.1002/prot.21123
187. Jakalian, A., Jack, D. B. & Bayly, C. I. (2002). Fast, efficient generation of high-quality atomic charges. AM1-BCC model: II. Parameterization and validation. *Journal of Computational Chemistry*, *23*(16). https://doi.org/10.1002/jcc.10128
188. Jusu, S. M., Obayemi, J. D., Salifu, A. A., Nwazojie, C. C., Uzonwanne, V. O., Odusanya, O. S. & Soboyejo, W. O. (2021). Plga-cs-peg microparticles for controlled drug delivery in the treatment of triple negative breast cancer cells. *Applied Sciences (Switzerland)*, *11*(15). https://doi.org/10.3390/app11157112
189. Kim, H. & Xue, X. (2020). Detection of total reactive oxygen species in adherent cells by 2',7'-dichlorodihydrofluorescein diacetate staining. *Journal of Visualized Experiments*, *2020*(160). https://doi.org/10.3791/60682

190. Kumar Pedapati, R., Pragyandipta, P., Pranathi Abburi, N., Chirra, N., Kantevari, S. & Naik, P. K. (2023). Antiproliferative Noscapinoids Bearing an Amidothiadiazole Scaffold as Apoptosis Inducers: Design, Synthesis and Molecular Docking. *Chemistry and Biodiversity*, *20*(2). https://doi.org/10.1002/cbdv.202201089
191. Kumar, S., Sagar, B., Gaur, A., Shukla, S., Pandey, E. & Gulati, S. (2022). Insight into the Tubulin-Targeted Anticancer Potential of Noscapine and its Structural Analogs. *Anti-Cancer Agents in Medicinal Chemistry*, *23*(6). https://doi.org/10.2174/1871520622666220804115551
192. Madan, J., Dhiman, N., Parmar, V. K., Sardana, S., Bharatam, P. V., Aneja, R., Chandra, R. & Katyal, A. (2010). Inclusion complexes of noscapine in β-cyclodextrin offer better solubility and improved pharmacokinetics. *Cancer Chemotherapy and Pharmacology*, *65*(3). https://doi.org/10.1007/s00280-009-1060-3
193. Makadia, H. K. & Siegel, S. J. (2011). Poly Lactic-co-Glycolic Acid (PLGA) as biodegradable controlled drug delivery carrier. *Polymers*, *3*(3). https://doi.org/10.3390/polym3031377
194. Patra, J. K., Das, G., Fraceto, L. F., Campos, E. V. R., Rodriguez-Torres, M. D. P., Acosta-Torres, L. S., Diaz-Torres, L. A., Grillo, R., Swamy, M. K., Sharma, S., Habtemariam, S. & Shin, H. S. (2018). Nano based drug delivery systems: Recent developments and future prospects. In *Journal of Nanobiotechnology* (Vol. 16, Issue 1). https://doi.org/10.1186/s12951-018-0392-8
195. Peer, D., Karp, J. M., Hong, S., Farokhzad, O. C., Margalit, R. & Langer, R. (2007). Nanocarriers as an emerging platform for cancer therapy. In *Nature Nanotechnology* (Vol. 2, Issue 12). https://doi.org/10.1038/nnano.2007.387
196. Pietro, W. J., Francl, M. M., Hehre, W. J., DeFrees, D. J., Pople, J. A. & Binkley, J. S. (1982). Self-Consistent Molecular Orbital Methods. 24. Supplemented Small Split-Valence Basis Sets for Second-Row Elements. *Journal of the American Chemical Society*, *104*(19). https://doi.org/10.1021/ja00383a007
197. Ponselvi Induja, M., Ezhilarasan, D. & Ashok Vardhan, N. (2018). Evolvulus alsinoides methanolic extract triggers apoptosis in HepG2 cells. *Avicenna Journal of Phytomedicine*, *8*(6).
198. Ryckaert, J. P., Ciccotti, G. & Berendsen, H. J. C. (1977). Numerical integration of the cartesian equations of motion of a system with constraints: molecular dynamics of n-alkanes. *Journal of Computational Physics*, *23*(3). https://doi.org/10.1016/0021-9991(77)90098-5
199. Santoshi, S. & Naik, P. K. (2014). Molecular insight of isotypes specific β-tubulin interaction of tubulin heterodimer with noscapinoids. *Journal of Computer-Aided Molecular Design*, *28*(7). https://doi.org/10.1007/s10822-014-9756-9
200. Yoo, H. S. & Park, T. G. (2004). Folate-receptor-targeted delivery of doxorubicin nano-aggregates stabilized by doxorubicin-PEG-folate conjugate. *Journal of Controlled Release*, *100*(2). https://doi.org/10.1016/j.jconrel.2004.08.017
201. Abraham, M. J., Murtola, T., Schulz, R., Páll, S., Smith, J. C., Hess, B. & Lindah, E. (2015). Gromacs: High performance molecular simulations through multi-level parallelism from laptops to supercomputers. SoftwareX, 1–2. https://doi.org/10.1016/j.softx.2015.06.001
202. Altinoz, M. A., Topcu, G., Hacimuftuoglu, A., Ozpinar, A., Ozpinar, A., Hacker, E. & Elmaci, İ. (2019). Noscapine, a Non-addictive Opioid and Microtubule-Inhibitor in Potential Treatment of Glioblastoma. In Neurochemical Research (Vol. 44, Issue 8). https://doi.org/10.1007/s11064-019-02837-x

203. Arnold, M., Morgan, E., Rumgay, H., Mafra, A., Singh, D., Laversanne, M., Vignat, J., Gralow, J. R., Cardoso, F., Siesling, S. & Soerjomataram, I. (2022). Current and future burden of breast cancer: Global statistics for 2020 and 2040. Breast, 66. https://doi.org/10.1016/j.breast.2022.08.010
204. Bag, S., Tawari, N. R., Degani, M. S. & Queener, S. F. (2010). Design, synthesis, biological evaluation and computational investigation of novel inhibitors of dihydrofolate reductase of opportunistic pathogens. Bioorganic and Medicinal Chemistry, 18(9). https://doi.org/10.1016/j.bmc.2010.03.031
205. Becke, A. D. (1993). A new mixing of Hartree-Fock and local density-functional theories. The Journal of Chemical Physics, 98(2). https://doi.org/10.1063/1.464304
206. Binkley, J. S., Pople, J. A. & Hehre, W. J. (1980). Self-consistent molecular orbital methods. 21. Small split-valence basis sets for first-row elements. Journal of the American Chemical Society, 102(3). https://doi.org/10.1021/ja00523a008
207. Dash, S. G., Joshi, H. C. & Naik, P. K. (2023). Noscapinoids: A Family of Microtubule-Targeted Anticancer Agent. In Materials Horizons: From Nature to Nanomaterials. https://doi.org/10.1007/978-981-19-7188-4_35
208. Friesner, R. A., Banks, J. L., Murphy, R. B., Halgren, T. A., Klicic, J. J., Mainz, D. T., Repasky, M. P., Knoll, E. H., Shelley, M., Perry, J. K., Shaw, D. E., Francis, P. & Shenkin, P. S. (2004). Glide: A New Approach for Rapid, Accurate Docking and Scoring. 1. Method and Assessment of Docking Accuracy. Journal of Medicinal Chemistry, 47(7). https://doi.org/10.1021/jm0306430
209. Gordon, M. S., Binkley, J. S., Pople, J. A., Pietro, W. J. & Hehre, W. J. (1982). Self-Consistent Molecular-Orbital Methods. 22. Small Split-Valence Basis Sets for Second-Row Elements. Journal of the American Chemical Society, 104(10). https://doi.org/10.1021/ja00374a017
210. Halgren, T. A., Murphy, R. B., Friesner, R. A., Beard, H. S., Frye, L. L., Pollard, W. T. & Banks, J. L. (2004). Glide: A New Approach for Rapid, Accurate Docking and Scoring. 2. Enrichment Factors in Database Screening. Journal of Medicinal Chemistry, 47(7). https://doi.org/10.1021/jm030644s
211. Hornak, V., Abel, R., Okur, A., Strockbine, B., Roitberg, A. & Simmerling, C. (2006). Comparison of multiple amber force fields and development of improved protein backbone parameters. In Proteins: Structure, Function and Genetics (Vol. 65, Issue 3). https://doi.org/10.1002/prot.21123
212. Jakalian, A., Jack, D. B. & Bayly, C. I. (2002). Fast, efficient generation of high-quality atomic charges. AM1-BCC model: II. Parameterization and validation. Journal of Computational Chemistry, 23(16). https://doi.org/10.1002/jcc.10128
213. Kasibhatla, S., Amarante-Mendes, G. P., Finucane, D., Brunner, T., Bossy-Wetzel, E. & Green, D. R. (2006). Acridine Orange/Ethidium Bromide (AO/EB) Staining to Detect Apoptosis. Cold Spring Harbor Protocols, 2006(3). https://doi.org/10.1101/pdb.prot4493
214. Kollman, P. A., Massova, I., Reyes, C., Kuhn, B., Huo, S., Chong, L., Lee, M., Lee, T., Duan, Y., Wang, W., Donini, O., Cieplak, P., Srinivasan, J., Case, D. A. & Cheatham, T. E. (2000). Calculating structures and free energies of complex molecules: Combining molecular mechanics and continuum models. Accounts of Chemical Research, 33(12). https://doi.org/10.1021/ar000033j
215. Kumar Pedapati, R., Pragyandipta, P., Pranathi Abburi, N., Chirra, N., Kantevari, S. & Naik, P. K. (2023). Antiproliferative Noscapinoids Bearing an Amidothiadiazole Scaffold as Apoptosis Inducers: Design, Synthesis and Molecular Docking. Chemistry and Biodiversity, 20(2). https://doi.org/10.1002/cbdv.202201089

216. Landen, J. W., Lang, R., McMahon, S. J., Rusan, N. M., Yvon, A. M., Adams, A. W., Sorcinelli, M. D., Campbell, R., Bonaccorsi, P., Ansel, J. C., Archer, D. R., Wadsworth, P., Armstrong, C. A. & Joshi, H. C. (2002). Noscapine alters microtubule dynamics in living cells and inhibits the progression of melanoma. Cancer Research, 62(14).
217. Lee, C., Yang, W. & Parr, R. G. (1988). Development of the Colle-Salvetti correlation-energy formula into a functional of the electron density. Physical Review B, 37(2). https://doi.org/10.1103/PhysRevB.37.785
218. Oliva, M. A., Prota, A. E., Rodríguez-Salarichs, J., Bennani, Y. L., Jiménez-Barbero, J., Bargsten, K., Canales, Á., Steinmetz, M. O. & Díaz, J. F. (2020). Structural Basis of Noscapine Activation for Tubulin Binding. Journal of Medicinal Chemistry, 63(15). https://doi.org/10.1021/acs.jmedchem.0c00855
219. Pietro, W. J., Francl, M. M., Hehre, W. J., DeFrees, D. J., Pople, J. A. & Binkley, J. S. (1982). Self-Consistent Molecular Orbital Methods. 24. Supplemented Small Split-Valence Basis Sets for Second-Row Elements. Journal of the American Chemical Society, 104(19). https://doi.org/10.1021/ja00383a007
220. Ryckaert, J. P., Ciccotti, G. & Berendsen, H. J. C. (1977). Numerical integration of the cartesian equations of motion of a system with constraints: molecular dynamics of n-alkanes. Journal of Computational Physics, 23(3). https://doi.org/10.1016/0021-9991(77)90098-5
221. Sousa Da Silva, A. W. & Vranken, W. F. (2012). ACPYPE - AnteChamber PYthon Parser interfacE. BMC Research Notes, 5. https://doi.org/10.1186/1756-0500-5-367
222. Tomayko, M. M. & Reynolds, C. P. (1989). Determination of subcutaneous tumor size in athymic (nude) mice. Cancer Chemotherapy and Pharmacology, 24(3). https://doi.org/10.1007/BF00300234
223. Vadhel, A., Bashir, S., Mir, A. H., Girdhar, M., Kumar, D., Kumar, A., Mohan, A., Malik, T. & Mohan, A. (2023). Opium alkaloids, biosynthesis, pharmacology and association with cancer occurrence. In Open Biology (Vol. 13, Issue 5). https://doi.org/10.1098/rsob.220355
224. Wallace, A. C., Laskowski, R. A. & Thornton, J. M. (1995). Ligplot: A program to generate schematic diagrams of protein-ligand interactions. Protein Engineering, Design and Selection, 8(2). https://doi.org/10.1093/protein/8.2.127
225. Wordeman, L. & Vicente, J. J. (2021). Microtubule targeting agents in disease: Classic drugs, novel roles. In Cancers (Vol. 13, Issue 22). https://doi.org/10.3390/cancers13225650

APPENDICES

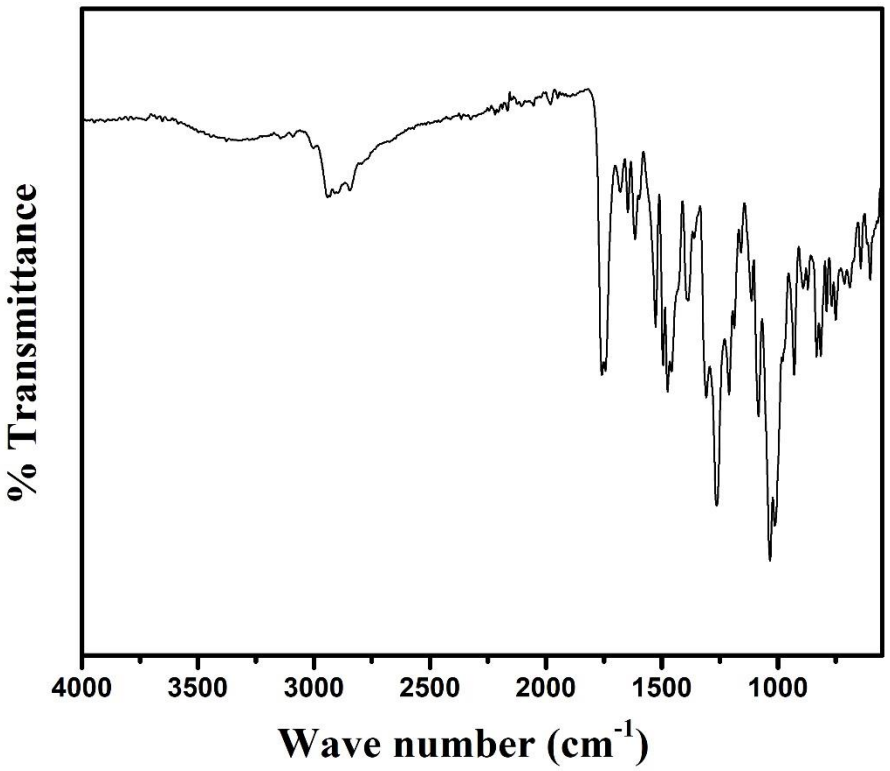

Figure S1. FT-IR spectra of **13**.

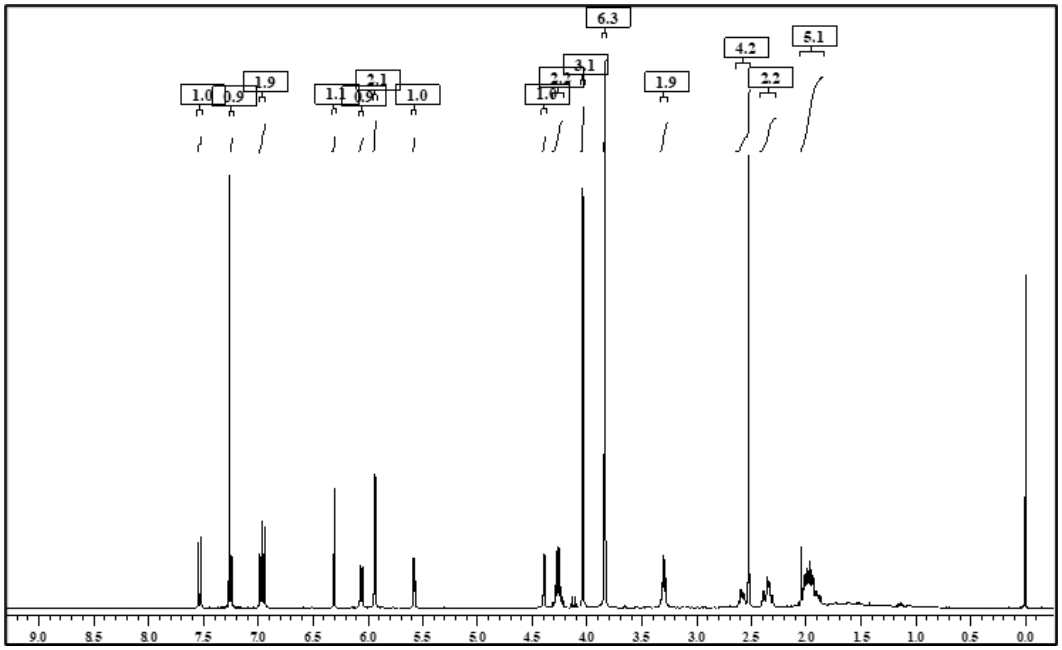

Figure S2. ^{1}H NMR spectra of **13**.

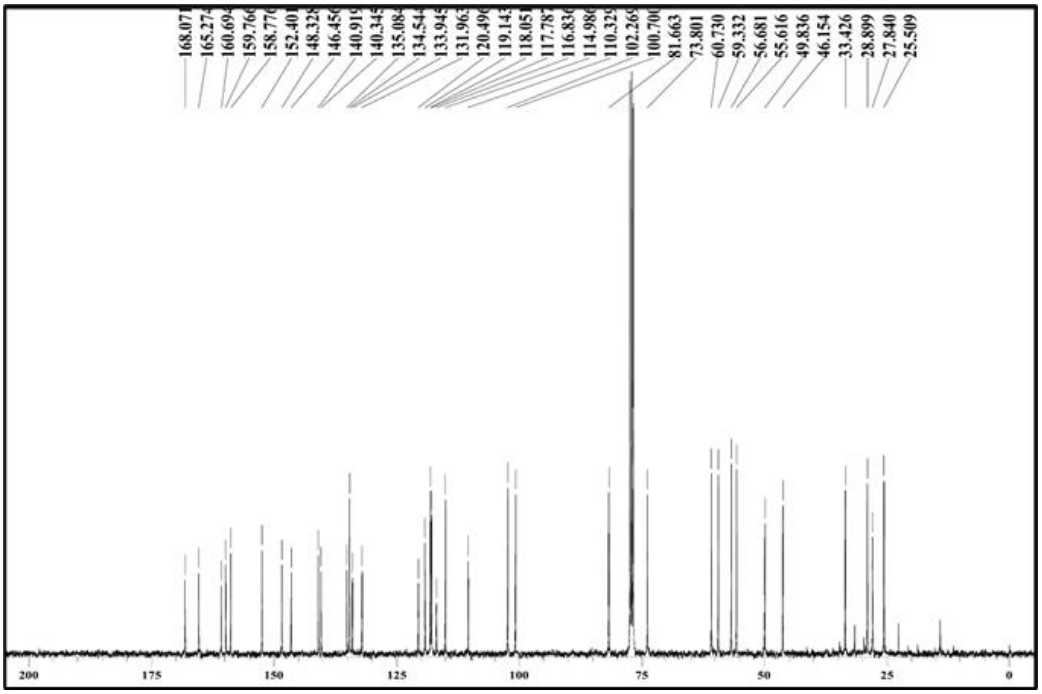

Figure S3. ^{1}H NMR spectra of **13**.

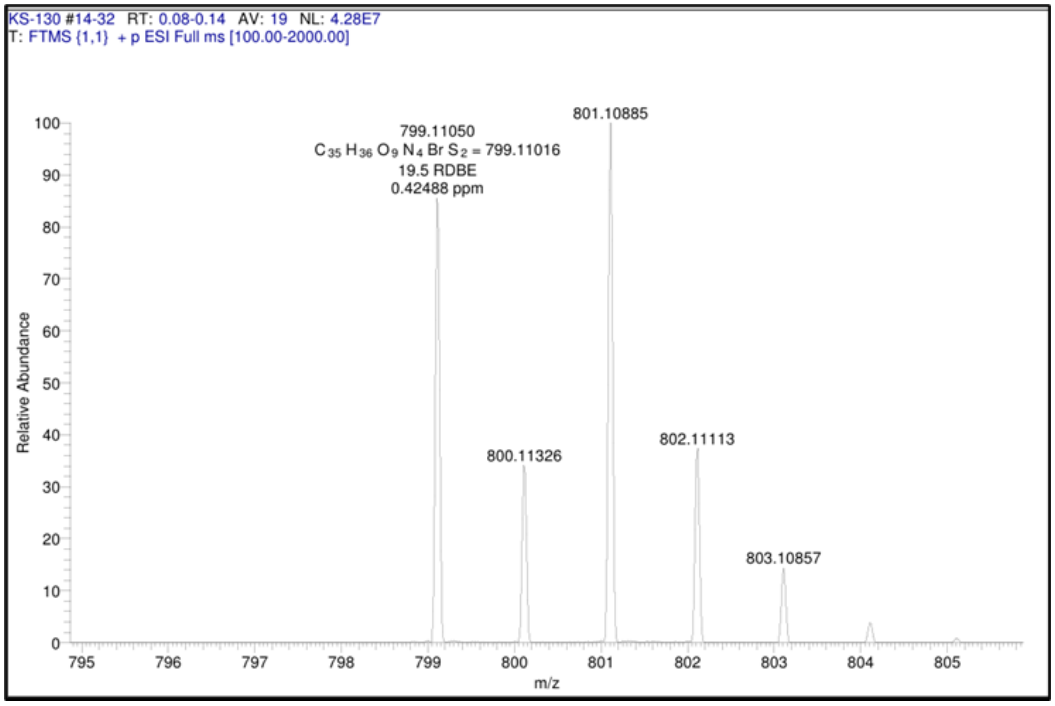

Figure S4. ESI-MS spectra of **13**.

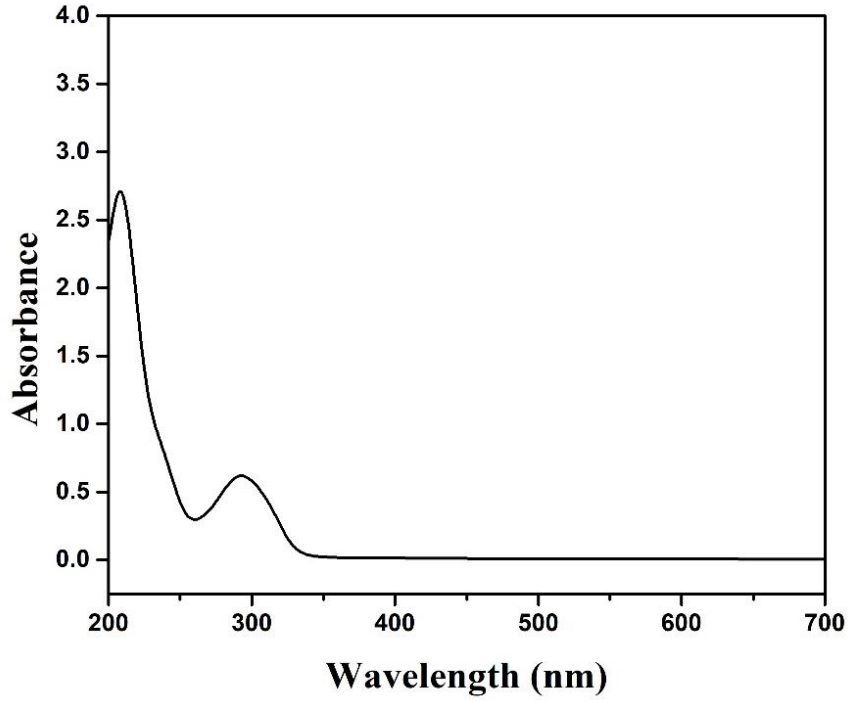

Figure S5. UV-Visible spectra of **13**.

The UV–Visible absorption spectrum of compound 13 (Figure 4.4 (e)) shows a prominent absorption maximum at 292 nm, indicating the presence of conjugated π-electron systems. This peak corresponds to π–π* transitions, commonly observed in aromatic compounds and supports the presence of the isoquinoline chromophore within the noscapine derivative.

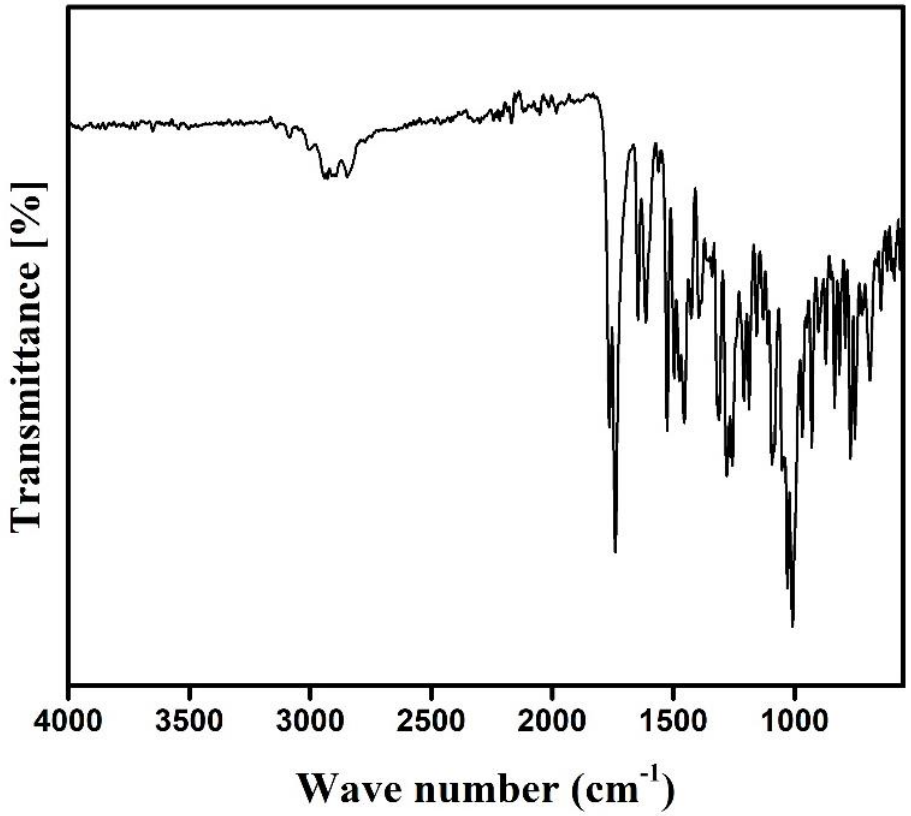

Figure S6. FT-IR spectra of **14**.

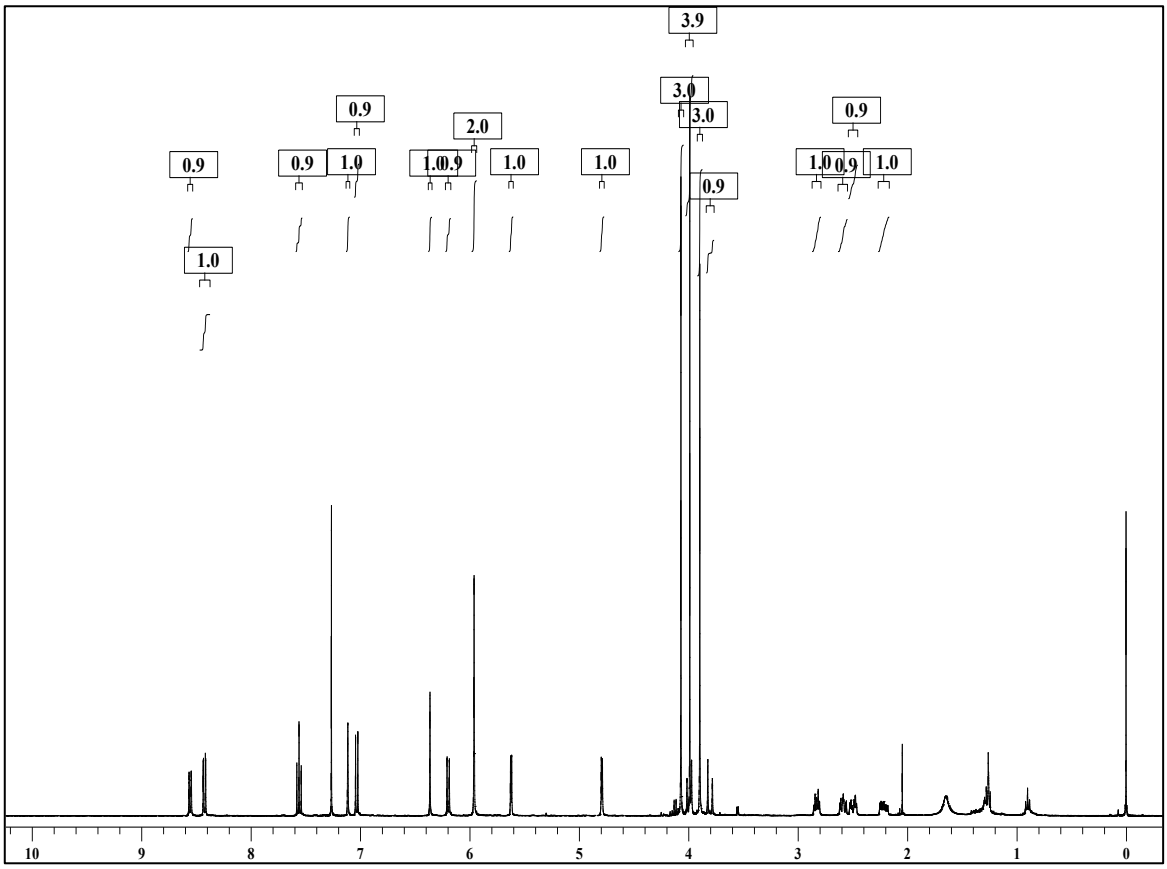

Figure S7. ^{1}H NMR spectra of **14**.

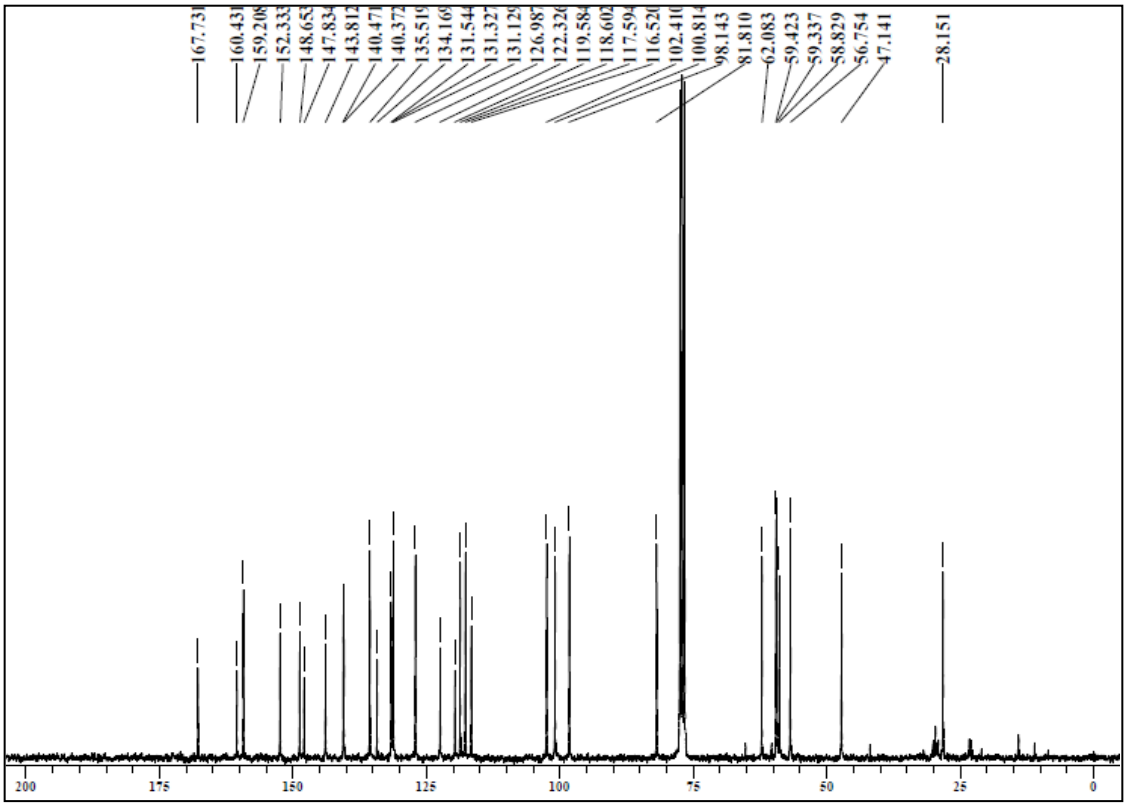

Figure S8. C^{13} NMR spectra of **14**.

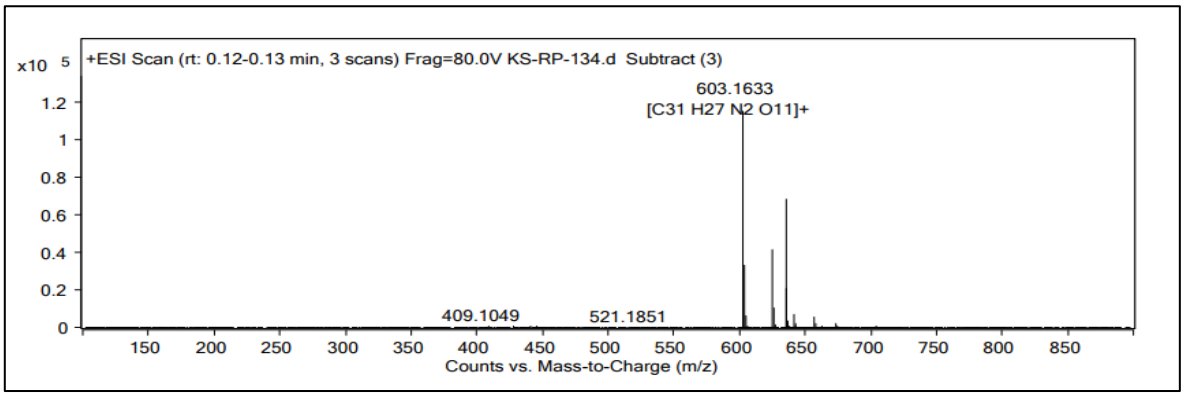

Figure S9. ESI-MS NMR spectra of **14**.

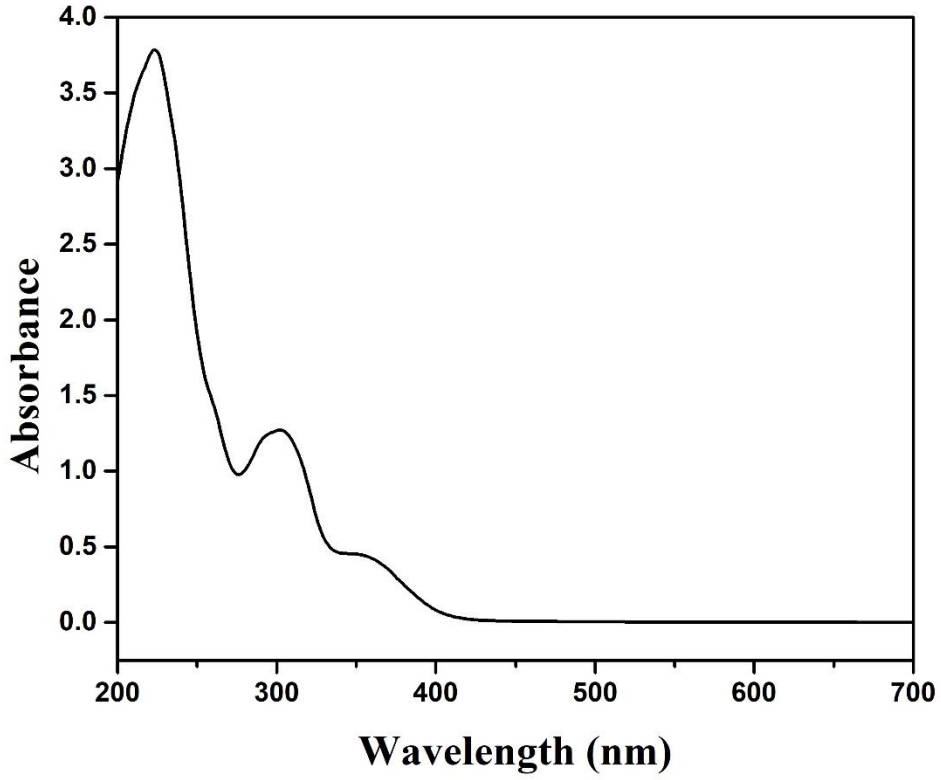

Figure S10. UV-Visible spectra of **14**.

The UV–Visible absorption spectrum of compound 14 exhibits two prominent absorption maxima at 302 nm and 359 nm. The peak at 302 nm corresponds to π–π* transitions, indicating the presence of aromatic and conjugated systems, while the peak at 359 nm is likely due to n–π* transitions associated with functional groups such as carbonyl or heteroatoms. These absorption features confirm the extended conjugation and electronic complexity of the compound 14 noscapine derivative.

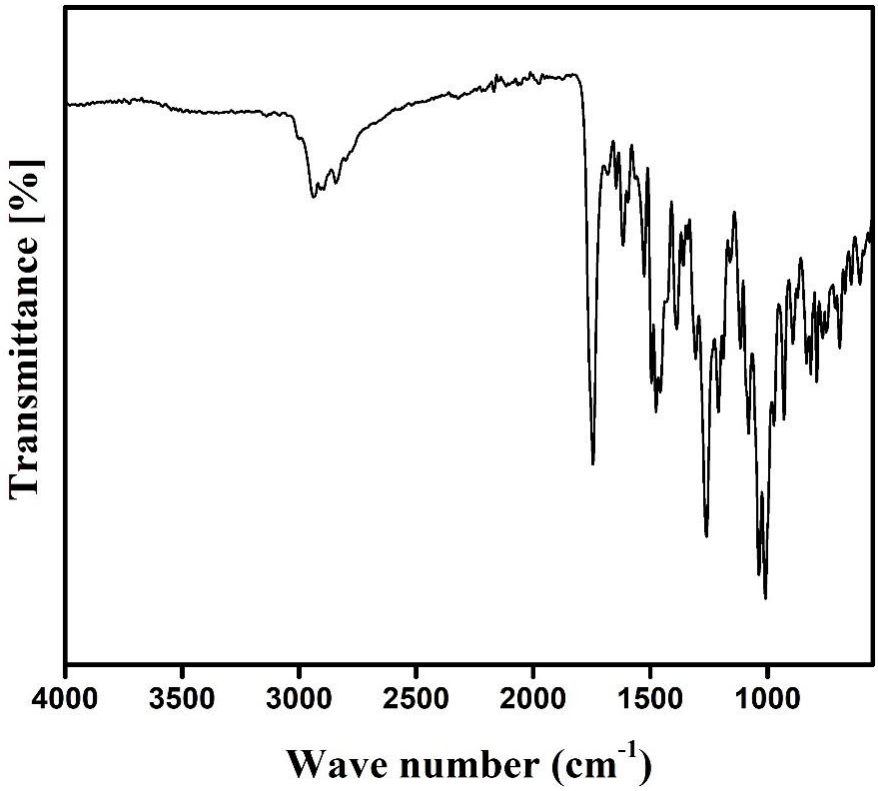

Figure S11. FT-IR spectra of 3-Br-Bn-Nos.

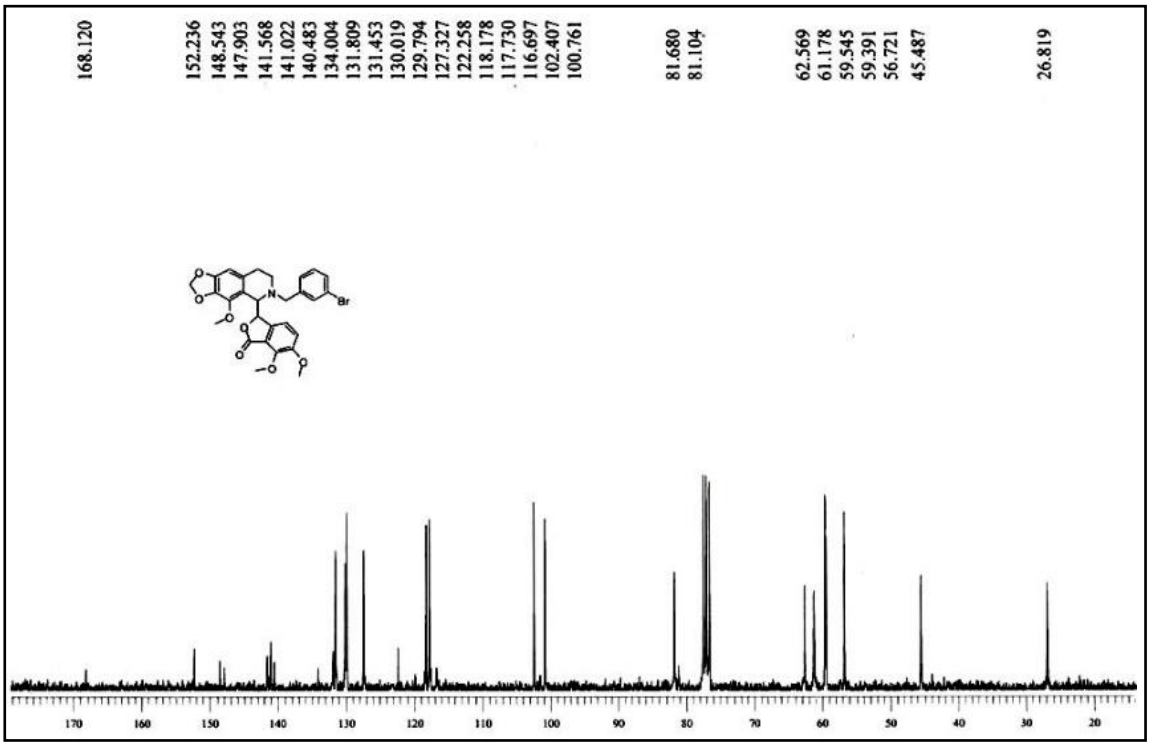

Figure S12. C^{13} NMR spectra of 3-Br-Bn-Nos.

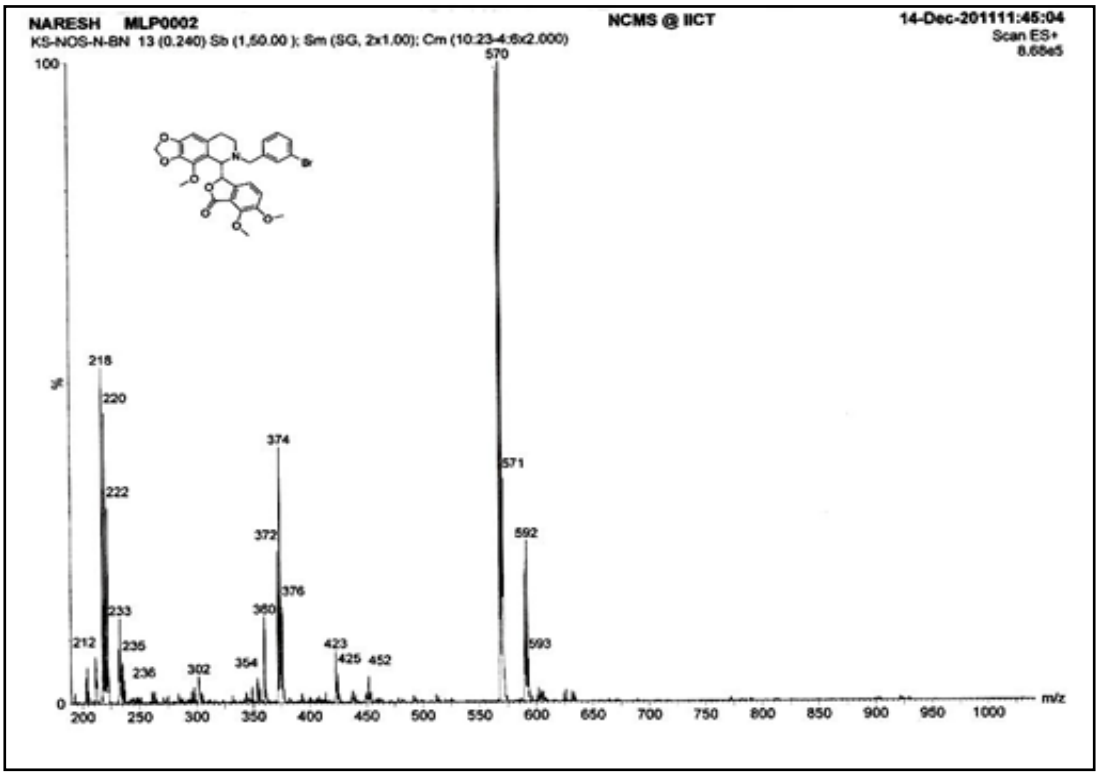

Figure S13. ESI-MS NMR spectra of 3-Br-Bn-Nos.

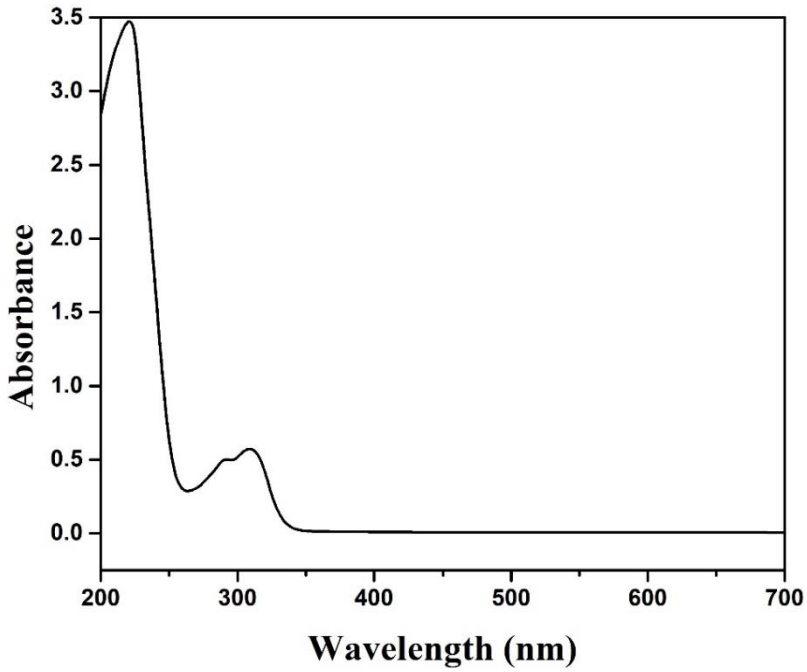

Figure S14. UV-Visible spectra of 3-Br-Bn-Nos.

The UV–Visible absorption spectrum of 3-Br-Bn-Nos shows a well-defined absorption maximum at 309 nm, which can be attributed to π–π* electronic transitions within the conjugated aromatic system. This λmax reflects the extended delocalization of electrons due to bromobenzyl substitution, suggesting enhanced conjugation relative to the parent noscapine structure.

Table S1. Geometry of hydrogen bonds and hydrophobic interaction of **3-Br-Bn-Nos** with the binding site residues of tubulin.

3-Br-Bn-Nos_Tubulin		
Hydrogen bonding		
Hydrogen Donor (D)	**Hydrogen Acceptor (A)**	**Distance (D-A) in Å**
GLN B 247	O5	2.78
Hydrophobic interaction		
15	**Tubulin**	**Distance**
UNK 900 C27	O	3.29
UNK 900 C13	O	3.42
UNK 900 O6	CD1	3.65
UNK 900 C27	CD1	3.85
UNK 900 C28	CG	3.71
UNK 900 O6	CG	3.39
UNK 900 C27	CG	3.89
UNK 900 C27	N	3.74
UNK 900 C26	OE1	3.77
UNK 900 C28	CG	3.76
UNK 900 C28	CB	3.85
UNK 900 O6	CB	3.48
UNK 900 O5	CB	3.73
UNK 900 C17	CB	3.83
UNK 900 O5	CA	3.69
UNK 900 C27	N	3.83
UNK 900 C16	N	3.72
UNK 900 O5	C	3.56
UNK 900 O5	CA	3.57
UNK 900 O1	CB	3.65
UNK 900 C13	O	3.78

Table S2. Geometry of hydrogen bonds and hydrophobic interaction of **13**, and **14** with the binding site residues of tubulin.

(a) 13_Tubulin			**(b) 14_Tubulin**		
Hydrogen bonding			**Hydrogen bonding**		
Hydrogen Donor (D)	**Hydrogen Acceptor (A)**	**Distance (D-A) in Å**	**Hydrogen Donor (D)**	**Hydrogen Acceptor (A)**	**Distance (D-A) in Å**
UNK 900	OD1	3.03	GLN A 15	O5	2.96
Hydrophobic interaction			**Hydrophobic interaction**		
13	**Tubulin**	**Distance**	**14**	**Tubulin**	**Distance**
UNK 900 O2	CD	3.49	UNK 900 O10	CD2	3.47
UNK 900 C7	CD	3.59	UNK 900 O10	CG	3.40
UNK 900 O2	CG1	3.70	UNK 900 C30	NE2	3.88
UNK 900 C6	OD1	3.08	UNK 900 C24	OE1	3.16
UNK 900 C5	OD1	3.89	UNK 900 C20	OE1	3.75
UNK 900 C1	OD1	3.44	UNK 900 C11	OE1	3.65
UNK 900 O1	CG	3.88	UNK 900 C9	OE1	3.66
UNK 900 C7	CB	3.60	UNK 900 O9	CD	3.72
UNK 900 O1	CB	3.30	UNK 900 C30	CD	3.88
UNK 900 C1	CB	3.85	UNK 900 O7	CD	3.59
UNK 900 C25	CG2	3.85	UNK 900 C30	CG	3.75
UNK 900 S1	N	3.83	UNK 900 O7	CG	3.78
UNK 900 S1	CA	3.89	UNK 900 O9	CB	3.72

UNK 900 S2	CB	3.83	UNK 900 N2	CB	3.83
UNK 900 S2	O	3.06	UNK 900 C24	O	3.42
UNK 900 S1	O	3.73	UNK 900 C13	O	3.22
UNK 900 S2	C	3.85	UNK 900 O7	C	3.56
UNK 900 C32	ND2	3.78	UNK 900 C13	C	3.89
UNK 900 C31	ND2	3.51	UNK 900 O7	CA	3.85
UNK 900 C30	ND2	3.52	UNK 900 C30	O	3.38
UNK 900 C29	ND2	3.80	UNK 900 C30	C	3.61
UNK 900 C29	OD1	3.86	UNK 900 O7	C	3.64
UNK 900 C27	OD1	3.69	UNK 900 C29	OE2	3.62
UNK 900 C33	O	3.37	UNK 900 C26	CZ	3.71
UNK 900 C32	O	3.82	UNK 900 C26	CE1	3.41
UNK 900 C27	CE	3.89	UNK 900 C25	CE1	3.63
UNK 900 N3	CE	3.40	UNK 900 C27	CD1	3.58
UNK 900 N2	CE	3.63	UNK 900 C26	CD1	3.29
UNK 900 N3	SD	3.62	UNK 900 C27	CG	3.73
UNK 900 N2	SD	3.41	UNK 900 C26	CG	3.59
UNK 900 C37	CB	3.77	UNK 900 C7	OG1	3.18
UNK 900 O10	CB	3.65	UNK 900 O1	CB	3.68
UNK 900 C18	O	3.70	UNK 900 C10	OE1	3.77
UNK 900 C17	O	3.83	UNK 900 C10	CD	3.69
UNK 900 C17	C	3.79	UNK 900 C6	CG	3.59
UNK 900 C36	O	3.48	UNK 900 C6	CB	3.43
UNK 900 C15	O	3.69	UNK 900 C1	CB	3.74
UNK 900 C12	O	3.44	UNK 900 O1	CA	3.49
UNK 900 O9	CD2	3.55	UNK 900 C1	CA	3.82
UNK 900 C36	CD1	3.59	UNK 900 O2	CB	3.76
UNK 900 O9	CD1	3.35	UNK 900 C7	CB	3.75
UNK 900 O9	CG	3.65	UNK 900 C7	O	3.88
UNK 900 C20	OG1	3.48	UNK 900 O1	C	3.81
UNK 900 C37	CD2	3.42	UNK 900 C29	CG2	3.45
UNK 900 O10	CD2	3.82	UNK 900 O6	CG2	2.99
UNK 900 C37	CE2	3.85	UNK 900 O6	CB	3.19
UNK 900 C37	CG	3.63	UNK 900 C3	CB	3.84
UNK 900 C37	CB	3.88	UNK 900 C3	O	3.89
UNK 900 C17	OG1	3.74	UNK 900 C21	NE2	3.75
UNK 900 O5	CG2	3.82	UNK 900 C21	NE2	3.83
UNK 900 C13	NH2	3.72	UNK 900 C25	OE1	3.50
UNK 900 C10	NH2	3.88	UNK 900 C25	CD	3.77
UNK 900 O7	CB	3.67	UNK 900 O5	CD	3.54
UNK 900 S2	O	3.45	UNK 900 O5	CG	3.86
UNK 900 C27	O	3.76			
UNK 900 O7	C	3.86			
UNK 900 O7	CA	3.44			

LIST OF PUBLICATION

RESEARCH ARTICLES

1. **Bhoi, N.**, Pradhan, L.K., Sahoo, D.R., Pradhan M.K., Mohanta P.P., Pragyandipta P., Baitharu, I. Naik, P.K. (2025) 'Potent therapeutic efficacy of 9-Bromo-Noscapine against Breast Cancer Cells via enhanced bioavailability of the Noscapine-Cyclodextrin inclusion complex'. Drug development research. (Manuscript ID: DDR-25-0062). DOI: 10.1002/ddr.70208 (*Published)*
2. **Bhoi, N.**, Kantevari S., Naik, P.K. (2025) Development of a FA-PLGA-PEG Loaded 3-Br-Benzyl-Noscapine Nanoparticle for Targeted Delivery into Breast Cancer Cell Lines: Chemical Synthesis and Experimental Validation. International Research Journal of Pharmacy and Medical Sciences. Volume 8, Issue 5, pp. 18-26, ISSN (Online): 2581-3277. *(Published)*
3. **Bhoi, N.,** Naik, P.K. (2025) Fabrication and Biological Evaluation of a 2:1 β-Cyclodextrin–Bromo-Noscapine Complex for Increased Solubility and Enhancing Anticancer Properties. Goya Journal. Volume 18, Issue 09, ISSN N0 :0017 – 2715. *(Published)*
4. **Bhoi, N.**, Naik, P.K. (2025) Design and Development of PLGA-PEG-FA Nanoparticles Encapsulating Noscapinoids for Receptor-mediated Breast Cancer Treatment. Journal of Drug Targeting. *(Under review)*
5. **Bhoi, N.**, Sahoo, D. R., Naik, E., Pradhan, A., Mishra, M., Pradhan, L. K., Rath S., Nayak N.R., Naik, P. K. (2025). Exploring the therapeutic potential of *Eulophia nuda* tuber by integrating phytochemical analysis with anticancer and antimicrobial efficacy, and in vivo safety profiling. Journal of Herbs, Spices & Medicinal Plants, 1–30. https://doi.org/10.1080/10496475.2025.2509183. *(Published)*
6. **Bhoi, N.**, Naik, P.K. (2025) Synthesis and biological evaluation of 6-Nitrocoumarin conjugated Noscapine as effective tubulin-targeting agent against breast cancer, Journal of Biomolecular Structure and Dynamics (Taylor and Francis). *(Under review)*
7. **Bhoi, N.**, Naik, P.K. (2025) Development of heterocyclic moiety conjugated noscapine analogs as novel tubulin-binding agent for breast cancer therapy, Bioorganic & Medicinal Chemistry (Elsevier). *(Under review)*
8. Sahoo, D.R., Babu, S.K., Naik, B.B., Hota, S.S., **Bhoi, N.**, Sarkar, B., Ali, S.K.M., Naik, P.K. UPLC–QToF–MS/MS screening and characterization of *Symphorema Polyandrum* Wight and in vitro assessment of its antioxidant, anticancer, and anti-

inflammatory potential. 3 Biotech, 14, 298 (2024). https://doi.org/10.1007/s13205-024-04144-x. *(Published)*

9. Wasupalli, G.K., **Bhoi, N.**, Sahoo, D.R., Mishra, M., Gartia, P., Rath, S., Naik, B.B. and Naik, P.K. (2025), Phytochemical Profiling and Bioactivity Assessment of Entada scandens Stem Extract: Insights In to Its Antioxidant, Antimicrobial, and Anticancer Activities. Chem. Biodiversity e00771. https://doi.org/10.1002/cbdv.202500771. *(Published)*
10. Behera, T., Rout, J., **Bhoi, N**., Mallik, S., Nag, S., Sethi, S., Pragyandipta, P., Nanda, P.K., Naik, P.K., Behera, N. Pyrazole-Infused Metal Complexes: Anticancer Activity, DNA Cleavage, and Biophysical Insights into DNA/BSA Interactions. ACS Applied Bio Materials 8, no. 10 (2025): 8611–8630. https://doi.org/10.1021/acsabm.5c00460.
11. **Bhoi, N.**, Mohanta P.P. 'Mimicking plant bionics for the development of advanced biosensors' published by Institute of Physics (IOP) Publishing in book project, titled "Advances in Biosensors: Applications in Environmental Monitoring, Plant Science and Human Welfare". *(Submitted)*

CONFERENCE PRESENTATION

1. **Namita Bhoi** and Pradeep Kumar Naik. "Metabolic labelling of glycerophospholipids; Phosphatidylethanolamine lipids (PE lipids) via clickable analogs with different derivatives of lipid head group''. Poster presentation at Odisha Research Conclave 2022. Organized by Odisha State Higher Education Council and Ravenshaw University, Odisha.
2. **Namita Bhoi** and Pradeep Kumar Naik. "Enhancing Breast Cancer Therapy with Nanoformulation of Bromo-Noscapine-Methyl-β-Cyclodextrin Complexes''. Poster presentation at Odisha Research Conclave 2023. Organized by Odisha State Higher Education Council and Sambalpur University, Odisha.
3. **Namita Bhoi** and Pradeep Kumar Naik. "*In silico*, *in vitro*, and *in vivo* evaluations of Noscapinoids loaded Methyl-β-Cyclodextrin Complex to improve Bioavailability and efficacy in Cancer therapy". Poster presentation at 29th Regional conference of Orissa Chemical society and National conference on Recent advances in Chemical Sciences 2024. Organized by Panchayat College Bargarh, Odisha.
4. **Namita Bhoi** and Pradeep Kumar Naik. "Development and Assessment of 9-Br-Noscapine-Mβ-Cyclodextrin Complex to Augment Bioavailability in Breast Cancer Therapy". Poster presentation in ETBB 2024. Organized by Department of Biotechnology and Bioinformatics, Sambalpur University, Odisha.

5. **Namita Bhoi** and Pradeep Kumar Naik. "*In-silico, in-vitro, and in-vivo* evaluation for enhancing Breast Cancer Therapy with 9-Bromo-Noscapine-Methyl-β-Cyclodextrin inclusion Complex". Oral presentation at International Conference on Biological Innovation, Technology, Engineering and Science (BITES-2024). Organized by the Department of Biotechnology and Medical Engineering and Department of Mechanical Engineering of National Institute of Technology, Rourkela, Odisha.
6. **Namita Bhoi** and Pradeep Kumar Naik. "Dual-Platform Drug Delivery System of Cyclodextrin and PLGA-PEG-FA Nanoparticles for Enhanced Solubility, Bioavailability, and Anticancer Efficacy of Brominated Noscapine''. Poster presentation at Odisha Research Conclave 2024. Organized by Odisha State Higher Education Council and Fakir Mohan University, Balasore, Odisha.
7. **Namita Bhoi** and Pradeep Kumar Naik. "Dual-Platform Drug Delivery System of Cyclodextrin and PLGA-PEG-FA Nanoparticles for Enhanced Solubility, Bioavailability, and Anticancer Efficacy of Brominated Noscapine". Poster presentation in Sambalpur University Research Conclave, 2025. Organized by Sambalpur University, Odisha.

TRAINING/WORKSHOP

1. Workshop On "Animal cell culture techniques and Screening of Drug molecules (ACTSDM-2022)" organized by Department of Biotechnology and Bioinformatics, Sambalpur university in association with Indian Institute of Technology, Gandhi Nagar under STUTI Programme.
2. Workshop On "Advanced characterisation technique" (2022) at School of Chemistry, in association with Banasthali Vidyapith, Rajasthan under STUTI Programme.

ACADEMIC HONORS AND AWARDS

1. **Best poster paper presentation award**, 2025 at Sambalpur University Research Conclave, 2025. Organized by Sambalpur University, Odisha. Poster Title: "Dual-Platform Drug Delivery System of Cyclodextrin and PLGA-PEG-FA Nanoparticles for Enhanced Solubility, Bioavailability, and Anticancer Efficacy of Brominated Noscapine".